



## City Research Online

### City, University of London Institutional Repository

---

**Citation:** Hauerhof, E. (2017). The assessment of oil products tanker design methods and technologies to enhance the Energy Efficiency Design Index measure by means of computer simulation and trend analysis. (Unpublished Doctoral thesis, City, University of London)

This is the accepted version of the paper.

This version of the publication may differ from the final published version.

---

**Permanent repository link:** <https://openaccess.city.ac.uk/id/eprint/17635/>

**Link to published version:**

**Copyright:** City Research Online aims to make research outputs of City, University of London available to a wider audience. Copyright and Moral Rights remain with the author(s) and/or copyright holders. URLs from City Research Online may be freely distributed and linked to.

**Reuse:** Copies of full items can be used for personal research or study, educational, or not-for-profit purposes without prior permission or charge. Provided that the authors, title and full bibliographic details are credited, a hyperlink and/or URL is given for the original metadata page and the content is not changed in any way.

**The assessment of oil products tanker  
design methods and technologies to enhance  
the Energy Efficiency Design Index measure  
by means of  
computer simulation and trend analysis**



**Elena Hauerhof**

This thesis is submitted for the degree of  
*Doctor of Philosophy*

Department of Mechanical Engineering and Aeronautics  
City University London

Supervisors

**Professor John Carlton, FREng**

**Professor Dinos Arcoumanis, FREng**

School of Mathematics, Computer Science and Engineering  
May 2017

# Table of Contents

Table of Contents.....	2
List of Figures.....	4
List of Tables.....	11
Acknowledgments.....	14
Abstract.....	15
Abbreviations and Explanatory Notes.....	16
General Nomenclature.....	19
EEDI Nomenclature.....	23
1 Introduction.....	24
2 Ship as a System Approach: Methods and Technologies to Enhance Ship Energy Efficiency.....	45
2.1 Operational Strategies.....	50
2.2 Hull Optimisation.....	56
2.3 Propellers and Energy Saving Devices.....	60
2.4 Machinery Improvements.....	67
2.5 Alternative Ship Propulsion and Fuels.....	75
3 Challenges in EEDI formulation.....	92
4 The Reference Ship: Oil Products Tanker.....	94
4.1 PhD Research Structure.....	97
5 Ship Performance Simulation Model.....	99
5.1 Module 1: Resistance and Propulsion.....	100
5.2 Module 2: Engine Performance Simulation.....	113
5.3 Module 3: Exhaust Emissions Prediction Model.....	117
5.4 Module 4: Energy Efficiency Design Index (EEDI) Calculator.....	143
6 Time Domain Voyage Simulation.....	144
7 Energy Efficient Propellers.....	154
7.1 The Effect of a Wake Equalising Duct.....	155
7.2 CLT Propellers.....	164
7.3 Ducted Propellers.....	169

7.4 Impact on the Energy Efficiency Indicators .....	176
8 Propeller Optimisation .....	181
8.1 The Effect of BAR on Ship Efficiency .....	183
8.2 The Effect of Artificially Increased Propeller Diameters .....	188
8.3 Impact on the Energy Efficiency Indicators .....	196
9 Maximum Propeller Diameter .....	203
9.1 The Estimation of the Optimum Diameter-RPM Combinations .....	203
9.2 Propeller Clearances .....	206
9.3 Propellers Performance Analysis .....	208
9.4 Impact on the Energy Efficiency Indicators .....	214
10 Energy Efficient Trim Optimisation .....	220
10.1 Trim Definition .....	221
10.2 Hull Design Parameters .....	223
10.3 Ship Resistance .....	223
10.4 Propulsive Efficiency .....	227
10.5 Impact on the Energy Efficiency Indicators .....	229
11 Future Hybrid Propulsion Concepts.....	233
11.1 On-Time Voyage Simulation .....	235
11.2 Optimum Load Voyage Simulation .....	240
12 EEDI Amendments Proposal .....	246
13 Conclusion .....	258
14 Recommendations .....	265
15 Suggestions for Further Research .....	266
References .....	267
Appendix I. The Energy Efficiency Design Index Methodology .....	273
Appendix II. Propeller Design Procedure for Wageningen series .....	282
Appendix III. Blade Area Ratio Estimation Procedure.....	287

## List of Figures

Figure 1.1 Growth of international seaborne trade over selected years.....	24
Figure 1.2. World seaborne trade in cargo ton–miles by cargo type.....	25
Figure 1.3 World fleet by vessel type.....	25
Figure 1.4 Percentage distribution of the world fleet by ship category in 2015.....	26
Figure 1.5 Simplified composition of the exhaust gas flow from the ship with 2-stroke diesel engine burning the ISO 8217 fuel oil.....	27
Figure 1.6 The total shipping $CO_2$ emissions for the period 2007-2012.....	28
Figure 1.7 The $NO_x$ emissions for the period of 2007 – 2012 in million tonnes of $NO_2$ .....	29
Figure 1.8 The $SO_x$ emissions for the period of 2007 – 2012 in million tonnes of $SO_2$ .....	30
Figure 1.9 The $CO$ emissions in million tonnes from shipping industry for the period of 2007-2012.....	31
Figure 1.10 The $NM VOC$ emissions in million tonnes from shipping industry for the period of 2007-2012.....	32
Figure 1.11 The $PM$ emissions in million tonnes from shipping industry for the period of 2007-2012.....	33
Figure 1.12 The overall impact of the atmospheric emissions from shipping on the environment.....	35
Figure 1.13 Top 10 Flags of registration with the largest registered fleets as of 1 January 2015...37	
Figure 1.14 Ownership of the world fleet as of 1 January 2015.....	37
Figure 1.15 Main components of the legislative framework of the shipping industry.....	39
Figure 1.16 IMO air pollution prevention legislative framework.....	40
Figure 2.1 Integrated ship system diagram.....	49
Figure 2.2 Average at-sea main engine load factor for oil tankers in 2007 - 2012.....	51
Figure 2.3 Oil tankers: percentage change in fuel consumption associated with the 1 percent reduction in steel weight.....	57
Figure 2.4 SFOC behaviour comparison under conventional and de-rated conditions.....	70
Figure 2.5 Average daily fuel oil consumption. Based on annual BP review.....	76
Figure 2.6 General range of biofuels types and their production routes.....	79
Figure 2.7 Aquarius MRE (Marine Renewable Energy) system by Eco Marine Power.....	83
Figure 2.8 Steam turbine plant powered by a nuclear reactor.....	85
Figure 2.9 Working principle of the basic solid polymer fuel cell.....	87
Figure 2.10 Battery based load leveling ship operation concept.....	91
Figure 4.1 World seaborne trade of petroleum products and gas in million of tonnes.....	94
Figure 4.2 Global tankers fleet distribution.....	95

Figure 5.1 Ship Performance Simulation (SPS) model .....	99
Figure 5.2 General components of ship's total resistance .....	101
Figure 5.3 The workflow of the ship resistance and propulsion prediction module.....	105
Figure 5.4 The comparison chart of the effective power from the model test report (MTR) and effective power obtained from the H&M regression-based simulation of the naked hull under the design load condition.....	107
Figure 5.5 The comparison chart of the effective power from the model test report (MTR) and effective power obtained from the H&M regression-based simulation of the naked hull under the ballast condition.....	107
Figure 5.6 Comparison diagram of the open water test (OWT) data from the model test report (MTR) and computations using the Wageningen B-screw series (WAG) regression-based method .....	110
Figure 5.7 The energy flow diagram of the conventional mechanical drive system installed on the reference tanker. ....	113
Figure 5.8 The resulting table of the CEAS engine simulation tool.....	116
Figure 5.9 The 5S50ME-C engine layout and performance diagram.....	116
Figure 5.10 <i>CO</i> and <i>HC</i> spline interpolation results .....	119
Figure 5.11 The absolute humidity of intake air <i>Ha</i> spline interpolation validation .....	120
Figure 5.12 Comparison pattern of the absolute humidity of the intake air and dry/wet correction factors over range of engine loads.....	121
Figure 5.13 Comparison pattern of the exhaust gas flow and dry/wet correction factors over range of engine loads.....	121
Figure 5.14 The comparison plot of the <i>CO</i> <sub>2</sub> concentrations in dry exhaust.....	127
Figure 5.15 The comparison analysis of the dry <i>O</i> <sub>2</sub> concentrations calculated using the reversed fuel analysis procedure and the dry <i>O</i> <sub>2</sub> concentrations listed in the <i>NO</i> <sub>x</sub> technical file of 7S50MC-C .....	134
Figure 5.16 Expanded initial <i>NO</i> <sub>x</sub> dataset based on cubic spline interpolation .....	137
Figure 5.17 The validation of <i>NO</i> <sub>x</sub> model output for 7S50MC-C engine: the <i>NO</i> <sub>x</sub> technical file based interpolated volumetric <i>NO</i> <sub>x</sub> concentrations vs. the <i>NO</i> <sub>x</sub> model output.....	138
Figure 5.18 Resulted <i>NO</i> <sub>x</sub> concentrations of 5S50MC-C engine compared to initial <i>NO</i> <sub>x</sub> concentrations of 7S50MC-C engine .....	138
Figure 5.19 The comparison of exhaust gas temperatures of 7S50MC-C and 5S50ME-C engines .....	139
Figure 5.20 Attained and required EEDIs for the reference oil products tanker .....	143
Figure 6.1 Typical service data relationships (Molland et al. 2011) .....	145
Figure 6.2. The effect of weather on ship's power requirements based on the trial allowances simulation model .....	147
Figure 6.3 Unfiltered Admiralty coefficient versus apparent slip .....	148

Figure 6.4 Filtered Admiralty coefficient versus apparent slip .....	149
Figure 6.5 Filtered service data in time domain. Numbers at the top of the graph are Beaufort numbers.....	149
Figure 6.6 Filtered service data with engine power corrected to the mean displacement.....	150
Figure 6.7 Filtered service data sorted by Beaufort number and speed.....	150
Figure 6.8 Artificial time-domain ship performance simulation. Numbers at the top of the graph are Beaufort numbers.....	151
Figure 6.9 Artificial ship performance in service sorted by Beaufort number, speed and load condition. Numbers at the top of the graph are Beaufort numbers .....	152
Figure 6.10 The reference ship time-domain voyage simulation. Numbers at the top of the graph are Beaufort numbers.....	153
Figure 7.1 Current propulsion system of the reference products tanker fitted with a CLT propeller .....	154
Figure 7.2 Effective power comparison between the propulsion systems with and without the wake equalizing duct.....	157
Figure 7.3 The open water efficiency correction to the Wageningen standards.....	158
Figure 7.4 The wake fraction comparison results of the fixed pitch propeller with the wake equalizing duct (FPP_WED) based on the model test report versus the conventional fixed pitch propeller (FPP) calculated using the Holtrop and Mennen approach .....	159
Figure 7.5 The thrust deduction comparison results of the fixed pitch propeller with the wake equalizing duct (FPP_WED) based on the model test report versus the conventional fixed pitch propeller (FPP) calculated using the Holtrop and Mennen approach .....	160
Figure 7.6 The hull efficiency comparison results of the fixed pitch propeller with the wake equalizing duct (FPP_WED) based on the model test report versus the conventional fixed pitch propeller (FPP) calculated using the Holtrop and Mennen approach .....	161
Figure 7.7 The open water efficiency comparison results of the fixed pitch propeller with the wake equalizing duct (FPP_WED) based on the model test report and corrected to the Wageningen standards versus the conventional fixed pitch propeller (FPP) calculated using the Holtrop and Mennen approach.....	162
Figure 7.8 The QPC comparison results of the fixed pitch propeller with the wake equalizing duct (FPP_WED) based on the model test report and corrected to the Wageningen standards versus the conventional fixed pitch propeller (FPP) calculated using the Holtrop and Mennen approach ...	162
Figure 7.9 The power absorption requirements of the fixed pitch propeller with the wake equalizing duct (FPP_WED) based on the model test report and corrected to the Wageningen standards versus the conventional fixed pitch propeller (FPP) calculated using the Holtrop and Mennen approach .....	163
Figure 7.10 The full-scale CLT propeller and the conventional fixed pitch (FP) propeller curves .....	166
Figure 7.11 The wake fraction comparison results of the fixed pitch propeller (FPP_WED) and the CLT propeller (CLT_WED) both with the wake equalising duct .....	166

Figure 7.12 The hull efficiency comparison results of the fixed pitch propeller (FPP_WED) and the CLT propeller (CLT_WED) both with the wake equalising duct .....	167
Figure 7.13 The open water efficiency comparison results of the fixed pitch propeller (FPP_WED) and the CLT propeller (CLT_WED) both with the wake equalising duct.....	168
Figure 7.14 The power absorption results of the fixed pitch propeller (FPP_WED) and the CLT propeller (CLT_WED) both with the wake equalising duct.....	168
Figure 7.15 The Ka 4-70 propeller diameter interpolation diagram as part of the propeller design procedure .....	171
Figure 7.16. Ducted propeller design procedure .....	172
Figure 7.17 The comparison results of the hull efficiency of the 19A ducted propeller (DUCT) and the conventional fixed pitch propeller (FPP).....	173
Figure 7.18 The comparison results of the propeller efficiency of the 19A ducted propeller (DUCT) and the conventional fixed pitch propeller .....	174
Figure 7.19 The comparison results of the propulsive efficiency (QPC) of the 19A ducted propeller (DUCT) and the conventional fixed pitch propeller (FPP) .....	175
Figure 7.20 The power absorption of the 19A ducted propeller system (DUCT) and the conventional fixed pitch propeller (FPP) .....	175
Figure 7.21 The comparative analysis of the required delivered power under different loads and corresponding operational speed .....	176
Figure 7.22 Engines service curves for all the propeller systems.....	177
Figure 7.23 The EEDI results for all propeller systems .....	179
Figure 7.24 The voyage simulation results of all propeller systems .....	180
Figure 8.1 Effect of $BAR$ on the relative-rotative efficiency $\eta_R$ .....	184
Figure 8.2 Effect of $BAR$ s on the open water efficiency for the 4-bladed propeller .....	185
Figure 8.3 Effect $BAR$ s on ship delivered power $P_D$ over a range of speeds. ....	186
Figure 8.4 Artificial $BAR$ cavitation performance based on Burrill's curves .....	186
Figure 8.5 Power absorption of the conventional fixed pitch propeller with the original $BAR = 0.5628$ vs $BAR = 0.4$ under design, ballast and loaded conditions.....	188
Figure 8.6 Thrust loading distribution for the artificial propeller diameters .....	189
Figure 8.7 Propeller design process based on the artificially selected propeller diameters .....	190
Figure 8.8 Hull efficiency behaviour with the artificially changing propeller diameters.....	191
Figure 8.9 Relative-rotative efficiency behaviour with changing propeller diameters .....	192
Figure 8.10 Open water efficiency behaviour with changing propeller diameters.....	193
Figure 8.11 Effect of the artificially increased propeller diameters on ship delivered power $P_D$ over a range of speeds. ....	193
Figure 8.12 Cavitation performance due to the artificial diameters based on Burrill's curves ....	194

Figure 8.13 Comparison plot of the power absorption requirements of the fixed pitch propeller with the original $D = 5.65\text{m}$ and the artificially increased and decreased diameters by 5 percent under design, ballast and loaded conditions.....	196
Figure 8.14 Comparative analysis of the required delivered power under different loads and corresponding operational speed.....	197
Figure 8.15 Engines service curves for FPP_ORG, FPP_BAR_MIN, FPP_D_PLUS_5% propeller systems.....	198
Figure 8.16 Enlarged version of Figure 8.15. Engines service curves for FPP_ORG, FPP_BAR_MIN, FPP_D_PLUS_5% propeller systems. ....	198
Figure 8.17 EEDI results for FPP_ORG, FPP_BAR_MIN, FPP_D_PLUS_5% propeller systems. ....	200
Figure 8.18 Voyage simulation results for FPP_ORG, FPP_BAR_MIN, FPP_D_PLUS_5% propeller systems. ....	200
Figure 9.1 Optimum RPM – diameter range design process .....	205
Figure 9.2 Resulted optimum RPM – diameter range .....	206
Figure 9.3 Hull surface pressure distribution.....	206
Figure 9.4 FPP_MAX (left) and FPP_MAX_SHAFT (right) applied to the reference stern design with the lifted shaft on the latter case. ....	207
Figure 9.5 $RPM$ – diameter ranges at different ship speeds (design conditions).....	209
Figure 9.6 Resulted $RPM$ distributions at different loads.....	210
Figure 9.7 Hull efficiency results for FPP, FPP_MAX and FPP_MAX_SHAFT at the ballast, design and loaded conditions. ....	211
Figure 9.8 Relative-rotative efficiency results for FPP, FPP_MAX and FPP_MAX_SHAFT at the ballast, design and loaded conditions.....	212
Figure 9.9 Open water efficiency results for FPP, FPP_MAX and FPP_MAX_SHAFT at the ballast, design and loaded conditions. ....	212
Figure 9.10 Delivered power results for FPP, FPP_MAX and FPP_MAX_SHAFT at the ballast, design and loaded conditions. ....	213
Figure 9.11 Hull surface pressures for FPP, FPP_MAX and FPP_MAX_SHAFT at the ballast, design and loaded conditions. ....	213
Figure 9.12 Engines service curves for all propeller systems.....	215
Figure 9.13 EEDI results for all propeller systems.....	217
Figure 9.14 Voyage simulation results of all propeller systems. ....	218
Figure 10.1 Schematic representation of considered trim conditions.....	221
Figure 10.2 Frictional resistance $R_F$ and frictional coefficient $C_F$ performance due to changing trim. ....	224
Figure 10.3 Bulbous bow resistance $R_{BB}$ and correlation resistance $R_A$ performance due to changing trim.....	225

Figure 10.4 Wave-making resistance $R_W$ performance due to changing trim.....	225
Figure 10.5 Total resistance $R_T$ and effective power $P_E$ performance due to changing trim. ....	226
Figure 10.6 Effect on the propulsive efficiency components due to changing trim. ....	228
Figure 10.7 Power absorption $R_D$ and $QPC$ performance due to changing trim. ....	228
Figure 10.8 Resulting level of gains and reductions of power in percentage due to changing trim .....	229
Figure 10.9 Engines service curves for partially loaded operation at both trim conditions and the even keel.....	230
Figure 10.10 Voyage simulation results for both trim conditions and the even keel. Numbers at the top of the graph are Beaufort numbers .....	231
Figure 11.1 Original voyage of the reference oil products tanker. Numbers at the top of the graph are rotational speeds .....	234
Figure 11.2 Hybrid-based machinery arrangement for the reference vessel .....	234
Figure 11.3 Ship speed distribution during the original voyage.....	236
Figure 11.4 Sea state probability analysis results.....	236
Figure 11.5 Speed, load and SFOC arrangements for the completed voyage on time (ON_TIME) operation.....	237
Figure 11.6 ON_TIME voyage simulation. Numbers at the top of the graph are Beaufort numbers .....	237
Figure 11.7 ON_TIME battery charging/discharging diagram .....	238
Figure 11.8 ON_TIME_SPEED voyage simulation.....	239
Figure 11.9 ON_TIME_SPEED battery charging/discharging diagram .....	239
Figure 11.10 Speed, load and SFOC arrangements for the OPTIMUM operation .....	241
Figure 11.11 OPTIMUM voyage simulation .....	242
Figure 11.12 OPTIMUM battery charging/discharging diagram.....	242
Figure 11.13 OPTIMUM_SPEED voyage simulation .....	243
Figure 11.14 OPTIMUM_SPEED battery charging/discharging diagram.....	243
Figure 12.1 Attained EEDI, required EEDI due to 2015 and the EEDI weather of the reference oil products tanker .....	247
Figure 12.2 Measured ship service engine power and ship speed observed.....	248
Figure 12.3 Service data used for the EEDI calculation: service SMCR, original engine power measurements and SFOC at 75 percent load corresponding to service SMCR.....	249
Figure 12.4 Service data used for the EEDI calculation: ship DWT and speed observed.....	250
Figure 12.5 Resulting service EEDI distribution sorted by Beaufort number.....	250
Figure 12.6 Mean service EEDI indexes grouped by Beaufort number in comparison with the original attained EEDI, reference EEDI and the EEDI weather.....	251

Figure 12.7 The effect of weather on service engine power and ship speed behaviour.....	251
Figure 12.8 Mean service DWT, mean service speeds and their linear trend lines. ....	252
Figure 12.9 3D map correlation between the Beaufort scale, ship displacement and the EEDI measure .....	253
Figure 12.10 Mean service EEDI indexes based on constant DWT grouped by Beaufort number in comparison with the original attained EEDI, reference EEDI and the EEDI weather.....	254
Figure 12.11 Resulting constant DWT EEDI distribution sorted by Beaufort number in comparison with the originally obtained service DWT.....	254
Figure 12.12 Sea state probability analysis results .....	255
Figure 12.13 Original attained EEDI, EEDI weather and the amended EEDI values .....	256

## List of Tables

Table 2.1 Potential applicability and implementation time frame of energy efficient measures and technologies .....	47
Table 2.2 General properties of hull coatings prevailed in service .....	55
Table 2.3 Maximum allowable ship dimensions in canals and channels .....	58
Table 2.4 Recommended WHRS for various propulsion systems based on the rule of thumb ..	74
Table 2.5 Li-ion cell comparison.....	89
Table 4.1 Basic propellers characteristics .....	95
Table 4.2 Principle ship dimensions based on model test report.....	96
Table 5.1 Complete resistance and propulsion module simulation results for designed, ballast and loaded conditions.....	111
Table 5.2 The $NO_x$ file emissions data related to the 7S50MC-C marine diesel engine .....	117
Table 5.3 The elemental chemical breakdown of the MDO fuel used .....	118
Table 5.4 Coefficient $u_{gas}$ for raw exhaust gas .....	122
Table 5.5 $CO$ calculation results for the reference engine 5S50ME-C.....	123
Table 5.6 $HC$ calculation results for the reference engine 5S50ME-C.....	124
Table 5.7 $CO_2$ calculation results for the reference engine 5S50ME-C .....	128
Table 5.8 The reference fuel analysis on required amount of combustion air.....	130
Table 5.9 The excess air approximation results for 7S50MC-C engine.....	131
Table 5.10 Masses of exhaust gas products with excess of $O_2$ .....	132
Table 5.11 The amount of substances of exhaust products on a wet and dry basis.....	132
Table 5.12 The proportion of exhaust products on wet and dry basis .....	133
Table 5.13 The results of the inverted fuel analysis procedure for the reference 5S50ME-C engine .....	134
Table 5.14 $NO_x$ multi linear regression model inputs.....	136
Table 5.15 Regression statistics.....	137
Table 5.16 $NO_x$ calculation results for the reference engine 5S50ME-C.....	140
Table 5.17 Fuel oil sulphur contents and corresponding emissions level .....	141
Table 5.18 $SO_2$ prediction results for the reference engine 5S50ME-C.....	142
Table 6.1 Beaufort scale .....	144
Table 6.2 The overall results of the reference ship voyage simulation .....	153
Table 7.1 The list of the researched propeller systems.....	155

Table 7.2 The comparison results of the conventional fixed pitch propeller (FPP) and the fixed pitch propeller with the wake equalizing duct (FPP_WED) performance at the design condition (14.6 knots) .....	159
Table 7.3 Delivered power reductions due to effect of the wake equalizing duct .....	163
Table 7.4 The comparison results of CLT propeller with wake equalizing duct (CLT_WED) and fixed pitch propeller with wake equalizing duct (FPP_WED) performance at design condition and 14.6 knots .....	165
Table 7.5 CLT propeller open water performance at the full scale based on the Hamburg Ship Model Basin (HSVA) tests .....	165
Table 7.6 Delivered power reductions due to the CLT propeller .....	168
Table 7.7 The comparison results of the 19A ducted propeller (DUCT) and the conventional fixed pitch propeller (FPP) at the design load condition and speed of 14.6 knots.....	173
Table 7.8 Delivered power reductions due to the ducted propeller .....	175
Table 7.9 The range of selected engines and their SMCR.....	177
Table 7.10 The summary table of propellers performance at the normal continuous rating (NCR) .....	178
Table 7.11 The fuel consumption and emissions footprint performance per voyage .....	180
Table 7.12 The average SFOC and engine load per voyage.. .....	180
Table 8.1 Considered propeller design characteristics.....	183
Table 8.2 Comparison results of fixed pitch performance with reduced <i>BARs</i> at design condition and operational speed of 14.6 knots.....	187
Table 8.3 Delivered power reductions due to <i>BAR</i> = 0.5 and <i>BAR</i> = 0.4 .....	188
Table 8.4 Results of the design procedure: the artificial propellers characteristics.....	189
Table 8.5 Comparison results of the fixed pitch propeller with artificial propeller diameters ad design condition and speed of 14.6 knots .....	195
Table 8.6 Average fluctuations of the delivered power $P_D$ due to artificially changing diameters .....	195
Table 8.7 List of SMCRs for each propeller case.....	197
Table 8.8 Summary table of propellers performance at NCR condition.....	199
Table 8.9 The fuel consumption and emissions footprint performance.....	201
Table 8.10 Average SFOC and engine load per voyage. ....	201
Table 9.1 FPP_MAX and FPP_MAX_SHAFT diameter calculation procedure.....	207
Table 9.2 Final propellers dimensions .....	208
Table 9.3 Comparison results of the FPP, FPP_MAX, and FPP_MAX_SHAFT performance at design condition and speed of 14.6 knots. ....	210
Table 9.4 Delivered power reductions at design ship speeds.....	214
Table 9.5 Range of selected engines and their SMCR.....	215

Table 9.6 Summary table of propellers performance at the NCR condition. ....	216
Table 9.7 Fuel consumption and emissions footprint performance per voyage. ....	218
Table 9.8 Average SFOC and engine load per voyage.....	218
Table 10.1 Initial hull dimensions at different trim conditions .....	222
Table 10.2 Changing hull parameters due to trim .....	223
Table 10.3 Ship resistance components under changing trim conditions (Design condition at 14.6 knots) .....	224
Table 10.4 Propulsive efficiency components under changing trim conditions (Design condition at 14.6 knots) .....	227
Table 10.5 Summary table of engine performance due to changing trim at 14.6 knots .....	230
Table 10.6 Fuel consumption and emissions footprint performance per voyage .....	231
Table 10.7 Average SFOC and engine load per voyage.....	232
Table 11.1 ON_TIME and ON_TIME_SPEED voyage results .....	240
Table 11.2 OPTIMUM and OPTIMUM_SPEED voyage results.....	244
Table 11.3 Fuel consumption and emissions footprint performance per voyage .....	245
Table 12.1 Obtained EEDI values .....	256
Table 12.2 Impact of amended EEDI values on global CO <sub>2</sub> reduction level.....	257
Table A 1. Parameters for determination of standard fw value.....	278
Table A 2. Variables for calculating the required EEDI.....	281

## **Acknowledgments**

My special gratitude goes to my supervisors Professor John Carlton and Professor Dinos Arcoumanis for their unconditional help, wisdom and support during the past four years.

My sincere thanks also go to Dr Zabi Bazari for his insightful comments and encouragement regarding the EEDI methodology as well as Philip Martin for his wise recommendations regarding the marine diesel engine performance simulation.

I thank my fellow colleagues and friends, Dr Saeed Javdani, Dr Maria Krotsiani and Dr Alexander Kachkaev for the stimulating discussions and for all the fun we have had in the last four years.

Last but not the least, I would like to thank my family: my parents Michael Shcherbakov and Svetlana Shcherbakova for supporting me spiritually throughout writing this thesis and my life in general as well as my husband and greatest friend Ilja Hauerhof for his unconditional support, useful criticism and patience during past four years.

## Abstract

The primary objective of this PhD research is *to develop an advanced understanding of the necessary and realistic performance expectations from a full form medium size ship system by means of numerical computer modelling. This includes the minimisation of the harmful environmental signature by increasing its efficiency in compliance with the EEDI requirements while in search of how the EEDI methodology might be enhanced.* The investigation has focused on a medium sized products tanker acting as a midpoint of the spectrum of ship sizes within the range of 20,000 – 60,000 DWT of this type.

In order to solve such an extensive problem, in the first place, it was important to analyse the energy efficient technology market in a structured manner and then, to identify the most favourable fuel consumption reduction methods that can be associated with the examined ship type. Next, an integrated computer simulation model, involving linked engine, propeller and hull analysis programs, has been developed and calibrated with the model tests and sea trial data. The ship system has been analysed under diverse conditions including various propulsion systems, innovative machinery arrangements, efficiency-enhancing hydrodynamic appendages as well as changing weather and load conditions.

The evaluation of potential benefits associated with the deployment of innovative technology(s), operation profile(s) or their combination has been made by comparing the designated Energy Efficiency Indicators (EDI), namely, the propulsive efficiency, fuel oil consumption, exhaust emissions footprint and EEDI, respectively associated with the technical, fuel savings, environmental and legal perspectives.

In addition, such a comprehensive analysis has also helped to detect a number of uncertainties in the current EEDI formulation while pointing out ways in which it can be improved.

## Abbreviations and Explanatory Notes

AFC	Alkaline Fuel Cell
AHR	Average Hull Roughness
BAU	Business as usual
BL	Base Line
CDP	Controlled Depletion Polymer
CFD	Computational Fluid Dynamics
CLT	Contracted and Loaded Tip Propeller
CO	Carbon monoxide
CO <sub>2</sub>	Carbon dioxide
CPP	Controllable Pitch Propeller
CRP	Contra-Rotating Propeller
DAS	Days at Sea
DME	Di-Methyl Ether
DMFC	Direct Methanol Fuel Cell
DWT	Deadweight tonnes
ECA	Environmental Control Areas
EDI	Energy Efficiency Indicator
EEDI	Energy Efficiency Design Index
EEOI	Energy Efficiency Operational Indicator
EGB	Exhaust Gas Bypass
EGR	Exhaust Gas Recirculation
EIAPP	Engine International Air Pollution Prevention
EIV	Estimated Index Values
ESD	Energy Saving Devices
FAME	Fatty Acid Methyl Ester
FC	Fuel Cell
FP	Fixed Pitch Propeller
GHG	Greenhouse gas
GT	Gross tonnage
H	Hydrogen
HC	Hydrocarbons
HFO	Heavy Fuel Oil
HVO	Hydro-Treated Vegetable Oil
IEEC	International Energy Efficiency Certificate
ILO	International Labour Organisation

IMO	International Maritime Organisation
IPCC	Intergovernmental Panel on Climate Change
LEU	Low Enrichment Uranium
LNG	Liquefied Natural Gas
MALS	Mitsubishi Air Lubrication System
MARPOL	International Convention for the Prevention of Pollution from Ships
MCFC	Molten Carbonate Fuel Cell
MCR	Maximum Continuous Rating
MDO	Marine Diesel Oil
MEP	Mean Effective Pressure
MEPC	Marine Environment Protection Committee
N <sub>2</sub>	Nitrogen
NaOH	Caustic Soda
NH <sub>3</sub>	Ammonia
NMC	Nickel Manganese Cobalt
NMVOG	Non-Methane Volatile Organic Compounds
NO <sub>x</sub>	Oxides of nitrogen
O <sub>2</sub>	Oxygen
O <sub>3</sub>	Ozone
ORC	Organic Rankine Cycle
PEFC	Phosphoric Acid Fuel Cell
PM	Particulate matter
PT	Power Turbine
PTG	Power Turbine and Generator
PV	Photovoltaic
QPC	Quasi Propulsive Coefficient
R&D	Research and Development
RC	Rankine Cycle
RF	Radiative Forcing
RNG	Re-Normalisation Group
RPM	Rotation per Minute
SCR	Selective Catalytic Reduction
SEEMP	Ship Energy Efficiency Management Plan
SFOC	Specific Fuel Oil Consumption
SMCR	Specific Maximum Continuous Rating
SO <sub>2</sub>	Sulphur dioxide

SO <sub>3</sub>	Sulphur trioxide
SO <sub>4</sub>	Sulphate
SOFC	Solid Oxide Fuel Cell
SO <sub>x</sub>	Oxides of sulphur
SPC	Self-Polishing Copolymer
ST	Steam Turbine
STG	Steam Turbine and Generator
TEU	Twenty-Foot Equivalent Unit
TOE	Tonnes of Oil Equivalent
UCL	University College London
UNCLOS	The United Nations Convention on the Law of the Sea
UNCTAD	The United Nations Conference on Trade and Development
UNFCCC	The United Nations Framework Convention on Climate Change
VLCC	Very Large Crude Carrier
VOC	Volatile organic compound
VTA	Variable Turbocharger Area
VTG	Variable Turbine Geometry
WED	Wake Equalising Duct
WHRS	Waste Heat Recovery System

## General Nomenclature

$(1 + k)$	Form factor of the hull describing the viscous resistance of the hull form in relation to $R_F$
$(1 + k_1)$	Form factor representation in the Holtrop and Mennen method
$\Delta$	Displacement tonnage
$\Delta S$	Speed reduction as percentage of the baseline speed
$\nabla$	Displacement volume
$A/F_{ACT}$	Actual air to fuel ratio
$A/F_{ST}$	Air to fuel ration stoichiometric
$A_{BB}$	Bulbous bow area
$A_C$	Admiralty coefficient
$A_E$	Propeller expanded area
$A_E/A_O$	Blade area ratio
$A_M$	Midship section area
$A_O$	Propeller disk area
$A_P$	Propeller projected area
$A_{TR}$	Immersed transom area
$A_{WPL}$	Waterplane area
$B$	Beam
$B_n$	Beaufort number
$B_p$	Admiral Taylor's coefficient
$B_{TR}$	Immersed transom breadth
$C_B$	Block Coefficient
$C_{CA}$	Correlation coefficient
$c_d$	Exhaust gas emissions component estimated on a dry basis
$C_F$	Skin friction coefficient
$c_{gas}$	Concentration of the respective component in the raw exhaust gas on a wet basis
$CL$	Depth of the centre line
$C_M$	Midship section area coefficient
$C_P$	Prismatic coefficient Reference coefficient for N.S.M.B Trial Allowances 1976
$C_{STERN}$	Stern shape coefficient (Holtrop and Mennen)
$c_w$	Exhaust gas emissions component estimated on a wet basis
$C_W$	Waterplane coefficient
$D$	Propeller diameter

DAS	Days at sea per year for ship type and size category
$e^-$	Negatively charged electron
F and $F_{SS}$	Number of vessels of ship type and size category in the fleet at normal speed and when slow steaming respectively
$f_c$	Carbon factor
$f_{fd}$	Fuel specific constant for the dry exhaust
$f_{fw}$	Fuel specific factor for exhaust flow calculation
$F_n$	Froude number
g	Acceleration due to gravity
H	Shaft centre line
$H^+$	Positively charged proton
$H_a$	Absolute humidity of the intake air
hb	Bulbous bow centre above the keel line
$H_T$	Total immersion
$H_{TR}$	Immersed transom height
$i_E$	The angle of the waterline at the bow
J	Advanced coefficient
$K_Q$	Torque coefficient
$K_T$	Thrust coefficient
$k_w$	Dry to wet correction factor
L	Overall length
$L_{BL}$	Minimum length to the baseline
lcb	Longitudinal position of the centre of buoyancy
$L_{OS}$	Length over surface which in case of design draught means length between the aft end of design waterline and the most forward point of ship below design waterline, while for ballast draught it represents length between aft end and forward end of ballast waterline, where rudder is not taken into account
$L_{PP}$	Length between perpendiculars representing the length between the foreside of the stem and the aft of the rudder post at the vessel's summer load
$L_R$	Length of the run
$L_{SB}$	Distance between shaft and ballast
$L_{WL}$	Length of the waterline
m	Product mass
$\tilde{m}$	Molar mass of each product
n	Amount of substance
N	Propeller rotational speed
P/D	Pitch to diameter ratio

$p_0$	Static pressure
$P_D$	Delivered power
$p^e$	Static head
$P_E$	Effective power
ppm	Parts per million
ppmC	Parts per million carbon
$p_v$	Saturated vapour pressure
$p_z$	Hull surface pressure
$q_{mad}$	Intake air mass flow rate on a dry basis
$q_{mew}$	Exhaust gas mass flow rate on a wet basis
$q_{mf}$	Fuel mass flow rate
$q_{mgas}$	Mass flow rate of individual gas component
QPC	Quasi Propulsive Coefficient
$q_T$	Dynamic head
$r$	Propeller radius
$R_{APP}$	Appendage skin friction resistance
$R_{BB}$	Additional pressure resistance due to a bulbous bow near the water surface
$R_{CA}$	Correlation allowance defined as a difference between the total measured resistance and the total estimated resistance
$R_F$	Frictional resistance
$R_n$	Reynolds number
$R_T$	Ship's total resistance
$R_{TR}$	Immersed transom resistance
$R_W$	Wave-making resistance
$S$	Wetted Surface Area
$S_a$	Apparent slip
SW	Stern wave
$t$	Thrust deduction coefficient which represents the losses of thrust due to water being sucked into the propeller
$T$	Draught
$T_A$	Draught aft
$T_F$	Draught forward
$T_{OUT}$	Exhaust gas temperature
$T_R$	Draught ratio introduced in Moor and O'Connor's method
$u_{gas}$	Ratio between density of the exhaust components and density of exhaust gas
$V$	Designed speed

$V_A$	Speed of advance
$w$	Wake fraction which represents the difference between the speed of advance of the propeller and the actual ship speed expressed in percentage
$w_{ALF}$	H content of fuel (%)
$w_{DEL}$	N content of fuel (%)
$w_{EPS}$	O content of fuel (%)
$Z$	Number of propeller blades
$\beta_0$	Regression intercept
$\beta_{input}$	Regression coefficients for each independent variable
$\delta_b$	Behind hull coefficient
$\delta_{opt}$	Regression based van Gunsteren coefficient for Wageningen B-Screw series
$\varepsilon$	Regression random error
$\eta_H$	Hull efficiency
$\eta_O$	Open water efficiency
$\eta_R$	Relative-rotative efficiency
$\theta$	Trim angle
$\lambda$	Stoichiometric ratio
$\mu$	Dynamic viscosity of water
$\rho$	Density of water
$\sigma$	Local cavitation number
$\tau_C$	Thrust loading coefficient

## EEDI Nomenclature

$C_{FME}/C_{FAE}$	Non-dimensional conversion factors for main or auxiliary systems. Applicable for diesel/gas oil, light fuel oil (LFO), heavy fuel oil (HFO), liquefied petroleum gas (LPG) in form of butane, LPG in form of propane, liquefied natural gas (LNG), methanol and ethanol.
$f_c$	Cubic capacity correction factor added in case of chemical tankers, gas carriers with direct diesel driven propulsion system constructed or adapted to use for the carriage in bulk of liquefied natural gas and ro-ro passenger ships with a DWT/GT ratio of less than 0.25.
$f_{eff}$	Availability factor of each innovative energy efficiency technology.
$f_i$	Correction factor related to any technical or regulatory limit on capacity in case of ice-classed ships, ships with specific voluntary enhancements or bulk carrier and oil tankers built in accordance with the Common Structural Rules (CSR) of the classification societies and assigned the class notation CSR.
$f_j$	Correction factor for ship specific design elements including ships designed with an ice class notation, shuttle tankers with propulsion redundancy, ro-ro cargo and ro-ro passenger ships and general cargo ships.
$f_l$	Correction factor for general cargo ships equipped with cranes and other cargo-related gear to compensate a loss of deadweight of the ship.
$f_w$	Correction factor representing the decrease in speed in certain sea conditions of wave height, wave frequency and wind speed at Beaufort Scale 6.
$P_{AEff}$	Auxiliary power reduction due to innovative electrical energy efficient technology.
$P_{eff}$	Output of the innovative mechanical energy efficient technology.
$P_{ME}/P_{AE}$	Main engine power/auxiliary engine power.
$P_{PTO}/P_{PTI}$	Power of each shaft generator /shaft motor power.
$SFC_{ME}/SFC_{AE}$	Certified specific fuel consumption of main or auxiliary systems measured at 75 percent or 50 percent of the MCR respectively.
$V_{ref}$	Ship's speed measured in nautical miles.

# 1 Introduction

Shipping always has been an essential human activity worldwide mostly in terms of international trade and transport of people between countries. Merchant shipping represents a major way to transport goods around the world enabling global trade as well as a growth of globalisation. In turn, the globalisation of the world’s embracing markets is an important determinant for the cyclic growth of the global fleet, stipulated by the differences in the economic progress between the countries and developments in the world trading system.

According to Clarkson Research findings, published in (RAE 2013), some 95 percent of the global cargo is moved by sea, resulting in 9.84 billion tonnes of goods transported in 2014 as shown in Figure 1.1 (UNCTAD 2015) which underlines the increasing trend of 3.04 percent in comparison to the previous year.

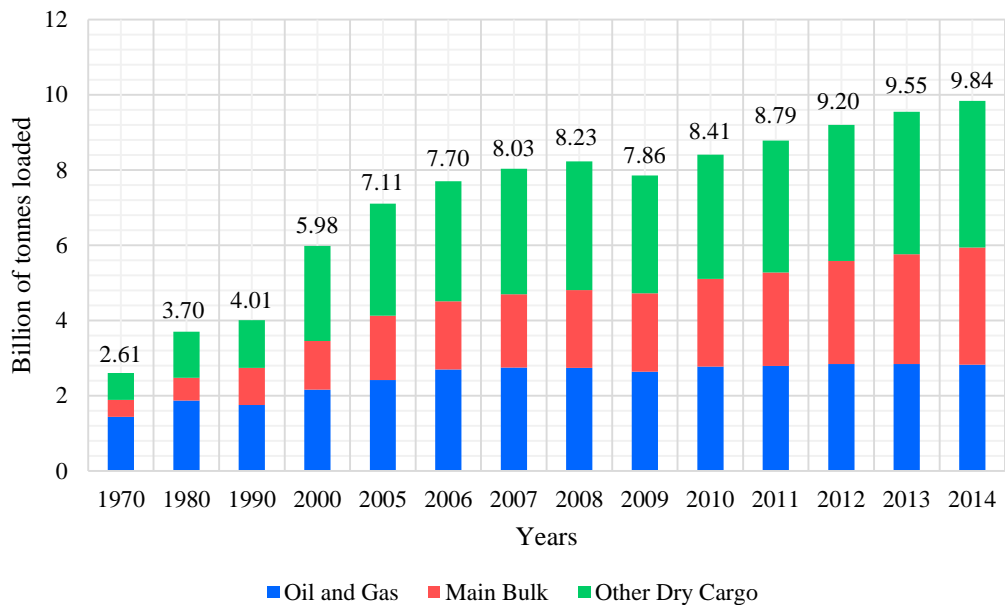


Figure 1.1 Growth of international seaborne trade over selected years. The graph is based on data published in the (UNCTAD 2015) where the main bulk category includes iron ore, grain, coal, bauxite/alumina and phosphate rock.

In addition, the diagram shown in Figure 1.2 indicates the growth of volumes of cargo in billion tonne-miles transported by sea in recent years. The absolute increase in 2014 equals to 4.36 percent making the total of 52,572 billion ton-miles transported over the year. In fact, the crude oil shipments fell by 1.7 percent as a result of the substantial drop in the crude oil imports into the United States and Europe. As such, a general increase in oil category is predominantly compensated by the rapid growth in the oil products trade.

In line with the continuously growing demand in various sectors of seaborne trade, the world fleet of propelled sea-going merchant ships of not less than 100 gross tonnage (GT) has reached 1.75 billion deadweight tonnes (DWT) in January 2015 with 3.5 percent increase in DWT compared to January 2014 (Figure 1.3). In fact, bulk carriers account for 43.5 percent of the current world fleet followed by oil tankers (28 percent) and container ships (13 percent) as shown in Figure 1.4. Such rising trends indicate a continuous economic growth in the maritime industry but at the cost of an increase in ship produced atmospheric emissions, which have a direct relationship to shipping activity.

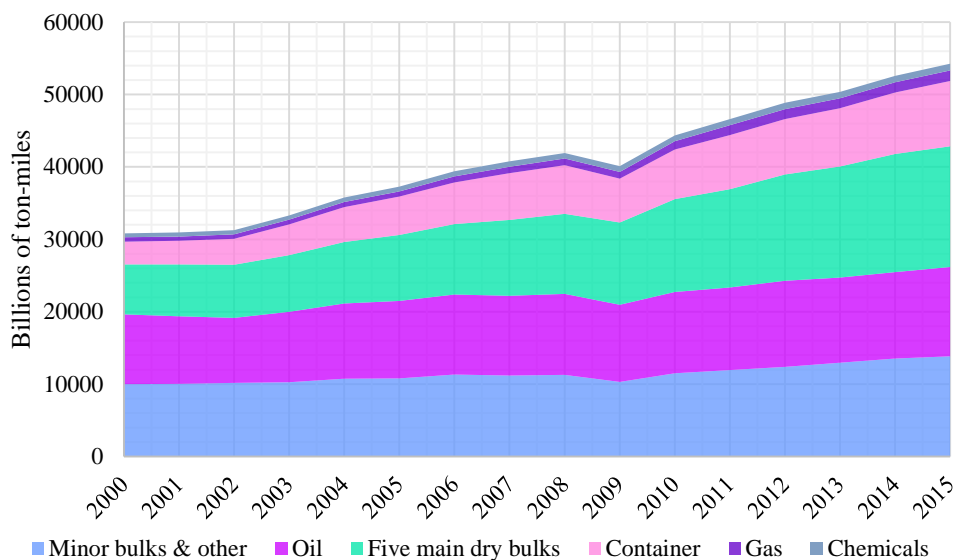


Figure 1.2. World seaborne trade in cargo ton-miles by cargo type based on data published in (UNCTAD 2015). The main bulk category comprises iron ore, grain, coal, bauxite/alumina and phosphate rock.

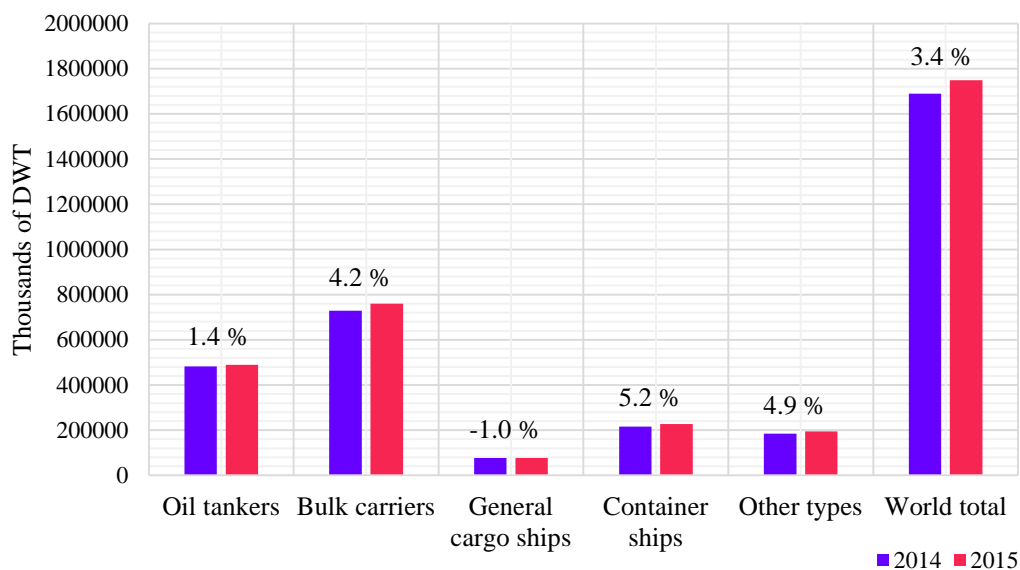


Figure 1.3 World fleet by vessel type. The percentage values above the columns represent the percentage change of particular ship category over the period 2014-2015. The graph is based on statistics published in (UNCTAD 2015).

## World Fleet 2015

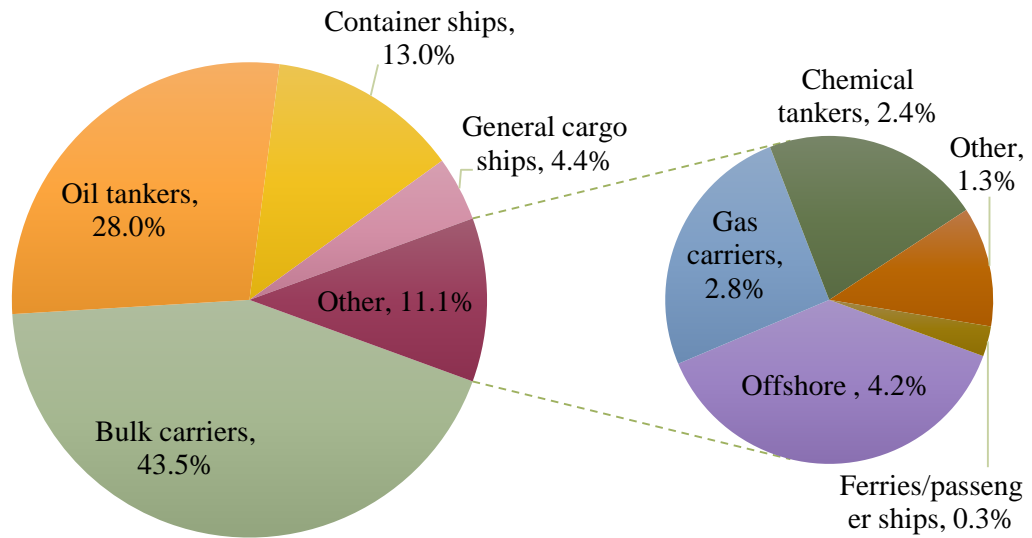


Figure 1.4 Percentage distribution of the world fleet by ship category in 2015. The graph is based on statistics published by (UNCTAD 2015).

Within the scope of internationally raising awareness of climate change, there are increasing calls for the maritime industry to reduce greenhouse gas (GHG) emissions, especially carbon dioxide ( $CO_2$ ). According to the Third GHG Study 2014 (IMO 2014b), the contribution of international shipping to global distribution of atmospheric emissions accounts for approximately 2.8 percent which corresponds to the total shipping emissions of 961 million tonnes. Evidently, these emissions originate from the fuel combustion processes resulting in an exhaust mixture of gaseous species including carbon dioxide ( $CO_2$ ), carbon monoxide ( $CO$ ), oxides of nitrogen ( $NO_x$ ), sulphur dioxide ( $SO_2$ ), hydrocarbons ( $HC$ ) also described as volatile organic compounds ( $VOC$ ), particular matter ( $PM$ ) and methane slip ( $CH_4$ ) in case when burning, for example, LNG.

However, the fraction comprising designated species is relatively small while the base of the exhaust gas flow mostly made of oxygen ( $O_2$ ), nitrogen ( $N_2$ ) and the moderate amount of vapour ( $H_2O$ ). The general proportional distribution of the exhaust gas species is shown in Figure 1.5. These fractions were calculated using the exhaust gas prediction model specified in Chapter 5.

In fact, greenhouse gases are important for natural regulation of the atmospheric temperature. When the sun passes energy through the atmosphere and warms the surface of the Earth, the planet emits heat, some of which is then integrated with the GHGs in the atmosphere. In turn, GHGs reflect the heat sending it back to the surface. Such a heating

process keeps the earth comfortably warm and largely dependent on greenhouse gases as otherwise, the temperature would drop by approximately 33°C (Metz 2007). Sufficient quantities of greenhouse gases contained in the atmosphere are provided by natural processes while an excessive continuous increase of  $CO_2$ , caused by industry activity, has a direct, global, and long-lasting climate forcing impact and leads to the irreversible processes.

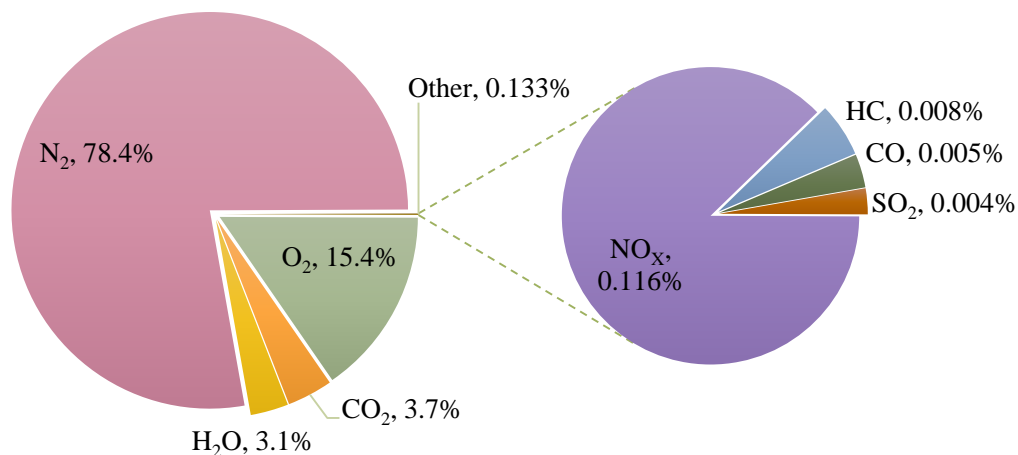


Figure 1.5 Simplified composition of the exhaust gas flow from the ship with 2-stroke diesel engine burning the ISO 8217 fuel oil. The graph is based on the results from exhaust gas prediction model described in full in Chapter 5.

### ***Carbon dioxide***

Carbon dioxide ( $CO_2$ ) is produced during the combustion processes of any hydrocarbon fuel with relative proportions principally associated with the hydrocarbon composition and quality of the fuel. The formation of  $CO_2$  is a function of the required power output, engine efficiency and the elementary composition of the fuel. Therefore, global  $CO_2$  emissions from shipping primarily correlate with the total number of ships as well as average annual fuel consumption, which is a function of days at sea and the extent of adoption of slow steaming. However, apart from its global effect as GHG,  $CO_2$  is considered to be a non-toxic (depending on concentration), colourless and odourless gas and is not identified as an air pollutant.

As reported in the Third GHG Study 2014 (IMO 2014b), the shipping industry is estimated to have produced 938 million tonnes of carbon dioxide emissions in 2012, which corresponds to 2.6 percent of the global  $CO_2$  emissions as shown in Figure 1.6. Whereas

international shipping is estimated to produce 796 million tonnes of  $CO_2$  which corresponds to 2.2 percent of the global  $CO_2$  emissions in 2012. In fact, the  $CO_2$  trend shown in Figure 1.6 has an overall decreasing tendency within the period 2007-2012 as a result of an extensive adoption of slow steaming among ship owners driven by recently introduced environmental regulations such as the Energy Efficiency Design Index (EEDI) by IMO as well as fluctuations in oil prices.

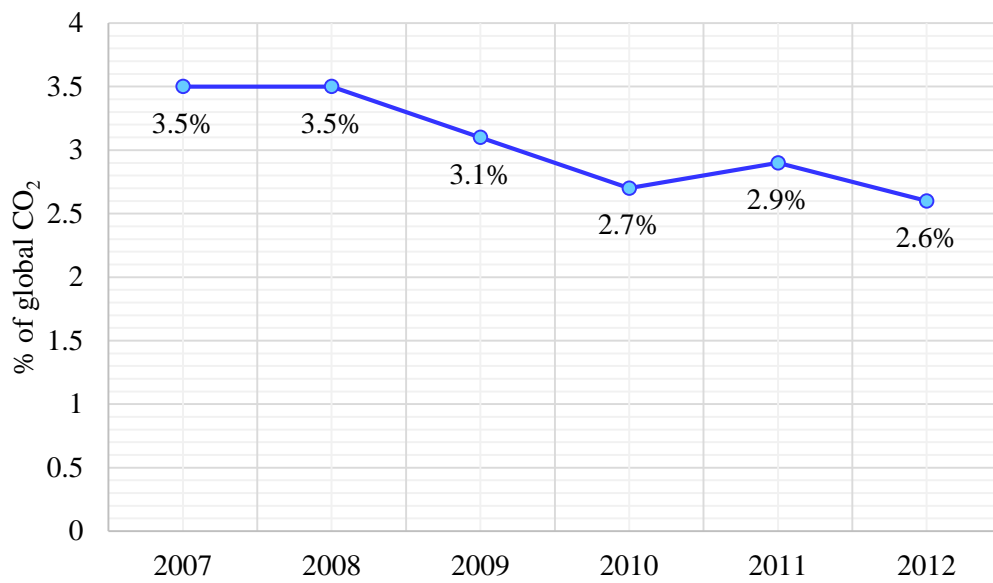


Figure 1.6 The total shipping  $CO_2$  emissions for the period 2007-2012. The graph is based on data published in (IMO 2014b).

Material from the Third IMO Greenhouse Gas Study 2014 and/or the IMO website [www.imo.org](http://www.imo.org) is reproduced with the permission of the International Maritime Organization (IMO), which does not accept responsibility for the correctness of the material as reproduced: in case of doubt, IMO's authentic text shall prevail. Readers should check with their national maritime Administration for any further amendments or latest advice. International Maritime Organization, 4 Albert Embankment, London, SE1 7SR, United Kingdom.

In 2012 the average reduction of ship service speed in comparison to design speed was 12 percent, thus, the average reduction in daily fuel consumption was 27 percent. Moreover, as noted in (IMO 2014b) many ship type and size categories have exceeded this average. For instance, in the case of some oil tanker and container ship size categories, reductions in day-to-day fuel consumption reached 50 percent and 70 percent respectively. However, according to the research conducted in the Third GHG Study 2014 the global shipping  $CO_2$  emissions are projected to increase by 50 - 250 percent (for example BAU scenarios) in the period to 2050 largely depending on future economic, energy and technical developments.

### ***Nitrogen oxides***

The formation of nitrogen oxides ( $NO_x$ ), also classified as a GHG, occurs during the combustion processes by the oxidation of the nitrogen molecules of the intake air at high burning temperatures and pressures or of the organic nitrogen in the fuel which, in relation to the fuel type, may account for a significant proportion of the overall  $NO_x$  output

especially in case of burning heavy fuel oil. Oxides of nitrogen are often described as  $NO_x$  in order to express the possibility of different combinations of nitrogen and oxygen, which, in most cases, are nitric oxide ( $NO$ ) or nitrogen dioxide ( $NO_2$ ). In fact, when an excess air is present during the combustion process,  $NO$  is being oxidized into  $NO_2$ , which has much more toxicity. Therefore, the formation of  $NO_x$  is a complex process being a non-linear function of the burning temperature (over  $1200^\circ C$ ), pressure, the engine load, air excess ratio as well as the humidity of the charge air.

Oxides of nitrogen ( $NO_x$ ) along with carbon monoxide ( $CO$ ) and emissions of volatile organic compounds lead to the formation of tropospheric ozone ( $O_3$ ) (Torvanger et al. 2007), which has a negative impact on plants and trees, agricultural crop yields and building materials (Gazley 2007). Moreover, ozone is known to have negative health effects and promotes development of harmful diseases such as irritation of the respiratory system, causing coughing and a chest pain, reduced lung function and asthma.

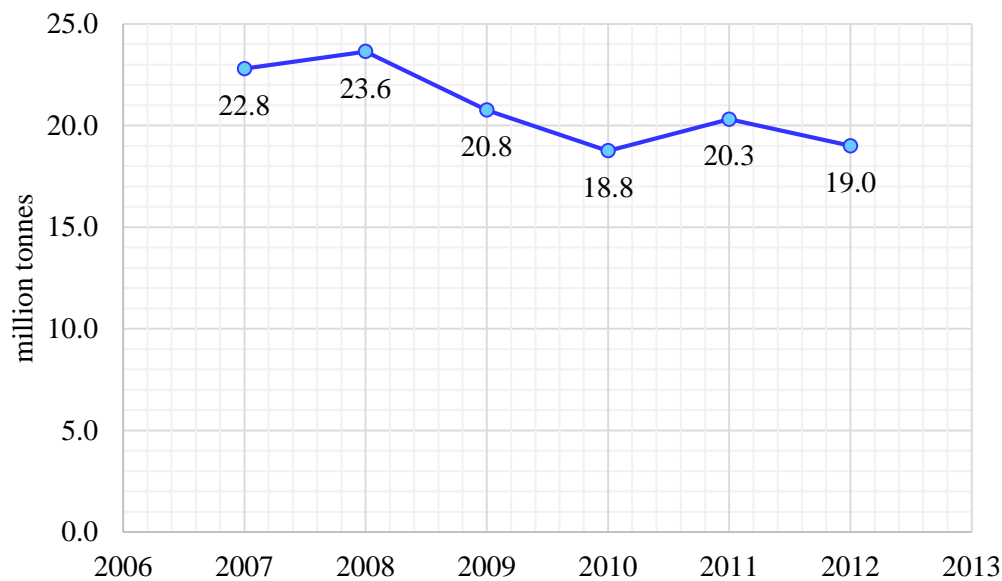


Figure 1.7 The  $NO_x$  emissions for the period of 2007 – 2012 in million tonnes of  $NO_2$ . Based on data published in (IMO 2014b).

In addition, it has been estimated in (IMO 2014b) that in 2012 the  $NO_x$  emissions from global shipping (including domestic) was 19 million tonnes as shown in Figure 1.7 which is, in fact, 6.4 percent lower in comparison with the previous year. Such reductions in emissions of nitrogen oxides are the consequence of Tier II and Tier III engines entering the fleet. However, the global  $NO_x$  emissions from all shipping represent approximately 15 percent of global  $NO_x$  from anthropogenic sources as reported in the IPCC Fifth Assessment Report (IPCC 2014).

### *Sulphur oxides*

Generally, the marine fuel oils contain a relatively high percentage of sulphur, when compared to other fuels and, as a result, form sulphur dioxide  $SO_2$ , which then, in a much smaller proportion of approximately 3.5 percent, is further oxidized into the sulphur trioxide  $SO_3$ . The negative effect of  $SO_x$  emissions is similar to  $NO_x$  comprising human respiration deceases, harmful effects on vegetation and construction materials. In addition, the sulphur dioxide particles may also transform into sulphate ( $SO_4$ ) (Torvanger et al. 2007), which is the dominant component of aerosol in the atmosphere caused by marine emissions (Corbett & Winebrake 2008). The particles of  $SO_4$  reflect the solar radiation, and result in Cloud Condensation Nuclei (CCN).

The CCN is a process whereby the marine exhaust emissions increase the number of particles in the atmosphere over the ocean. Consequently, it increases the number of water droplets in a volume of cloud, and hence droplets become smaller and the cloud reflects more sunlight back into space (Crist 2009) while the cloud seems to be optically brighter (Corbett et al. 2009). This process is called the first indirect effect of sulphate. Remarkably, in the atmosphere, the sulphur oxides tend to dissolve relatively fast and have an average lifetime of just two days.

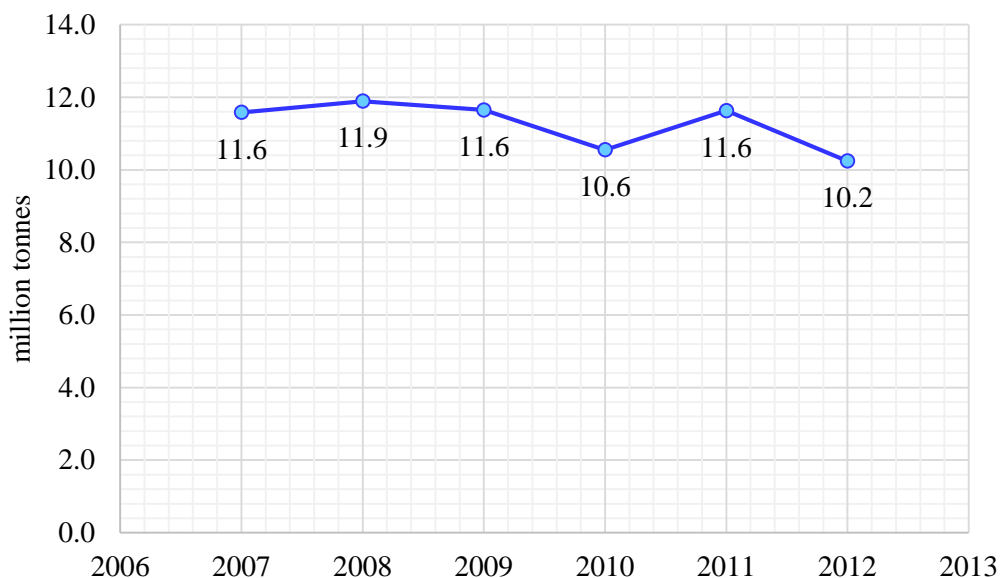


Figure 1.8 The  $SO_x$  emissions for the period of 2007 – 2012 in million tonnes of  $SO_2$ . Based on data published in (IMO 2014b).

According to recent figures published by (IMO 2014b), in 2012 global shipping has contributed to approximately 13 percent of global  $SO_x$  emissions corresponding to 10.24 million tonnes. However, as shown in Figure 1.8 the amount of global  $SO_x$  emissions from

shipping in 2012 has decreased by 12 percent in comparison to 2011 as a result of new stricter regulations for reduction of  $SO_x$  which came into force from 1<sup>st</sup> of January 2012 and will continue to tighten in the coming years. The regulations, as stated in MARPOL Annex IV (regulation 14), are imposing a strict limitations of sulphur content in fuels being used for marine applications or engaging to use some additional technologies for reduction of excess sulphur from the exhaust gas.

### ***Carbon monoxide***

Similar to  $CO_2$ , the carbon monoxide ( $CO$ ) emissions are the result of the combustion process of hydrocarbon based fossil fuel. The major difference is that  $CO_2$  is formed by a complete oxidation of the carbon molecules in the fuel while  $CO$  comes from the incomplete combustion due to local areas of air supply deficiency. As such, its formation in the combustion process is primarily a function of the excess air ratio, the burning temperature and the homogeneity of the air/fuel mixture in the combustion chamber. In practice, due to oversupply of excess air for the combustion process, the  $CO$  emissions are low. However, the concentration of  $CO$  varies with engine load and could be expected to increase at low loads or in poorly maintained engines.

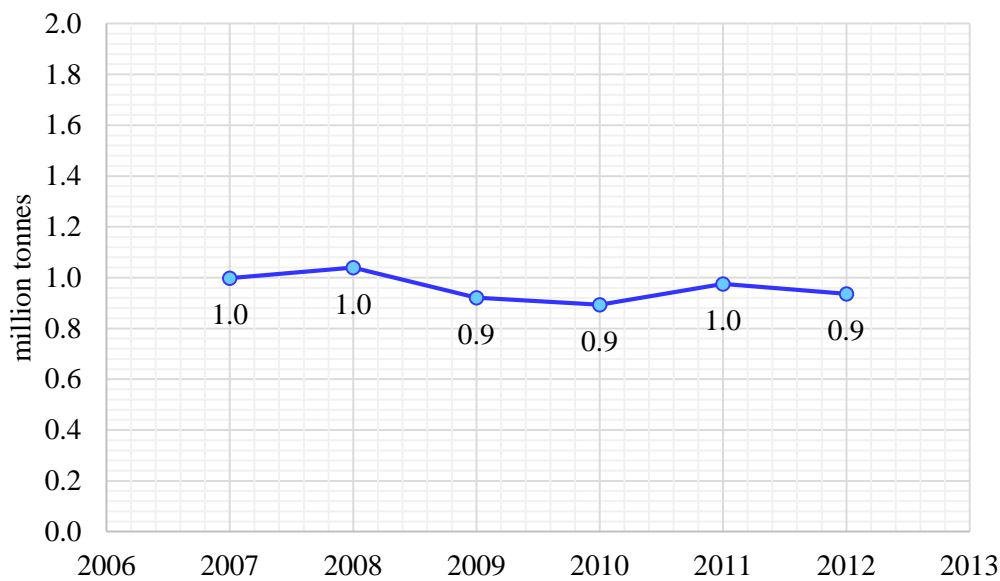


Figure 1.9 The  $CO$  emissions in million tonnes from shipping industry for the period of 2007-2012. Based on data published in (IMO 2014b).

Unlike carbon dioxide, carbon monoxide is very toxic and harmful to humans, even though, it is naturally present in the atmosphere in very low concentrations. In moderate concentrations  $CO$  causes headache and giddiness and in higher doses could lead to respiratory failure and, possibly, death. In fact,  $CO$  emitted during the combustion, process

does not transform into  $CO_2$  but may react with radicals in the air and, in some cases, contribute to the formation of ground level ozone. However, its environmental impact is not fully estimated but suspected to have a marginal effect on climate change. The global contribution of  $CO$  emissions from the shipping industry has been relatively constant over recent years and shown on Figure 1.9.

### ***Hydrocarbons***

According to the Third GHG Study (IMO 2014b), in the year of 2012 global shipping contributed to 0.696 million tonnes of NMVOC emissions (Non-Methane Volatile Organic Compounds) as shown in Figure 1.10, which are also referred to as the hydrocarbon ( $HC$ ) emissions. Hydrocarbons are, generally, found in the exhaust gas in low concentrations and mainly consist of unburned or partially unburned particles of fuel and lubrication oil, which comprise various compositions of carbon, hydrogen, oxygen, nitrogen and sulphur.

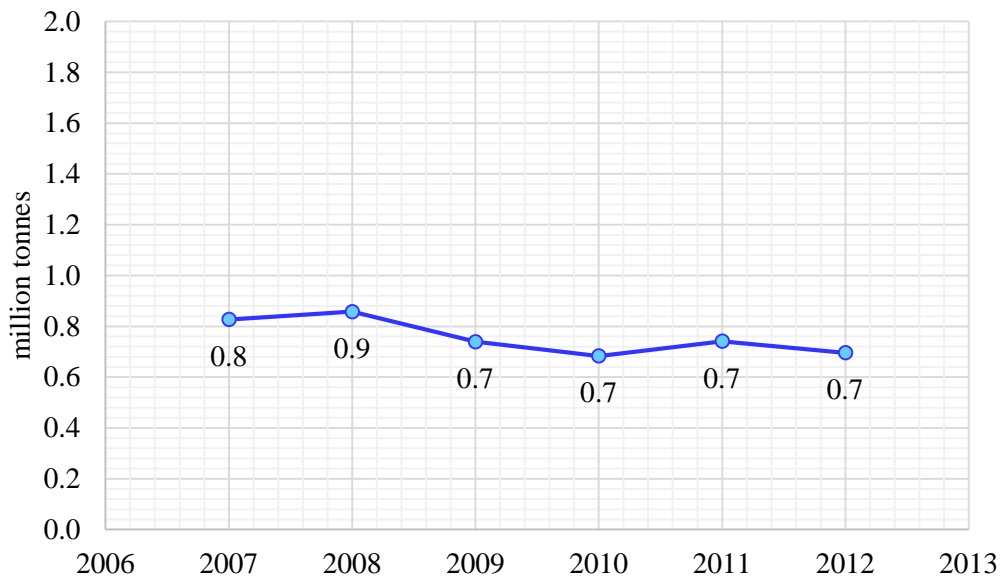


Figure 1.10 The *NMVOC* emissions in million tonnes from shipping industry for the period of 2007-2012. Based on data published in (IMO 2014b).

Since  $HC$  emissions result from an incomplete combustion, their concentration in the exhaust gas flow is influenced by the engine load, condition and thermal efficiency. The concentration of the  $HC$  emissions has a constantly changing distribution as a result of a transforming behaviour from vapour to particulate phases involving evaporation, condensation and polymerization reactions (Kristensen 2012). This makes it difficult to quantify the emissions as well as to accurately identify its negative impact on human health and the environment.

Generally, hydrocarbon emissions are highly toxic and found to have mutagenesis and carcinogenesis properties. In terms of environmental effects, the volatile organic compounds are engaged in photochemical reactions contributing to the formation of tropospheric ozone and global climate change.

### ***Particulate matter***

Particulate matter (*PM*) emissions are directly related to incomplete combustion of “dirty” marine fuels comprising a complex mixture of inorganic and organic compounds such as elemental carbon, ash minerals, heavy metals and a variety of non- or partially-combusted hydrocarbon components of the fuel and lubricating oils.

In general, the quantity and composition of *PM* emissions are a function of an air/fuel ratio. In other words, the completeness of combustion where the appearance and colour of the exhaust gas plume is traditionally a measure of combustion quality. However, the accurate estimation of this fraction is difficult due to the complex nature of the particulate emissions and multiple terms are used to describe both the nature and quantity of *PM*.

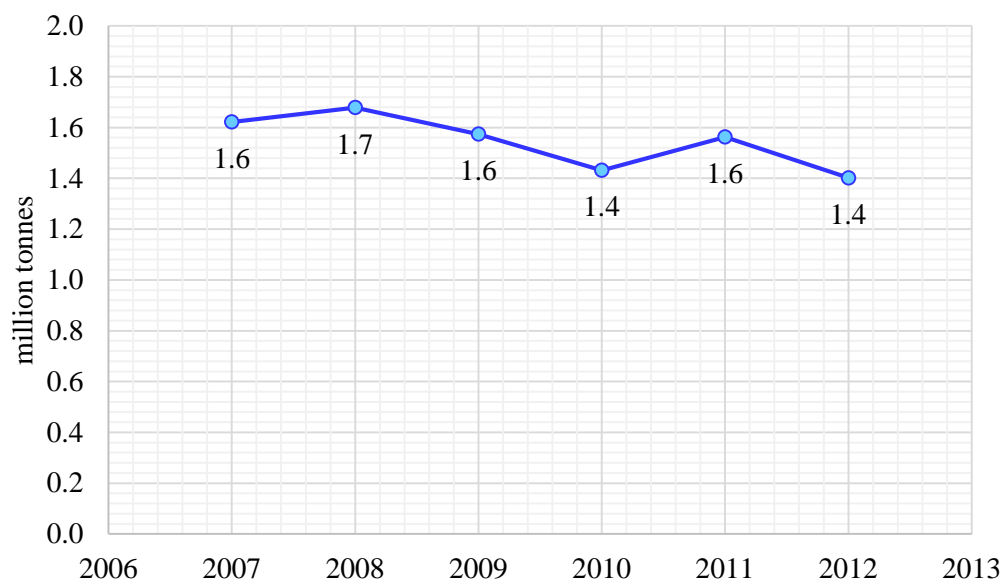


Figure 1.11 The *PM* emissions in million tonnes from shipping industry for the period of 2007-2012. Based on data published in (IMO 2014b).

To a great extent, particulate matter emissions have a negative impact on public health. Small particles less than 10 micrometres ( $PM_{10}$ ) in diameter pose the greatest problems making it easily dissipated by wind and inhaled deep into lungs. Therefore, since *PM* consists of the organic carbon compounds, in other words, carcinogens, it is responsible for serious human health problems and, according to (Corbett et al. 2007), a number of epidemiological studies have found a link between diesel exhaust emissions and cancer.

For instance, (Lauer et al. 2007) in the “Mortality from Ship Emissions: A Global Assessment” concluded that particulates from shipping industry could cause lung cancer and cardiopulmonary diseases that lead to premature death of approximately 60,000 people annually. In fact, as estimated in the Third GHG Study 2014 (IMO 2014b), *PM* amounts from the global shipping in 2012 equal to 1.4 million tonnes (Figure 1.11).

As such, the exhaust emissions from the shipping industry, along with the atmospheric emissions contributed by other industries, affect radiative forcing of the climate (RF), which is the conventional climate metric, expressed in watts per square metre, and used in climate science. RF represents a change in the energy budget of the atmosphere relative to 1750, by the definition of the Intergovernmental Panel on Climate Change (IPCC). In other words, radiative forcing identifies the change in the balance between radiation coming into the atmosphere and radiation going out (MEPC 53th Session & Agenda Item 4 2005). Radiative forcing is usually expressed as a global mean, and positive numbers denote warming while negative numbers denote cooling. The effects of marine emissions on radiative forcing are as follows:

- The  $\text{CO}_2$  emissions have a warming effect and positive radiative forcing (RF);
- The emissions of  $\text{NO}_x$  result in the formation of tropospheric ozone  $\text{O}_3$  with the positive effect to RF (Torvanger et al. 2007).
- The oxides of sulphur ( $\text{SO}_x$ ) have a negative direct RF.
- The *PM* particles and *HC* emissions have a positive direct and indirect effect (for example snow) RF (Corbett et al. 2009).

The overall impact of exhaust emissions on the atmosphere, as schematically represented in Figure 1.12, is rather complex but clearly leads to the increase of its impurity content while disturbing its natural balance. Through the atmospheric reactions, the emitted particles may be involved in various microphysical processes or be removed by land or water surfaces through dry or wet deposition while further affecting its radiative balance. Such imbalance in radiative forcing may impact a climate in different ways including the global and local mean surface temperature, sea level, changes in precipitation, snow and ice cover and more. In turn, these physical impacts may have social implications through their effects on agriculture, forestry, energy production, human health, etc. Finally, all these effects have a social cost, which can be difficult to estimate.

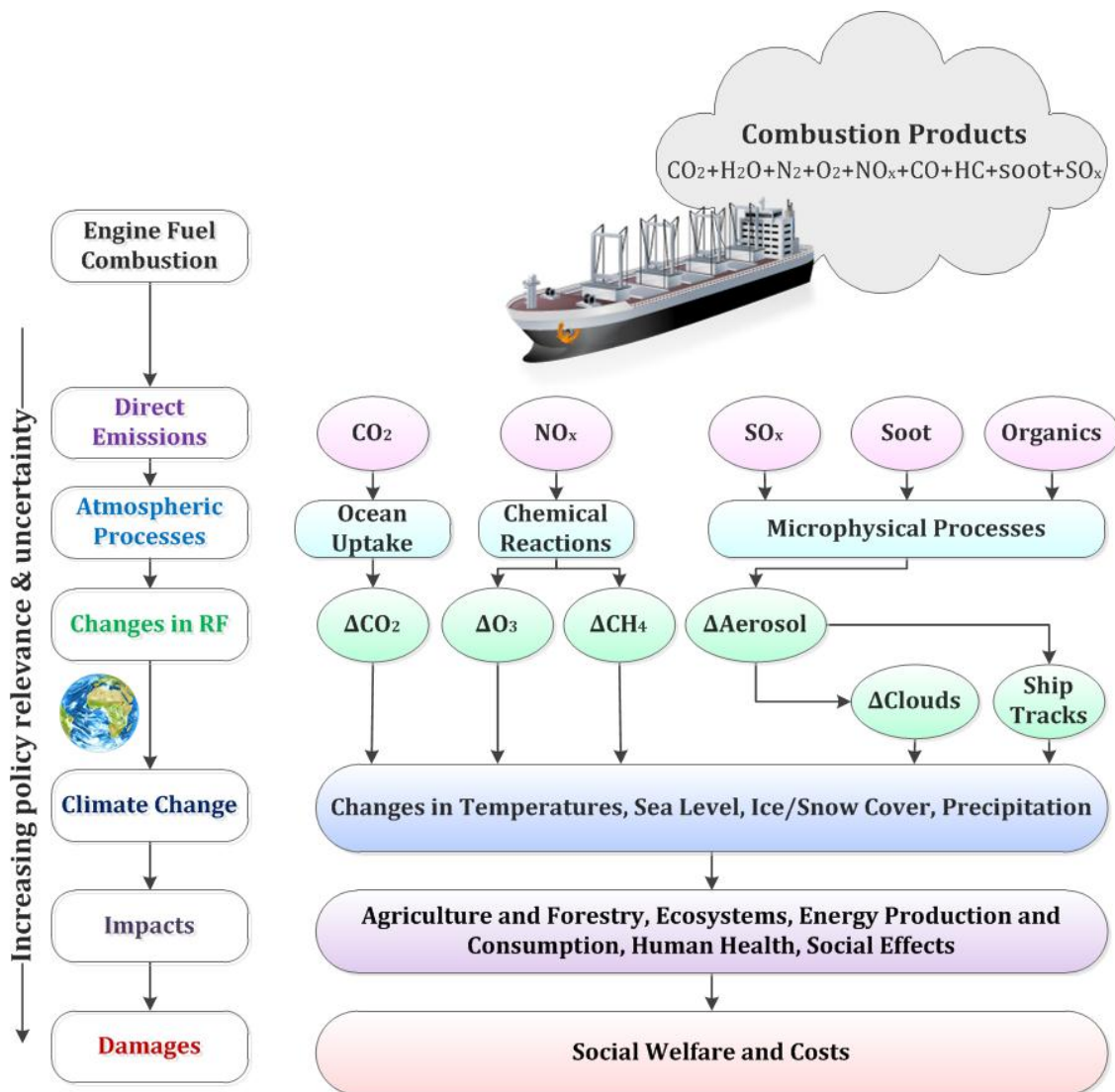


Figure 1.12 The overall impact of the atmospheric emissions from shipping on the environment. The diagram is adapted from IMO GHG study 2009 (Corbett et al. 2009).

The future shipping emissions scenarios (2012 – 2050) were investigated in the recent Third GHG Study 2014 (IMO 2014b) conducted by IMO where the emissions projections have indicated that improvements in ship efficiency including both technical and operational methods while being forced and controlled by environmental regulations, are important in mitigating emissions increase. However, the projections have also shown that changes in the fuel mix will have a limited impact on GHG emissions compared to regulatory or economy driven improvements in efficiency. On the other end of the spectrum, the reduction methods, even with the greatest energy savings, could not reverse the process as the shipping industry will continue to grow as outlined in (RAE 2013) by Dr Stopford while keeping the fossil fuels dominant. As such, the  $CO_2$  emissions will increase in accordance with fuel consumption by 50 – 250 percent, depending on the future scenario, as concluded in the IMO GHG study. However, the emissions of particulate matter demonstrate an

absolute decrease up to 2020 as well as oxides of sulphur continue to decline through to 2050, primarily because of MARPOL Annex VI requirements on the sulphur content in fuels.

In the context of the environmental protection activities, the situation with the development of a global climate policy framework to control the ship produced emissions is very complicated mainly due to its international nature. In particular, one certain aspect makes the shipping industry a very complex issue since every ship is registered to a specific Flag State that could be different from the owner's country and nationality. One of the reasons for this phenomenon is that the ship owners are likely to register their vessels in the most favourable tax jurisdiction rather than their country of origin or their operational headquarter. For instance, it wouldn't be unusual for a ship to be built in China, owned by a company based in the United Kingdom managed by a Greek ship owner and, at the same time, registered under the Panamanian Flag in order to move goods from India to Italy.

According to statistics compiled by the UNCTAD secretariat on the basis of data supplied by Clarkson Research (UNCTAD 2015) as of 1<sup>st</sup> January 2015 the top 10 ship registries control about 51.3 percent of the total world fleet by the number of ships and approximately 76.7 percent of the world's fleet total DWT (Figure 1.13). Whilst Panama dominates the world fleet by the country of registration, the list of world's top ship owning countries is very different as shown in Figure 1.14. These top 10 countries by ownership together control 67 percent of the total DWT with the United Kingdom taking up the 8<sup>th</sup> position. In fact, according to (UNCTAD 2015), for 11.8 percent of the world fleet in DWT, the owner's nationality differs from the country of ownership. All these circumstances could be explained by having a deeper look into the framework of the international maritime law and regulations.

In order to understand the general principles of maritime regulations, it is important to note that maritime activities such as international shipping are regulated not only by the international law of the sea but also by the law of a particular country (State). The United Nations Convention on the Law of the Sea (UNCLOS) is the cornerstone of international maritime law. UNCLOS endorses the right of any sovereign State to have a ship register and thus become a Flag State, and it provides ships with the right to innocent passage through territorial waters and economic zones (Corbett et al. 2009). International law regulates maritime activities in a particular Flag State but does not apply directly to individual vessels.

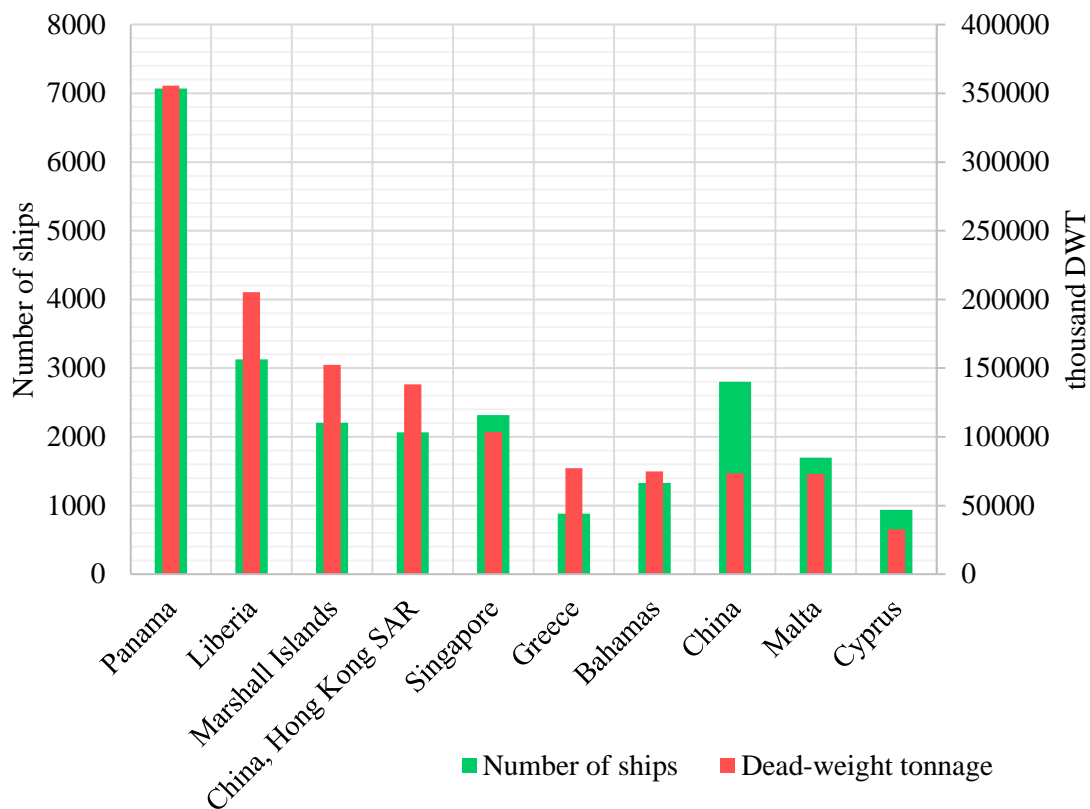


Figure 1.13 Top 10 Flags of registration with the largest registered fleets as of 1 January 2015 (UNCTAD 2015).

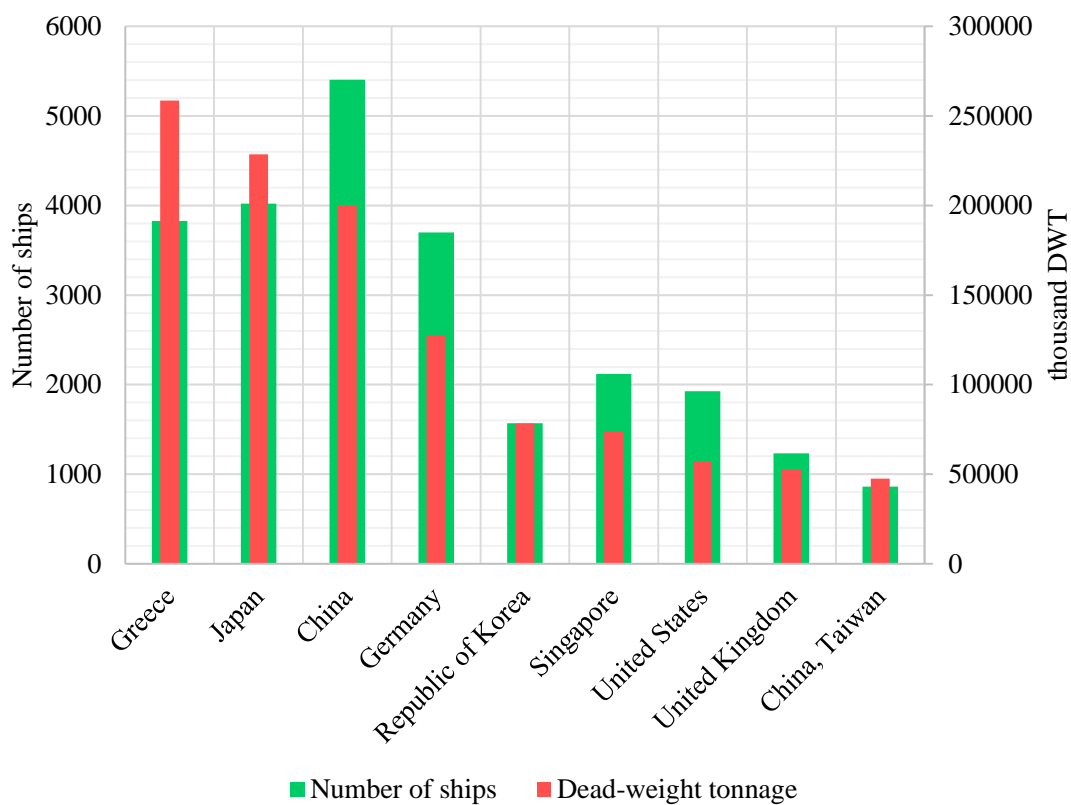


Figure 1.14 Ownership of the world fleet as of 1 January 2015 (UNCTAD 2015).

Therefore, the regulations directly related to ships are referred to the Flag State. In fact, the requirements for granting a ship access to the registry in different States may vary. For example, some countries may require specific criteria, such as a ship owning company should have a registration in the particular State or ship should be built on their territory, along with special requirements to the citizenship of the owning company and more. On the other hand, some States may not have restrictions on access and are termed an “open registries”, yet if the ship is designed to sail in international waters and pass over the international boundaries then the Flag State is obliged to ensure that ship complies with regulations and requirements specified by international conventions.

Generally, the legislative framework of international shipping comprises approximately 50 conventions and protocols, created and managed by the International Maritime Organization (IMO). The government’s responsibility is to adopt these international conventions into the national legal system and enforce it. Once the government has ratified the IMO legislative instrument, the legislative act applies to all ships moving under its Flag and, in most cases, to all other ships as a condition of entering their ports or internal waters is regardless of Flag (Lun et al. 2010). Therefore, ships that enter the international ports or waters under the jurisdiction of a country that has ratified the IMO instrument will have to follow the legislative rules, irrespectively of their Flag (Corbett et al. 2009). This important principle may also be called the principle of “no more favourable treatment”.

In some cases, the government of a particular Flag State passes certain survey activities to classification societies, which implement legislation on its behalf. The classification societies are the non-governmental organisations that establish and maintain technical standards for construction and operation of ships and, in certain circumstances, undertake surveys on behalf of the particular Flag. In addition, the classification societies establish their own classification rules with technical requirements in relation to the design, construction, and the ship’s survey. A simplified diagram shown in Figure 1.15 demonstrates the complex relationships between key stakeholders of the legislative framework, which control the shipping industry. By implication, this demonstrates the complexity of design and operation of a ship to trade efficiently and in an environmentally responsible manner.

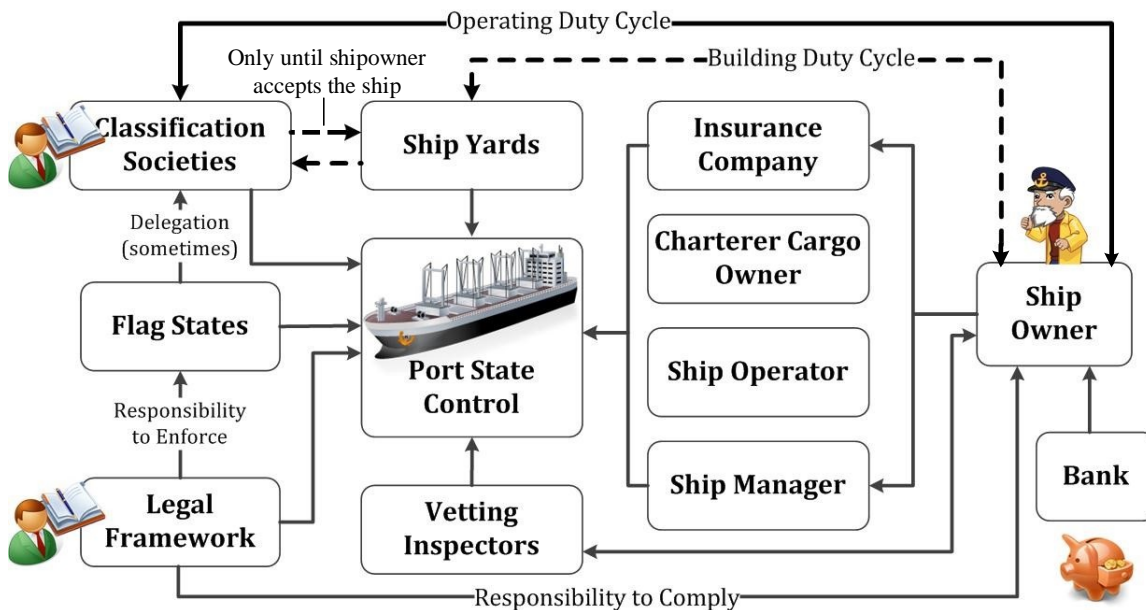


Figure 1.15 Main components of the legislative framework of the shipping industry.

Consequently, in order to develop a global climate policy framework as a part of the Kyoto Protocol, a great number of different options were studied aiming to allocate emission policies into each State's legislation system. The Kyoto Protocol is an international agreement linked to the United Nations Framework Convention on Climate Change (UNFCCC) adopted in Japan and responsible for the global emissions from international shipping.

Instead, in 2003, the International Maritime Organization (IMO) adopted a Resolution A.963 (23) on IMO Policies and Practices related to the Reduction of Greenhouse Gas Emissions from Ships which is based on equal treatment of all ships, regardless of their Flag State. This resolution urges the Marine Environment Protection Committee (MEPC) to identify and develop the mechanism or mechanisms needed to achieve the limitation or reduction of GHG emissions from international shipping giving the priority to technical, operational, and market-based solutions (UNFCCC 1998). As such, the Energy Efficiency Design Index (EEDI) measure and the Ship Energy Efficiency Management Plan (SEEMP) have been developed and implemented as being mandatory for all new builds of 400 GT and above from January 2013. In fact, the EEDI and SEEMP have extended the already existing marine environment protection framework, namely, MARPOL Annex VI, which is targeting  $NO_x$ ,  $SO_x$ ,  $PM$  and  $VOC$  emissions. The complete marine air pollution prevention legislative framework is summarised in Figure 1.16 below.

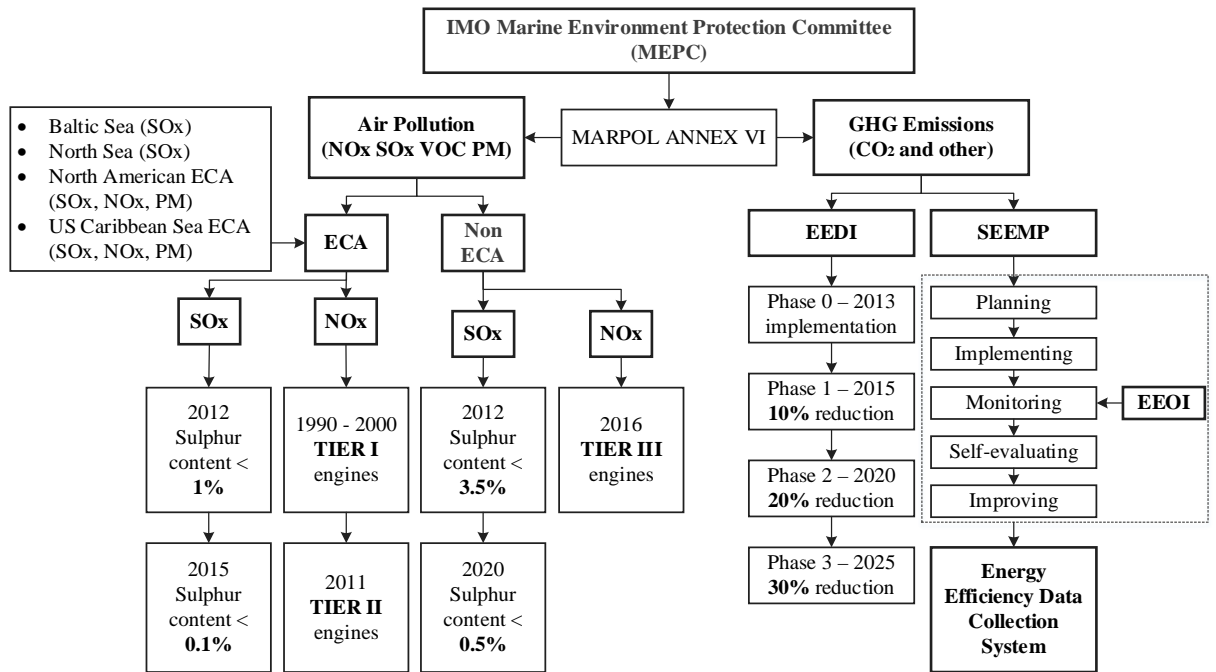


Figure 1.16 IMO air pollution prevention legislative framework.

Both mechanisms, which can be associated with the energy efficiency and emissions standards, are the first ever mandatory GHG regulations for the shipping industry. While the EEDI imposes an energy efficiency criterion for new ships, which, when implemented, would have to be verified against the defined standard by an independent organisation in order to obtain certification, the SEEMP enables ship owners to measure the fuel efficiency of existing ships and to monitor the effects of any changes in operation.

### ***Energy Efficiency Design Index***

In simplest terms, the EEDI can be described as the ratio between  $CO_2$  production potential of the ship and its benefit to society. Whereas, the  $CO_2$  production potential comprises the  $CO_2$  associated with the ship's main propulsion, auxiliary and hotel power consumption including the expected benefits from the energy efficiency technologies that generate additional electrical power such as waste heat recovery system (WHRS) minus the innovative energy efficiency technologies incorporated in the design for example wind assistance or a hull air lubricating system added to enhance the propulsive efficiency of the ship. The benefit to society is a function of the ship's speed and its cargo carrying capacity. The EEDI also includes a number of correction factors that have been introduced for specific ship types or particular design features. However, the formula is presently not applicable to ships with diesel-electric propulsion, turbine propulsion or a hybrid propulsion system, except for cruise passenger ships and liquefied natural gas (LNG)

carriers. The main components of the EEDI formula are illustrated by Equation 1.1. Additionally, extensive explanation of EEDI formula components as well as the history of EEDI development are specified in Appendix I.

$$\begin{aligned}
 & \text{Main engine(s) CO}_2 \text{ emissions} \\
 EEDI_{Attained} = & \left\{ \left( \prod_{j=1}^n f_j \right) * \left( \sum_{i=1}^{n_{ME}} P_{ME(i)} * C_{FME(i)} * SFC_{ME(i)} \right) \right\} + \\
 & \text{Auxiliary engine(s) CO}_2 \text{ emissions} \\
 + & (P_{AE} * C_{FAE} * SFC_{AE}) * \left( \left( \prod_{j=1}^n f_j * \sum_{i=1}^{n_{PTI}} P_{PTI(i)} - \underbrace{\sum_{i=1}^{n_{eff}} f_{eff(i)} * P_{AEeff(i)}}_{\text{Technology(s) that generate electrical power}} \right) * C_{FAE} * SFC_{AE} \right) - \\
 & \underbrace{\left( \sum_{i=1}^{n_{eff}} f_{eff(i)} * P_{eff(i)} * C_{FME} * SFC_{ME} \right)}_{\text{Technology(s) that reduce propulsion power}} * \underbrace{\frac{1}{f_i * f_l * f_w * f_c * Capacity * V_{ref}}}_{\text{Transport work}}
 \end{aligned}$$

To facilitate the calculation procedure for ship owners, detailed “Guidelines on the method of calculation of the attained EEDI for new ships” (IMO 2014a) have been adopted by IMO on the 66<sup>th</sup> MEPC session in 2014. However, during its 68<sup>th</sup> session, which took place on 6<sup>th</sup> of March 2015, the “Industry guidelines on calculation and verification of the EEDI” (MEPC 68/INF.30 2015) have been additionally prepared in order to clarify the estimation and verification processes by providing a number of examples of calculation for all ship types.

It is important to note, that  $EEDI_{Attained}$  is associated with ship’s energy efficiency under calm weather conditions with no wind and no waves. Therefore, one of the correction factors,  $f_w$  has been additionally introduced for indicating the decrease in speed in representative sea conditions of wave height, wave frequency and wind speed. In case of including this coefficient into the EEDI calculation, which is an optional action, the EEDI

index should be specified as  $EEDI_{Weather}$ . The detailed guidance on estimating of the  $f_w$  coefficient is described in (MEPC.1/Circ.796 2012).

To define the energy efficiency criteria, some parametric studies have been undertaken for a number of ship types built between 2000 and 2010. As a result, the EEDI reference lines have been introduced for a range of ship types of various sizes including bulk carrier, gas carrier, tanker, container ship, general cargo ship, refrigerated cargo carrier, combination carrier, ro-ro cargo ship, ro-ro cargo ship (vehicle), ro-ro passenger ships and LNG carrier excluding passenger ships other than cruise passenger ship having non-conventional propulsion. The reference line methodology is also explained in Appendix I.

The  $CO_2$  reduction is expected to be achieved within a phased process such as a reduction level (grams of  $CO_2$  per tonne mile) for the first phase (2015-2019) is set to 10 percent and will be tightened every five years as outlined in Figure 1.16. Therefore, in order to obtain an International Energy Efficiency Certificate (IEEC), the  $EEDI_{Attained}$  must be less than or equal to the  $EEDI_{Required}$  in accordance to the current reference phase.

#### ***Ship Energy Efficiency Management Plan***

In turn, the Ship Energy Efficiency Management Plan (SEEMP) is an operational measure that establishes a mechanism to improve the energy efficiency of a ship in a cost-effective manner by providing an approach for shipping companies to manage ship and fleet efficiency performance over time using, for example, the Energy Efficiency Operational Indicator (EEOI) (MEPC.1/Circ.684 2009) as a monitoring tool.

Generally, the SEEMP approach aims to enhance ship's energy efficiency through the following steps: planning, implementation, monitoring, and self-evaluation and improvement. Whereas the EEOI helps to analyse the effect of any changes in operation, such as an improved voyage planning, by means of the continuous ship performance monitoring onboard. The SEEMP also invites the ship owner to consider new energy efficient technologies, for instance, the introduction of a waste heat recovery systems or a new propeller, for achieving a better performance.

In addition, according to the 68<sup>th</sup> MEPC session, it has been agreed to develop a global ship data collection system for fuel consumption of ships of 5000 GT and above in order to analyse its energy efficiency. The system is planned to include the ship identification number, technical characteristics, and total annual fuel consumption by the fuel type as well as transport work. The methodology for collecting the data would be added to the

SEEMP (MEPC.213(63) 2012). The annually collected data would be reported by the ship owner to the Flag State which would submit the data to IMO for inclusion in a database.

### ***Air pollution reduction***

The main purpose of the MARPOL Annex VI and the associated  $NO_x$  Technical Code 2008 (MEPC 12th Session & Agenda Item 6 2007), which entered into force on 1 July 2010, is to identify the emissions standards and to limit air pollution to its maximum particularly in Emissions Control Areas (ECAs) addressing both new builds and existing ships. As shown in Figure 1.16, there are four currently active ECAs: Baltic Sea for  $SO_x$ , North Sea for  $SO_x$ , North American ECA for  $SO_x$ ,  $NO_x$  and  $PM$  and US Caribbean Sea for  $SO_x$ ,  $NO_x$  and  $PM$ . However, some additional ECAs in Singapore, Japan and the Mediterranean region have been appointed to enter into force in the coming years. As such, for ECAs the maximum sulphur content in fuels must be under or equal 0.1 percent which came into force from 1<sup>st</sup> January 2015. For the areas outside the ECA, the maximum sulphur content is 3.5 percent and will be further reduced to 0.5 percent by 1<sup>st</sup> January 2020.

With regard to the reduction of  $NO_x$  emissions from marine diesel engines, there are a Tier II emission limit for engines installed on a ship constructed on or after 1 January 2011 and a more straightened Tier III emission limit for the engines installed on a ship constructed on or after 1 January 2016 and operating in ECAs (North American Emission Control Area and the U.S. Caribbean Sea Emission Control Area). Marine diesel engines installed on a ship constructed on or after 1 January 1990 but prior to 1 January 2000 are required to comply with Tier I emission limits.

Clearly, the reductions in exhaust emissions can be achieved through the incorporation of innovative energy efficient technologies and low-carbon or alternative fuels as well as the use of renewable power sources in addition to a well-planned operational profile while taking into account the fluctuations in freight rates and daily fuel costs. However, in such a hostile environment, there is always a portion of the risk associated with innovative technologies. As such, in order to achieve full potential efficiency and minimise the rising uncertainty, a ship must be considered as an integrated engineering system within its intended operational profile.

### ***Research objectives***

The primary objective of this PhD research is *to develop an advanced understanding of the necessary and realistic performance expectations from a full form medium size ship system by means of numerical computer modelling. This includes the minimisation of the harmful environmental signature by increasing its efficiency in compliance with the EEDI requirements while in search of how the EEDI methodology might be enhanced.* The investigation has focused on a medium sized products tanker acting as a midpoint of the spectrum of ship sizes within the range of 20,000 – 60,000 DWT of this type.

In order to solve such an extensive problem, in the first place, it was important to analyse the energy efficient technology market in a structured manner and then, to identify the most favourable fuel consumption reduction methods that can be associated with the examined ship type. Next, an integrated computer simulation model, involving linked engine, propeller and hull analysis programs, has been developed and calibrated with model tests and sea trial data. The ship system has been analysed under diverse conditions including various propulsion systems, innovative machinery arrangements, efficiency-enhancing hydrodynamic appendages as well as changing weather and load conditions.

The evaluation of potential benefits associated with the deployment of innovative technology(s), operation profile(s) or their combination has been made by comparing the designated Energy Efficiency Indicators (EDI), namely, the propulsive efficiency, fuel oil consumption, exhaust emissions footprint and EEDI, respectively associated with the technical, fuel savings, environmental and legal perspectives.

In addition, such a comprehensive analysis has also helped to detect a number of uncertainties in the current EEDI formulation while pointing out ways in which it can be improved.

## **2 Ship as a System Approach: Methods and Technologies to Enhance Ship Energy Efficiency**

The historical development of merchant shipping has been to a large extent driven by a constantly increasing demand for greater propulsion efficiency or higher operating speed. However, due to unstable oil prices as well as rising environmental pressure, the increase in ship's speed is no longer the highest priority. This has stimulated a deeper interest in alternative fuels and propulsion options such as a possibility to burn LNG in reciprocating engines, incorporating renewable energy technologies, hybrid propulsion and innovative energy saving appendages with an increasing concern in fuel cells and nuclear power.

A historical analysis of ship design efficiency has been conducted in several studies. The IMO GHG Study 2009 (Corbett et al. 2009) gives brief analysis of average design efficiency over time measured in  $gCO_2/ton - nm$ , which indicate significant improvements in ship efficiency over the past century. However, according to historical curves in (Corbett et al. 2009) the efficiency of cargo ships, container ships in particular, has slightly declined in the 1990s. Another research, conducted by Mortensen (Mortensen 2009) verifies the overall energy efficiency trend in (Corbett et al. 2009) specifying that the design efficiency of VLCC tankers improved between 1995 and 2000, but decreased in the next period, while the efficiency of handy size bulkers does not show any notable trend.

A complete study on ship efficiency historical trends elaborated by (Faber 2015) indicates that depending on the ship size and type, ship efficiency improved by 22 – 28 percent in the 1980s, which has been a result of increasing oil prices and relatively low freight rates. In some cases, the efficiency improvements were stimulated by reductions in design speed and main engine power or due to increased ship sizes. On the other hand, the overall efficiency decrease in the 1990s seems to be the result of ship designs where capital costs and capacity had a greater priority than fuel efficiency, making it comparable to the current situation of lower oil prices.

Therefore, (Faber 2015) concludes that in order to improve ship efficiency by 5 – 15 percent it might be beneficial to look back at the 1990s designs. In fact, the design efficiency of new builds after 2009 have already been supporting this trend, meaning that lower design speeds could improve efficiency where appropriate. Additionally, technological progress such as the development of computational fluid dynamics (CFD), although having some limitations (for example turbulence modelling for thick boundary layers), has significantly

contributed to the understanding of hull, propulsion and engine efficiency, indicating the potential of much greater efficiency improvements to come.

### ***Economical triggers***

The overall changes in design efficiency strongly depend upon the global economic circumstances. One of the most important triggers for the ship owner to invest in the more energy efficient designs is an increase in oil prices, helping to reduce the total ownership costs. In fact, as the innovative hull designs are generally more expensive, the amortisation of the additional investments is shorter when fuel prices are high. Another important factor is high freight rates that promote yards to build more ships with standard designs at a potentially low risk with an increased profit margin. In turn, when freight rates are low, shipyards have to compete for clients offering them more efficient designs.

One of the most significant aspects that slow down demand for more efficient ships among the ship owners is that in many cases they do not receive a financial reward provided with the efficiency benefits. The truth is that fuel savings achieved by the energy efficient design or technologies often belong to the charterer who is actually paying for the fuel. However, in some cases, the ship owner has to have a competitive ship in order to compete for better contracts.

The other critical factors that influence ship owners to prefer less efficient ships include dimensional restrictions in some ports and canals or gaps in the infrastructure, limiting the maximum cargo capacity. Such limitations have especially negative implications on ship efficiency under high freight rates and low oil prices. Regardless, a desire for innovations is strongly influenced by the global environmental policies described in the Introduction.

### ***Ship as a system approach***

In order to effectively comply with tightening environmental regulations, it is important for the ship owner to have a clear picture of what realistically could be achieved by implementing the innovative technologies and strategies as well as to evaluate possible risks and benefits while keeping costs to a minimum. Moreover, sometimes it is difficult for the shipowner to establish what particular design package is the most beneficial as a wide range of variables should be considered. As stated in (MEPC.1/Circ.683 2009) “the best package of measures for a ship to improve efficiency differs to a great extent depending upon ship type, cargoes, routes and other factors...”. The problem is in determining which factors are the most appropriate for a particular ship and operational profile. Therefore, it is important to understand the ship system holistically as well as the relationship between

its principal components, operational strategies and ship designs, which should be mutually optimised in order to achieve maximum reduction of exhaust emissions while keeping the potential risks to the minimum.

Several industrial, research institutions and academic collaborations have been recently undertaken a number of research studies regarding the evaluation of the energy efficient methods and technologies while considering the ship as an integrated system and looking deeply into the current industry problems.

Table 2.1 Potential applicability and implementation time frame of energy efficient measures and technologies discussed in (RAE 2013). Abbreviations: NB – new builds, ES – existing ships, OP – operational measure, S – short term, M – medium term, L – long term.

<i>Ship Type</i>	<i>Tanker/Bulk carriers</i>			<i>Container ships</i>		
	NB	ES	OP	NB	ES	OP
<i>Conventional propulsion options</i>						
Diesel engines including modifications	S M	S M		S M	S M	
Biofuels	M L	M L		M L	M L	
Natural gas (LNG)	S M L	S M L		S M L	S M L	
Gas turbines						
<i>Other propulsion technology options</i>						
Nuclear	L			L		
Batteries for main propulsion						
Fuel cells for main propulsion						
Renewable energy	S M	S M				
Hydrogen	M L	M L		M L	M L	
Comp air/nitrogen						
Hybrid propulsion	M L	M L		M L	M L	
<i>Further propulsion considerations</i>						
Energy saving devices	S M L	S M L		S M L	S M L	
Hull optimisation appendages	S M L			S M L		
Hull coating	S M L	S M L		S M L	S M L	
Hull cleaning			S M L			S M L
Propeller redesign to suit operational profile		S M L			S M L	
CRP propulsion	S M L			S M L		
Propeller cleaning			S M L			S M L
Weather routing and voyage planning			S M L			S M L
Slow steaming and/or propeller mo.			S M L			S M L
Machinery conditioning monitoring			S M L			S M L
Crew training			S M L			S M L

One of these studies is the “Future Ship Powering Options” report (RAE 2013) prepared by the industry experts and academics, where a wide range of energy efficient technologies and methods were discussed and assessed in terms of their capability with new builds or

retrofitting while being allocated over the implementation time frame, namely, short, medium and long terms as shown in Table 2.1 by the example of bulk carriers/tankers and container ships.

Another key project, the scenario planning model for global shipping, GloTram, has been developed as a part of the Low Carbon Shipping Consortium (Smith, Day, et al. 2014). The model analyses the evolution of the global fleet in response to external factors including fuel prices, transport demand, technology availability, cost and technical capability. In other words, GloTram is aimed to quantify the drivers of the global shipping system, their mutual interactions and explore potential future scenarios for the shipping industry. The model's outputs include the outlook of the future fleet size, costs revenues, future carbon emissions level as well as the potential market share of energy efficient technologies and marine fuels. Additionally, the decision-making process allows determining technical and operational recommendations for new build or existing ships aiming to maximise the ship owners profit and comply with environmental regulations.

To have a clear picture of the effect that could be achieved by efficiency improvements using technical developments and innovations, it is essential to analyse, implement and evaluate technical solutions for new and existing ships. As such, the Green Ship of the Future, an open private-public partnership of the Danish maritime community with the support of more than 40 global maritime industry parties, has been established in order to explore, develop and demonstrate ambitious technical methods for cleaner, efficient and sustainable ships and maritime operations. The project conducted a number of case studies involving existing ship designs. One of their study (Klimt-Møllenbach et al. 2012) is focusing on the 38,500 DWT tanker, being a similar ship to the tanker used in this PhD research, while aiming to analyse the effect and costs of the most realistic alternatives to the heavy fuel oil (HFO), namely low sulphur, LNG and scrubber technology, in order to comply with the IMOs sulphur level regulations in emissions control areas (ECA). In fact, this PhD research aims and objectives are extending the (Klimt-Møllenbach et al. 2012) project as it focuses on the reductions of carbon emissions and therefore analyses an additional set of technologies and methods, helping to create a complete picture of the potential benefits from the energy efficient design and operational principals for this type of ship.

Many of the energy efficient technologies are not applicable to all ship types nor are they complementing each other or may even cause some damage and safety issues onboard. For

example, engine de-rating, being very effective for significant reductions in the fuel oil consumption, may cause damage to the engine components due to shorter periods of acceleration as well as difficulties to provide sufficient power to operate under poor weather conditions.

In addition, some suppliers may overestimate the benefits of their energy saving devices and appendages, as their technology has only been tested on a limited number of ship models or CFD simulations being far from the full-scale ship and operating conditions as well as overlooking the uniqueness of a particular ship system. It is important to note that some of the devices are still pushing the technological boundaries and might not be ready for implementation due to the high production cost, the difficult integration into the conventional ship system or the infrastructure restrictions. Therefore, a holistic approach taken for an individual ship, considered as an integrated engineering system within its intended operational profile, helps to determine an optimised set of technologies suitable for a particular vessel while detecting and overcoming the potential issues associated with them.

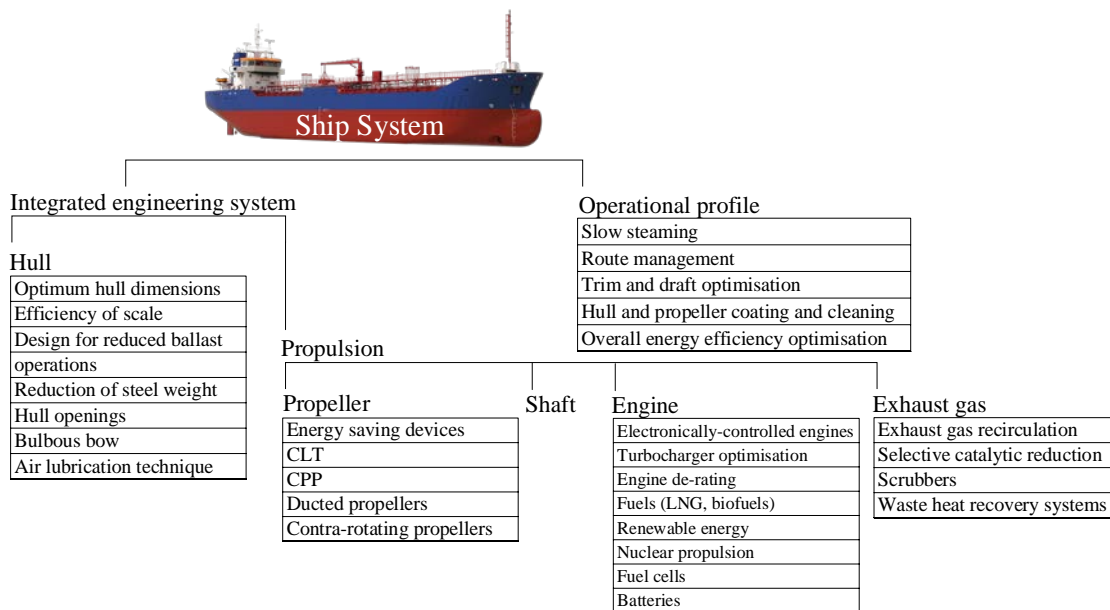


Figure 2.1 Integrated ship system diagram.

The integrated ship system with potential efficiency-enhancing technologies and methods for each system component is schematically represented in Figure 2.1. These fundamental categories of methods to improve ship’s energy efficiency are discussed in this chapter: more specifically, improvements in hull design, propeller design and engine configurations, alternative fuels and renewable energy sources as well as the energy efficient operational

strategies, that aim to provide more useful work while keeping the energy consumption unchanged. Combining these solutions in the appropriate way and treating them as an integrated system may result in a truly efficient ship design.

## 2.1 Operational Strategies

The most direct methods to improve an existing ship's performance are the operational strategies that could be executed by the ship's operator and crew on a day to day basis including speed, trim and draught optimisation, hull and propeller coating and cleaning as well as the overall efficiency monitoring.

### *Slow steaming*

The relationship between ship's speed and required propulsion power opens up a substantial opportunity to improve the energy utilisation. Generally, an engine power output, as an approximation, is a cubic power function of speed while its carbon footprint is a square of ship's speed. Hence, slow steaming is based on a "cubic relationship" between speed and power consumption, where a 10 percent reduction of ship's speed should provide approximately 27 percent reduction of shaft power. However, because a reduction of speed increases the time of transportation, it has been estimated that 10 percent reduction of speed leads to 19 percent reduction of fuel consumption.

Over the past decade, ships have slowed down in response to increasing, until recently, fuel prices and relatively low freight rates. According to the IMO GHG Study 2014, in 2012 the reduction of average fuel consumption at-sea in tonnes per day for tankers equalled up to 50 percent compared to the year of 2007. The relationship between average at-sea engine load factor in 2007 and slow steaming in 2012 for the oil tankers' ship category is shown in Figure 2.2. However, depending on market conditions, slow steaming can also result in some commercial loss, because market requirements place expectations for the time of cargo transportations, therefore, charter parties may restrict a ship's speed reduction level as well as extremely low load operation may affect the machinery and other equipment.

An interesting comment concerning slow steaming was made in (Smith, Day, et al. 2014) that lower ship speed may actually stimulate the demand to construct more vessels, which, in turn, may result in the increase of the GHG emissions associated with the manufacturing processes eliminating the reduced emissions benefit of slow steaming.

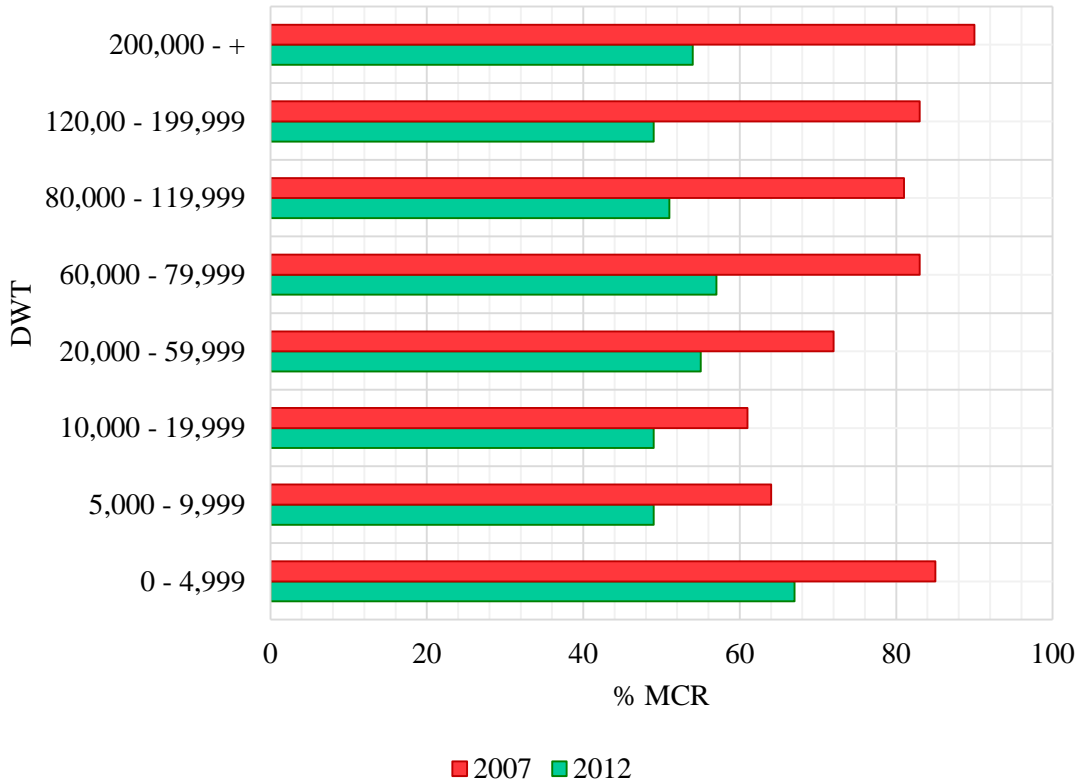


Figure 2.2 Average at-sea main engine load factor for oil tankers in 2007 – 2012.

This matter has also been discussed in (Tsimplis et al. 2012) concluding that a speed reduction of  $x\%$  requires a  $1/(1 - x\%)$  larger fleet to achieve the same transport performance and provides equation 2.1 for estimating the increasing demand in ships under slow steaming conditions:

$$F_{SS} = F * \left( \frac{\frac{DAS}{1 - \Delta S} + (365 - DAS)}{365} \right) \quad 2.1$$

Where:

$F$  and  $F_{SS}$  - the number of vessels of ship type and size category in the fleet at normal speed and when slow steaming respectively

$DAS$  - days at sea per year for ship type and size category

$\Delta S$  - speed reduction as percentage of the baseline speed

In addition, since slow steaming is achieved by operating the main and axillary engines at loads often below standard manufacturer recommendations for long periods, there is a risk of an accelerated wear of the machinery components. Moreover, in the case of loads lower than 40 percent of MCR running for a long time, some additional adjustments should be made in order to prevent soot deposits in the exhaust gas boiler, soot build-ups in the

turbocharger, increased heat load on components as well as excessive lube oil consumption. However, these negative effects can be diminished by special fuel valves, exhaust gas boiler bypass, reductions in cylinder oil feed rate, decreasing the turbocharger cleaning interval and adding cut-out valves (ABS 2013). Additionally, electronically controlled engines are designed to conform and may operate at lower loads.

Finally, the main engine's specific fuel oil consumption (SFOC) is actually increasing up to 10 percent at very low load operations, this being a function of the engine characteristics, engine age and ship type. Therefore, this should be taken into account in the economic assessment of slow steaming options and potential fuel savings.

### ***Route management***

Due to prevailing currents, wave heights, winds and weather patterns, the shortest Great Circle distance between two points is not necessarily the fastest or the most fuel-efficient, mainly because the maintenance of speed in poor weather increases the added resistance, which, in turn, affects the fuel consumption. Alternatively, the reduction of ship's speed in adverse weather conditions causes delays in the transportation schedule. Therefore, weather routing became essential in voyage performance management and aims to predict the optimum speed with reduced fuel consumption while ensuring the safety of the crew, passengers and the cargo.

Nowadays, weather and sea condition monitoring systems combined with navigational software can contribute to approximately 10 percent fuel savings (Crist 2009). Such systems are equipped with the real-time weather forecast data receivers and able to select an optimal route with calmer sea conditions. Therefore, weather routing is a service provided to the operator by a company which specialises in gathering and interpreting metocean data to identify wind and sea condition and, finally, to estimate ship system behaviour during its voyage using either a generic simulation model that matches ship's type and size or real geometric characteristics of the examinee ship. Such a ship behaviour prediction simulation model is based on the model test data, empirical methods, full-scale measurements or a real-time calculation of ship motions and added resistance.

The meteorological data processing is based on the mathematical modelling of the atmosphere and weather system supplemented with the ocean wave forecasting models based on the wind and the ocean current. In turn, the routing process is based on the simulation of the various routes considering estimated weather conditions and safety limits. In fact, weather routing is the most beneficial during longer voyages allowing to choose

from a wider range of possible routes as well as when the weather factor has a greater influence on the fuel consumption.

### ***Trim and draught optimisation***

Since the hull forms are normally designed for a limited number of draughts (normally 1 – 3 draught levels such as ballast, design and laden) and often with no trim considered, when in service, even small changes of trim may result in significant increase of ship's resistance and, therefore, negatively affect the fuel consumption. In fact, poorly optimised trim at low load conditions may result in higher fuel consumption than in the case of a fully loaded ship at proper trim. Therefore, it is vital for the operator to ensure a proper distribution of the ballast and cargo while taking into account a specific combination of draught and trim to minimise the power requirements. This is in addition to maintaining adequate margin against the shear forces and bending moment acting on the hull.

In order to satisfy such demand, a number of trim optimisation tools have been developed. Such tools are, normally, onboard software applications that estimate most favourable trim conditions for the required draught as well as optimising the distribution of cargo or ballast. The effectiveness of these trim optimisation tools, to a large extent, depends on the estimation methods which could be classified as theoretical calculations/testing and real-time measurements.

Normally, the estimation procedure of an optimum trim is based on model test data under calm weather conditions where the resistance is estimated for a number of draught and trim combinations generating a set of curves that indicate changes in resistance in accordance with the required trim. This matrix is then incorporated into the onboard trim optimisation tool. In fact, larger scale models provide more accurate predictions as they better match the full-scale ship performance. However, large models require significant investments. In addition, self-propulsion tests are also important to perform at the design stage as it helps to detect sensitivity of the wake fraction and thrust deduction with changing trim and draught, which are, generally, small but may have a significant impact on the propulsion power demand.

Also, with the constantly increasing pace of technological development, a computational fluid dynamics (CFD) approach is gaining more attention for trim optimisation purposes being able to fairly correctly predict even small changes in resistance.

As such, the alternative method to overcome the uncertainty of calm weather predictions is to integrate real-time on-board measurements for optimum trim estimations, which include

ship system performance under the corresponding draught and trim data harvesting in order to generate the optimum trim tables. However, this method also has gaps in accuracy associated with the difficulties in the elimination of the realistic trim/draught impact on the power consumption from the other contributing components.

### ***Hull and propeller coating and cleaning***

The condition of the hull surface and its level of roughness may have a significant effect on a ship's performance. These factors may influence the scale of the boundary layer, thus leading to an increase of the frictional resistance component when poorly maintained.

A hull surface roughness mainly depends upon two factors: permanent roughness, which includes mechanical damage of the steel plates, corrosion or construction deficiencies; and temporary roughness, often referred to marine biological fouling, but also influenced by coating damage, coating deterioration or rough coating application and inaccurate polishing of the surface before hull coating.

Marine biological fouling caused by spreading of living organisms over the wetted surface includes bacteria, diatoms, algae, weed or even barnacles and mussels. The spread of marine bacteria on a non-toxic hull surface has been described in many recent studies as immediate, with the population reaching several thousand within few hours and several million within two to three days. The primary slime film of 10  $\mu\text{m}$  to 20  $\mu\text{m}$  formed in early stages of hull surface colonisation by the mixture of bacteria, diatoms and algae may increase the total resistance by 1 percent for full-form ships and by 0.5 percent for fine-form ships at high speeds.

The prevention of hull fouling lies with the performance of the hull coating. At present, the main types of anti-fouling paints include Controlled Depletion Polymer (CDP), Self-Polishing Copolymer (SPC) and silicone or fluoropolymer based Foul-Release Coatings. All these coatings offer distinct levels of fouling protection, average hull roughness (AHR) and lifetime. However, since CDP and SPC paints are based on the slow release of toxic chemicals, biocides, they become depleted and require replacement after some years. The main properties of these coatings are briefly described in Table 2.2. In fact, slow steaming operation increases a risk of biological fouling making it difficult to keep the surface smooth even for the most advanced coatings.

Despite the fouling protection and the level of smoothness, another valuable property of antifouling hull paints is the ability to maintain its original state without often recoating. This can be achieved through the proper monitoring and regular cleaning of the wetted

surface. It is important to note, that the surface cleaning, depending on the type of coating, may have an additional benefit of reactivating its biocide layer. As such, a hull surface cleaning should be performed regularly while taking into account IMO (MEPC.207(62) Annex 26 2011) regulations developed to prevent the spread of aquatic species into the inappropriate habitat.

Table 2.2 General properties of hull coatings prevailed in service.

<i>Type</i>	<b>Controlled Depletion Polymer (CDP)</b>	<b>Self-Polishing Copolymer (SPC)</b>	<b>Foul-Release Coatings (biocide free)</b>
<i>Working principle</i>	Water-soluble natural or synthetic pine rosin mixed with a biocide with an added insoluble reinforcing polymer resin, which creates a skeleton for stronger mechanical properties.	Metallic or organic synthetic polymer such as copper-acrylate or silyl-acrylate mixed with a biocide, which releases by a hydrolysis or ion exchange reaction of an acrylic polymer with seawater.	Innovative non-stick silicone or fluoropolymer based coating without biocide. The technology works by providing a very smooth and low friction surface onto which fouling organisms have difficulty attaching
<i>Specific aspects</i>	- a build-up of insoluble materials at the surface in a leached layer slows the release of biocide and makes recoating difficult.	+ hydrolysis stimulates solid dissolution resulting in relatively thin leached layer and smooth surface (compared to CDP).  + SPC does not require ship movement since there is self-smoothing surface without residual “skeleton”.	+ resistant to the adhesion and settlement of organisms that make up slime colonisation.  - requires a special care in operations, as a mechanical damage (for example from fenders or tags) cancels out its anti-fouling properties.
<i>Lifetime</i>	3 years	5 years	3 – 5 years
<i>AHR</i>	40 µm per year	20 µm per year	5 µm per year

In the cases when propellers and rudders are coated with special protective coatings, the propeller and rudder cleaning and coating could be additionally incorporated into the ship’s surface maintaining routine as it is also exposed to increasing surface roughness which creates by corrosion, cavitation erosion, impingement attack or, simply, improper maintenance, caused by, for example, overspray from hull coatings or nicked edges and, therefore, affects propulsion efficiency. Some of the advanced foul-release coatings for propeller blades provide smoother propeller surface than originally polished. However, these coatings are still subject to damage by a cavitation erosion, which, in fact, has fouling

preventing properties itself. In addition, it should be noted that some propellers will naturally get smoother in operation depending on waters while other become rougher in service.

## 2.2 Hull Optimisation

The hull efficiency is a subject to a set of rules and constraints based on the underlying principles of hydrodynamics. The constraints are subject to many factors including design restrictions determined by docks, ports and channels specifications. The main objective of defining the principal hull dimensions is to fulfil the set of shipowners' requirements which mainly include the construction cost, sufficient cargo carrying capacity and structural strength, service speed and endurance range, ship's hydrodynamic efficiency as well as manoeuvrability and stability, while complying with the IMO and national safety regulations and construction standards provided by a relevant classification society. The fulfilment of the aforementioned requirements should be associated with finding the optimal solution aiming to minimise the cost for ship's construction and to maximise the hydrodynamic efficiency.

Finding an optimum length and block coefficient ( $C_B$ ) has a significant impact on ship performance. Optimal length is a function of the Froude number and speed. It strongly affects both the ship's calm water resistance and seakeeping performance as well as having a significant influence on the weight of the steel structure and accommodation and hence on the construction cost. In fact, a partial replacement of traditional steel by a lighter weight alternative materials: for example, high strength steel, innovative composites or aluminium structures can reduce the displacement of a ship and consequently fuel consumption of the order of 1 percent. A further example in the case of a tanker might be that if the steel weight could be reduced, the fuel consumption is likely to result in approximately 0.2 percent lower as shown in Figure 2.3.

Typically, for a given DWT and displacement, increasing the length generally leads to an increase of the ship's structural weight and to a reduction of the ship's required propulsion power for achieving the specified speed due to a moderate reduction of the wave-making resistance. Additionally, the increase of length implies an increase of the steel cost, while a limited reduction of the cost of the propulsion machinery system may be expected. At the same time, depending on the ship type, an extension of a hull may cause an increase of the ship's frictional resistance due to a larger wetted surface area, which can be outweighed

by a reduction of beam to draught ( $B/T$ ) ratio or by designing a vessel with lower ballast requirements. It has been illustrated by (Wärtsilä 2010) that removing 3000 tonnes of permanent ballast from a vehicle carrier while increasing its beam by 0.25 metres, in order to achieve same stability level, resulted in a reduction of the propulsion power demand by 8.5 percent.

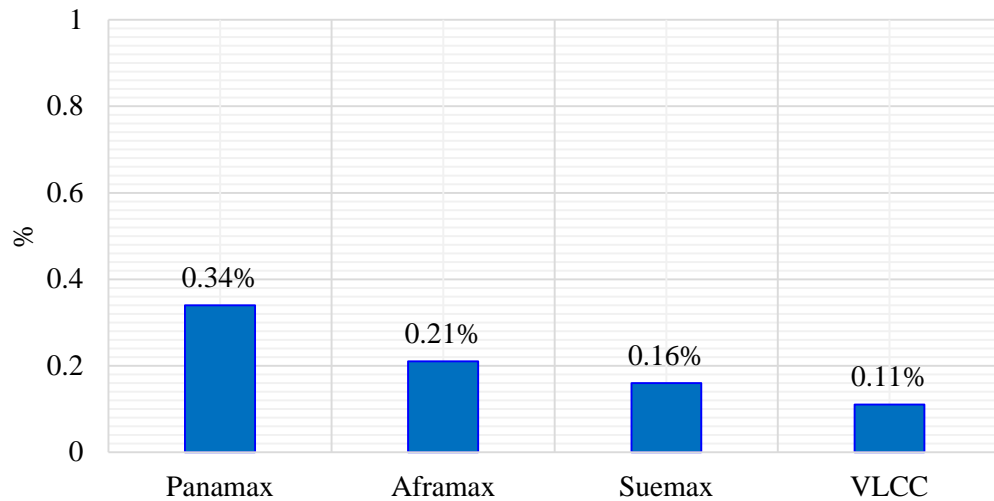


Figure 2.3 Oil tankers: percentage change in fuel consumption associated with the 1 percent reduction in steel weight, based on data provided in (ABS 2013).

Depending on the ship type, increasing draught by reducing block coefficient ( $C_B$ ) results in improvements of hull efficiency as well as potentially providing an additional advantage of allowing for a larger propeller to be fitted. Alternatively, a considerable increase of  $C_B$  makes the hull excessively bulky, which has a negative effect on the ship's wave-making resistance.

These and other similar relationships between hull design particulars are extensively described in a number of sources including (Schneekluth & Bertram 1998; Molland et al. 2011; Papanikolaou 2014) underlying the scale of challenge that naval architects are facing in their way to achieve the most hydrodynamically efficient hull form.

Larger vessels, in terms of their capacity, have a relatively better energy efficiency per unit of work associated with the amount of cargo transported than smaller ships with the same speed. This results in a lower power consumption per unit of cargo. According to (Corbett et al. 2009), the regression analysis based on the recent new-builds indicate approximately 4 percent greater specific efficiency due to an increase of the ship's size by 10 percent. According to the (ABS 2013) statistics, scaling up the size of a container ship from 4,500 TEU to 8,000 TEU results in a reduction of the fuel consumption per transport work by up

to 25 percent while an additional increase by 4,500 TEU (from 8,000 TEU) boosts the overall transport efficiency by approximately 10 percent. As for July 2015, the world’s largest containership is the Malta-flagged “Barzan” built by Hyundai Samho Heavy Industries in South Korea. Launched in May 2015 by the United Arab Shipping Company, the vessel is 400 meters long while having 18,800 TEU capacity. As reported by DNV GL, she has the latest energy efficient technologies as well as “has been designed and constructed with the vision of undertaking a quick and cost-efficient retrofit to LNG at a later stage”. Moreover, Barzan’s EEDI value is approximately 50 percent lower than it is required by 2025.

Table 2.3 Maximum allowable ship dimensions in canals and channels.

Route	Maximum passing dimensions
Panama Canal	New Panamax (since 2014): $L < 366$ m $B < 49$ m $T < 15.2$ m Capacity of containers 12,000 TEU
Suez Canal	$L$ – no limit $B < 71.02$ m $T < 10.67$ m (concerning stern draught in ballast condition) $T < 12.80$ m (maximum allowable draught for $B < 47.55$ m, concerning fully loaded voyages southbound) $T < 16.15$ m (maximum allowable draught for $B < 42.67$ m, concerning fully loaded voyages northbound)
Canal St. Lorenz (linking the inland Great Lakes of North America with the Atlantic Ocean)	$L < 225.6$ m $B < 23.8$ m $T < 8.1$ m
Northeast Sea Channel (Nord-Ostseekanal – Northern Europe)	$L < 315$ m $B < 40$ m $T < 9.5$ m
Malacca Straits (between Malaysia Peninsular and Sumatra island)	$T < 25$ m

However, the main ship dimensions such as length ( $L$ ), beam ( $B$ ), draught ( $T$ ) and capacity are often affected by the topological limits of the route, namely, the dimensions of ports, channels and canals that the projected ship needs to pass through. Some typical maximum allowable ship dimensions of the most recognised canals and channels are listed in Table 2.3. In some cases, the ship length may also be restricted by the length of slipways or docks

of selected shipyards, with which the shipowner has a long-term collaboration in building the new vessels and/or the maintenance of his fleet.

Additional efficiency savings may be achieved by incorporating the hull-enhancing appendages. Perhaps, the most well-known among them is a bulbous bow. Generally, the bulbous bow is applicable to a number of ship types with the waterline length longer than about 15 meters that operate most of the time at or near its maximum speed. At lower speeds, however, the bulbous bow may cause a minor gain in the frictional resistance due to expanded, by its presence, wetted surface. Large ships, having relatively small changes between loaded and ballast draughts with bulbous bow, would normally benefit by approximately 10 percent in fuel efficiency in contrast to similar vessels without one.

Bulbous bows require a proper optimisation for gaining greater efficiency benefits. A set of principal factors including the cross-sectional area at the forward perpendicular, volume, vertical extension of the centre of volume as well as bulb section form and profile are normally considered in bulbous bow design and optimisation process. For instance, a pear-shaped bulbous bow is more efficient in combination with ballast or partially loaded draughts while cylindrically shaped bulbs provide a compromise solution. Fuller ship forms, normally tankers and bulk carriers, are often designed with bulbous bows that have a large sectional area and a V-shaped transition of the bulb into the hull, which helps to extend the waterline length at ballast conditions while traditionally acting when fully loaded.

The added resistance due to turbulence, caused by the interrupted water flow around bow thrusters tunnels or sea chest openings, can reach up to 2 percent of calm water resistance. In order to reduce a negative effect of a pressure variation across the bow thruster tunnel, the anti-suction tunnels can be additionally incorporated. It is also important to ensure that the hull openings are properly faired so as to avoid any undue turbulence in flow along the hull resulting from the discontinuity in the hull surface. At higher ship speeds, typically above 25 knots, the use of actuating doors at the tunnel exits will minimise the ship resistance penalty and noise emissions.

Possibly the most innovative hull-enhancing technology is the air lubrication technique. The general idea is to cover the bottom of the ship with fine air bubbles, acting as a lubricant which separates the hull's wetted surface from water and, therefore, reduces frictional resistance. For example, Mitsubishi Air Lubrication System (MALS), suitable for large heavy cargo and passenger ships, claims to reduce fuel consumption by up to 10 percent

(Kawabuchi et al. 2011). At the same time, Maersk recently deployed a prototype of the air lubrication system on one of their vessels, namely Olivia Maersk, aiming to verify the potential energy efficiency benefits. The results did not prove the expected benefits. This is because it was difficult to maintain the micro-bubbles size at full scale as they tend to merge which significantly reduces the frictional resistance benefits.

Besides the resistance and propulsion performance, during the design process a proper care should be taken regarding the stability, strength and manoeuvrability of a vessel while meeting its desired operational profile. In addition, a hull design process should be inseparably associated with the propeller design and engine matching underlining the importance of the holistic system approach in ship hydrodynamic design.

### 2.3 Propellers and Energy Saving Devices

The overall ship efficiency performance is strongly influenced by the type and configuration of its propulsion system. The most commonly used propulsor types are the fixed pitch propellers (FP), followed by the controllable pitch propellers (CP) (about 35 percent of the market) and ducted propellers (about 25 percent of the market), which, in turn, can be equipped with either FP or CP propellers.

#### *Fixed pitch propeller*

In the case of fixed pitch propellers, an open water efficiency is normally expected to range from approximately 50 percent for tankers and bulk carriers up to 75 percent for high speed and slender vessels. Moreover, there are several options available for designers to enhance the open water efficiency while controlling unwanted cavitation excitation and erosion on the propeller blades. One of them is an introduction of the modified blade tip propeller geometry, commonly known as the Contracted and Loaded Tip (CLT) propeller featuring a blade end-plate technology. Another option for this type is the Kappel propeller. The core idea is to reduce the tip vortex while obtaining a higher circulation towards the blade tips. The working principle of these designs is similar to that of winglets at the end of aeroplane wings. However, while a system such as a CLT propeller is claimed to significantly improve an overall propulsion efficiency, the additional blade end-plates are increasing the wetted surface of the propeller disk and, thus, causing extra frictional resistance. Additionally, it is important to set the end plates at the correct attitude in relation to the slipstream flow to prevent undue drag characteristics.

Another method to influence the open water efficiency is the reduction of rotational speed (RPM) while allowing the diameter to increase at its optimum dimensions. However, there are some design constraints which limit the scale of change including the hull and baseline clearances, insufficient immersion as well as an increasing hull pressure and propeller weight. Therefore, it is important to find an optimum balance to satisfy these constraints while achieving the best performance of the propeller/engine combination.

Generally, with an increase of the propeller-specific loading, there is a growing risk of cavitation erosion, predominantly caused by the pressure field in the flow (Bertram 2012), which requires an additional expansion of the propeller's blade area. On the other end of the spectrum, there is a potential to increase the propeller efficiency through reduction of the blade area, commonly expressed as a blade area ratio, which decreases frictional losses associated with a larger wetted surface. However, any blade area reduction should be consistent with the thrust loading requirements of the propeller from the cavitation point of view.

The common way for preliminary estimation of the optimum blade area ratio while keeping the global and harmful effects of cavitation under control is to undertake either Burrill's or Keller's analysis procedure, both described in (Carlton 2012). The Keller's method is based on the empirical equations, while the Burrill's procedure provides a cavitation diagram based on model tests with a set of curves relating to back sheet cavitation extents applicable to the uniform flow. These curves demonstrate the relationship between thrust loading coefficient and the local cavitation number.

Thus, it is important to better understand the cavitation margins in relation to the blade area ratio and propeller section design as well as to evaluate the potential efficiency benefits associated with the reduction of the blade area ratio. This will help to find an optimum balance between these factors. In addition, with growing industry interest in the research and development of innovative propeller materials and coatings, the possibility for further modification of the blade area ratio to achieve a better performance with a lower risk of cavitation may substantially increase.

### ***Controllable pitch propellers***

Unlike fixed pitch propellers whose only operational variable is the rotational speed; the controllable pitch propeller provides an additional possibility to adjust blade pitch. This is particularly useful when a ship has two or more distinct operating conditions: for example free running/trawling, anchor handling, day and night ferry services and so on.

Controllable pitch propellers are especially beneficial for ship manoeuvrability and the applications involving shaft-driven generators, which require to keep the rotational speed constant while managing the power absorption by changing the propeller pitch. The controllable pitch propeller type is mostly preferred for the tugs, passenger, ferry and general cargo ship types.

When operating in off-design conditions under constant rotational speed, the overall propeller efficiency performance of CPP might be lower compared to the conventional FPP. This is because when operating at a constant rotational speed in off-design conditions, the efficiency may fall off because the hydrodynamic conditions no longer relate to the propeller design point. This also extends to the cavitation environment in which the propeller operates since at off-design conditions there can be a tendency to develop face cavitation as opposed to back cavitation in same conditions as well as to potentially increase the level of vibration and noise. Conversely, CP propellers can be operated under combinator-control where blade pitch and shaft RPM are varied simultaneously, which may provide a slightly enhanced propeller efficiency and a more benign cavitation environment. Alternatively, CPPs provide considerable benefits when the vessel is required to operate under changing conditions such as manoeuvring or dynamic positioning situations.

### ***Ducted propellers***

Ducted propulsion system represents a propeller operating inside an annular duct. Since the cross section of the nozzle has an aerofoil profile, it could have accelerating or decelerating properties depending on its hydrodynamic profile. The latter one is commonly used to manage cavitation and rarely, if at all, applied in large merchant vessels. Accelerating ducts, often referred as Kort nozzles, are widely used for vessels with a high propeller-power coefficient ( $B_p$ ), commonly tankers, bulk carriers, offshore service vessels, trawlers, tugs and anchor handlers. The aim of the accelerating duct is to enhance the propulsion efficiency by generating a lift on the duct by accelerating the inflow around the duct surface and, thus, creating an additional thrust, which is the actual component of the generated lift force. However, with increasing ship speed the level of propulsion efficiency benefits due to the accelerating duct may fall to relatively modest amounts. It is also possible for a duct to give a negative contribution to the propulsor thrust at high advance speeds. Nevertheless, as reported by (AEA Energy and Environment 2008), power savings of up to 5 percent can be expected from the ducted propeller performance compared to an open propeller depending on the operating conditions.

### ***Contra-rotating propellers***

The contra-rotating propeller concept implies a pair of propellers placed one behind other while rotating in opposite directions, where the aft propeller is designed to share the propulsive load and recover some of the rotational energy in the slipstream from the forward propeller. In addition, such a design philosophy allows lower propeller blade loading compared to a single propeller resulting in better efficiency, which in the case of a single screw vessel, as outlined in (Wärtsilä 2010), can reach up to 10 – 15 percent. Although the principle of contra-rotating propellers has been known since 1876 de Bay's contra-rotating propeller for the steam yacht *Iolaire*, it was not prevalent until Morgan's research in 1960 when the fundamental principles of design begun to be more fully understood.

In marine applications of contra-rotating propellers, it is common for the aftermost propeller to have a smaller diameter than the forward propeller. This helps to accommodate the slipstream contraction effects. Likewise, in order to avoid vibration due to blade parsing frequencies, the blade numbers of the forward and aft propellers are usually different. The contra-rotating propellers have found a significant number of applications in smaller high-speed vessels and boats with the rotational speed around 1500 – 2000 rpm as well as with torpedoes in order to eliminate the torque reaction. The application for larger merchant vessels is rather limited due to a mechanical complexity of the shafting system.

In recent times, a novel application of the contra-rotating principle has been developed by ABB which comprises a conventional fixed or controllable pitch propeller used in association with podded propulsor. In this configuration, the conventional propeller is coupled to the shaft line while the podded propulsor, which replaces the rudder, rotates in the opposite direction thereby regaining some of the otherwise lost slipstream energy.

### ***Energy saving devices***

Coupled with the propeller, the energy saving devices (ESD) are intended to increase the propulsive efficiency of a ship characterised by the Quasi Propulsive Coefficient (QPC), which is a function of hull efficiency ( $\eta_H$ ), relative-rotative efficiency ( $\eta_R$ ) and open water efficiency ( $\eta_O$ ) and defined as follows:

$$QPC = \eta_H * \eta_R * \eta_O \quad 2.2$$

Among these elements, the open water efficiency ( $\eta_O$ ) has the most substantial influence on the overall propulsive efficiency. The open water efficiency of the propeller for a given ship, by definition in (Molland et al. 2011), is a product of an ideal efficiency characterised

by axial momentum theory for a propeller with a finite number of blades, losses associated with the fluid rotation caused by the propeller as well as losses due to blade friction drag. Energy saving devices can be categorised as the devices operating before the propeller (pre-swirl devices), devices at the propeller and the post-swirl devices. The pre-swirl devices stimulate a reaction with the boundary layer at the stern of the ship to provide more homogenised flow beneficial for the propeller performance. In turn, the post-swirl devices and the devices located at the propeller are aimed to recover energy losses by modification to the flow field and the slipstream of the propeller.

#### *Pre-swirl devices*

Generally, the pre-swirl devices are easier to integrate with the hull structure. The most known pre-swirl devices are Schneekluth wake equalizing duct (WED), Mewis duct, Grothues spoilers, flow conditioning ducts, pre-swirl fins and Grim vane wheel.

- Schneekluth wake equalizing duct (WED)

The wake equalising duct (WED), initially proposed by Schneekluth, aims to reduce the separation around the ship's stern by redirecting the flow to the upper part of the propeller while establishing a more homogenous wake field (Schneekluth & Bertram 1998). This helps to enhance the hull and open water efficiencies by moderate reduction of the wake fraction and thrust deduction coefficients. Moreover, WED may cause a generation of the low-pressure areas in the front part of the duct which could provide additional efficiency benefits by reattaching separated flow to the hull. However, in case the flow around the stern is fine and uniform, such low-pressure regions may increase the thrust deduction coefficient. According to the manufacturers, the guidance energy saving benefits of WED amount up to 12 percent depending on the flow configurations and propeller thrust loading.

- Grothues spoilers

Grothues spoilers (Grothues-Spork 1988) represent a hydrodynamic fin system, consisting of small curved triangular plates fitted to the stern of the hull in front of the propeller disk and above the propeller axis. The main idea of Grothues spoilers is to straighten the flow directed towards the propeller due to the curved shape of fins helping to align the leading edge of the fin with the surrounding flow direction thereby minimising the vorticity in the incident flow field into the propeller. Ideally, spoilers may generate an additional thrust by inclining the vertical flow in the horizontal direction.

The expected benefits from the application of such spoilers are strongly dependent upon the correct adjustment of a curvature angle of each spoiler in line with the incoming flow as well as positioning along the stern surface in order to prevent an additional friction.

- Flow conditioning ducts and pre-swirl fins

The main purpose of the flow conditioning ducts is to bring uniformity to the propeller inflow by the action of the duct, which is normally positioned ahead of the propeller. The pre-swirl fins represent a simple system of fins located directly ahead of the propeller around the shaft axis and designed to improve the propulsive efficiency through pre-rotating the propeller inflow. When combined with the pre-swirl fins, the flow conditioning ducts enhance the inflow to the stator which increases their efficiency.

There are several types of the flow conditioning duct systems available on market including Mitsui integrated ducted propeller, Hitachi's Zosen nozzle, Sumitomo's Integrated Lammeren duct and Mewis duct. As an example, the Mewis duct consists of a duct positioned ahead of the propeller together with an integrated fin system within. It is claimed to provide energy savings of 3 – 8 percent depending on the hull form. Mewis ducts were tested and installed on medium sized ships ranging from 45,000 to 50,000 DWT with reported reductions in propeller pressure pulses and tip cavitation (MER 2012).

- Grim vane wheel

The Grim vane wheel is a freely rotating device located behind the propeller, namely on the tail shaft or the rudder horn (Grim 1980). It aims to capture energy from the propeller slipstream and convert this energy into an additional propulsive thrust. The vane wheel consists of the turbine section inside the propeller slipstream and a propeller section outside the propeller slipstream. Therefore, the diameter of the vane wheel is normally larger than the actual propeller diameter while having a greater number of blades in comparison to the original propeller.

Grim vane wheels are suitable for a wide range of conventional cargo ships and could provide 7 – 10 percent in efficiency improvements (Breslin & Andersen 1994). However, there are concerns that collisions with wood or ice floes may damage the vane wheel and in some cases the bearing upon which the wheel sits. Therefore, since the system is mechanically sensitive and involves considerable investment, only a few actual installations have been reported (Bertram 2012).

### *Post-swirl devices*

Alternatively, the post-swirl devices are designed to condition the post-propeller flow while operating behind the propeller within its slipstream region and include a range of rudder bulbs, fins, stators and other concepts as well as combinations of them.

- Rudder – bulb systems

Rudder – bulb system is designed to prevent flow separation as well as excessive vorticity behind the hub by successfully extending the propeller boss. Typically, the system comprises a large bulb with the diameter of some 20 percent of the actual propeller diameter. The bulb is placed on the rudder immediately behind the propeller boss. In some cases, the system also incorporates a set of four fins located in an X – shape manner. Since the fins operate in the helical slip – stream and, thus, receive the flow at incidence, they produce a lift force, which acts in the forward direction and results in additional propulsive thrust.

- Asymmetric rudder

Asymmetric rudder system consists of two distinctive regions. The regions above and below the propeller axis have aerofoil properties and both regions are optimised to work in the wake field of the propeller. The system allows the effects of the rotation of the propeller’s slipstream to be countered which results in the reduced drag. Other important benefits are directed towards reducing rudder cavitation erosion and, hence, extending the lifespan for the rudders and lowering the level of vibration and noise.

As stated in (Corbett et al. 2009), for these devices, a gain in propulsive efficiency vary from 1 to 8 percent based on the model test results, whereas full-scale measurements are only available for the combination of fins with rudder and estimated to be 8 – 9 percent. Additionally, post-swirl devices are often combined with pre-swirl devices, which, in fact, may reduce a contribution of the post-swirl devices into the overall efficiency due to pre-swirl devices would already neutralise the post-rotational flow of the propeller. In addition, a potential gain in energy efficiency from such devices is generally lower for optimal hull and propeller designs as their initial purpose was to improve the flow around the hull in order to eliminate energy losses due to poorly designed stern or propulsor. In the design of these devices, it is important to endeavour to take into account the scaling effects from model to full scale. In this contexts, the use of CFD methods can be helpful.

- Boss cap fins

Some devices may be attached to the propeller hub to break up the hub vortex generated behind the rotating propeller. The boss cap fin comprises a small vane propeller fixed to the tip of a cone-shaped boss cap, which may have more blades than the propeller itself. First developed and manufactured at the end of the 1980s in Japan, it has had over 2,000 installations worldwide with the manufacturer's savings claims of 3-5 percent. However, according to at-sea performance tests, their effectiveness was reduced at slower steaming speeds.

It is important to emphasise that manufacturers often claim very promising figures of reductions in fuel consumption, which seem to be very optimistic and require independent research. Such evaluations have been conducted by (Smith, Day, et al. 2014) and included several case studies of the hydrodynamic performance of vessels incorporated with WEDs, a combination of WED and pre-swirl fins, a twisted rudder and propeller boss cap fins using simplified CFD models. The obtained results have shown that in all cases the expected benefits were lower than originally claimed.

Since it is difficult to discriminate the performance improvements below 3-4 percent, it can be extremely difficult to justify efficiency claims for particular devices which claim the benefits below this region. This is due to the statistical errors encountered in continuously monitored data while bearing in mind the variabilities of machinery operations, signal measurement and environmental conditions.

## 2.4 Machinery Improvements

Since low-speed diesel engines are designated as the most efficient, diesel propelled machinery became the most common choice for the marine propulsion of large merchant vessels. At the current state of technology, the diesel engine fuel efficiency can reach up to 50 percent (MAN Diesel and Turbo 2014c). Therefore, only half of the fuel's specific energy is converted into the mechanical energy and can be directly transmitted to the propeller. Medium speed diesel engines generally have 3 – 4 percent lower fuel efficiency. In addition, they are normally connected to the propeller through the speed reduction devices, commonly a reduction gear box or electric drive system, which induce additional efficiency losses of about 2 - 3 percent in case of reduction gear and up to 8 percent when an electric drive system is used (MAN Diesel and Turbo 2015). Such losses are reflected in the fuel consumption to satisfy the ship's power requirements. Low-speed diesel engines

are commonly used for main propulsion on large merchant vessels, especially tankers, bulk carriers and container/general cargo ships, while medium speed diesel engines are generally applied as a part of an auxiliary system of these ship types or as the main propulsion for smaller commercial vessels, cruise ships, ferries and large fishing boats. In addition, LNG carriers are normally equipped with steam, diesel-electric propulsion systems or dual fuel slow speed engines.

With increasing demand for sustainable shipping, engine designers and manufacturers are constantly striving to reduce exhaust emissions while improving fuel efficiency. Currently, MAN, Wärtsilä, Rolls-Royce and Caterpillar are among the biggest engine market players to satisfy the energy efficiency demand while complying with exhaust emissions regulations by offering a vast portfolio of marine technologies and devices including dual fuel engines that can operate on both, the fuel oil and natural gas.

Since enhanced efficiency can be achieved through the introduction of innovative equipment or by improving engine's operation philosophy, the following section is aimed to discuss the most attractive innovative technologies and methods designed to enhance fuel efficiency.

#### ***Electronically controlled engines***

Many modern marine diesel engines are supported by a digital electronic control of fuel injection quantity, fuel injection timing, exhaust valve timing and etc., which results in approximately 2 – 2.5 percent reduction in SFOC at low and medium loads compared to conventional engine performance (MAN Diesel and Turbo 2014b). Electronically controlled low-speed diesel engines, referred as ME type in MAN and Flex type in Wärtsilä, are also associated with a common rail technique, where the fuel is supplied by high-pressure common rails equipped with solenoid valves and controlled by the electronic system. This electronic system helps to optimise the fuel injection point in the thermodynamic cycle in accordance with the required engine load and to maximise its efficiency, while the exhaust valve control, allows variable timing to maximise scavenging (Smith, Day, et al. 2014).

Engine control tuning is another innovative method available for low speed electronically controlled engines, which is designed to control the exhaust valve timing and injection profiling in order to reduce SFOC via the automatic adjustment of a maximum cylinder pressure in accordance with the engine load. In fact, while for conventional low-speed diesel engines the introduction of SFOC reduction methods via compression adjustments

may result in increased level of  $NO_x$  for low load operations and, thus, should be monitored and balanced in accordance to IMO Tier II regulations; in the case of electronically controlled engines, it is possible to reduce SFOC while keeping the  $NO_x$  level to its minimum as required by Tier II compliance.

### ***Turbocharger optimisation***

For ships continuously operating under slow steaming conditions, turbocharger control systems can be incorporated to reduce SFOC by 2 to 4 g/kWh. Examples of such systems include the Variable Turbocharger Area (VTA) by MAN or Variable Turbine Geometry (VTG) by Wärtsilä, both compatible with large-bore two- or four- stroke diesel and gas engines with camshaft or electronically controlled system.

The idea is to adjust the nozzle ring of the turbocharger in accordance with the engine load such as the nozzle ring is expanded with full load operation while narrowing down with the decreasing load. As a result, SFOC at full load is higher while at partial or low load is optimally reduced. In the case of multiple turbochargers installed, similar effects can be achieved by cutting out one turbocharger unit.

Another method to enhance fuel efficiency at lower loads is the Exhaust Gas Bypass (EGB). The system is optimised to work under the both, low and high loads. For the lower loads operation, a smaller turbocharger system is used to provide the engine with its efficiency demand. In the case of a full load operation, the exhaust gas is bypassed beyond the turbocharger to prevent it from the over-speeding. An additional benefit from EGB system is an increase of the exhaust gas temperature, resulting in the greater amount of steam at the exhaust gas boiler. The most efficient utilisation of the bypass technology may be achieved when used in combination with the common rail technology.

### ***Engine de-rating***

Another effective method of SFOC reduction is the engine de-rating. Thermodynamic efficiency of an engine is defined by a relationship between the maximum burning pressure and mean effective pressure (MEP). The engine de-rating means the operation of an engine at its maximum cylinder pressure for the design continuous service rating, but at a lower mean effective pressure and/or shaft speed. For example, a higher-power engine de-rated to a lower Specific Maximum Continuous Rating (SMCR), while meeting the required design performance of a ship, will develop lower MEP, which, therefore, will result in lower SFOC at the operating design point.

For an existing ship and without changing the propeller, the engine de-rating will result in a lower ship speed. In the case of newbuildings, the de-rated engine horsepower is that which will drive the ship at a given speed with the propeller optimised to absorb this horsepower at a lower than normal shaft speed. The optimisation would normally require an installation of a more efficient propeller, a larger propeller diameter operating at its optimum RPM, reduction of a blade area ratio or a larger stroke to bore ratio.

For newbuildings, it is also common to install the engine with the increased number of cylinders. An extra expense associated with the additional cylinder would normally be paid back in 3-4 years (MAN Diesel and Turbo 2014a). For example, if the ship's required propulsion power with an applied sea margin is 8300 kW at 127 RPM, a conventional option is to choose an engine with the maximum installed MCR = 8300 kW at 127 RPM (SMCR = MCR). In this case, MAN 5S50ME-C will perfectly suit the ship's requirements. In the case of de-rating, the same model of the engine at the same speed is selected but with one additional cylinder, namely MAN 6S50ME-C with MCR = 9960 kW at 127 RPM, and then de-rated to SMCR = 8300 kW at 127 RPM. The average reduction in SFOC under the de-rated condition, as illustrated in Figure 2.4, will reach up to 3 percent, taking into account additional losses due to increased friction of the extra cylinder and piston. In addition, engine de-rating has a great influence on the EEDI measure as it allows to reduce SFOC while keeping the power and ship speed unchanged.

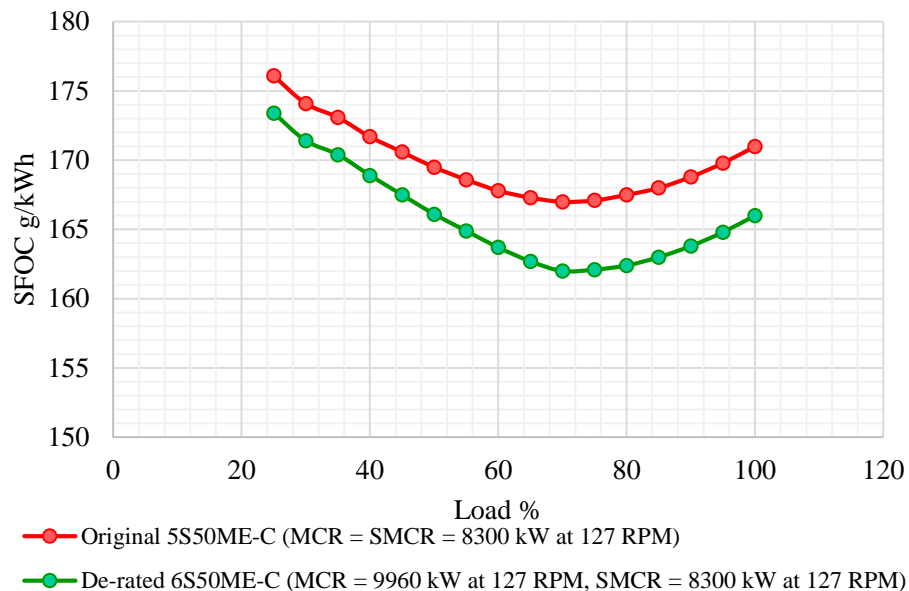


Figure 2.4 SFOC behaviour comparison under conventional and de-rated conditions. Based on MAN CEAS engine calculations.

It should be emphasised that de-rating of an existing engine will require reducing ship's maximum speed, which should be considered with extra caution as the engine must provide a sufficient power to operate under poor weather conditions or to manoeuvre in restricted areas. Engine de-rating also increase a risk of accelerated wear of the machinery components and may cause the engine inner damage due to shorter periods of acceleration. Finally, uprating the de-rated engine back to its designed conditions in order to increase ship's speed is only possible if the auxiliary equipment supports a larger rating.

### ***NO<sub>x</sub> control technologies***

Since the MARPOL Annex VI Tier II and further Tier III requirements, aiming to reduce the level of *NO<sub>x</sub>* emissions, tend to negatively influence SFOC, there is an increasing demand for alternative treatments that will keep both the *NO<sub>x</sub>* level and SFOC to the minimum.

Generally, the quantity of *NO<sub>x</sub>* emissions is a function of combustion temperature, duration of the combustion process and the quality of combustion. Therefore, primary methods of *NO<sub>x</sub>* reduction are focused on a decrease of the combustion duration time and firing temperature, control of fuel injection and the introduction of higher-pressure turbocharging (RAE 2013), which resulted in extensive development of innovative turbocharging technologies. For example, by means of two-stage turbocharging techniques the charge air pressure can be increased substantially resulting in higher power density (if required) and, in conjunction with Miller engine cycle, where the engine is compressing against the pressure of the turbocharger rather than the pressure of the cylinder walls, reduced exhaust emissions and lower fuel consumption.

Moreover, there is a range of alternative treatments for *NO<sub>x</sub>* which are now commonly used including the exhaust gas recirculation (EGR) and selective catalytic reduction (SCR).

As the name implies, exhaust gas recirculation system recirculates the exhaust gas flow to the engine intake manifold for *NO<sub>x</sub>* reduction purposes and is suitable for slow and medium speed diesel engines. The effect of this system is derived from a slightly increased heat capacity of the scavenge air where a minor part of the oxygen in the scavenge air is replaced by carbon dioxide from the combustion. This also helps to reduce the temperature peaks of the combustion (Kristensen 2012). In fact, preliminary studies have shown that application of EGR systems in terms of Tier III regulations may result in sufficient increase in SFOC (1 – 2 g/kWh) compared to Tier II engines. An interesting example of the in-service

application of EGR system on-board of the Alexander Maersk, illustrated in (RAE 2013), has shown a good performance and supported further idea of the EGR application.

The basic idea of a selective catalytic reduction (SCR) is to remove unwanted  $NO_x$  footprint from the exhaust gas via chemical reaction, which relies on the injection of ammonia into the exhaust gas flow, usually in the form of a urea solution. This promotes a chemical reaction with  $NO_x$  species at the surface of the selective catalytic reduction system, leading to formation of nitrogen and steam. The SCR system, while not involving significant modifications to the existing propulsion system, requires an additional space for urea storage in the engine room. In case of low-speed diesel engines, the SCR system is recommended to be installed between the turbocharger and the exhaust gas manifold, providing higher exhaust gas temperatures for more efficient SCR reaction. However, this may result in slight reduction of the overall engine efficiency as it negatively affects the turbocharger. Alternatively, for medium speed diesel engines the SCR system should be installed after the turbocharger. The SCR technology, according to (MAN Diesel and Turbo n.d.), is capable to remove up to 95 percent of  $NO_x$  in the exhaust flow making it a promising solution when operating in ECA areas. However, since it is usually a challenge to find the required space for the catalyst, piping, support, auxiliary equipment as well as  $NO_x$ ,  $O_2$  and ammonia ( $NH_3$ ) measuring devices, it is far more complicated to retrofit the installation than to integrate the SCR system into the newbuilding.

### ***Scrubbers***

With increasing concern and upcoming regulatory restrictions in emission control areas (ECAs) regarding harmful environmental and health impact of sulphur content in marine fuels, there is a continuing research and development of alternative methods, such as exhaust gas after-treatment systems, that aimed to remove sulphur oxides from the exhaust gas flow and can be used in addition to relatively expensive low sulphur fuels while keeping conventional MDO and HFO as a primary option outside ECA.

Seawater scrubbing is one of them. The method involves utilisation of alkalines  $HCO_3$  and  $SO_4$  present in sea water to neutralise  $SO_x$  species in the exhaust gas via a chemical reaction. This reaction results in production of sulphates, which are being recirculated back into the sea. Before the discharge, the sea water is also filtered to remove heavy metals and particulate matter. Such systems have a relatively simple operating cycle and do not require large amounts of waste storage and handling on board. However, there is an uncertainty on the potential consequences of the sulphates-rich waste discharged after the exhaust gas

treatment and some ports and areas may not permit to discharge of the waste water containing sulphur. Alternatively, since sea water already contains a relatively high amount of sulphur, its impact on the marine environment is relatively low and IMO has already approved this technology by adopting (MEPC.184(59) Annex 9 2010).

In fact, the effectiveness of sea water scrubbing systems decreases in some areas including the northern part of the Baltic Sea and Alaska since the alkalinity level in those regions is considerably lower. Therefore, in order to avoid such alkalinity issues, there is an alternative to seawater scrubbers, namely freshwater scrubbers (or closed loop scrubbing system) that additionally involve a caustic soda (*NaOH*) solution to neutralise the sulphur in the marine exhaust. Most of the scrubbing agent is recirculated with only minimal water intake and discharge. These systems are more complex and costly to exploit, while creating waste storage and handling issues on board. A variation on the closed loop system is a hybrid system which can operate as an open loop system while outside special control areas. According to the analytical study conducted by (Boer & Hoen 2015), scrubbers reduce the emission of sulphur to the atmosphere by more than 90 percent. In addition, scrubbing helps to reduce PM (by mass) by 60-90 percent while the amount of  $NO_x$  can be reduced by up to 10 percent. However, due to the extra power required to operate pumps and caustic soda consumption, the estimated additional GHG emissions range between 1.5 and 3.5 percent, while the consumption of additional MGO in the ECA causes a rise of GHG refinery emissions by roughly 6.5 percent.

Since the scrubber technologies can be retrofitted into existing ships, the (Klimt-Møllenbach et al. 2012) project, based on the existing tanker, undertook a case study of a hybrid scrubbing system. This system is capable of operating on both, fresh water and sea water while burning heavy fuel oil. The results have shown a necessity for a new funnel layout due to the introduction of the scrubber together with relevant machinery and new tanks. Moreover, the installation costs of the scrubbing system are estimated to be USD 5.84 million, whereas the cost of scrubbers and its relevant equipment amounted to USD 2.6 million.

#### ***Waste heat recovery system (WHRS)***

Although the thermal efficiency of modern diesel engines is continuously improving with the technological progress, a significant amount of waste heat is still being generated especially when operating under high loads. Normally, the waste heat is utilised onboard to produce fresh water or for accommodation heating purposes. However, with increasing

sizes of ships and engines, the amount of exhaust gas is also increasing. This results in an excessive amount of waste heat accessible on ships. In addition, since the modern turbocharger technologies require less energy, they have also contributed to the additional free heat available in the exhaust flow. As such, waste heat recovery systems (WHRS) (commonly based on the Rankine cycle) are designed to absorb part of the waste heat by evaporating the working fluid under the high pressure and, when the fluid expands in a turbine, convert the available heat into mechanical and then electrical energy. The recovered energy could be used as part of a marine propulsion system providing additional efficiency benefits.

The amount of available waste heat is a function of the outlet temperatures and the exhaust gas flow rates and, although the mass flow varies linearly with the engine load, the temperature of exhaust gas may increase under low load operations while significantly dropping at the normal continuous rating. Moreover, the waste heat recovery performance depends upon the inlet temperature, which, in turn, is a function of the engine and turbocharger efficiencies. In addition to preliminary estimation of the available waste heat, a selection process of the most suitable waste heat recovery system requires careful evaluation of a number of factors including restrictions of the machinery arrangement, ship's operational profile, payback time as well as emissions limits. Table 2.4 illustrates the principle recommendations by MAN (MAN Diesel and Turbo 2014d) when selecting the waste heat recovery system based on the engine's MCR.

Table 2.4 Recommended WHRS for various propulsion systems based on the rule of thumb (MAN Diesel and Turbo 2014d).

Main engine power	Recommended waste heat recovery system
MCR > 25,000 kW	Combined steam turbine (ST) and power turbine (PT)
15,000 < MCR < 25,000 kW	Power turbine and generator (PTG) or steam turbine and generator (STG) with super heater
MCR < 15,000 kW	PTG or Organic Rankine Cycle (ORC)

The cheapest and simplest waste heat recovery system example is the power turbine with a generator, which consists of an exhaust gas turbine (sometimes referred as power turbine) mounted in the exhaust gas bypass and a generator for converting the resulting power into the electricity. Since the power turbine is operating using the part of the exhaust gas flow which bypasses the turbochargers, the output power for electricity production generated by the power turbine, to a large extent, depends on the amount of the bypassed exhaust gas flow. The exhaust gas bypass valve is designed to lock when the power load is less than

approximately 40 percent. As such, depending on the engine size, the power turbine and generator based waste heat recovery system will provide up to 5 percent recovery ratio (MAN Diesel and Turbo 2014d).

Another example of a waste heat recovery system is a steam turbine, where, to enhance the heat to the boiler, the exhaust gas bypass flow is mixed with the stream from the turbocharger. This results in increased exhaust gas temperature before the boiler inlet. Therefore, the amount of potential steam production and, hence, the resulted power output is greater compared to power turbine, which estimated to reach up to 8 percent depending on the main engine size and ambient conditions.

In case of increased power demand, the power turbine can be used in conjunction with the steam turbine connected via reduction gear boxes forming a joint system, such as the steam turbine is specified to start first at 30 – 35 percent SMCR followed by the power turbine at 40 – 50 percent SMCR, which will result in up to 11 percent of recovered power.

The preferred working fluid used in a thermodynamic waste heat recovery system is water since it provides high power outputs without chemical decomposition and extensive condensation inside the turbine. However, it is possible to increase the power output as well as the thermal efficiency using organic fluids (for example based on carbon molecules) instead of water. For instance, the comparison study conducted by (Suarez et al. 2013) aiming to compare the performance of water and a number of organic working fluids, namely Heptane, Benzene, Toluene and Hexamethyldisiloxane in the Rankine cycle based waste heat recovery system while operating 14 cylinders 87 MW 2-stroke diesel engine, has shown that the maximum net power output (2,233 kW at a thermal efficiency of 22.1 percent) was delivered by benzene, while water-based Rankine cycle generated 1,987 kW at 18.6 percent.

## 2.5 Alternative Ship Propulsion and Fuels

According to recent figures by (IMO 2014b), the shipping industry on a global level annually consumes approximately 330 million tonnes of fuel where 80 – 85 percent account for residual fuel, commonly referred as a heavy fuel oil (HFO), with a high sulphur content. Alternatively, ships engaged in coastal voyages and environmentally controlled areas, in the majority of cases, burn lighter marine diesel oil (MDO) being a blend of gasoline and heavy fuel oil. Since HFO is a residual product remaining at the end of the crude oil refining chain, it contains a generous amount of impurities such as oxides, sulphur, and water (Crist

2009). In fact, HFO can be solid enough to support a human walking on the surface at a room temperature (Harrould-Kolieb 2008), thus it needs to be heated before use. A significant factor that reflects the quality of fuels is the crude oil origin. For instance, the residue of a typical “lighter” North African crude oil accounts for 28 percent while in the case of “heavy” Venezuelan crude oil, the residue could be as high as 85 percent (Leigh-Jones 2008). This has influenced a fluctuation of heavy fuel standards in the marine industry (RAE 2013), whilst distillate fuels comply with stricter regulations.

As illustrated in Figure 2.5, the average daily marine fuel oil consumption has gradually been decreasing over the past decade. This trend could partially be a result of the generally increasing propulsion efficiency of marine diesel engines. The recently adopted regulations regarding the sulphur content levels in fuel acted as a demand trigger for low-sulphur fuels. This could be an additional reason for decreasing trend of an average daily heavy marine bunker consumption starting from 2009 when the sulphur regulations were adopted. Such rising demand for the low-sulphur fuels will certainly influence their costs, which are projected to rise significantly after 2020 – 2025 stimulated by further reductions of the sulphur fraction (Florentinus et al. 2012; McGill et al. 2013). Therefore, the introduction of alternative sulphur-free fuels or propulsion methods can be vital and, perhaps, long-term solution to this problem.

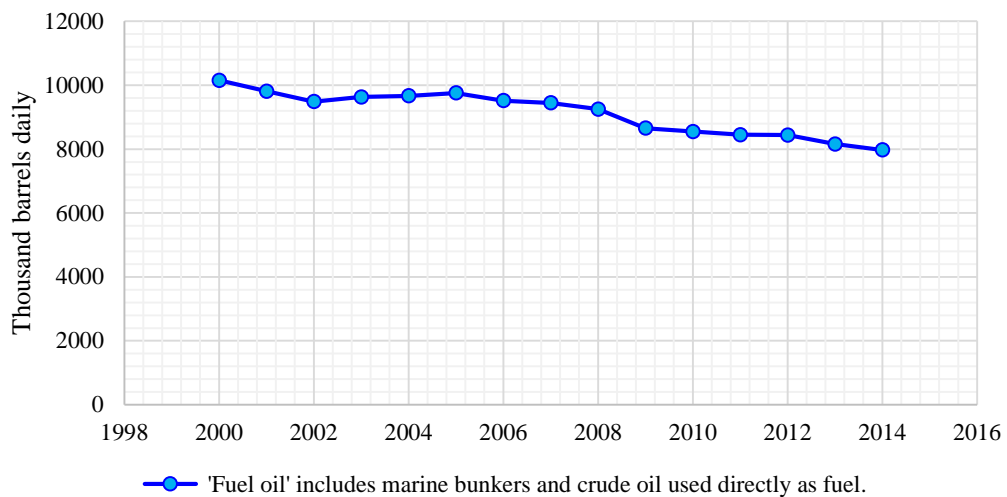


Figure 2.5 Average daily fuel oil consumption. Based on annual BP review (BP 2015).

There are a number of fuels or alternative energy solutions that can extend and potentially replace conventional marine fuels and propulsion methods including liquefied natural gas (LNG), biofuels, methanol, dimethyl ether (DME), hydrogen-based fuel cells, nuclear propulsion as well as hybrid propulsion and renewable energy sources. For instance, it has

been estimated in Lloyds Register's Global Marine Trends 2030 (Smith, Argyros, et al. 2014) that in addition to current low sulphur choices such as MDO/MGO or low sulphur HFO, LNG will reach up to an 11 percent share by 2030 while opening possibilities for hydrogen to enter the market as an emerging shipping fuel. In the opinion of DNV GL (Chryssakis et al. 2014), in addition to LNG, liquid biofuels, batteries and hydrogen-based fuel cells could gradually replace oil-based fuels and become an essential solution for auxiliary and main propulsion.

However, nowadays some of the methods are still pushing the boundaries of the current state of technology and may not be ready for a large-scale implementation while others can supplement the conventional marine propulsion by covering only a part of ship's power demand. In addition, lack of appropriate infrastructure including bunkering facilities and supply chain as well as uncertainty regarding the long-term availability of fuels illustrate additional barriers for the implementation of any innovative methods or fuels requiring a coordinated, global effort and investments in the development of new infrastructure.

#### ***Liquefied natural gas (LNG)***

Using LNG as fuel offers clear environmental benefits, namely elimination of  $SO_x$  as well as significant reduction of  $NO_x$  (by up to 85 percent) and particulate matter. In addition, since LNG has a lower value of carbon to hydrogen ratio than diesel fuels, the level of  $CO_2$  emissions is also reduced by approximately 25 percent. Reduction of  $NO_x$  is achieved due to lower combustion temperature in comparison with oil fuels.

According to (Bagniewski 2013), a ship conversion into LNG requires an investment approximately 3-4 times higher than that of a scrubber installation. The main problem, however, is a large amount of space required for the LNG tanks onboard. Compared with marine diesel oil (MDO), an equal energy content of LNG requires about 1.8 times more volume than MDO. When adding the tank insulation with the maximum filling ratio of 95 percent the required volume is increased to about 2.3 times. However, LNG became an interesting fuel to retrofit for tankers since there is a considerable space available for LNG fuel tanks on deck.

Since the natural gas must be stored in the liquid phase under pressure, and then heated up to transform into a gaseous state before the combustion, there are technical challenges in storage and piping arrangements (Townsend 2009). For instance, a medium-sized oil products tanker has been converted to burn LNG in the previously mentioned retrofit study (Klimt-Møllenbach et al. 2012), where the existing 6S50MC-C low-speed diesel engine

has been converted into the ME-GI dual fuel engine. Several operational issues such as crew training, safety during operation and bunkering, gas venting, limited maximum range when running on LNG, maintenance of system components had to be overcome. An additional issue is the limited LNG bunkering infrastructure, which is currently only available in Europe, Incheon (Korea) and Buenos Aires (Argentina).

According to (Chryssakis et al. 2014), approximately 40 LNG fuelled ships (non-LNG carriers) are currently in service around the world and additional 40 LNG based new buildings are being under construction.

On the other end of the spectrum, when burning LNG at low loads, some of the fuel is emitted unburned to the atmosphere precipitating the increased emissions of methane which reduces the actual environmental benefit of LNG to approximately 15 percent of  $CO_2$  equivalent emissions (Corbett et al. 2009).

The first comparison study of a ship running on LNG, aiming to characterise both particle and gaseous emissions, has been conducted by (Anderson et al. 2015). The measurements were made in December 2013 onboard a cruise ferry running on LNG in the Baltic Sea. The ship was equipped with dual fuel engines, using MGO as a pilot fuel. Emissions were measured under different engine loads and both LNG and MGO were used for propulsion. When using LNG for propulsion a small amount of MGO (1 – 5 percent of total energy) was injected to ignite the LNG. The results have shown that emission of particles by both mass and number,  $NO_x$  and  $CO_2$  were considerably lower in the case of LNG compared to MGO and other marine fuel oils, while the emissions of  $CO$  as well as total hydrocarbons were higher. Analysis of the exhaust gases revealed that around 85 percent of hydrocarbon emissions from LNG were methane.

More precisely, emissions of the methane slip were around 7g per kg LNG at higher engine loads, rising to 23–36g at lower loads, which could be due to slow combustion at lower temperatures, allowing small quantities of gas to avoid the combustion process. Since methane has a global warming potential which is 28 times higher than that for  $CO_2$  over a 100-year perspective, the resulted amount of methane emissions is significant.

A new generation of marine gas engines based on the Otto cycle, as outlined in (IMO 2014b), is reported to significantly reduce methane slip with improvements made to valve systems, cylinder head and the cylinder itself. However, the positive effect may dissipate over time as the engine gets older. As reported by Wärtsilä, an introduction of a lower boost pressure and adjusted timing help to reduce methane emissions. Increasing receiver air

temperatures also improves the combustion of methane, but increases  $NO_x$  emissions. In addition, skip firing, which allows to inject a fuel only at the particular part of the cylinder, remarkably improves methane slip emissions. Other methane reduction methods include processing exhaust gases through a bed of sand or a pre-combustion application of the pre-turbine oxygen catalyst.

### **Biofuels**

Biofuels represent a sulphur free alternative to conventional fossil fuels. The range of biofuels available for marine propulsion includes straight vegetable oil (SVO), biodiesel, bio-methane, bio-ethanol, bio-methanol, di-methyl ether (DME) as well as hydro-treated vegetable oil (HVO) and pyrolysis oil.

Generally, biofuels are made by fermentation of sugar or starch to alcohol or by extraction and further trans-esterification of vegetable oil or animal fats, where many combinations and specifications are possible. These include various range of plant sizes and types or accompanying products. Apart from the conventional methods, a number of innovative technologies are currently being developed promising to improve biofuel quality, environmental performance, heat capacity as well as to reduce their production costs. Examples include hydro-treatment or hydro-thermal upgrading, thermochemical processes via gasification as well as advanced biological processes involving hydrolysis and fermentation. Figure 2.6 illustrates a map of currently available biofuels in combination with their production technologies and sources of origin.

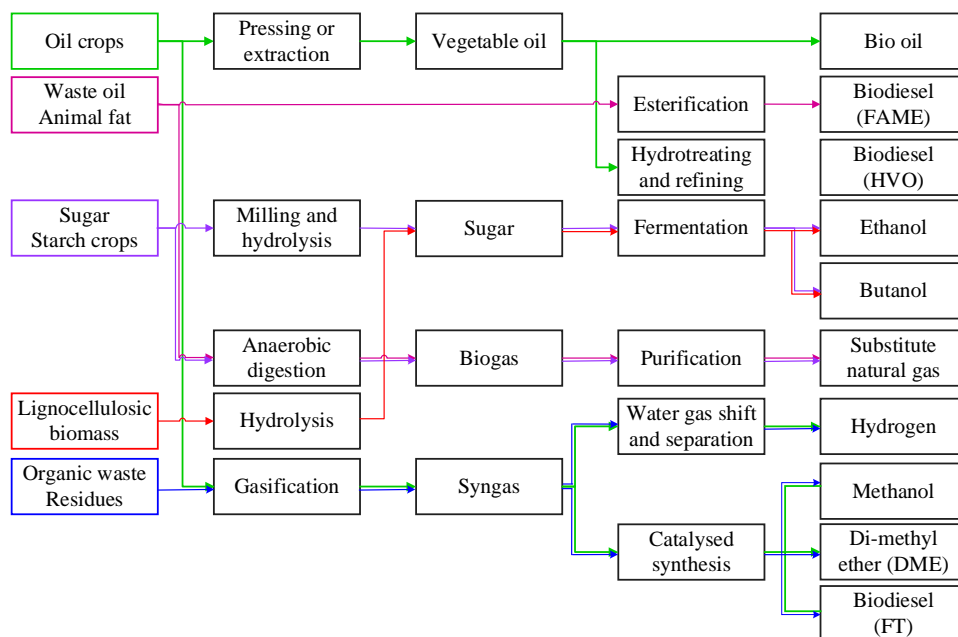


Figure 2.6 General range of biofuels types and their production routes. The diagram reproduced from (Florentinus et al. 2012).

Regardless of a lack of practical application in-service, there are a number of studies and industry opinions supporting the idea that most of the biofuels are technically compatible with marine engines as well as could be mixed with conventional fuels. For instance, biodiesel FAME (Fatty Acid Methyl Ester) and vegetable oils, as stated in (Corbett et al. 2009), can readily be used in-service without extensive modifications of the existing propulsion system although, in their present state, they require careful fuel management in order to prevent the clogging of filters. In turn, biodiesel could potentially substitute distillate fuels while vegetable oils may become an alternative to residual fuels, such as soybean oil which has already been used by the Mols Linien (Ferry line) in Denmark, as reported by (Mcgill et al. 2013). However, more investments are needed to the fuel supply chain in order to introduce these fuels. In addition, since the biofuel's sources and production methods are varying greatly, the final products have different consistency and heat capacity, which, in fact, is generally lower than energy capacity of most conventional marine fuels meaning that more biofuel quantity is needed to meet the ship's power demand.

With some biofuels, there are potential issues associated with long-term storage stability, acidity and corrosion, lack of water-shedding, filter plugging, wax formation suggesting that selection and adaptation of any type of biofuel require careful evaluation.

Although, as long as properly managed, biodiesel FAME (a refined version of vegetable oils or animal fat) does not cause complications to the engine itself, there are some specific problems associated with its long-term storage, since it is not compatible with certain non-metallic and metallic materials. Therefore, an internal coating of a storage tank, non-metallic and some metallic fuel-wetted compounds may need to be adapted to FAME. However, as outlined in (Mcgill et al. 2013), the main issue associated with FAME is sustainability since its production generally relies on palm oil which conflicts with the preservation of natural rain forests, making it an impractical solution for a long-term perspective.

Another example is di-methyl ether (DME) that has been known for the last 20 years as a substitute for diesel in small engines. This does not guarantee its sustainability in case of large applications since DME together with methanol is attributed to the biofuels with a low flashpoint and require additional safety measures (Florentinus et al. 2012). However, as outlined in (Chryssakis et al. 2014), the biomass-to-methanol/DME has been receiving

a lot of attention lately, as it is anticipated to become the most energy-efficient option by 2050.

In addition, the conversion of a marine propulsion system to methanol is considered to be cheaper than LNG due to the relative simplicity of the methanol storage system. Furthermore, since methanol has similar combustion properties with methane, it can be used in marine dual-fuel engines, as outlined by Wärtsilä and MAN. In fact, the CEAS engine calculator by MAN has recently included biofuels namely methane, ethane and methanol in addition to the conventional fuel options for preliminary estimation of their Tier III engines performance.

Currently, biofuels are significantly more expensive than oil derived fuels. However, biocrude, commonly referred as pyrolysis oil, is potentially a very cheap option since it can be produced from any sort of biowaste or residue. Similarly to fossil crude, biocrude can be further refined into lighter (biodiesel) products. Among the first, in 2013 Wärtsilä has successfully tested several low speed engines to burn pyrolysis oil resulting in a combined capacity of 680 MW.

Finally, since biofuels have an organic origin, they biodegrade rapidly, providing relative safety to the marine environment in case of a spill when compared to conventional fossil marine fuels. Nevertheless, as outlined in (Florentinus et al. 2012), there is a challenge to secure a required production volume, since a production scale of 300 M Tonnes of Oil Equivalent (TOE) biodiesel based on a current state of technology, requires more than 5 percent of the global agricultural land.

### ***Renewable energy sources***

In the past decade, the utilisation of renewable energy has been a spotlight of attention for a range of applications. For the shipping industry, the primary focus lies on solar energy and wind power. The latter one can be produced on-board by sails and kites or Flettner rotors. Some early trials to utilise wind energy as part of the propulsion system have been made with wing-sails, which represent essentially rigid panels on a rotating mast. These include the *Walker Wingsail*, fitted to the 6,500 DWT Ashington in 1986. The trials demonstrated negligibly small energy benefit. However, some current projects, including UT Wind Challenger and EffShip, are aiming to enhance the wing-sail principle of design; for example, by allowing sails to reef down on telescoping masts in the case of heavy weather or in-port situations.

Traditional sail configurations with advanced fabric and kites can provide wind power for forward propulsion while greatly reducing primary energy requirements. The success, however, strongly depends upon the wind speed and direction. Kite sails attached to the foremast of the vessel operate at altitudes to maximise wind speeds. A small number of innovative companies have been advocating this technology for more than a decade. For example, the innovative kite solution *Skysails* is able to tow giant cargo ships while claiming potential reductions of  $CO_2$  emission by 35 percent. For the first time this technology was deployed at MS Beluga Skysails, the world's first commercial container cargo ship partially powered by a 160-square-metre kite.

Another innovative renewable technology is the Flettner rotor, first introduced in the 1920s. The system represents a spinning vertical rotor that generates wind power irrespective of its direction. The rotor is driven by a motor to create a propulsive force acting in a perpendicular direction to that of the wind as a result of the Magnus effect. Flettner rotors can considerably contribute to the reduction of fuel consumption, although its performance depends upon wind speed and strength as well as requiring free deck space for rotor placement. In addition, rotors will increase a ship's air resistance while not in use unless they are made to collapse onto the deck. In case if more than one rotor is installed on a vessel, the vorticity in the wake of a rotor could result in the issue of vortex interaction between rotors and with the ship's structure. This requires additional analysis of the ship superstructure to be conducted prior the installation.

A set of four Flettner rotors were installed on the deck of 12,800 dwt E-Ship in 2010. In this case, the ship's exhaust gas boilers are connected to a downstream steam turbine, which, in turn, drive the Flettner rotors. Lately, the attention has been brought to retrofitting the bulk carriers and tankers up to VLCC class with Flettner rotors, while the availability of deck space for other ship types is remaining a key consideration.

Along with wind power, solar energy acts as one of the potential primary sources of the renewable energy used in shipping. Solar energy implicates a deployment of photovoltaic (PV) solar panels for auxiliary power generation, which, as outlined in (Smith, Day, et al. 2014), may potentially contribute up to 10 percent of reductions in  $CO_2$  emissions. General performance of the photovoltaic panel, to a large extent, depends upon the latitude and the angle at which PV cell is positioned relative to the sun. In addition, the effect of cloud cover has a great influence on the amount of generated energy that can be derived from the sun. Another factor is sufficient available deck space. Therefore, solar power is most suitable

for tankers, vehicle carriers and Ro-Ro ships. However, because of the generally low electrical output per unit surface as well as the limited area available on a deck of a conventional merchant vessel, the PV solar panels are better suited as supporting energy source for auxiliary system. Nevertheless, there have been successful attempts to use solar energy for main propulsion of a small catamaran, namely the 31-meter-long *Planet Solar*, built by Knierim Yachtbau in Germany and designed to circumnavigate the world on 537 square meters of solar panels rated at 93 kW.

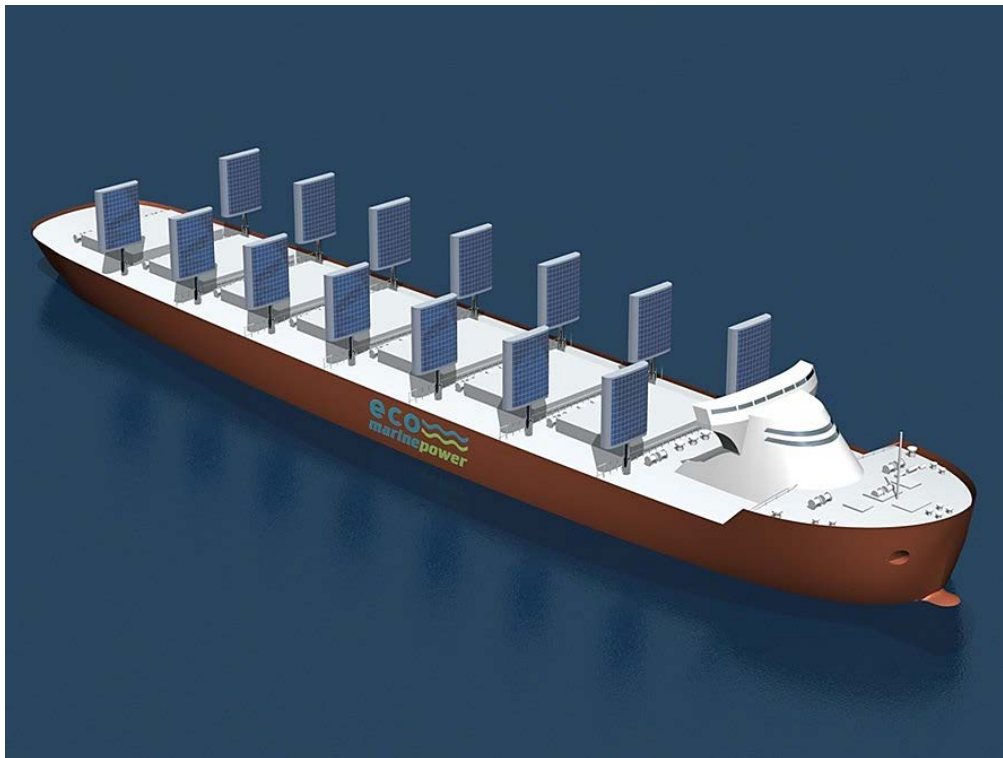


Figure 2.7 Aquarius MRE (Marine Renewable Energy) system by Eco Marine Power.

In addition to being a part of the auxiliary system, the PV panels may support the performance of a hybrid propulsion or to work in conjunction with other renewable energy sources. For instance, the Greenheart project proposed using solar-charged lead-acid batteries to provide auxiliary propulsion for its primary sail rig. The OCIUS Technology's *SolarSailor* design involves hybrid wing-sails to work in tandem with solar PV arrays, while Japan-based Eco Marine Power is developing a large solar-sail *Aquarius MRE* (Marine Renewable Energy) system for tankers and bulk carriers as illustrated in Figure 2.7. The company claims that, depending on the number, size, shape and configuration of the solar-sail, a fossil fuel-powered ship's annual fuel consumption could be reduced by up to 20 percent, while vessels powered by an electrical propulsion system could benefit by around 40 percent in terms of their efficiency.

### *Nuclear propulsion*

Nuclear propulsion has many potential advantages associated with the emissions reduction. Originally developed for the U.S. Navy in the 1950/60s, nuclear marine propulsion has found its way to the civil application, in particular, icebreakers, where the first nuclear-powered ship was the 20,000 DWT icebreaker, *Lenin*. In addition, there are four nuclear-powered civil cargo vessels that have been built, namely the first nuclear cargo/passenger vessel *Savannah* by the United States (1962), German ore and passenger carrier *Otto Hahn* (1970), Japanese nuclear-powered freighter *Mutsu* and the Russian container vessel *Sevmorput* (1988). The most recent nuclear-powered civil vessel is the Russian Arktika-class icebreaker *50 Years of Victory (50 Let Pobedy)* which was built in 2007.

Moreover, a new series LK-60 of Russian icebreakers is currently under development. This includes the icebreaker *Arctica*, whose keel was laid in November 2013 and is to be delivered by the end of 2017. The LK-60 icebreaker is planned to be 173 m long and 34 m wide while having a dual-draught with 33,530 tonnes displacement and designed to break through 3 m thick ice at up to 2 knots. The LK-60 will be powered by two RITM-200 reactors with a thermal capacity of 175 MW each fuelled by low-enriched uranium fuel (less than 20 percent). The propulsion power of this class of ships is 60MW to deliver at the three propellers via twin turbine-generators and three motors. In addition, a more powerful Russian LK-110 icebreaker of 110 MW net and 55,600 DWT is planned.

Generally, nuclear power plant generates high power from a very small volume of fuel by fission of enriched uranium. Typically, a nuclear power plant requires refuelling only after 5-7 years, while new cores are designed to last up to 50 years. Therefore, since nuclear fission does not have  $CO_2$ ,  $NO_x$ ,  $SO_x$  and particulate matter emissions, there has been growing interest attributed to the development of nuclear-powered merchant vessels of a new generation. The most common type of nuclear reactor is the uranium-fuelled pressurised water reactor, where the energy is being released through the fission of  $^{235}U$  coming from the following sources: the kinetic energy of the charged fission particles, the energy of neutrinos as well as the gamma rays and the subsequent beta and gamma decay (Carlton et al. 2011). For merchant applications, the level of enrichment of uranium is limited by 20 percent by law.

To convert released chemical energy into the mechanical energy necessary for propulsion, a geared steam turbine or turbo-generator are installed (Woud & Stapersma 2012). A geared steam turbine plant is shown in Figure 2.8. While a nuclear power plant does not need air

compared to a boiler or a combustion engine, it does need an auxiliary backup system in case of unexpected failure.

Typical nuclear power plant working principle is extensively described in (Carlton et al. 2011; Woud & Stapersma 2012). First, the released thermal energy from the fission process heats up a primary water circuit, followed by a secondary water circuit consisting of the water/steam system, similar to conventional steam plant while obtaining heat from the primary circuit in a heat exchanger. In fact, the thermodynamic efficiency of this system is lower compared to the conventional steam cycle.

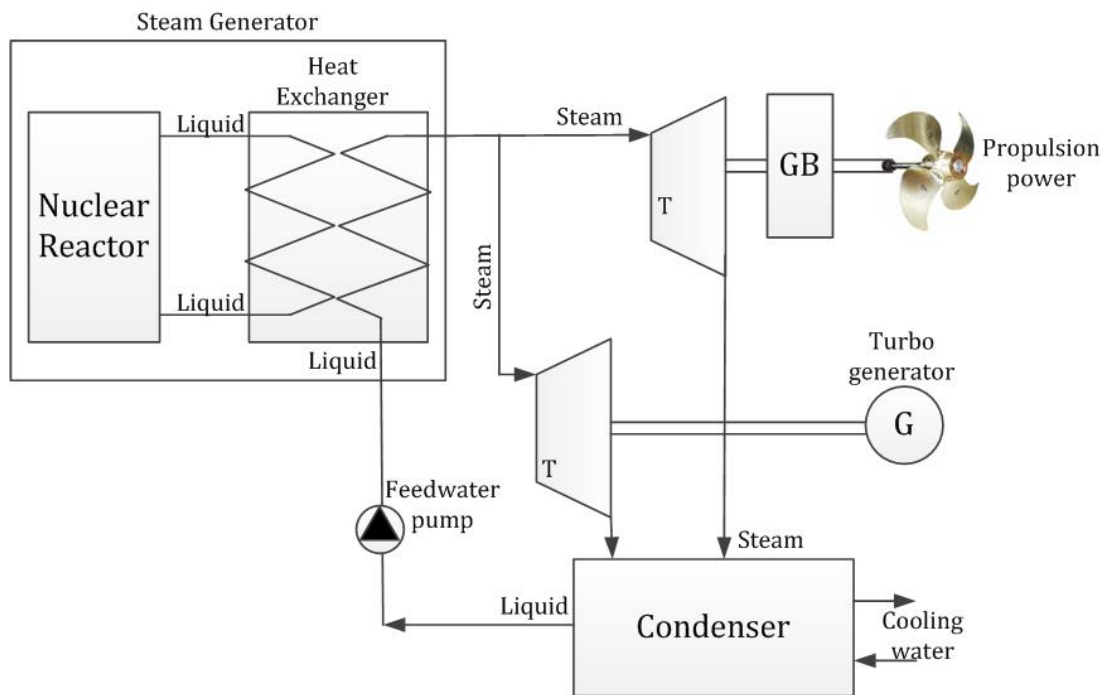


Figure 2.8 Steam turbine plant powered by a nuclear reactor.

New types of nuclear reactor design have been recently proposed by a number of manufacturers such as Mitsubishi, Toshiba and Hyperion Energy (Dedes et al. 2011), namely smaller modular reactors which can be better described as a nuclear battery rather than having a reactor propulsion layout. These reactors are fuelled with low enrichment uranium while being compact (fitting into a twenty-foot container) and weighing up to two tonnes per installed MWe.

In 2010 Lloyd's Register conducted a two-year research study in collaboration with US-based Hyperion Power Generation (Gen4Energy), BMT Group, and Greek ship operator Enterprises Shipping and Trading SA. The main purpose of this study was "to investigate the practical maritime applications for small modular reactors". As part of this project

together with their other research studies, Lloyd's Register has updated its regulations for nuclear ships concerning the integration of a nuclear reactor into ship system.

Arising from this research-collaboration project with Lloyd's Register, the (Hirdaris et al. 2014) report on commercial nuclear marine propulsion was published. The report comprises past and recent work in the area of marine nuclear propulsion while describing a preliminary concept design study for a 155,000 DWT tanker with a conventional hull form but alternative arrangements for accommodating a 70 MWt nuclear propulsion plant. The reactor was designed by Gen4Energy and has a potential to deliver up to 23.5 MW shaft power at MCR. This is a small fast-neutron reactor using lead-bismuth eutectic cooling and able to operate for ten full-power years before refuelling. As a result, the concept has been considered feasible. However, the further maturity of nuclear technology along with development and harmonisation of the regulatory framework is required.

Therefore, a widespread adoption of nuclear propulsion will face many constraints. One of them being very high initial cost, estimated to be up to three times the cost of conventional ships, (Dedes et al. 2011) as well as increased pricing for insurance and decommissioning. In addition, there are potential harbour restrictions and uncertainty in legislation and safety policy, which will need to particularly focus on the principle features of building, operating, maintaining and decommissioning nuclear-powered vessels.

### ***Hydrogen and fuel cells***

Hydrogen, perhaps, is one of the most suitable yet innovative fuels theoretically applicable for marine propulsions mainly due to its infinite source potential and clean burning characteristics. Generally, hydrogen is the lightest gas offering the highest specific heat per unit weight among other fuels. However, hydrogen can be difficult and expensive to produce, transport and store. Hydrogen can be produced on-land by a nuclear power plant and then transferred as fuel or, alternatively, on-board renewable energy sources can be employed. Compressed hydrogen should be stored at high pressure (above 700 bars), however, this requires six times more space compared to HFO while liquid hydrogen should be transported at extremely low temperatures (-253 °C). This will significantly impact the overall ship's energy demand and require strongly insulated fuel tanks.

Fuel cells are the most commonly used devices to convert the chemical energy of hydrogen into electrical energy with significantly higher efficiency, with noiseless operation and without pollutant emissions compared with conventional combustion engines. However, even though fuel cells do not have moving parts, they still require additional support

equipment such as pumps, fans and humidifiers (RAE 2013). In case a fuel reformer is additionally installed, natural gas and methanol can also be processed in the fuel cells.

The working principle of the basic fuel cell is illustrated in Figure 2.9. Generally, the fuel cell consists of two gas diffusion electrodes (commonly with a platinum catalyst), one cathode and one anode, with an electrolyte in the middle and carbon sheets on each side.

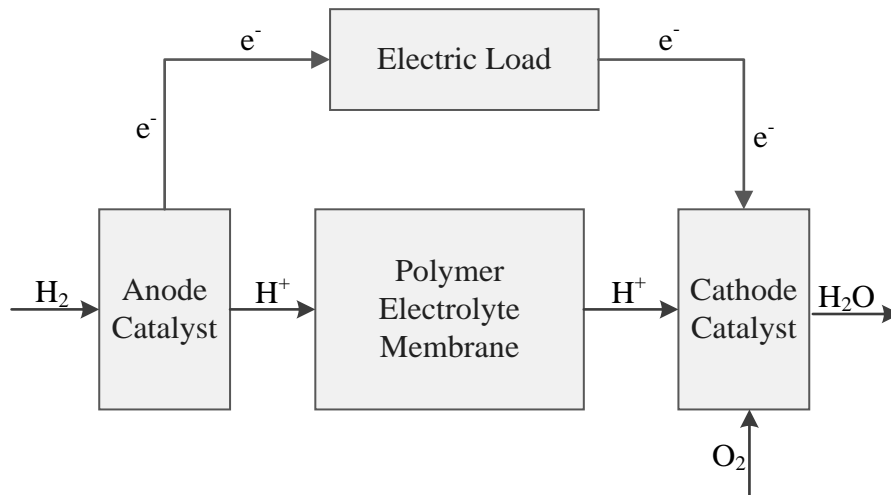


Figure 2.9 Working principle of the basic solid polymer fuel cell.

The purpose of the electrolyte is to control the spontaneous combustion of hydrogen and oxygen, known as a detonating gas explosion. In order to release a chemical energy, hydrogen is delivered to the anode where it splits into one proton and electrons ( $e^-$ ) on the catalyst layer. See equation 2.3.



The positively charged proton ( $H^+$ ) passes through the completely gas-tight polymer electrolyte membrane (Woud & Stapersma 2012). The electrons, in the form of electric energy, are directed back to the cathode via a consumer. On the second catalyst layer on the cathode side, the proton reacts with the oxygen from the air to form water being the only waste product. See equations 2.4 – 2.5.



Unlike a conventional battery, where the reactants are stored internally and eventually depleted, the reactants used in the fuel cell are stored externally and continuously supplied to the fuel cell similarly to a conventional diesel engine. As a result, they are able to generate electricity as long as the supply of reactants lasts. The theoretical voltage of an

$H_2/O_2$  fuel cell is 1.48 V, which is referred to the upper heat value of hydrogen. At zero-load conditions, slightly more than one volt per cell is available. The cooling units or bipolar plates, in combination with carbon diffusion layers, distribute the reactants uniformly across the area of the cell, conduct the electrons across the stack, remove the heat from the electrodes and separate the media from each other (Siemens 2013).

At the present time, several fuel cells technologies are commercially available while some are still under development. Fuel cells for low power applications based on hydrogen and oxygen as reactants with an incorporated fuel reformer needed to transform hydrocarbon fuels. These include an alkaline fuel cell (AFC) which is widely used in the space missions by NASA, a phosphoric acid fuel cell (PAFC), which is available on the market but having a relatively low efficiency, as well as a solid polymer fuel cell (SPFC).

Fuel cell technologies without a fuel reformer, which are able to use hydrocarbon directly, include a direct methanol fuel cell (DMFC), molten carbonate fuel cell (MCFC), and solid oxide fuel cell (SOFC) where the latest two are still under development.

When compared to a conventional marine diesel engine, a fuel cell technology provides higher efficiency and lower fuel consumption while keeping exhaust emissions at bay. However, the volume and weight of a fuel cell plant are generally greater than in the case of conventional marine engine with the same power range. In addition, the current cost of a fuel cell system is estimated to be higher than marine diesel engine while its maintenance is predicted to be significantly less expensive (RAE 2013).

Several other characteristics of fuel cells could provide benefits for specific applications. The fact that fuel cells are of modular design enables flexibility in the arrangement of plant components and could lead to a more cost-effective layout of power and cargo spaces and of basic ship structure. Therefore, since the fuel cells are highly efficient, silent and sustainable, they can become a part of the future power production on ships. Nevertheless, further research and development are necessary to overcome certain challenges associated with the high investment costs, dimensions and weight of the fuel cell plant as well as a particular attention should be given to storage of hydrogen on-board and safety aspects. As such, fuel cells might become a niche powering option, particularly in combination with hybrid battery systems (Chryssakis et al. 2014).

### ***Batteries and hybrid propulsion***

Recent developments in battery technologies and marine hybridisation hold significant promise for more energy efficient shipping, since electric and hybrid ships with battery

energy storage and optimised power control can significantly contribute to the reduction of ship produced emissions as well as bring down fuel and maintenance costs.

Over the past several years, there have been extensive developments in lithium-ion batteries field, namely the adaptation of high-quality batteries for marine electrification and hybridisation purposes. Although lithium is the lightest metal element in the periodic table and its substitution by another metal will not result in principally new lighter battery concept, there are several long-term future developments such as Li-Sulphur and Li-air, also known as Li- $O_2$ , that can potentially contribute to energy-optimised battery system.

Both of these technologies are claimed to provide up to five times more energy than the lithium-ion batteries. In the case of Li-Sulphur, since sulphur is being a natural cathode partner for metallic lithium, the chemical process include dissolution from the anode surface during discharge and inverse lithium plating to the anode while charging. The Li-air technology is based on the lithium metal anode whose atoms supply the electrons for the electric circuit when it is being used. However, for recent marine applications, the lithium-ion batteries with nickel manganese cobalt oxide (NMC) cathodes and graphite anodes as well as systems based on iron-phosphate cathodes have mainly been used, representing an adequate combination of safety, energy, power density, life cycle and cost (DNV GL 2015).

During the hybrid ferry project performed by Scottish Caledonian Maritime Assets Limited (CMAL), three lithium-ion batteries, namely Lithium Iron Phosphate ( $LiFePO_4$ ), Lithium Nickel Manganese Cobalt Oxide ( $LiNMC$ ) and Lithium Manganese Ion Phosphate ( $LiMeMgPO_4$ ) have been compared by the set of parameters (Anderson 2015). The resulted Li-ion cell comparison Table 2.5 is shown below.

Table 2.5 Li-ion cell comparison (Anderson 2015).

Technology	$LiFePO_4$	$LiNMC$	$LiMeMgPO_4$
Number of cycles	>3,457 cycles at 100% depth of discharge	>5,000 cycles at 80% depth of discharge	>5,000 cycles at 80% depth of discharge
Weight	6,174 kg	6,720 kg	7,488 kg
Volume (no racks)	4.52 $m^3$	6.44 $m^3$	4.55 $m^3$
Cost per w/h	£0.46 - £0.53	£0.54	£0.49
Cost per 750 kWh	£345,000 - £397,000	£405,000	£367,500

As a result of this project, the reference ferry could accommodate the weight and volume of all three battery types. However, in the case of the  $LiMeMgPO_4$  battery, there would be

a weight penalty of 1 tonne. The numerical assessment of  $LiMgMgPO_4$  and  $LiNMC$  potential performance showed greater number of cycles in comparison to  $LiFePO_4$  increasing the lifetime of the batteries which results in lower overall costs. Moreover, since safety, by far, is one of the most significant criteria; the research showed that  $LiFePO_4$  unit has one of the safest chemistries, thus,  $LiFePO_4$  was finally selected as the battery to be installed in the candidate ferry.

Battery powered propulsion systems have already been introduced for smaller vessels while the technology development for large ships is mainly focused on hybrid propulsion. Examples include a hybrid installation on offshore supply vessel *Viking Lady*, where the 500 kWh battery was retrofitted in 2013 and additionally supported by an extensive monitoring programme that has helped to generate important efficiency and emission data reflecting the battery system behaviour. In addition, several vessels from the ferry segment, such as Denmark's ro-ro/passenger ship *Prinsesse Benedicte*, have been retrofitted and supplied with the large battery hybrid systems. The first entirely electric battery powered 120-car and 350-passenger Norwegian car ferry *Ampere* that came into operation in January 2015 is driven by two electric motors, each with an output of 450 kilowatts being powered by lithium-ion batteries. The batteries have a combined capacity of 1,000 kWh and should be recharged directly from the grid at night after the ferry stops operating. In addition, the cargo sector is also emerging for electrical propulsion, in particular, liquid cargoes such as LNG and crude oil tankers (RAE 2013).

Generally, there are several concepts of ship's machinery arrangements that involve utilisation of batteries. For instance, batteries can be introduced to support main propulsion under large load steps or to provide additional power for large engine motors. In addition, battery based hybrid systems with plug-in possibilities and a DC distribution allows the speed of the prime movers to be adjusted according to the load-dependent optimum fuel level while reducing the fuel consumption. Moreover, further potential efficiency improvements can be achieved while the main propulsion system is working in conjunction with the energy storage systems through load leveling: for example, the prime mover is constantly working at the most efficient operating point (Holsonback et al. 2006), while extra power is supplied by batteries when required. In the case when the ship power requirements are low, the batteries can be charged using the excess energy generated by main propulsion at the optimal load as schematically shown in Figure 2.10. In addition, under very low loads, the ship may be able to operate on battery power alone.

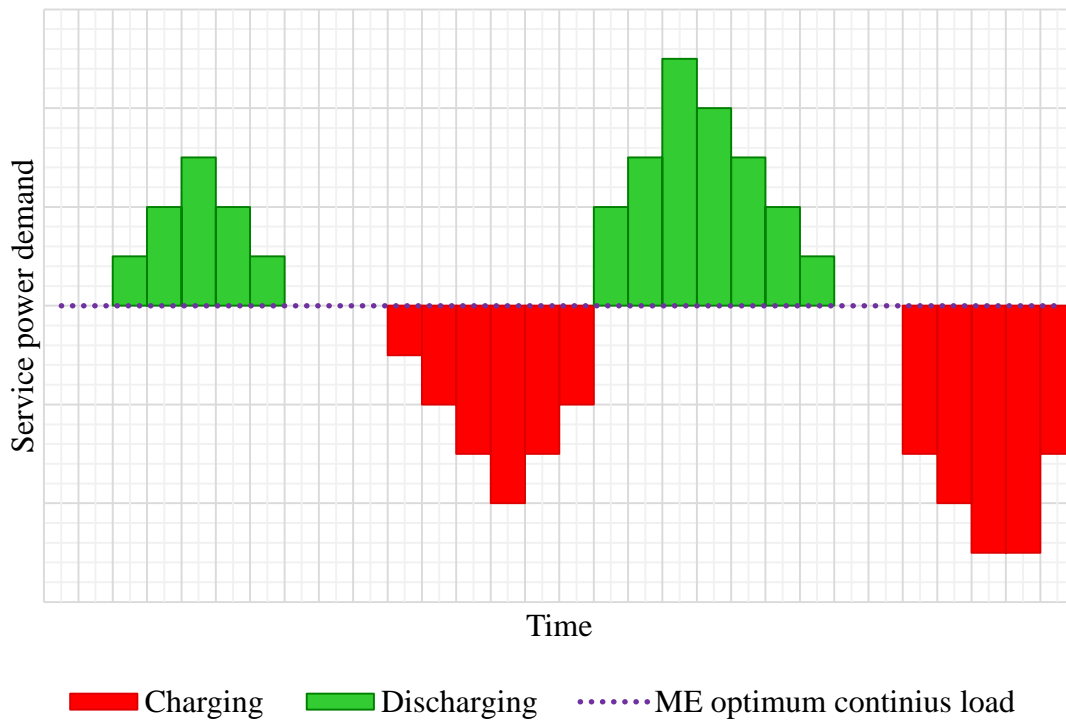


Figure 2.10 Battery based load leveling ship operation concept.

In fact, as outlined in (Whitelegg & Bucknall 2013), load leveling can contribute to 17 – 35 percent of fuel savings with potential periods of zero greenhouse gas emission operation, which is particularly beneficial when operating in ports under strict emission regulations or in ECA. In addition, load leveling can also be advantageous for the engine maintenance cost, since it helps to avoid the risk of lubrication oil contamination as well as the possible carbon residue when operating under low loads.

In future, a hybrid power system will possibly include a fuel cell, diesel generating set and batteries charged by nuclear power or renewable energy while an intelligent control system will balance the loading of each component to maximise the system efficiency. Therefore, as outlined in (Wärtsilä 2010), such system could contribute to the reduction of  $NO_x$  by 78 percent,  $CO_2$  by 30 percent as well as  $PM$  emissions could be reduced by 83 percent.

However, even though the pace of technology is advancing rapidly, possible challenges associated with safety, availability of necessary materials as well as battery life cycle and further decomposition should be addressed to ensure that marine hybridization is competitive to conventional propulsion.

### **3 Challenges in EEDI formulation**

The EEDI methodology, previously discussed in the Introduction, has been developed by IMO using average simplifying assumptions based on available ship data since the access to complete ship design data was limited. As such, a specific fuel oil consumption for all main engines is assumed to be 190 g/kWh and 215 g/kWh for auxiliary systems while both are burning HFO (see Appendix I).

However, a number of recent studies, as specified in (IMO 2014b), have demonstrated that the actual average SFOC of new buildings is lower. For instance, a study conducted in CE Delft (Faber et al. 2015) has shown that ships built between 2009 and 2014 have an average SFOC of 175 g/kWh while (Kristensen 2012) finds that modern marine diesel engines have SFOCs of 170 g/kWh. Moreover, according to (IMO 2014b), for large modern slow speed diesel engines that are normally used for marine application, SFOC ranges from 165 g/kWh to 185 g/kWh. Therefore, as estimated in (IMO 2014b), such SFOC uncertainty leads to the depletion of actual efficiency improvements by 7.5 percent compared to the specified reduction levels. In addition, for EEDI estimation purposes it is required to apply specific propulsion data taken from the Engine International Air Pollution Prevention (EIAPP) certificate, where all measurements are normally conducted under standard ISO conditions using MDO as a fuel instead of HFO as required by EEDI guidelines.

Moreover, there is a considerable uncertainty associated with the historical data used for estimation of the EEDI reference lines, in particular ship's service speeds, as well as the margin of error due to fitting of a single exponential curve to the data, which in some cases does not reflect the desired average performance for all ship sizes.

In addition, a number of recent studies have illustrated that most of the current ship designs have already satisfied the long term EEDI requirements. Such as, the detailed analysis of estimated index values (EIV), being a simplified version of the EEDI measure, conducted by (Faber et al. 2015) for different ship types showed that most of the recent new buildings that have entered the fleet after 2013. These include tankers, gas carriers, combination carriers and bulk carriers, container ships and general cargo ships have an EIV more than 10 percent below the reference line, suggesting that the majority of these vessels went beyond required EEDI for the period of 2015 - 2020.

American Bureau of Shipping in their positioning paper (ABS 2013) has compared the attained EEDI values of the standard tanker and container ship designs to their current

reference lines as well as the reference lines reduced by 10 percent. The considered ship designs were based on the principal dimensions and service speeds typical for those built in the last ten years. The corresponding propulsion power values were based on the efficiency that is specific to the modern designs and the results have shown that all of the standard tankers and containerships have satisfied the current reference line, while most of them have met the EEDI requirements through 2020.

These facts introduce a question whether the EEDI measure will stimulate the efficiency design improvements of vessels that have already satisfied its requirements. For instance, Bazari and Longve in (IMO MEPC 63/INF.2 et al. 2011) have assumed that the level of improvement in the average attained EEDI value will be larger than the level required by EEDI reference lines for all ships except the most efficient ones while Anink and Krikke in (Anink & Krikke 2011) have concluded that only the design of ships above the reference line will be affected.

Finally, in some cases, as outlined in (ABS 2013), the EEDI measure does not reflect actual efficiency benefits of some ship design features. For example, a comparison assessment of the neopanamax and panamax container ship designs, has shown that even though the neopanamax is more economically efficient than the panamax design, since the fuel oil consumption per tonne-nm of cargo transported for the neopanamax containership was approximately 14 percent less than the panamax containership of the same nominal TEU capacity, the EEDI methodology rates the panamax design as more energy efficient. The reason is that the hull of the panamax containership have a higher length/beam ratio making it hydrodynamically more efficient. However, the wider beam on the neopanamax containership enables a more stable hull form and, thus, significantly reduces the need for ballast. As such, since EEDI uses DWT instead of TEU as a capacity measure, it could not reflect the differences between a tonne of cargo and a tonne of ballast.

## 4 The Reference Ship: Oil Products Tanker

Although, in 2014, the global oil consumption increased by 0.9 percent (BP 2015), the crude oil shipments were estimated 1.7 billion tonnes, which is 1.7 percent lower compared to the previous year (UNCTAD 2015). This is a result of the firm import demand of Asian countries, namely China and India, combined with the effect of lower oil prices on the stock building as well as general oil oversupply. At the same time, in 2014, the global refinery capacity increased by 1.4 percent (BP 2015), driven mainly by growth in Brazil, China, Singapore and Western Asia. According to (UNCTAD 2015) estimates, which include gas trade, the volume of petroleum products and gas transported in 2014 increased by 2.3 percent and reached 1.11 billion tonnes (Figure 4.1), whereas, according to Clarkson's Research, the seaborne trade of petroleum products alone has increased by 1.7 percent and reached 977 million tonnes. As a result, there is an increasing demand for products tankers.

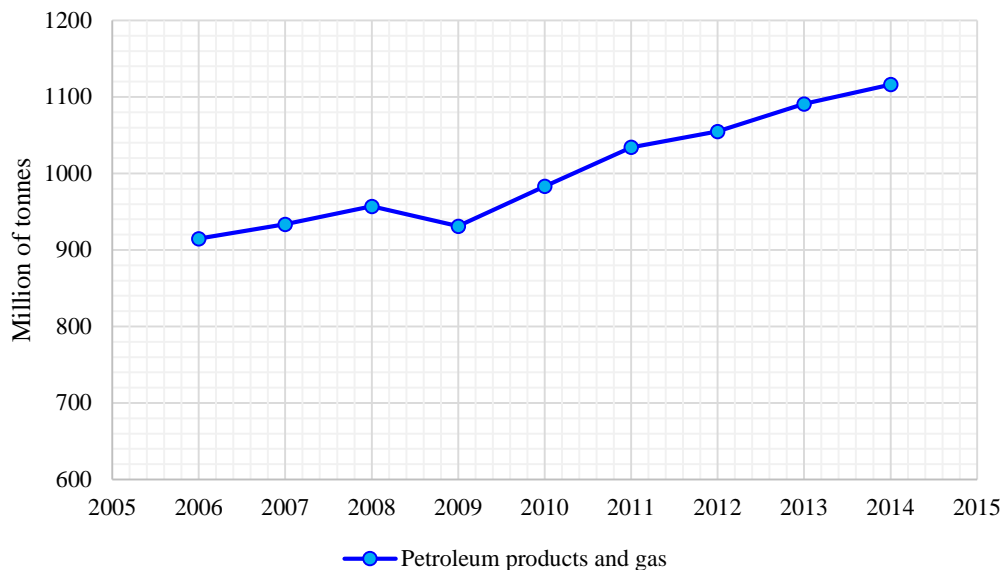


Figure 4.1 World seaborne trade of petroleum products and gas in million of tonnes (UNCTAD 2015).

The case study vessel is chosen to be a medium size oil products tanker illustrating an important sector of the global fleet. Products tankers comprise almost one-third of the world total amount of cargo carrying fleet (RAE 2013). The vessel represents a double hull oil products tanker of 35,190 DWT and was built in 2005 and is of a conventional design. A ship of this size corresponds to approximately 10 percent of all tankers range (Figure 4.2), many of which operate in ECAs. This ship is a good model for analysis and improvements since the results of this research could potentially be applied to other products tankers in the range of 20,000 – 60,000 DWT by acting as a midpoint of the spectrum of ship sizes of this type.

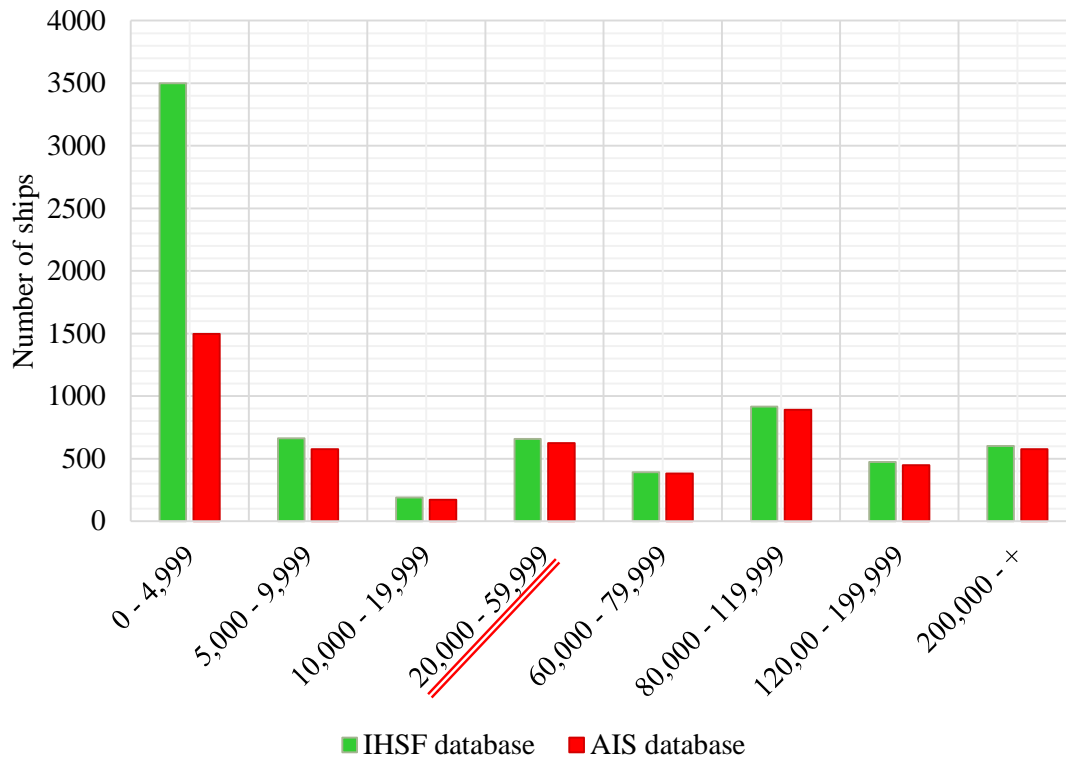


Figure 4.2 Global tankers fleet distribution (UNCTAD 2015).

The vessel's reference data has been provided by one of the world's leading shipping companies. The dataset includes the model test results for loaded, designed and ballast conditions, hull offset table, general arrangement plan reflecting ship principal dimensions, service performance data as well as the entry in register book. The main ship characteristics are listed in Table 4.2. She is equipped with appendages: namely, bilge keels, rudder behind its skeg and Schneekluth wake equalizing duct (WED).

In 2009, the ship has been fitted with 5.25m contracted and loaded tip (CLT) propeller instead of the former conventional 5.65m fixed pitch (FP) propeller while still retaining the WED. The principal characteristics of the conventional FP and CLT propellers are listed in Table 4.1.

Table 4.1 Basic propellers characteristics.

Propeller	<i>FP</i>	<i>CLT</i>
Diameter	5.65 (m)	5.25 (m)
<i>P/D</i>	0.65	-
<i>A<sub>E</sub>/A<sub>O</sub></i>	0.56	0.49
Number of Blades	4	4

Table 4.2 Principle ship dimensions based on model test report.

Parameters	Value			Metric
	<i>Loaded</i>	<i>Designed</i>	<i>Ballast</i>	
Designed speed $V$	14.7	14.6	15.02	knots
Overall length $L$	171.2			m
Length between perpendiculars $L_{PP}$	162			m
Length of the waterline $L_{WL}$	166.5	165.8	160.22	m
Moulded breadth $B$	27.4			m
Draught forward	11.8	9.75	6.45	m
Draught aft	11.8	9.75	6.55	m
Displacement Volume	42571	34418	22174	m <sup>3</sup>
Wetted Surface Area $WSA$	7071	6361	5201.5	m <sup>2</sup>
Block Coefficient $C_B$	0.791	0.777	0.769	-

It should be noted that there are some gaps in data regarding the CLT principal characteristics. However, the open water characteristics for both propellers are available. Considering the machinery, the ship is equipped with the conventional propulsion system as follows:

- One slow speed diesel engine (MAN 2 stroke 5 Cy. 500 x 1910) of total power 7,150 kW at 127 RPM
- Three Dalian auxiliary generators, each 910kW, 450V 60Hz

The relevant performance data has been provided and covers the service period starting from the ship's birth on January 2005 until October 2009. The data set includes the information regarding date, water depth, period observed, draughts and trims, ship's observed and logged speeds, weather conditions defined as wind speed and Beaufort number as well as the engine power and rotational speed.

## 4.1 PhD Research Structure

Based on the assessment of current energy efficiency-enhancing technologies and methods along with the available ship, propellers and service data, the following research structure includes a purpose developed computer basis ship simulation model as a base for the number of case studies. The short summary of each case study is briefly described below while a detailed explanation along with its relevance based on the literature review, calculation procedure, results and conclusions are presented in each of the following chapters.

As such, Chapter 5 is dedicated to a detailed description of the computer based ship simulation model with specified range of methods and algorithms used. The ship simulation model, referred to Ship Performance Simulation model (SPS), is then verified and correlated with the available data to ensure its correct performance. In addition, this chapter describes the energy efficiency measures developed in this study to compare the ship energy efficiency behaviour under different conditions, namely the Energy Efficiency Indicators (EEI) comprising propulsion efficiency, fuel consumption, exhaust emissions flow rate as well as EEDI index.

A time domain voyage simulation model is described in Chapter 6. This model predicts the power increase due to changing weather based on the ship's service data in combination with the trial allowances approach. The voyage simulation acts as a base for the estimation of potential fuel and emissions reductions due to the introduction of various energy saving technologies and methods in the following chapters.

Chapter 7 focuses on the high-efficiency propellers analysis, namely the effect of wake equalising duct on ship efficiency as well as the comparison analysis of conventional fixed pitch, CLT and ducted propellers and their effect on ship propulsion behaviour under ballast and loaded conditions.

Propeller optimisation strategies are discussed in Chapter 8. The case study is based on a conventional fixed pitch propeller and include the analysis of the effect of reduced blade area ratio (BAR) as well as artificially increased propeller diameters on propulsion efficiency with reference to propeller cavitation margins.

Chapter 9 explores the low RPM/increased diameter propeller design concept by comparing two conventional fixed pitch propellers with the maximised diameter. The first represents a maximum diameter that could be fitted into the current ship arrangement while second illustrates the maximum possible diameter with a relocated shaft. The study answers

a question of whether the maximising of the propeller diameter to its limit while changing stern arrangements would bring a significant difference to the fuel consumption and EEDI value.

Chapter 10 is focused on the effect of trim on ship resistance and, therefore, fuel consumption and exhaust emissions flow. This case study is centred on a partly loaded condition with changing forward trim. Along with ship resistance, the analysis has also covered propulsion characteristics and propeller efficiency.

Chapter 11 is dedicated to innovative, for the shipping industry, hybrid propulsion concepts also referred as load levelling. This allows to continuously operate at the most efficient load while charging and discharging batteries. This case study is looking at the load leveling operation under changing weather conditions in order to estimate potential long-term efficiency benefits as well as the effect on the level of atmospheric emissions.

Finally, Chapter 12 is focused on the EEDI formulation philosophy, where EEDI values have been estimated in accordance with ships' performance data and further analysed under changing weather conditions (Beaufort number). This has helped to uncover some potential uncertainties associated with the effect of real sea state on EEDI index and ship's energy efficiency level while providing recommendations and strategies on how they might be improved.

## 5 Ship Performance Simulation Model

As it has been outlined previously, there are a number of non-linear factors that influence shipping industry on a day to day basis such as fuel prices, freight rates, regulations, changing weather, port infrastructure and many more, making each ship and voyage a unique case which requires an individual approach. As such, it is important to consider a ship as an integrated system with linked and interrelated components under various conditions rather than look at the performance of each factor separately while overlooking many significant trends.

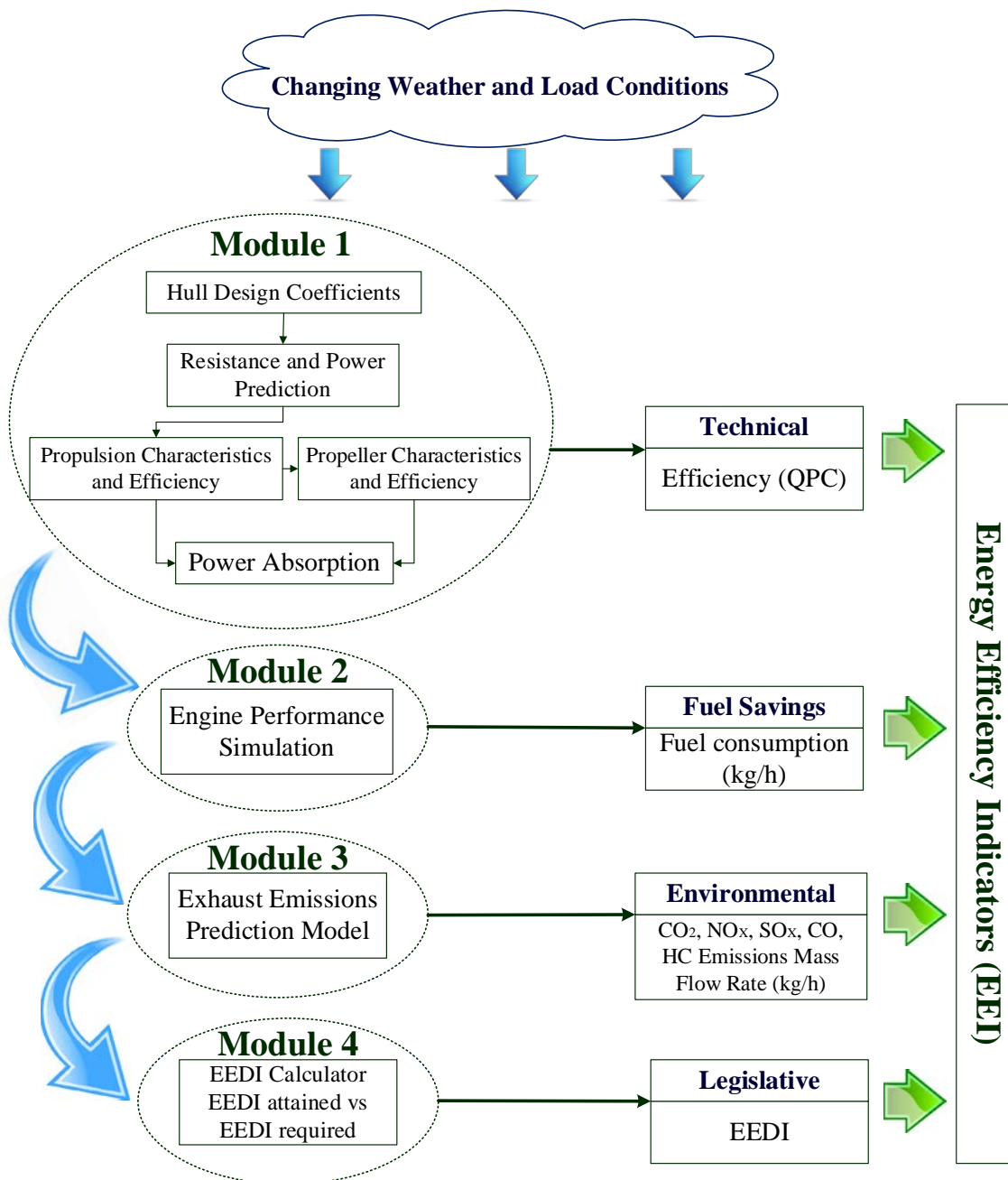


Figure 5.1 Ship Performance Simulation (SPS) model.

Therefore, in order to undertake a number of case studies regarding the implementation of various methods and strategies designed to enhance ship energy efficiency, a computer-based integrated ship simulation model, namely Ship Performance Simulation (SPS) model, has been developed in a connected Matlab and Excel environment operating in both steady state and time domain modes. The model consists of four fundamental modules as schematically shown in Figure 5.1.

The modules are ship resistance and propulsion simulation model, engine performance model, exhaust emissions prediction model and the EEDI calculator. Each module has a number of outputs, used as inputs into the subsequent modules. However, in order to compare the ship's performance in different case studies, each module has an output that is considered as an energy efficiency indicator (EEI) reflecting one of four outlined forces. The first module has an overall propulsion efficiency (QPC) as an indicator of technological performance, the second module has a fuel consumption output to evaluate the cost-effectiveness of a proposed technology or method. The third module demonstrates an exhaust emissions footprint as an environmental indicator while the fourth module estimates the EEDI index acting as an indicator of the legal feasibility in coming years.

Moreover, the system would not be complete without the ship performance analysis under different loads such as ballast/loaded and changing weather. Therefore, ship performance results are also analysed using the time domain simulation taking into account the ship's speed and load behaviour as well as sea state distribution in accordance with the provided service data, where the effect of weather is evaluated using the Beaufort wind force scale for fully developed seas.

It is important to emphasise that approaches and methods used in some modules may vary in different case studies while in this chapter the fundamental principles of each module as well as a time-domain model have been described and validated in accordance with the provided data.

## 5.1 Module 1: Resistance and Propulsion

Based on William Froude's similarity law stating that the wave-making resistance coefficients of two geometrically similar models are the same when towing with the same speed to length ratio, in combination with additional dimensionless analysis, the ship's total resistance coefficient  $C_T$  can be described as follows:

$$C_T = \frac{R_T}{\frac{1}{2} \rho S V^2} = f\left(\frac{VL\rho}{\mu}, \frac{V}{\sqrt{Lg}}\right) = f(R_n, F_n) \quad 5.1$$

where the wetted surface area  $S$  is proportional to the ship's length squared  $L^2$ . In this formula  $\mu$  is the dynamic viscosity of water,  $\rho$  is the density of water and  $g$  is the acceleration due to gravity. As such, the ship's total resistance  $R_T$  is a function of Reynolds number  $R_n$  and Froude number  $F_n$  respectively representing the frictional and wave resistances.

At this point, the Reynolds number  $R_n$  represents a ratio of the inertial forces over the viscous forces of the fluid which can be estimated using the expression (5.2):

$$R_n = \frac{VL\rho}{\mu} \quad 5.2$$

where  $V$  is the ship velocity,  $L$  is the length of the ship,  $\rho$  is the water density and  $\mu$  corresponds to the dynamic viscosity of water.

In parallel, the Froude number is a ratio of the inertial forces over the gravity forces which can be described as follows:

$$F_n = \frac{V}{\sqrt{gL}} \quad 5.3$$

In modern ship design practice, for a vessel that is undergoing a steady motion at slow speed where "the ship's weight balances the displacement upthrust without the significant contribution of hydrodynamic lift forces" (Carlton 2012), the components of the total resistance can be subdivided as presented in Figure 5.2.

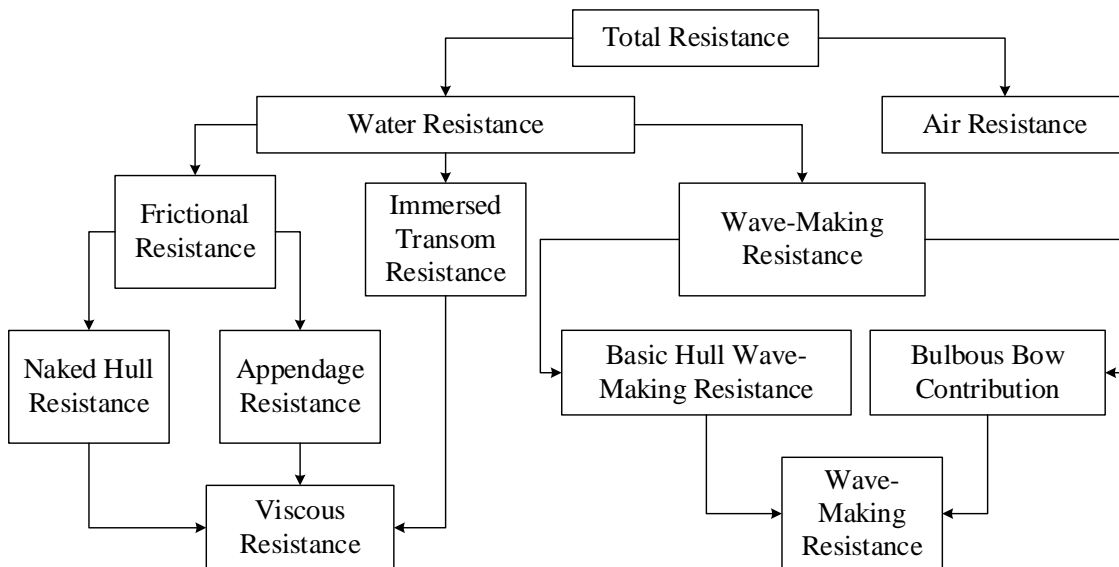


Figure 5.2 General components of ship's total resistance.

Since the ship encounters two different fluids (water and air) with a great variation in density, the total ship resistance has been subdivided into two major groups, namely water resistance (submerged part of a hull) and air resistance (upper part of hull and superstructure), where the water resistance is made up of a number of different elements interacting with each other in a quite complex manner. Such a concept of resistance decomposition helps in designing the hull forms as the designer can focus on the effect of individual resistance components (Bertram 2012).

As such, in order to estimate the total resistance  $R_T$  of a ship, the following expression (5.4) can be used where the number of variables depends on weather conditions and hull design characteristics:

$$R_T = R_F * (1 + k) + R_{APP} + R_W + R_{TR} + R_{CA} \quad 5.4$$

where  $R_F$  is the frictional resistance,  $(1 + k)$  is a form factor,  $R_{APP}$  is the appendage skin friction resistance,  $R_W$  represents the wave-making resistance,  $R_{TR}$  is the immersed transom resistance and  $R_{CA}$  represents the correlation allowance, which is defined as a difference between the total measured resistance and the total estimated resistance.

During the preliminary stage of the ship design process, it is important to predict the total resistance of the designed ship while estimating future requirements for the installed power. To perform this there are several options available: the traditional and standard series, the regression-based procedures, the direct model test, and computational fluid dynamics (CFD). The choice of method, to a large extent, depends upon the technology and budget available as well as desired accuracy of the predictions. It is important to emphasise that unlike the direct model tests and CFD methods, the regression-based and standard series methods are based on the traditional naval architecture principles and have some restrictions on the values of the hull form parameters, such as block coefficient, prismatic coefficient, length to beam ratio etc.

- Direct model resistance test

During the direct model resistance test, the model is towed by the carriage where the total longitudinal force of the model is measured under different speeds. The model is often made of paraffin wax, glass-reinforced plastic, or wood. Turbulent flow simulators should be placed at the bow of the model in order to simulate the transition from laminar flow into the turbulent flow regime and, thereby, simulate the full-scale flow structures in the model tests.

- Traditional and standard series

Traditional and standard series prediction methods are generally based on testing of series of models that were carried out in order to predict ship resistance. These are represented by a range of works such as Taylor’s method, Ayer’s method, Auf’m Keller method, Harvald method (Harvald 1983) as well as British Ship Research Association (BSRA) and American Series, being the most applicable and useful method for resistance prediction purposes from this section.

- Regression-based methods

If sufficient data for a large number of ship design parameters (for example model test reports) is available, then statistical regression analysis provides an alternative to standard series. However, there are some limitations of regressions analysis mainly associated with the “statistical quality” of the data, such as standard error. In addition, great care should be taken to make sure that the prediction lies within the limits of the database, in particular in the case of hull form optimisation. Consequently, predictions should not be made for unrealistic combinations of hull parameters.

Holtrop and Mennen have published series of papers (Holtrop & Mennen 1982), (Holtrop 1984) dedicated to the resistance and propulsion prediction analysis, where authors divided the ship hull resistance into six components, as shown in equation (5.5).

$$R_T = R_F * (1 + k_1) + R_W + R_{TR} + R_{BB} + R_{APP} + R_{CA} \quad 5.5$$

where

- $R_F$  is the frictional resistance representing the sum of all tangential forces on the hull and calculated according to the 1957 ITTC friction formulation;
- $(1 + k_1)$  is the form factor of the hull describing the viscous resistance of the hull form in relation to  $R_F$ ;
- $R_W$  is the resistance caused by the wave system generated by ship;
- $R_{TR}$  is the additional pressure resistance due to transom immersion;
- $R_{BB}$  is the additional pressure resistance due to a bulbous bow near the water surface;
- $R_{APP}$  is the appendage resistance;
- $R_{CA}$  is the model-ship correlation resistance allowance.

Based on the 334 model tests and some full-scale trials, formulas for each resistance component were derived by regression analysis. In addition, in (Holtrop 1984), regression-based formulations for the wake fraction coefficient  $w$ , thrust deduction factor  $t$  and the

propeller relative-rotative efficiency  $\eta_R$  are presented. The formulation and implementation of these factors are discussed later in this section. However, this approach is only suitable for the standard ship designs as the more complex or non-conventional ship forms may affect its accuracy.

Another regression-based approach has been carried out by Hollenbach (Hollenbach 1998) based on the results of resistance tests on 433 models at the Vienna Ship Model Basin from 1980 to 1995. The models were both, of single-screw and twin-screw ships. In this method, the data has been analysed and presented in two ways depending on the application and available data. A ‘mean’ value of resistance is calculated when normal constraints on the hull form are available for design purposes and a ‘minimum’ resistance which might be achieved for hull parameters established after extensive optimisation of the ship lines if ship’s design is not subject to restrictions.

In addition to length between perpendiculars  $L_{PP}$  and the waterline length  $L_{WL}$ , Hollenbach introduced a new term, a length over surface  $L_{OS}$ , which in case of design draught means length between the aft end of design waterline and the most forward point of ship below design waterline, while for ballast draught  $L_{OS}$  represents length between aft end and forward end of ballast waterline, where rudder is not taken into account.

- Computational fluid dynamics (CFD)

CFD allows the investigator to predict ship’s resistance curve and further mathematical modelling of three-dimensional fluid flow using one of the following methods: the finite element method of analysis (FEM), boundary element methods (BEM), finite difference method (FDM) or finite volume methods (FVM), specified in (Bertram 2012; Carlton 2012). According to (Bertram 2012) FVM, FDM and FEM are referred to “field methods”, as they use discretization of the whole fluid field. Alternatively, the boundary element method can be applied to discretise the boundaries. However, in these computationally based analyses turbulence modelling has been problematic. Reasonable estimates of the frictional resistance have been made for fine form ships using  $k - \Omega$  and  $k - \Omega$  shear stress transport (SST) models, while the more computationally intensive Reynolds stress models have improved the accuracy of the prediction for the finer hull forms.

CFD requires a high-performance computer as there is an ample quantity of equations to be solved. The water flow dynamic simulation is very complex, especially flow around a stern and, in many cases, it is difficult to analyse it using the computer modelling.

Therefore, computational fluid dynamics is used in combination with the analysis performed during the model testing.

**Resistance prediction method selection**

Since the regression-based methods are traditionally recognised by naval architects as the most useful approaches in the pre-design phase, the Holtrop and Mennen method has been selected as a principal resistance and propulsion prediction methodology to use in the Ship Performance Simulation model. In comparison to (Hollenbach 1998) approach, the Holtrop and Mennen method allows one to track the dynamic changes of each resistance component separately, thus being vital for the research principal aims. In addition, the implementation of this approach provides a satisfactory correlation with the model basin tests and also with the full-scale trials. The workflow of the complete resistance and propulsion prediction module is schematically represented in Figure 5.3

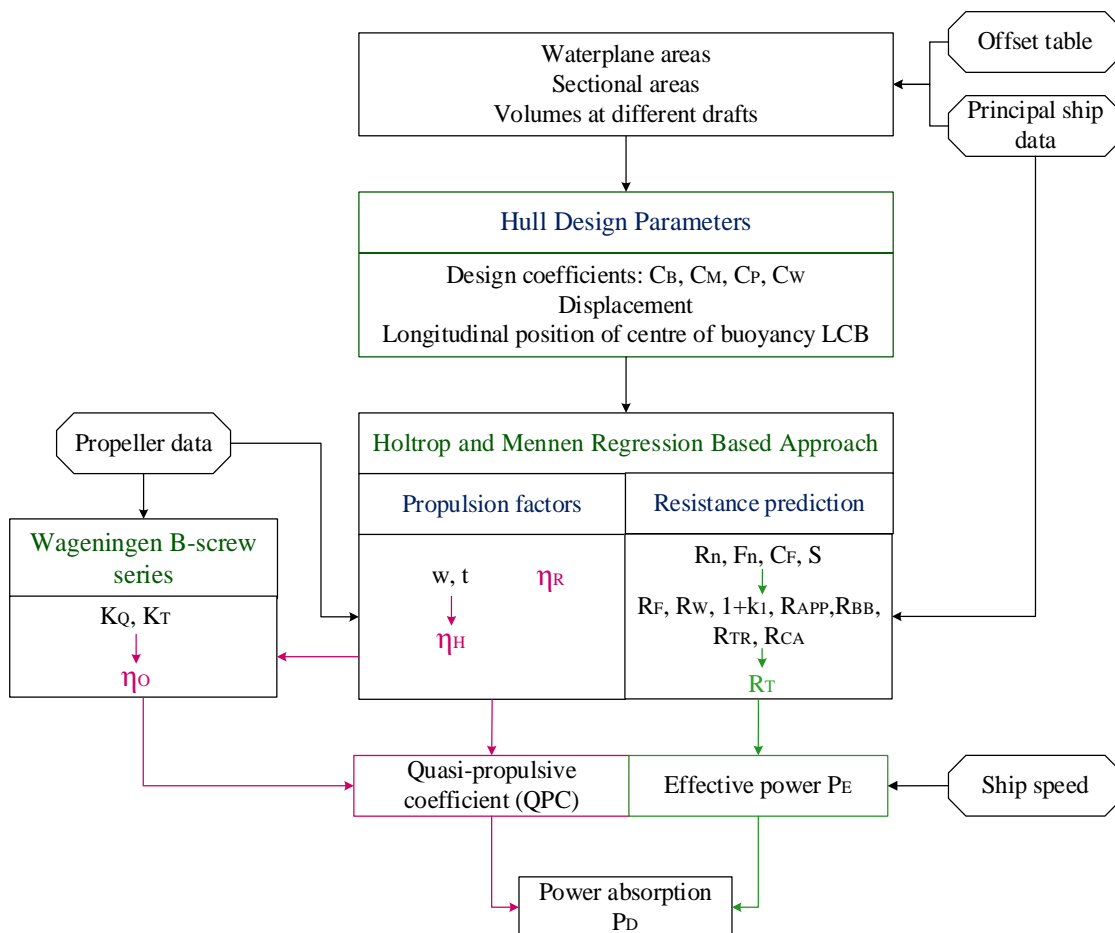


Figure 5.3 The workflow of the ship resistance and propulsion prediction module where  $C_B$  – block coefficient,  $C_P$  – prismatic coefficient,  $C_M$  – midship section area coefficient,  $C_W$  – waterplane coefficient,  $w$  – wake fraction,  $t$  – thrust deduction,  $R_n$  – Reynolds number,  $F_n$  – Froude number,  $C_F$  – skin friction coefficient,  $S$  – wetted surface area,  $K_Q$  – torque coefficient,  $K_T$  – thrust coefficient,  $\eta_H$  – hull efficiency,  $\eta_R$  – relative-rotative efficiency,  $\eta_o$  – open water efficiency.

The Holtrop and Mennen approach requires a set of hull design parameters, such as designed coefficients, the longitudinal position of the centre of buoyancy, displacement and etc., which are not always provided in the supporting documentation for each load. Therefore, a set of intermediate parameters including the ship's sectional areas, waterplane areas and volumes at different draughts has been estimated in accordance with the hull offset table and ship's principal dimensions taken from the model test report using the Simpson's First Rule described in (Munro-Smith n.d.). In the case of the ballast and scantling conditions, the sectional areas have been approximated using the least-squares sense approximation based on areas estimated for the designed condition.

Using the Holtrop and Mennen (H&M) calculation procedure and a full set of the obtained hull design parameters, the Reynolds number ( $R_n$ ), the Froude number ( $F_n$ ), the wetted surface area ( $S$ ) and the form factor ( $1 + k_1$ ) were evaluated. The obtained results acted as a base for further calculations of the ship's resistance components including the frictional resistance ( $R_F$ ), the appendage resistance ( $R_{APP}$ ), the wave-making resistance ( $R_W$ ), the immersed transom resistance ( $R_{TR}$ ), the additional resistance due to bulbous bow ( $R_{BB}$ ) as well as the model-test correlation allowance ( $R_{CA}$ ). Finally, the total ship resistance ( $R_T$ ) and, therefore, the effective power ( $P_E$ ) were calculated based on the desired ship speed ( $V$ ) as follows:

$$P_E = R_T * V \quad 5.6$$

The total ship resistance and effective power prediction results obtained at this stage of the H&M simulation have been verified against the model test data. However, since the original ship was initially equipped with a wake equalising duct (WED), the majority of tests listed in the model test report have been conducted with the influence of WED. Hence, the naked hull resistance tests are only provided for the design and ballast conditions while omitting the scantling load. The obtained H&M results were plotted against the naked hull resistance test data only for design and ballast conditions in the form of the effective power curves vs. ship speed as shown in Figure 5.4 and Figure 5.5 below. The resulted plots confirm that the H&M regression-based method can be used as a base in further case studies.

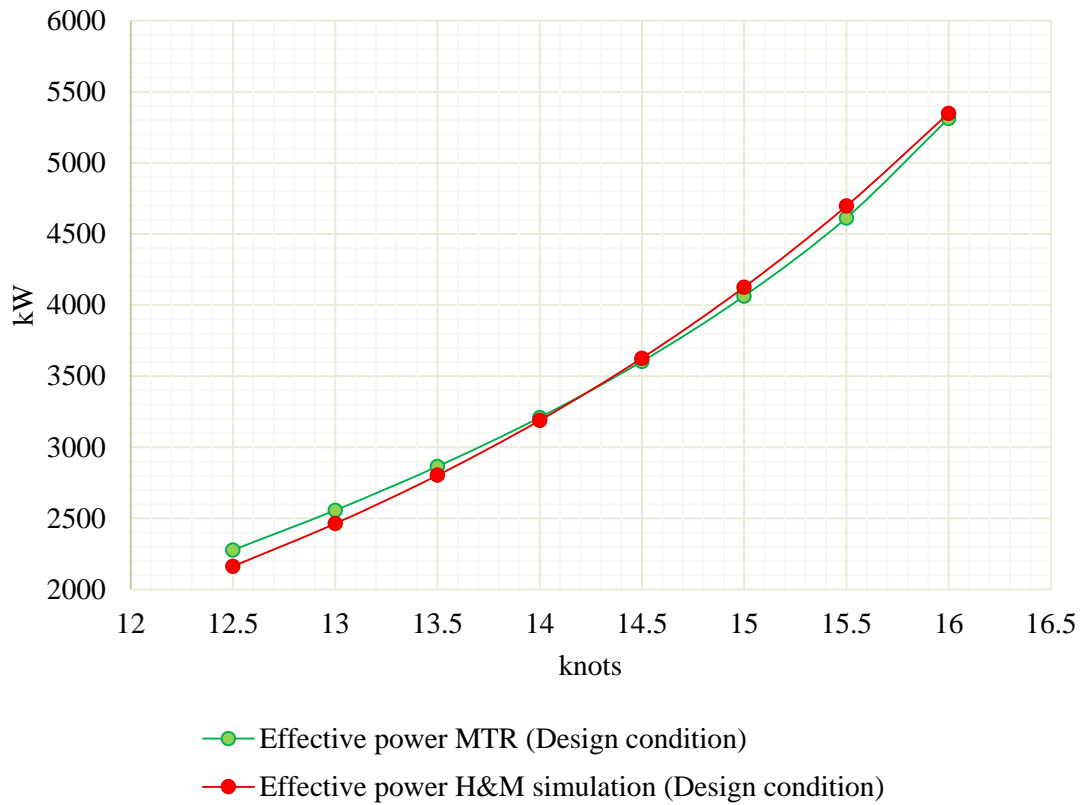


Figure 5.4 The comparison chart of the effective power from the model test report (MTR) and effective power obtained from the H&M regression-based simulation of the naked hull under the design load condition.

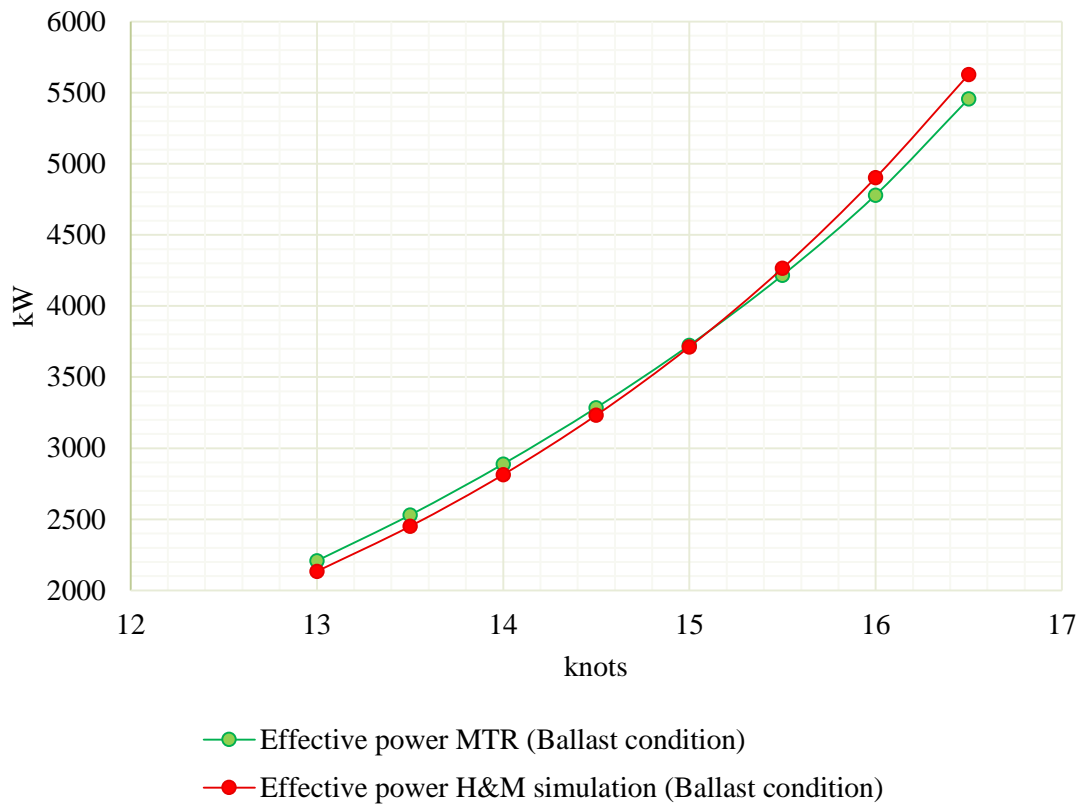


Figure 5.5 The comparison chart of the effective power from the model test report (MTR) and effective power obtained from the H&M regression-based simulation of the naked hull under the ballast condition.

Thereafter, using the obtained results and the main propeller characteristics, the wake fraction ( $w$ ) (5.7), which represents the difference between the speed of advance of the propeller and the actual ship speed expressed in percentage, thrust deduction coefficient, ( $t$ ) (5.8), which represents the losses of thrust due to water being sucked into the propeller, and relative-rotative efficiency ( $\eta_R$ ) (5.9) were estimated using the following regression-based formulations adopted from the Propulsion Factors Prediction method (Holtrop 1984). These regressions are based on 168 data full scale trials of new built ships.

$$w = c_9 c_{20} C_V \frac{L_{WL}}{T_A} \left( 0.050776 + 0.93405 c_{11} \frac{C_V}{(1-C_{P1})} \right) + 0.27915 c_{20} \sqrt{\frac{B}{L_{WL}(1-C_{P1})}} + c_{19} c_{20} \quad 5.7$$

where  $L_{WL}$  is the length of the waterline,  $T_A$  is the draught aft,  $B$  is the moulded breadth. The equations for coefficients  $c_9$ ,  $c_{11}$ ,  $c_{19}$ ,  $c_{20}$ ,  $C_V$  and  $C_{P1}$  are defined in (Holtrop 1984).

$$t = \frac{0.2514 \left( \frac{B}{L_{WL}} \right)^{0.28956} \left( \frac{\sqrt{BT}}{D} \right)^{0.2624}}{(1 - C_P + 0.0225lcb)^{0.01762} + 0.0015 C_{STERN}} \quad 5.8$$

where  $T$  is the ship's draught,  $D$  is the propeller diameter,  $lcb$  is the longitudinal position of the centre of buoyancy forward of  $0.5L_{WL}$  as a percentage of  $L_{WL}$ ,  $C_P$  is the prismatic coefficient and  $C_{STERN}$  is the stern shape coefficient.

$$\eta_R = 0.9922 - 0.05908 * BAR + 0.07424(C_P - 0.0225lcb) \quad 5.9$$

where  $BAR$  is the propeller's blade area ratio.

Hence, with obtained coefficients, it is possible to calculate the hull efficiency  $\eta_H$  as follows:

$$\eta_H = \frac{(1 - t)}{(1 - w)} \quad 5.10$$

However, since the H&M approach is designed for the loaded and design conditions while the wake fraction at ballast and partially loaded conditions tends to be 5 – 15 percent larger than the wake fraction at the loaded condition (Molland et al. 2011), the Moor and O'Connor's equations, which predict the change in wake fraction and thrust deduction with draught ratio ( $T_R$ ) have been additionally incorporated into the model for ballast calculations:

$$(1 - w)_R = 1 + [T_R - 1](0.2882 + 0.1054\theta) \quad 5.11$$

where  $\theta$  is the trim angle expressed as

$$\theta = (100 * trim_{bow})/L_{PP} \quad 5.12$$

where  $L_{PP}$  is the length between perpendiculars.

$$(1 - t)_R = 1 + [T_R - 1](0.4322 - 0.4880C_B) \quad 5.13$$

with

$$(1 - w)_R = \frac{(1 - w)_{Ballast}}{(1 - w)_{Load}} \quad (1 - t)_R = \frac{(1 - t)_{Ballast}}{(1 - t)_{Load}} \quad T_R = \frac{T_{Ballast}}{T_{Load}} \quad 5.14$$

where  $(1 - t)_{Load}$  and  $(1 - w)_{Load}$  are calculated using the Holtrop and Mennen approach.

As outlined in Chapter 4, the reference products tanker was originally fitted with the standard fixed pitch (FP) propeller, where the basic design parameters are listed in Table 4.1. The fixed pitch propeller data provided in the model test report is limited and comprises only basic propeller characteristic and the open water test diagram while the type of the propeller is not specified. Thus, based on the ship's standard design, it was initially assumed that the reference four bladed FP propeller might have similar geometric characteristics with the Wageningen B-screw series representing the most extensive and widely used propeller series including vessels of this type and size. As such, Wageningen B-screw series regression-based computational approach by (Oosterveld & Van Oossanen 1975) based on the  $Rn = 10^6$  (without additional Reynolds number corrections) has been used to estimate the model scale propeller coefficients  $K_Q$  and  $K_T$  and then compared with the open water test data from the model test report. Based on the results of this comparison, presented in Figure 5.6, it can be concluded that the original FP propeller model has similar open water performance with the propeller model predicted using Wageningen B-screw series regression-based method, which, therefore, has been adopted for use as a base method for prediction of the propeller coefficients for further full scale propeller design and analysis in the following case studies.

Therefore, using the Wageningen B-Screw Series method, with the applied Reynolds number corrections, the full-scale propeller thrust  $K_T$  and torque  $K_Q$  coefficients were obtained, followed by the estimation of the propeller efficiency ( $\eta_O$ ) as shown below:

$$\eta_O = \frac{J}{2\pi} * \frac{K_T}{K_Q} \quad 5.15$$

where  $J$  is the advanced coefficient, which, in turn, can be estimated using the following expression:

$$J = \frac{V_A}{RPM * D} \quad 5.16$$

where  $V_A$  is the speed of advance while  $RPM$  stands for the propeller rotational speed.

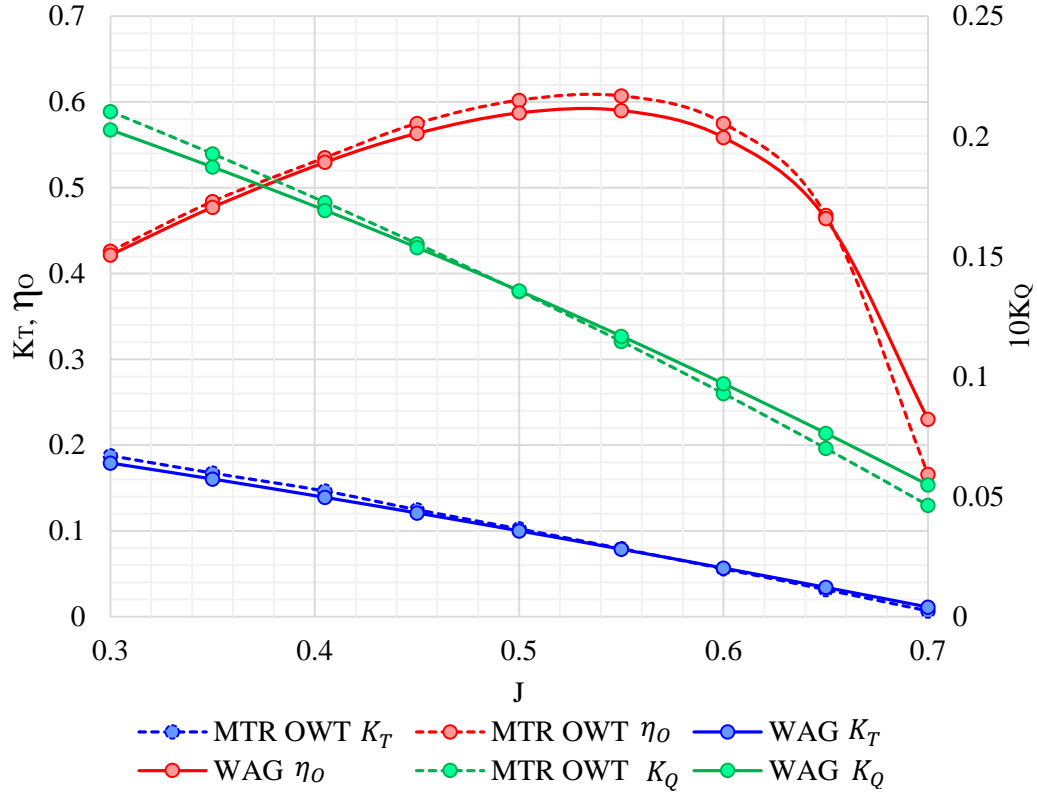


Figure 5.6 Comparison diagram of the open water test (OWT) data from the model test report (MTR) and computations using the Wageningen B-screw series (WAG) regression-based method.

Finally, based on previously estimated efficiencies, the quasi-propulsive coefficient ( $QPC$ ) and the power absorption ( $P_D$ ) can be estimated using the following equations 5.17 and 5.18 respectively.

$$QPC = \eta_H \eta_R \eta_o \quad 5.17$$

$$P_D = \frac{P_E}{QPC} \quad 5.18$$

The obtained simulation results for designed, ballast and fully loaded conditions of the naked hull operating at the designed speed of 14.6, 14.07 and 15.02 knots respectively to their load are listed below in Table 5.1.

Table 5.1 Complete resistance and propulsion module simulation results for designed, ballast and loaded conditions.

Parameter	Symbol	<i>Ballast</i>	<i>Designed</i>	<i>Loaded</i>	Metric
Ship speed	$V$	15.02	14.6	14.07	knots
Longitudinal position of centre of bouncy forward of $0.5L_{WL}$	$lcb$	9.6	4.8	2.8	m
		6	2.9	1.7	%
Waterplane area	$A_{WPL}$	3749	4039	4199	m <sup>2</sup>
Midship section area	$A_M$	117	266	322	m <sup>2</sup>
Wetted surface area	$S$	5202	6361	7071	m <sup>2</sup>
Displacement volume	$\nabla$	22174	34418	42571	m <sup>3</sup>
Displacement tonnage	$\Delta$	22728	35278	43635	tonnes
<i>Design Coefficients</i>					
Block coefficient	$C_B$	0.777	0.777	0.791	-
Midship section area coefficient	$C_M$	0.992	0.995	0.996	-
Prismatic coefficient	$C_P$	0.783	0.781	0.794	-
Waterplane coefficient	$C_W$	0.814	0.889	0.921	-
<i>Immersed Transom</i>					
Immersed transom breadth	$B_{TR}$	0	1.55	7.56	m
Immersed transom height	$H_{TR}$	0	0.35	2.36	m
Immersed transom area	$A_{TR}$	0	0.54	17.84	m <sup>2</sup>
<i>Bulbous Bow</i>					
Bulbous bow centre above the keel line	$hb$	2.49	4.19	5.14	m
Bulbous bow area	$A_{BB}$	20.1	29.6	31.5	m <sup>2</sup>
Reynolds number	$R_n$	1.04E+09	1.05E+0.9	1.01E+0.9	-
Froude number	$F_n$	0.195	0.186	0.179	-
Frictional coefficient	$C_F$	0.001523	0.001522	0.001528	-
Form factor	$1 + k_1$	1.26	1.25	1.27	-
Correlation coefficient	$C_{CA}$	0.000414	0.000406	0.000405	-
Stern shape coefficient	$C_{STERN}$	0	0	0	-
Length of the run	$L_R$	55.9	49.3	42.9	m
The angle of the waterline at the bow	$i_E$	51	40	42	°

Parameter	Symbol	<i>Ballast</i>	<i>Designed</i>	<i>Loaded</i>	Metric
<i>Resistance Components</i>					
Frictional resistance	$R_F$	242	280	288	kN
Appendage resistance	$R_{APP}$	4.3	4.07	3.76	kN
Wave-making resistance	$R_W$	105.3	64.9	55.4	kN
Bulbous bow resistance	$R_{BB}$	2.33	1.60	0.53	kN
Immersed transom resistance	$R_{TR}$	0.00	0.00	41.9	kN
Correlation resistance	$R_{CA}$	65.8	74.7	76.2	kN
Total ship resistance	$R_T$	481	496	543	kN
Effective power	$P_E$	3713	3722	3912	kW
<i>Propulsion Characteristics and Flow Conditions</i>					
Propeller rotational speed	$N$	119.9	122.1	122.4	rpm
Wake fraction coefficient	$w$	0.44	0.39	0.36	-
Thrust deduction coefficient	$t$	0.25	0.23	0.22	-
Advanced coefficient	$J$	0.38	0.40	0.40	-
<i>Propeller Coefficients based on the Wageningen B-Screw Series</i>					
Thrust coefficient	$K_T$	0.154	0.141	0.142	-
Torque coefficient	$K_Q$	0.0173	0.0166	0.0166	-
<i>Efficiencies and Power Absorption</i>					
Relative-rotative efficiency	$\eta_R$	1.01	1.01	1.01	-
Hull efficiency	$\eta_H$	1.35	1.25	1.22	-
Open water efficiency	$\eta_O$	0.52	0.54	0.54	-
Quasi propulsive coefficient	$QPC$	0.71	0.69	0.67	-
Delivered power	$P_D$	5227	5400	5808	kW

It should be noted that since the model test report does not contain complete propulsion and power absorption tests of the naked hull, a propeller rotational speed for each load condition is taken from the model test report data influenced by the wake equalising duct and, therefore, for the full scale delivered power estimation purposes it has been assumed that the propeller rotational speed will be the same with and without wake equalising duct. In addition, in this module, the water density, kinematic viscosity and dynamic viscosity are based on the standard seawater conditions at 15 C° for all cases.

## 5.2 Module 2: Engine Performance Simulation

In present days, the majority of vessels, including the reference products tanker in this study, are equipped with a mechanical drive. Generally, in a conventional mechanical train, the power plant consists of the propulsion and electric power systems, where the propulsion system is powered by the main engine, providing a mechanical energy through the transmission shaft to the propulsor (propeller), while the electric propulsion system is powered by the auxiliary engines.

As it has been previously outlined, the reference power plant in this research represents a conventional mechanical train with directly connected low speed diesel engine (5-cylinder MAN S50MC-C engine of 7150kW in total) and propulsor while also having a set of three auxiliary medium speed engines for electric power supply purposes, namely 3 Dalian auxiliary generators, each of 910kW (450V 60Hz). The energy flow diagram of a reference ship is schematically shown in Figure 5.7.

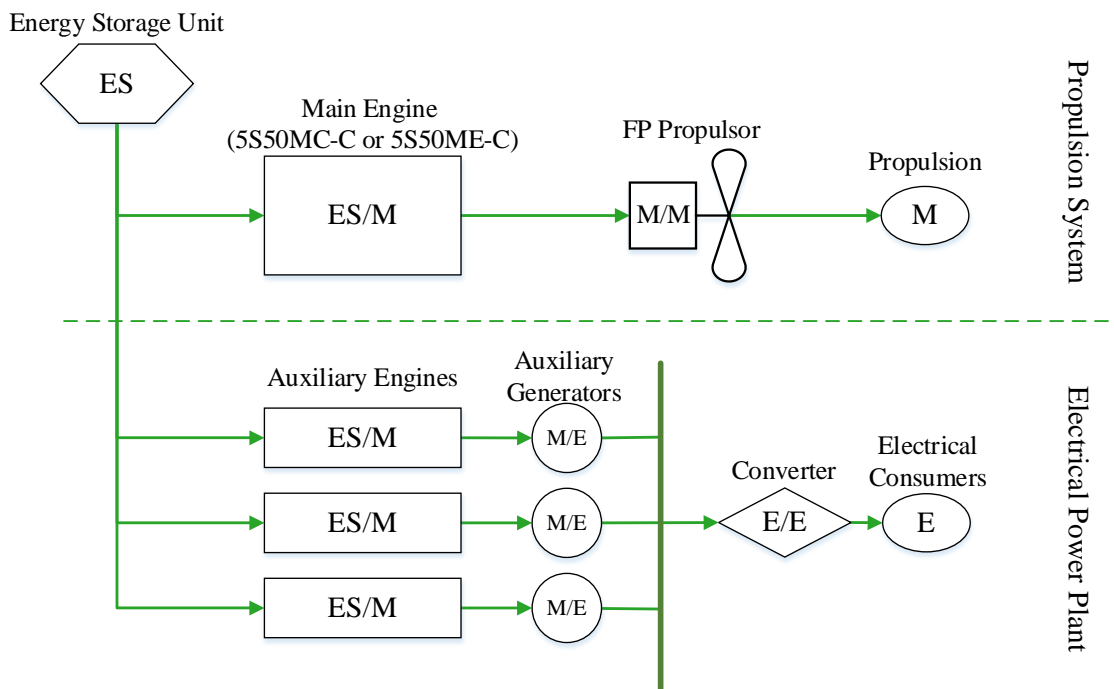


Figure 5.7 The energy flow diagram of the conventional mechanical drive system installed on the reference tanker. ES – energy storage, M – mechanical energy, E – Electricity.

Since, in the following case studies, the effect of various technologies and methods on ship energy efficiency will mostly affect the main propulsion system rather than the auxiliary system, it has been decided to simulate a performance of the main engine while keeping the auxiliary system behaviour constant.

There are several methods available to predict a performance of the marine diesel engine including CFD simulation, multi-zone simulation models and a look-up table approach.

- CFD simulations

The CFD-based simulations, such as the model of large 2-stroke marine diesel engine outlined in (Jin & Vassalos 2013) that has been developed and validated using CFD computational approach, can be used to understand and analyse the combustion process in great details. For instance, the (Jin & Vassalos 2013) model consists of the RNG (Re-Normalisation Group)  $k-\varepsilon$  turbulence simulation component, aimed to capture the in-cylinder flow compression and mixing, and the combustion simulation model based on the finite-rate approach designed to simulate the chemical reactions while taking into account the turbulence effect on the combustion processes. However, at the current stage, such models are only able to simulate the combustion process but not calculate the engine fuel consumption while the requirements from the model in terms of the level of details are high. In addition, such simulations do not include the effect of the turbocharger.

- Multi-zone engine simulations

The multi-zone engine simulation models, including the early work by (Banisoleiman et al. n.d.) and recent NTUA Engine Performance and Emissions code developed by (Hountalas et al. 2013), are purely based on thermodynamics which allows a detailed analysis of the engine performance of both 2- and 4-stroke diesel engines as well as to predict the level of atmospheric emissions. Both models allow to adjust the injection and combustion profiles, namely to modify pressure, temperature, injection angle and gas composition in order to uncover the principal forces affecting the efficiency and emissions profile. However, for the simulation purposes, it is required to provide an extensive engine geometry, as well as the initial fuel consumption rate, power output values for each load and other supporting information which are not always available and in some cases remain confidential to the manufacturer. Moreover, in terms of this research, the fuel consumption rate is one of the energy efficiency indicators (EEI) and needs to be predicted by this module in order to be able to estimate the effect of certain energy efficiency innovation on the ship's overall efficiency level.

- Look-up table approach

The lookup-table approach is a fast and accurate method while its applicability is strongly restricted by the availability of required information. For instance, an open source Computational Engine Application System (CEAS) engine calculation tool developed by

MAN has an extensive engine performance database including the Tier III engines and innovative fuels such as methane, ethane, LPG and methanol. The model allows choosing preferable types of the turbocharger, to modify engine cooling system as well as to specify the ambient conditions, propeller type and the fuel sulphur content. The CEAS engine calculation tool also provides a user with the engine layout diagram option to choose the required power and rotational speed in accordance with the permitted values. As such, the CEAS is able to calculate the power, rotational speed, SFOC, exhaust gas flow, exhaust gas temperature and even the potential steam production capacity for each load. However, this model does not calculate the exhaust emissions level neither does it provide any insights on the engine inner behaviour.

Since the reference ship is already equipped with the MAN low-speed diesel engine, plus the main purpose of this engine simulation module is to help to evaluate and compare the effect of a particular energy efficiency-enhancing technology, or method as a part of the holistic ship simulation analysis rather than looking deeply into the engine behaviour itself, the CEAS engine calculation tool has been selected as an engine simulation module. However, this tool does not predict the atmospheric emissions level meaning that the additional emissions prediction model has been separately developed and outlined in the next section.

The CEAS database has recently been updated with the Tier III engines data while the entire Tier I engines data (the mechanical MC/MC-C range) has been removed. At the same time, according to the entry in the register book, the examinee oil products tanker is equipped with the Tier I mechanically controlled MC/MC-C (5S50MC-C) engine. Hence, since the Tier I engines do not comply with the modern regulations while this research is dedicated to the future developments, the main reference MC/MC-C engine has been switched to the electronically controlled ME/ME-C engine (5S50ME-C) of the same size which complies with the Tier II regulations. It is important to note that MC/MC-C engines still can achieve the Tier II requirements by introducing new fuel system components such as plunger/barrel and fuel valve nozzles as well as by an adjustment of the combustion chamber volume by piston rod shims, the scavenge air pressure and the exhaust cam profile (MAN Diesel and Turbo 2014a). However, the electronically controlled ME/ME-C engines have a major advantage with respect to operating at even very low load for long periods of time, whilst offering a substantial reduction in fuel oil consumption compared to MC/MC-C engines at such low loads possible due to an adjustment of the programming of the

electronically controlled injection of the fuel oil. Moreover, one of the key benefits of the ME/ME-C engines is the ability to operate in different modes without the interference of the operator (MAN Diesel and Turbo n.d.).

**ISO ambient conditions (ambient air: 25 °C, scavenge air coolant: 25 °C)**

Load % SMCR	Power kW	Speed r/min	SFOC g/kWh	Exh. gas kg/s	Exh. gas <sup>1)</sup> °C	Steam <sup>2)</sup> kg/h
100	7,150	127.0	166.8	16.0	252	1,640
95	6,793	124.8	165.6	15.5	245	1,410
90	6,435	122.6	164.6	14.9	240	1,240
85	6,078	120.3	163.9	14.4	236	1,100
80	5,720	117.9	163.3	13.7	233	1,000
75	5,363	115.4	162.9	13.1	232	920
70	5,005	112.8	162.8	12.4	232	880
65	4,648	110.0	163.5	11.7	234	860
60	4,290	107.1	164.4	11.0	237	860
55	3,933	104.1	165.5	10.2	241	870
50	3,575	100.8	166.7	9.4	247	890
45	3,218	97.3	168.0	8.6	255	920
40	2,860	93.6	169.4	7.7	265	940
35	2,503	89.5	170.8	6.8	273	920
30	2,145	85.0	171.8	7.0	231	490
25	1,788	80.0	173.8	5.9	237	470

Figure 5.8 The resulting table of the CEAS engine simulation tool.

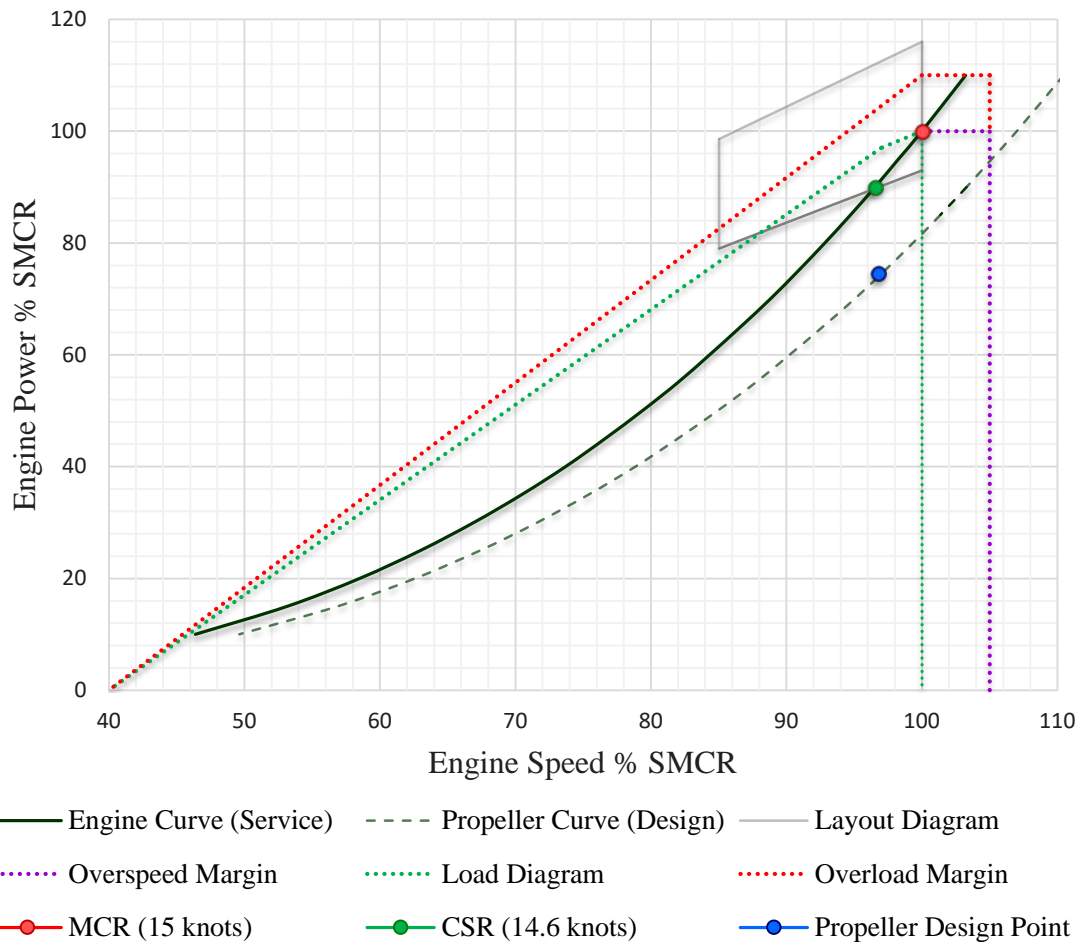


Figure 5.9 The 5S50ME-C engine layout and performance diagram.

The Computational Engine Application System (CEAS) simulation results of the 5S50ME-C engine with SMCR power of 7150kW and SMCR speed 127 rpm have been arranged into a table shown in Figure 5.8, while the engine layout/performance diagram for the reference ship design condition is illustrated in Figure 5.9.

In Figure 5.9, the normal continuous rating (NCR) has been set as 90 percent of SMCR corresponding to ship's design speed of 14.6 knots while the propeller design point is estimated using the propeller law with deducted 15 percent of sea-margin and 2 percent of potential shaft losses from the NCR power.

### 5.3 Module 3: Exhaust Emissions Prediction Model

The main objective of Module 3 of the Ship Performance Simulation (SPS) model is to predict and compare changes in the exhaust emissions profile under different conditions reflecting the environmental component of the energy efficiency indicators (EEIs). In this research, the emissions footprint comprises carbon monoxide  $CO$ , carbon dioxide  $CO_2$ , hydrocarbons  $HC$ , nitrogen oxides  $NO_x$  and oxides of sulphur  $SO_x$ .

Since the engine performance simulation module does not provide any data on the emissions behaviour it has been decided to predict the emissions breakdown based on the available sources and then to link the outcome in relation with the particular engine performance. The most convenient source of data is found to be engine shop tests supported by a  $NO_x$  technical file. The provided emissions data is based on the performance of similar but larger engine of MAN origin, namely 7S50MC-C with the SMCR power of 11069.4 kW and the SMCR speed of 127 rpm covering most of the targeted emissions types as listed in Table 5.2.

Table 5.2 The  $NO_x$  file emissions data related to the 7S50MC-C marine diesel engine.

Engine Load	$CO$	$CO_2$	$HC$	$O_2$	$NO_x$	$NO_x$ humidity factor	Dry/Wet factor	$NO_x$ mass flow	$NO_x$ specific
%	ppm	%	ppmC	%	ppm	factor		kg/h	g/kWh
100	62	4.34	74	15.23	1172	0.873	0.965	155.83	14.08
75	54	3.79	79	15.95	1186	0.864	0.969	131.58	15.85
50	42	3.67	79.5	16.15	1218	0.864	0.97	94.62	17.08
25	44	3.32	75.5	16.58	1152	0.885	0.972	51.52	18.63

In addition, for comparison purposes, the fuel used in all calculations at this stage is also taken from the provided engine performance data files and considered to be a standard Bunker-A ISO 8217 marine diesel oil with the lower calorific value of 42,700 kJ/kg and

the sulphur content of 0.23 percent. The fuel chemical breakdown based on the elemental analysis is shown in Table 5.3.

Table 5.3 The elemental chemical breakdown of the MDO fuel used.

Constituent	<i>C</i>	<i>H</i>	<i>N</i>	<i>O</i>	<i>S</i>	Ash	Total
Mass Fraction	0.8732	0.1186	0.0007	0.005	0.0023	0.0002	1

As such, this section is mainly focused on finding the right method to match the exhaust emissions components with the required engine specifications in order to develop a cross-functional model for further use in the following case studies.

- Carbon monoxide (*CO*) and hydrocarbons (*HC*)

The concentrations of carbon monoxides *CO* and hydrocarbons *HC* in the exhaust gas flow of modern diesel engines are generally very low and, as shown in Table 5.2, normally defined in ppm (parts per million) and ppmC (parts per million carbon) respectively. Both *CO* and *HC* species occur as a result of the incomplete combustion due to poor quality of fuel, improper air mixing or combustion air deficiency influenced by engine load, engine condition and thermal efficiency. The most accurate results in determining their concentrations could be achieved via direct measurements or dry exhaust analysis (or wet in case of *HC*) in the same manner as in the *NO<sub>x</sub>* technical file while being difficult to predict using computational methods. As such, in this research, the changes in concentrations of *CO* and *HC* from the engine to engine have been neglected. However, since the volumetric ratio (ppm and ppmC) does not provide straightforward information from a cost/benefit point of view, the environmental energy efficiency indicator of each exhaust emissions component should be defined as kg/h or as a specific rate g/kWh, which is often used for the legislation purposes. Therefore, for all further calculations the changes in *CO* and *HC* emissions will be estimated as kg/h and g/kWh using the IMO calculation approach (MEPC.177(58) Annex 14 2010) while taking into account the fuel consumption and the exhaust gas flow rates but keeping their general load distribution in accordance with the provided trends.

To achieve this, first, the provided *CO* and *HC* values should be connected with the CEAS engine calculation tool (Module 2) by “stretching” them in accordance with the required loads (25 – 100 percent load) using cubic spline interpolation in the Matlab environment as shown in Figure 5.10.

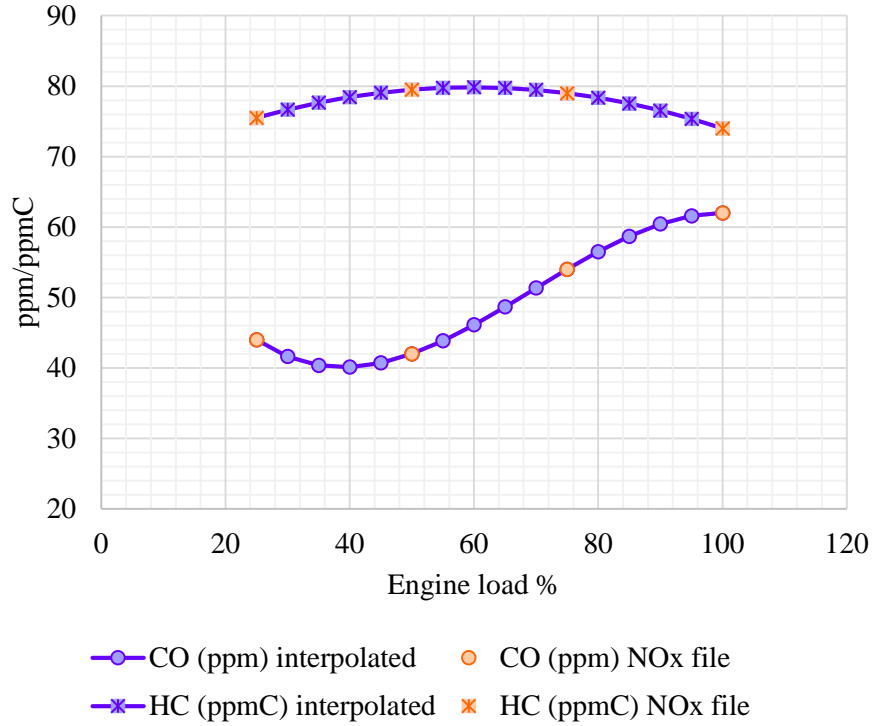


Figure 5.10 *CO* and *HC* spline interpolation results.

By definition, the gaseous emissions concentration measured on “wet” basis meaning that the study sample contains the moisture (vapour) content. When a “dry” value is reported, the vapour molecules have been deducted from the sample while the calculated concentrations are based on the percent of solids present in the sample. Therefore, since the *CO* emissions have been measured on a dry basis, the obtained concentration should be converted to a wet basis in accordance with formulations (5.19 – 5.21), while the *HC* emissions concentrations are normally measured on a wet basis and, therefore, should not be changed.

$$c_W = k_W c_D \quad 5.19$$

where  $c_W$  is the exhaust gas emissions component estimated on a wet basis,  $c_D$  stands for the species estimated on a dry basis, while  $k_W$  is a dry/wet correction factor calculated in accordance with the IMO recommendations, based on basic chemistry principles and described in (MEPC.177(58) Annex 14 2010) as follows:

$$k_W = \left( 1 - \frac{1.2442H_a + 111.19W_{ALF} \frac{q_{mf}}{q_{mad}}}{773.4 + 1.2442H_a + \frac{q_{mf}}{q_{mad}} f_{fw} 1000} \right) * 1.008 \quad 5.20$$

with 
$$f_{fw} = 0.055594w_{ALF} + 0.0080021w_{DEL} + 0.0070046w_{EPS} \quad 5.21$$

where

- $f_{fw}$  represents the fuel specific factor for exhaust flow calculation;
- $q_{mf}$  is the fuel mass flow rate (kg/h);
- $q_{mad}$  is the intake air mass flow rate on a dry basis (kg/h);
- $H_a$  stands for the absolute humidity of the intake air (g water /kg dry air);
- $w_{ALF}$  – H content of fuel (%);
- $w_{DEL}$  – N content of fuel (%);
- $w_{EPS}$  – O content of fuel (%)

where  $w_{ALF}$ ,  $w_{DEL}$  and  $w_{EPS}$  values are taken from Table 5.3.

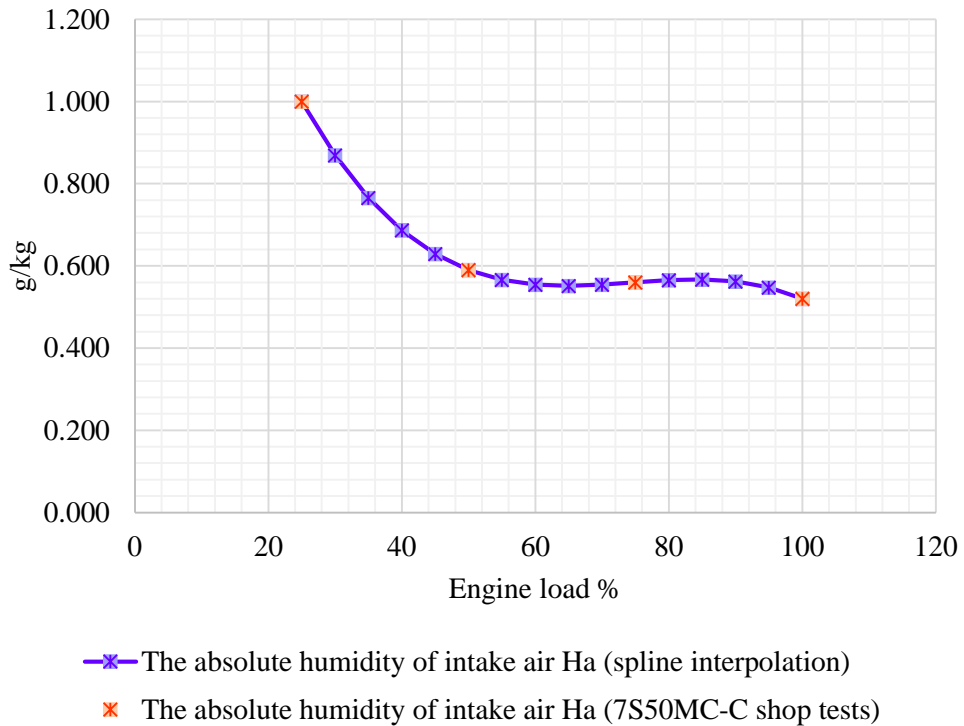


Figure 5.11 The absolute humidity of intake air  $H_a$  spline interpolation validation.

The absolute humidity of the intake air  $H_a$  values for each load have been interpolated (cubic spline interpolation) in accordance with the 7S50MC-C engine shop test documentation and will be kept the same for all upcoming engine modifications. In fact, the absolute humidity of the intake air  $H_a$  does not seem to have a significant impact on fluctuations of the dry/wet correction factor  $k_W$  (Figure 5.12), while a strong influence of the exhaust gas flow  $q_{mew}$  on the dry/wet correction factor  $k_W$  can be observed in Figure 5.13. The absolute humidity interpolation results are represented in Figure 5.11.

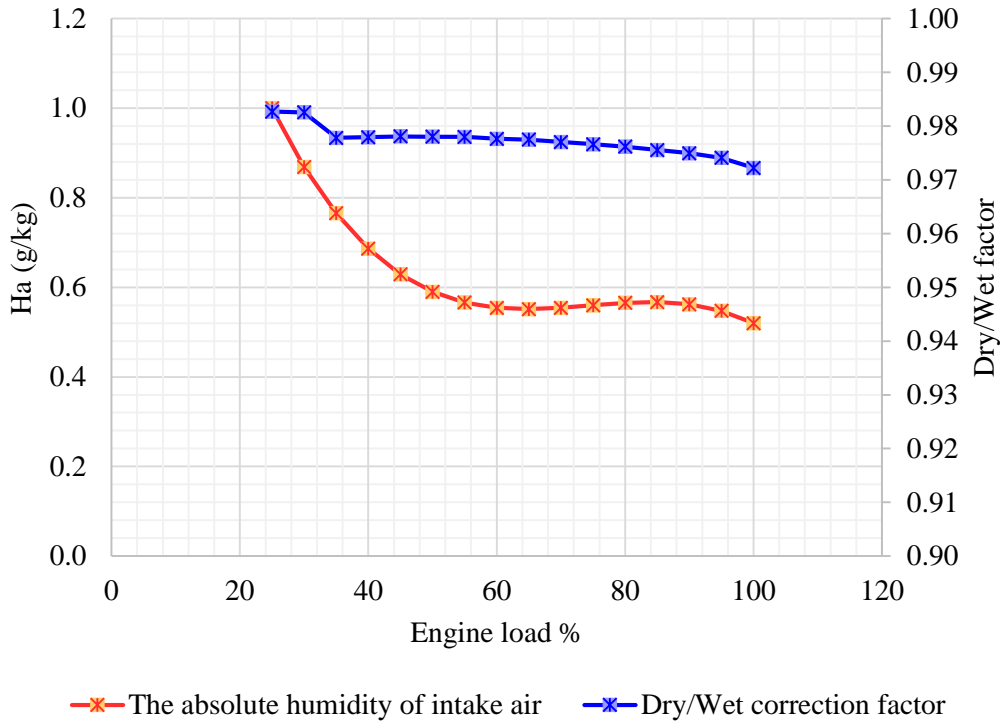


Figure 5.12 Comparison pattern of the absolute humidity of the intake air and dry/wet correction factors over range of engine loads.

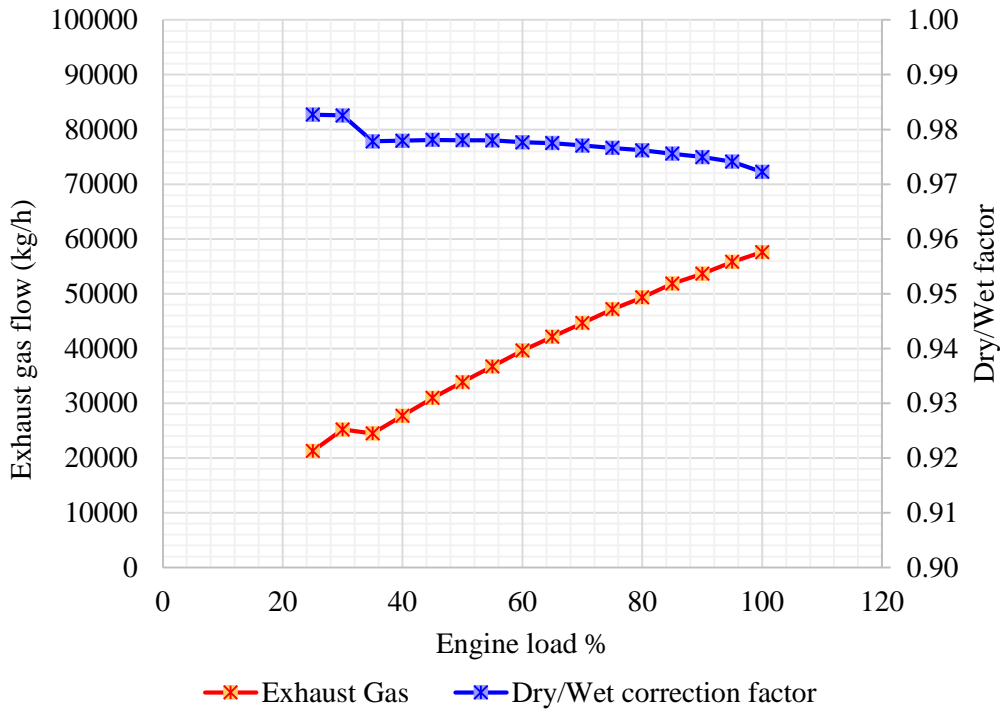


Figure 5.13 Comparison pattern of the exhaust gas flow and dry/wet correction factors over range of engine loads.

The intake air mass flow rate on dry basis  $q_{mad}$  for this model is obtained as follows:

$$q_{mad} = q_{mew} - \frac{P_B SFOC}{1000} \quad 5.22$$

where  $q_{mew}$  is the exhaust gas mass flow rate on a wet basis (kg/h),  $P_B$  is the engine brake power (kW),  $SFOC$  is the specific fuel oil consumption (g/kWh), all based on the Module 2 CEAS engine calculation tool.

When  $CO$  (or other species) concentrations have been converted into the wet basis, the mass flow rate in g/h of individual gas component should be calculated in accordance with the following IMO formulation applicable to all gas species except  $NO_X$ :

$$q_{mgas} = u_{gas} c_{gas} q_{mew} \quad 5.23$$

where  $q_{mew}$  is the exhaust gas mass flow rate on a wet basis (kg/h),  $c_{gas}$  is the concentration of the respective component in the raw exhaust gas wet (ppm),  $u_{gas}$  is ratio between density of the exhaust components and density of exhaust gas corresponding to Table 5.4.

Table 5.4 Coefficient  $u_{gas}$  for raw exhaust gas (MEPC 12th Session & Agenda Item 6 2007).

Exhaust gas component	$NO_X$	$CO$	$HC$	$CO_2$	$O_2$
$u_{gas}$ MDO	0.001586	0.000966	0.000479	0.001517	0.001103

As such, the calculation results of carbon monoxide ( $CO$ ) and hydrocarbon ( $HC$ ) emissions including the mass flow rates based on the reference engine 5S50ME-C are presented in Table 5.5 and Table 5.6 respectively.

Table 5.5 CO calculation results for the reference engine 5S50ME-C.

Engine load	Engine brake power	Specific fuel oil consumption	Exhaust gas mass flow rate (wet)	CO concentration dry	Fuel mass flow rate	Intake air mass flow rate dry	Absolute humidity of intake air	Dry/wet correction factor	CO concentration wet	IMO exhaust gas component coefficient	CO mass flow rate	CO specific
%	$P_B$ <i>kW</i>	<i>SFOC</i> <i>g/kWh</i>	$q_{mew}$ <i>kg/h</i>	$c_{dCO}$ <i>ppm</i>	$q_{mf}$ <i>kg/h</i>	$q_{mad}$ <i>kg/h</i>	$H_a$ <i>g/kg</i>	$k_W$ -	$c_{wCO}$ <i>ppm</i>	$u_{CO}$ -	$q_{mCO}$ <i>kg/h</i>	- <i>g/kWh</i>
100	7150	166.8	57600	62	1193	56407	0.520	0.972	60	0.000966	3.35	0.47
95	6793	165.6	55800	62	1125	54675	0.548	0.974	60		3.23	0.47
90	6435	164.6	53640	60	1059	52581	0.562	0.975	59		3.05	0.47
85	6078	163.9	51840	59	996	50844	0.567	0.976	57		2.86	0.47
80	5720	163.3	49320	56	934	48386	0.565	0.976	55		2.62	0.46
75	5363	162.9	47160	54	874	46286	0.560	0.977	53		2.40	0.45
70	5005	162.8	44640	51	815	43825	0.554	0.977	50		2.16	0.43
65	4648	163.5	42120	49	760	41360	0.551	0.978	47		1.93	0.42
60	4290	164.4	39600	46	705	38895	0.554	0.978	45		1.72	0.40
55	3933	165.5	36720	44	651	36069	0.566	0.978	43		1.52	0.39
50	3575	166.7	33840	42	596	33244	0.590	0.978	41		1.34	0.37
45	3218	168.0	30960	41	541	30419	0.629	0.978	40		1.19	0.37
40	2860	169.4	27720	40	484	27236	0.687	0.978	39		1.05	0.37
35	2503	170.8	24480	40	428	24052	0.765	0.978	39		0.93	0.37
30	2145	171.8	25200	42	369	24831	0.869	0.983	41		0.99	0.46
25	1788	173.8	21240	44	311	20929	1.000	0.983	43		0.89	0.50

Table 5.6 HC calculation results for the reference engine 5S50ME-C.

Engine load	Engine brake power	Exhaust gas mass flow rate (wet)	HC concentration wet	IMO exhaust gas component coefficient	HC mass flow rate	HC specific
%	$P_B$	$q_{mew}$	$c_{wHC}$	$u_{HC}$	$q_{mHC}$	-
	$kW$	$kg/h$	$ppmC$	-	$kg/h$	$g/kWh$
100	7150	57600	74	0.000479	2.04	0.29
95	6793	55800	75		2.01	0.30
90	6435	53640	77		1.97	0.31
85	6078	51840	78		1.93	0.32
80	5720	49320	78		1.85	0.32
75	5363	47160	79		1.78	0.33
70	5005	44640	79		1.70	0.34
65	4648	42120	80		1.61	0.35
60	4290	39600	80		1.51	0.35
55	3933	36720	80		1.40	0.36
50	3575	33840	80		1.29	0.36
45	3218	30960	79		1.17	0.36
40	2860	27720	78		1.04	0.36
35	2503	24480	78		0.91	0.36
30	2145	25200	77		0.93	0.43
25	1788	21240	76		0.77	0.43

- Carbon dioxide ( $CO_2$ )

Since the concentrations of  $CO_2$  in the raw exhaust flow is much higher than of other species, it is important to address their fluctuations when considering different engines in addition to changes associated with the fuel consumption rate. In fact, the measured concentrations of  $CO_2$  in the dry exhaust are normally described in a form of percentage (%) rather than using a volumetric expression (ppm).

With respect to predictions of the  $CO_2$  concentrations, since the  $CO_2$  emissions are directly linked with fuel consumption and fuel composition, it was decided to incorporate a carbon balance method. This method is based on basic chemistry principles and adopted by IMO as one step calculation procedure recommended for the prediction of exhaust gas mass flow in accordance with fuel consumption, fuel composition and the exhaust gas concentrations using the formulations (5.24), (5.25) and (5.26) (MEPC.177(58) Annex 14 2010). Moreover, the idea is to convert this formula into an equation targeting the prediction of the  $CO_2$  concentrations on a dry basis ( $c_{CO_2,d}$ ) while the exhaust gas mass flow rate ( $q_{mew}$ ) as well as the fuel consumption ( $q_{mf}$ ) should be estimated using the engine simulation module. This will help in establishing a continuous relationship between the fuel consumption required under certain conditions in the following case studies (Chapters 7-11) and the fluctuations of the  $CO_2$  emissions concentrations associated with it.

$$q_{mew} = q_{mf} \left( \left( \frac{1.4(w_{BET}w_{BET})}{\left( \frac{1.4w_{BET}}{f_c} + 0.08936w_{ALF} - 1 \right) \frac{1}{1.293} + f_{fd}} + 0.08936w_{ALF} - 1 \right) * \left( 1 + \frac{H_a}{1000} \right) + 1 \right) \quad 5.24$$

where

- $q_{mew}$  is the exhaust gas mass flow rate on a wet basis (kg/h) estimated using the CEAS engine calculation tool (Module 2);
- $q_{mf}$  is the fuel mass flow rate also calculated using the engine simulation module (kg/h);
- $H_a$  is the absolute humidity of intake air, in gram water per kg dry air, which represents a set of constants for each load as explained in the previous subsection dedicated to the estimation of the carbon monoxide  $CO$  and hydrocarbon  $HC$  emissions;
- $w_{ALF}$  –  $H$  content of fuel (%);
- $w_{BET}$  –  $C$  content of fuel (%), both are taken from Table 5.3.
- $f_{fd}$  is the fuel specific constant for the dry exhaust, estimated by the following equation:

$$f_{fd} = -0.055593w_{ALF} + 0.008002w_{DEL} + 0.0070046w_{EPS} \quad 5.25$$

where  $w_{DEL}$  –  $O$  content of fuel (%) and  $w_{EPS}$  –  $N$  content of fuel (%), also listed in Table 5.3.

- $f_c$  is the carbon factor, calculated using the following equation:

$$f_c = 0.5441(c_{CO_2d} - c_{CO_2ad}) + \frac{c_{COd}}{18522} + \frac{c_{HCw}}{17355} \quad 5.26$$

where  $c_{CO_2d}$  is the unknown variable of dry  $CO_2$  concentration in the raw exhaust (%), which should be derived from these equations,  $c_{CO_2ad}$  is a dry  $CO_2$  concentration in the ambient air (natural content in ambient air about 0.03 percent),  $c_{COd}$  and  $c_{HCw}$  are dry and wet concentrations of  $CO$  and  $HC$  respectively in the raw exhaust expressed in ppm while representing two sets of constants for each load as described  $CO$  and  $HC$  subsection.

To obtain the  $CO_2$  concentrations ( $c_{CO_2d}$ ), the set of equations 5.24, 5.25 and 5.26 has to be solved. The resulting  $CO_2$  concentrations for the reference engine 5S50ME-C are plotted in Figure 5.14 in comparison with the concentrations listed in the  $NO_x$  technical file of 7S50MC-C engine. The plot illustrates that the electronically controlled 5S50ME-C engine is generally more fuel efficient than the mechanically controlled 7S50MC-C since the most efficient and cost-effective use of fuel takes place when the  $CO_2$  concentrations in the exhaust are maximized.

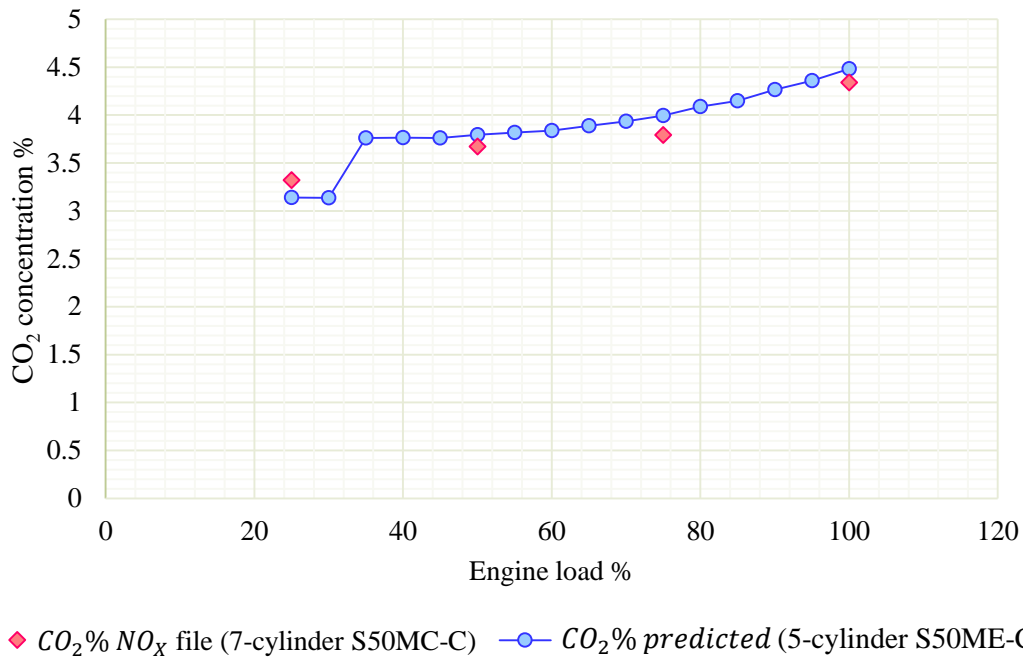


Figure 5.14 The comparison plot of the  $CO_2$  concentrations in dry exhaust.

In fact, since the  $CO_2$  concentrations are directly related to the amount of exhaust gas flow at each load, they share a similar pattern over the engine loads. Therefore, the “jump” between 30 and 35 percent engine loads is caused by the behaviour pattern of the exhaust gas flow, which in turn is influenced by the performance of turbocharger at low loads. The primary reason for such pattern is that with decreasing load the scavenge air pressure drops. When the pressure drops below a preset in turbocharger value, auxiliary blowers are started up to supply more air to the engine air intake to ensure sufficient air supply for combustion. This normally occurs around 25 to 35 percent load. In the CEAS engine calculation tool at inlet ISO condition this occurs at 35 percent load. The engine is then suddenly experiencing a surplus of intake air and this effectively cools the exhaust produced from the combustion, while the exhaust amount is increased.

Then, by following the previously described procedure, in accordance with the formulations 5.19 – 5.23 and Table 5.4, the obtained  $CO_2$  concentrations on a dry basis  $c_{d\ CO_2}$  have been converted into the wet concentrations  $c_{w\ CO_2}$  using the dry to wet correction factor  $k_W$  with further application of the IMO exhaust gas component coefficient  $u_{CO_2}$  designed to estimate the  $CO_2$  mass flow rate  $q_{m\ CO_2}$  as well as the  $CO_2$  specific. The  $CO_2$  prediction results for the reference 5S50ME-C engine are listed in Table 5.7.

Table 5.7  $CO_2$  calculation results for the reference engine 5S50ME-C.

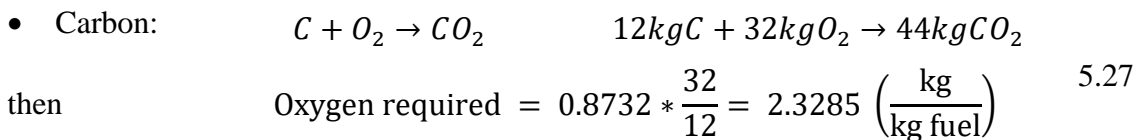
Engine load	Engine power	Specific fuel oil consumption	Exhaust gas mass flow rate (wet)	$CO_2$ concentration dry	Fuel mass flow rate	Intake air mass flow rate dry	Absolute humidity of intake air	Dry/wet correction factor	$CO_2$ concentration wet	IMO exhaust gas component coefficient	$CO_2$ mass flow rate	$CO_2$ specific
%	$P_B$	$SFOC$	$q_{mew}$	$c_{d\ CO_2}$	$q_{mf}$	$q_{mad}$	$H_a$	$k_W$	$c_{w\ CO_2}$	$u_{CO_2}$	$q_{m\ CO_2}$	-
	$kW$	$g/kWh$	$kg/h$	%	$kg/h$	$kg/h$	$g/kg$	-	%	-	$kg/h$	$g/kWh$
100	7150	166.8	57600	4.48	1193	56407	0.520	0.972	4.36	0.001517	3807.23	532.48
95	6793	165.6	55800	4.36	1125	54675	0.548	0.974	4.24		3591.28	528.67
90	6435	164.6	53640	4.27	1059	52581	0.562	0.975	4.16		3381.64	525.51
85	6078	163.9	51840	4.15	996	50844	0.567	0.976	4.04		3180.68	523.31
80	5720	163.3	49320	4.09	934	48386	0.565	0.976	3.99		2982.55	521.43
75	5363	162.9	47160	3.99	874	46286	0.560	0.977	3.90		2789.80	520.19
70	5005	162.8	44640	3.93	815	43825	0.554	0.977	3.84		2602.19	519.92
65	4648	163.5	42120	3.89	760	41360	0.551	0.978	3.80		2427.18	522.20
60	4290	164.4	39600	3.84	705	38895	0.554	0.978	3.75		2252.79	525.13
55	3933	165.5	36720	3.82	651	36069	0.566	0.978	3.73		2079.32	528.69
50	3575	166.7	33840	3.79	596	33244	0.590	0.978	3.71		1903.94	532.57
45	3218	168.0	30960	3.76	541	30419	0.629	0.978	3.68		1727.37	536.78
40	2860	169.4	27720	3.76	484	27236	0.687	0.978	3.68		1548.13	541.31
35	2503	170.8	24480	3.76	428	24052	0.765	0.978	3.68		1366.22	545.83
30	2145	171.8	25200	3.14	369	24831	0.869	0.983	3.08		1178.56	549.45
25	1788	173.8	21240	3.14	311	20929	1.000	0.983	3.08		993.94	555.89

- Excess air

In stoichiometric combustion, when  $O_2$  appears in the exhaust gas, it usually indicates that larger amount of air (20.9 percent of which is  $O_2$ ) has been supplied for the combustion reaction than it is theoretically required to complete combustion. Alternatively, the deficiency of air means that there are not enough oxygen molecules to completely form  $CO_2$  with all of the carbon in the fuel leading to unwanted consequences when oxygen combines with carbon to form carbon monoxide  $CO$ .

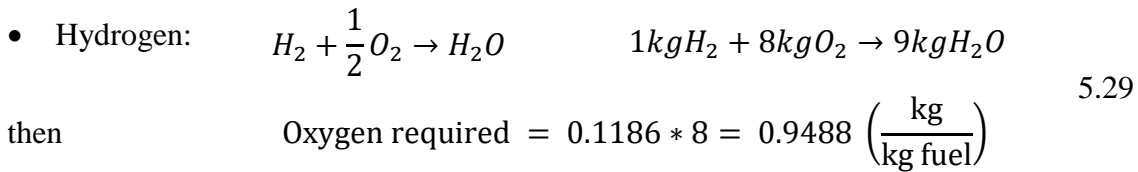
In actual combustion processes, it is common practice to use more air than the stoichiometric amount to increase the chances of complete combustion or to control the temperature of the combustion chamber. The amount of air in excess of the stoichiometric amount is termed excess air and is usually expressed in terms of the percent excess air over the stoichiometric air. In reality, the excess air required for gaseous fuels is typically slightly above 20 percent while significantly more may be needed for liquid and solid fuels (Woodyard 2009; Eastop & McConkey 1993).

Since the fuel used for simulations in this research is the MDO with the composition by mass as listed in Table 5.3, it is possible to estimate the amount of oxygen required for complete combustion using the following chemical equations:



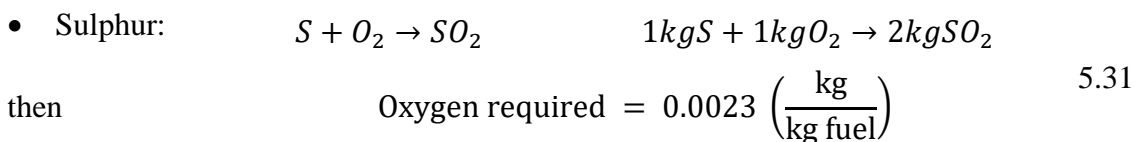
where the carbon content is 0.8732 kg per kg of fuel.

$$CO_2 \text{ produced} = 0.8732 * \frac{44}{12} = 3.2017 \text{ (kg } CO_2) \quad 5.28$$



where the hydrogen content is 0.1186 kg per kg of fuel.

$$H_2O \text{ (steam) produced} = 0.1186 * 9 = 1.0674 \text{ (kg } H_2O) \quad 5.30$$



where the sulphur content is 0.0023 kg per kg of fuel.

$$SO_2 \text{ produced} = 0.0023 * 2 = 0.0046 \text{ (kg } SO_2) \quad 5.32$$

The results are listed in Table 5.8. It is important to emphasise that oxygen in the fuel is considered as a negative quantity for this calculation procedure.

Table 5.8 The reference fuel analysis on required amount of combustion air.

Constituent	Mass Fraction	Atomic mass	Molecular grouping	Molecular mass	Oxygen required	Product	$\tilde{m}_i$	Product mass	Air breakdown by mass	
					kg/kg fuel		kg/kmol	$m_i$ kg/kg fuel		
C	0.8732	12	C	12	2.3285	CO <sub>2</sub>	44	3.2017	O <sub>2</sub>	0.233
H	0.1186	1	H <sub>2</sub>	2	0.9488	H <sub>2</sub> O	18	1.0674	N <sub>2</sub>	0.767
N	0.0007	14	N <sub>2</sub>	28		N <sub>2</sub>	28	0.0007		
O	0.005	16	O <sub>2</sub>	32	-0.0050	O <sub>2</sub>	32	0.0050		
S	0.0023	32	S	32	0.0023	SO <sub>2</sub>	64	0.0046		
Ash	0.0002	Total O <sub>2</sub>			3.2746					
Total	1									

As such, the total amount of O<sub>2</sub> required per kilogram of fuel equals to 3.28 kg, while the total air required per kilogram of fuel, also referred as stoichiometric air-fuel ratio, is 14.05 kg.

$$A/F_{ST} = \frac{3.2746}{0.233} = 14.05 \quad 5.33$$

where the air is assumed to contain 23.3 percent of O<sub>2</sub> by mass.

Since in reality the required theoretical air is rarely enough to conduct a complete combustion, in order to estimate an actual air fuel ratio, first the potential amount of excess air should be predicted.

An approximate estimate of excess air can be determined using the following relationship derived from basic chemistry considerations:

$$AIR_{EXCESS} = \frac{c_{d_{O_2}}(\%)}{20.9 - c_{d_{O_2}}(\%)} \quad 5.34$$

where  $c_{d_{O_2}}$  is the oxygen concentration on a dry basis in the exhaust gas (actual air), 20.9 is the normal concentration of O<sub>2</sub> in the air by volume (stoichiometric air).

Therefore, it is possible to approximate the amount of excess air used in combustion during engine trials provided in the NO<sub>x</sub> technical file of the 7S50MC-C engine. The calculation results are listed in Table 5.9 while the initial oxygen concentrations  $c_{d_{O_2}}$  are taken from Table 5.2.

Table 5.9 The excess air approximation results for 7S50MC-C engine.

Engine load	$O_2$	Excess air
%	%	ratio
100	15.23	2.69
75	15.95	3.22
50	16.15	3.4
25	16.58	3.84

Based on predicted excess air supply for each load, the actual air-fuel ratios estimated using the following procedure:

$$A/F_{ACT} = A/F_{ST} + A/F_{ST} * AIR_{EXCESS} \quad 5.35$$

where  $A/F_{ST}$  is the stoichiometric air-fuel ratio and  $AIR_{EXCESS}$  is the excess air ratio estimated for each load.

Thus, it is possible to calculate the amount of  $N_2$  and  $O_2$  products supplied by mass for combustion with the influence of excess air as well as to find the overall mass of products at each engine load using the following relationships based on the basic chemistry considerations:

$$\text{Nitrogen:} \quad m_{N_2AIR} = 0.767 A/F_{ACT} + m_{N_2} \quad 5.36$$

$$\text{Oxygen:} \quad m_{O_2AIR} = 0.233 A/F_{ACT} - O_{2TOTAL} \quad 5.37$$

$$\text{Total mass:} \quad m_{TOTAL} = m_{CO_2} + m_{H_2O} + m_{N_2EXC AIR} + m_{O_2EXC AIR} + m_{SO_2} \quad 5.38$$

where

- $m_{N_2}$  is the mass of exhaust nitrogen without the influence of excess air;
- $O_{2TOTAL}$  is the total amount of  $O_2$  required per kilogram of fuel;
- $m_{N_2AIR}$  and  $m_{O_2AIR}$  are the amounts of nitrogen and oxygen with respect to the excess air obtained for each load;
- $m_{CO_2}$ ,  $m_{H_2O}$ ,  $m_{SO_2}$  are the product masses of carbon dioxide, steam and sulphur dioxide per kg of fuel respectively.

The results of this calculation procedure based on the  $NO_x$  technical file data of the 7S50MC-C engine are tabulated in Table 5.10.

In Table 5.11 the amount of substance ( $n$ ) in kmol per kilogram of fuel is given by equation (5.39).

$$n = \frac{m}{\tilde{m}} \quad 5.39$$

where  $\tilde{m}$  is the molar mass of each product in kg/kmol and  $m$  is the products mass in kg/kg fuel.

The total amount of the substance on a wet basis is calculated by summing up all of the amounts of substances while the total amount of the substance of dry products is obtained by subtracting the amount of substance of  $H_2O$  from the total amount on a wet basis.

Table 5.10 Masses of exhaust gas products with excess of  $O_2$ .

Engine load	Stoichiometric A/F ratio	Excess air ratio	Actual A/F ratio	Product mass with excess $O_2$ <i>kg/kg fuel</i>					Total mass <i>kg/kg fuel</i>
%		$AIR_{EXCESS}$		$m_{CO_2}$	$m_{H_2O}$	$m_{N_2AIR}$	$m_{O_2AIR}$	$m_{SO_2}$	$m_{TOTAL}$
100	14.05	2.69	51.80	3.20	1.07	39.73	8.81	0.0046	52.80
75	14.05	3.22	59.34	3.20	1.07	45.51	10.55		60.34
50	14.05	3.4	61.84	3.20	1.07	47.43	11.13		62.84
25	14.05	3.84	67.99	3.20	1.07	52.15	12.57		68.99

Table 5.11 The amount of substances of exhaust products on a wet and dry basis.

Engine load	Amount of substance $n_i = \frac{m_i}{\tilde{m}_i}$ <i>kmol/kg fuel</i>					Total amount of substance <i>kmol/kg fuel</i>	
%	$n_{CO_2}$	$n_{H_2O}$	$n_{N_2}$	$n_{O_2}$	$n_{SO_2}$	$n_{WET}$	$n_{DRY}$
100	0.073	0.059	1.42	0.28	0.000072	1.83	1.77
75	0.073	0.059	1.63	0.33	0.000072	2.09	2.03
50	0.073	0.059	1.69	0.35	0.000072	2.17	2.12
25	0.073	0.059	1.86	0.39	0.000072	2.39	2.33

The following Table 5.12 gives the proportion of each constituent on the wet and dry basis by the amount of substance from the previous Table 5.11 expressed as a percentage of the total amount of substance, also referred as concentrations, of wet and dry products respectively.

Table 5.12 The proportion of exhaust products on wet and dry basis.

Engine load	Wet %					Dry %				
	%	$c_{w\ CO_2}$	$c_{w\ H_2O}$	$c_{w\ N_2}$	$c_{w\ O_2}$	$c_{w\ SO_2}$	$c_{d\ CO_2}$	$c_{d\ H_2O}$	$c_{d\ N_2}$	$c_{d\ O_2}$
100	3.98	3.25	77.71	15.05	0.0039	4.12	-	80.3	15.56	0.0041
75	3.49	2.84	77.87	15.80	0.0034	3.59	-	80.2	16.26	0.0035
50	3.35	2.73	77.92	16.00	0.0033	3.44	-	80.1	16.45	0.0034
25	3.05	2.48	78.01	16.45	0.0030	3.13	-	80.0	16.87	0.0031

This procedure allows the prediction of the approximate concentrations of  $CO_2$  and other products on a wet and dry basis with the requirement that the initial dry concentrations of  $O_2$  are known in order to roughly estimate the amount of excess air for each load using equation 5.34. However, since the concentrations of dry  $CO_2$  are already known from the previous calculations based on the Carbon Balance method, the concentrations of  $O_2$ ,  $N_2$  and  $H_2O$  as well as the amount of excess air, which are necessary for further estimations of  $NO_x$  and  $SO_x$ , can be estimated using the inverse procedure.

Figure 5.15 demonstrated the results of dry  $O_2$  predictions based on the inverse fuel analysis procedure performed in accordance with the dry  $CO_2$  concentrations from the  $NO_x$  technical file of the 7S50MC-C engine. The obtained dry  $O_2$  concentrations are compared with the relevant concentrations listed in the same engine documentation, showing almost identical figures.

Table 5.13 demonstrates the final fuel analysis simulation results for the reference engine 5S50ME-C based on the CEAS engine calculation tool (Module 2). In this table, an expression of the excess air is also referred as  $\lambda$  (the stoichiometric ratio), which relationship with the excess air is described by equation 5.40. The rest of the Table 5.13 is calculated in accordance with the previously explained fuel dry/wet proportions analysis.

$$\lambda = AIR_{EXCESS} + 1 \quad 5.40$$

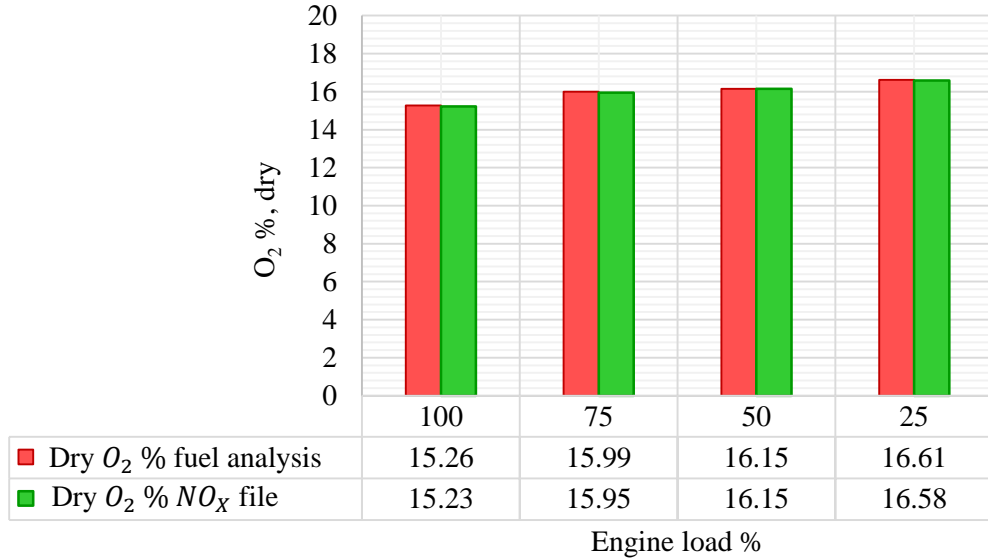


Figure 5.15 The comparison analysis of the dry  $O_2$  concentrations calculated using the reversed fuel analysis procedure and the dry  $O_2$  concentrations listed in the  $NO_x$  technical file of 7S50MC-C.

Table 5.13 The results of the inverted fuel analysis procedure for the reference 5S50ME-C engine.

Engine load	Brake power	Excess air ratio	Actual A/F	$\lambda$	$\dot{m}_{O_2}$	$\dot{m}_{N_2}$	$n_{O_2}$	$n_{N_2}$	Total $\eta_{WET}$	Total $\eta_{DRY}$	$O_2$ Dry	$N_2$ Dry	$H_2O$
%	kW		-	-	kg/kg fuel		$n_i = m_i/\dot{m}_i$				%	%	%
100	7150	2.39	48	3.39	7.84	36.57	0.24	1.31	1.68	1.62	15.08	80.44	3.52
95	6793	2.49	49	3.49	8.14	37.58	0.25	1.34	1.73	1.67	15.24	80.40	3.43
90	6435	2.56	50	3.56	8.38	38.38	0.26	1.37	1.76	1.71	15.36	80.37	3.36
85	6078	2.66	51	3.66	8.71	39.45	0.27	1.41	1.81	1.75	15.52	80.33	3.27
80	5720	2.71	52	3.71	8.89	40.04	0.28	1.43	1.84	1.78	15.60	80.31	3.22
75	5363	2.80	53	3.80	9.16	40.94	0.29	1.46	1.88	1.82	15.72	80.28	3.15
70	5005	2.86	54	3.86	9.35	41.56	0.29	1.48	1.91	1.85	15.80	80.26	3.11
65	4648	2.90	55	3.90	9.50	42.05	0.30	1.50	1.93	1.87	15.86	80.25	3.07
60	4290	2.95	56	3.95	9.67	42.60	0.30	1.52	1.96	1.90	15.93	80.23	3.03
55	3933	2.97	56	3.97	9.73	42.80	0.30	1.53	1.96	1.91	15.95	80.22	3.02
50	3575	3.00	56	4.00	9.81	43.08	0.31	1.54	1.98	1.92	15.99	80.22	3.00
45	3218	3.03	57	4.03	9.93	43.45	0.31	1.55	1.99	1.93	16.03	80.21	2.97
40	2860	3.03	57	4.03	9.91	43.41	0.31	1.55	1.99	1.93	16.02	80.21	2.98
35	2503	3.03	57	4.03	9.92	43.44	0.31	1.55	1.99	1.93	16.03	80.21	2.97
30	2145	3.82	68	4.82	12.51	51.97	0.39	1.86	2.38	2.32	16.85	80.01	2.49
25	1788	3.82	68	4.82	12.50	51.94	0.39	1.85	2.38	2.32	16.85	80.01	2.49

- Nitrogen oxides ( $NO_x$ )

While nitric oxide ( $NO$ ) and nitric dioxide ( $NO_2$ ) are normally grouped together as  $NO_x$  emissions, nitric oxide ( $NO$ ) is the predominant nitrogen component formed inside the engine cylinder. The principal source of  $NO$  is the oxidation of atmospheric nitrogen at high temperatures (Heywood 1985). However, if the fuel contains a significant amount of nitrogen, its oxidation becomes an additional source of  $NO$ , which is particularly common for diesel fuels.

In a number of publications, including (Heywood 1985; Flagan & Seinfeld 1988; Flynn 2003), a general principle of thermal  $NO$  formation is described by the ‘extended Zeldovich’ mechanism influenced by a local combustion environment. This approach has been successfully verified by experimental analysis and considered to be an effective method for  $NO_x$  prediction. For instance, a multi-zone combustion diagnostic model developed by (Egnell 1998), is able to estimate  $NO$  at the combustion zone and post-combustion zones separately by means of the Zeldovich mechanism based on the measured pressure data, which is necessary to calculate the local temperatures, and the arbitrarily chosen stoichiometric ratio  $\lambda$  in each zone.

In general, the combustion diagnostic approaches could be very precise in predicting  $NO_x$  emissions and other species, mainly due to a detailed simulation of the thermodynamic processes. However, since the cylinder space is divided into a number of zones, while each zone has to solve a set of differential equations, the overall model algorithm is complicated and requires extensive initial data and considered to be very time-consuming.

In addition, a number of computational methods are available to approximate  $NO_x$  concentrations in the exhaust gas. The choice of the right method is, to a large extent, influenced by the availability of the required data to perform a simulation. For instance, black box simulation models, based on advanced non-linear approximations using mathematical algorithms, or artificial neural networks require an extensive engine performance dataset or direct measurements. A neural network based  $NO_x$  prediction models outlined in (Kristensen 2012) require real-time inputs of the inlet pressure, the inlet temperature, the engine speed as well as the fuel rack position supported by several initial data points in order to successfully train the model.

Alternatively, the analytical approaches based on polynomial regression analysis can be used for  $NO_x$  prediction purposes and the accuracy level of such methods can be high. For instance, in (Murphy et al. 2013), a multi linear regression method is used to develop a

formula for main engine operating on the propeller law for the subject ship operating with the fixed pitch propeller. This formula reflects the relationship of the percentage of power and the percentage of speed with the  $NO_x$  emission factor while the predicted results from this model have been statistically analysed to ascertain the simulation accuracy.

In the case of this study, since the available initial data was limited, the multi-linear regression based analytical approach based on (Freund & Wilson 2003) has been used for prediction of dry  $NO_x$  concentrations in the exhaust gas flow.

Since the  $NO_x$  concentration in the exhaust gas flow is not only influenced by the fuel consumption and fuel composition, but also by the engine speed, local combustion temperatures as well as oxygen concentration, the following model inputs have been selected:

Table 5.14  $NO_x$  multi linear regression model inputs.

Model inputs	Description	Metric
$LOAD_{\%}$	The engine load	%
$RPM_{\%}$	The engine rotational speed	%
$SFOC$	Specific fuel oil consumption	$g/kWh$
$T_{OUT}$	The exhaust gas temperature	$^{\circ}C$
$\lambda$	Lambda	-

In this model, the exhaust gas temperature  $T_{OUT}$  reflects the fluctuations of the combustion temperature which directly influences the thermal  $NO$  formation, while lambda  $\lambda$  represents the changes in oxygen concentration. The chemical fuel composition is not covered in this formula since the fuel is considered to be constant in this study. All the model inputs are estimated in accordance with the Computational Engine Application System (CEAS) engine calculation tool (Module 2), while lambda values are predicted using chemical stoichiometry previously explained in this chapter. As such, with respect to the parameters listed in Table 5.14, the multi linear model for  $NO_x$  concentration on a dry basis can be written as follows:

$$c_{d_{NO_x}} = \beta_0 + \beta_{LOAD_{\%}}LOAD_{\%} + \beta_{RPM_{\%}}RPM_{\%} + \beta_{SFOC}SFOC + \beta_{T_{OUT}}T_{OUT} + \beta_{\lambda}\lambda + \varepsilon \quad 5.41$$

where

- $c_{d_{NO_x}}$  is the dependent or response variable representing the  $NO_x$  concentrations on a dry basis;

- the inputs from Table 5.14 are the independent variables changing for each load;
- $\beta_{input}$  is the regression coefficients for each independent variable;
- $\beta_0$  is the intercept;
- $\varepsilon$  is the random error.

In order to obtain the regression formula, the initial  $NO_x$  points from the  $NO_x$  technical file of the 7S50MC-C engine measured in  $ppm$ , have been expanded for each engine load in accordance with the engine simulation module using the cubic spline interpolation method as shown in Figure 5.16.

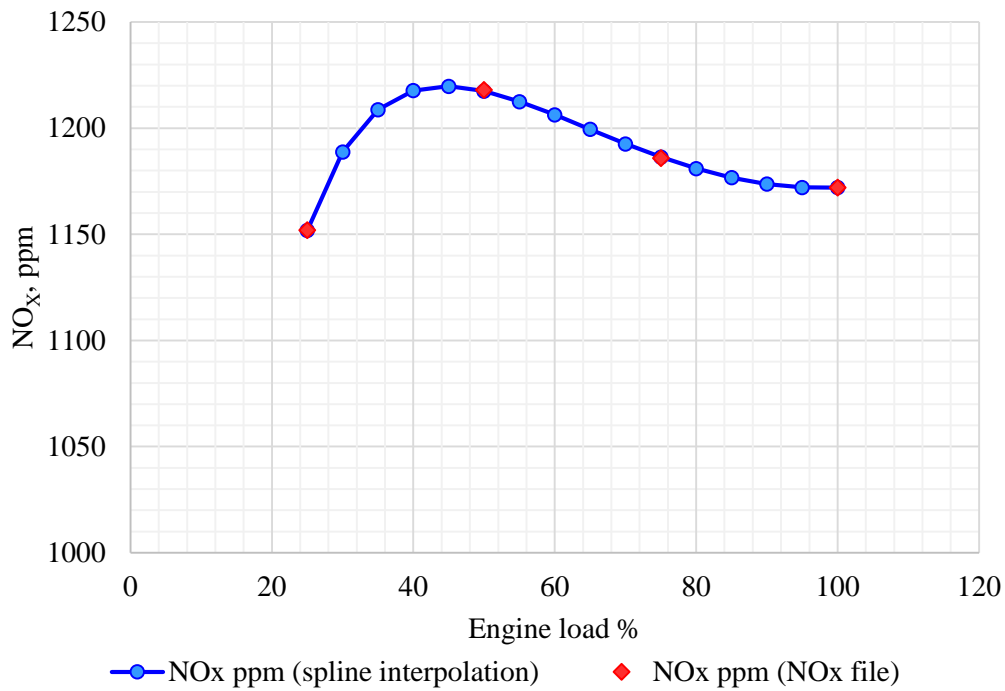


Figure 5.16 Expanded initial  $NO_x$  dataset based on cubic spline interpolation.

Subsequently, a multi-linear regression formula has been derived for the calculation of  $NO_x$  emissions concentrations and the following regression statistics have been calculated:

Table 5.15 Regression statistics.

Multiple R	R Square	Adjusted R Square	Standard Error	Observations
0.99	0.98	0.97	3.48	16

The resulting regression formula for  $NO_x$  concentration prediction is presented next:

$$c_{dNO_x} = -2552 - 12.11LOAD_{\%} + 17.67RPM_{\%} + 1.08SFOC + 1.45T_{OUT} + 2.55\lambda \quad 5.42$$

The validation of  $NO_x$  model output for 7S50MC-C engine is shown in Figure 5.17.

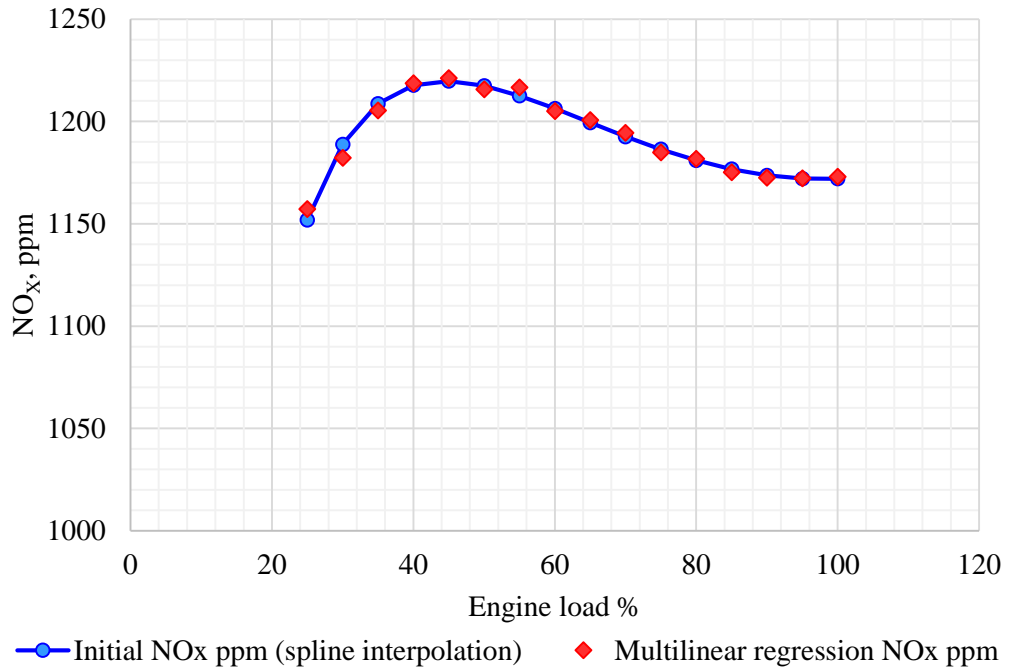


Figure 5.17 The validation of  $NO_x$  model output for 7S50MC-C engine: the  $NO_x$  technical file based interpolated volumetric  $NO_x$  concentrations vs. the  $NO_x$  model output.

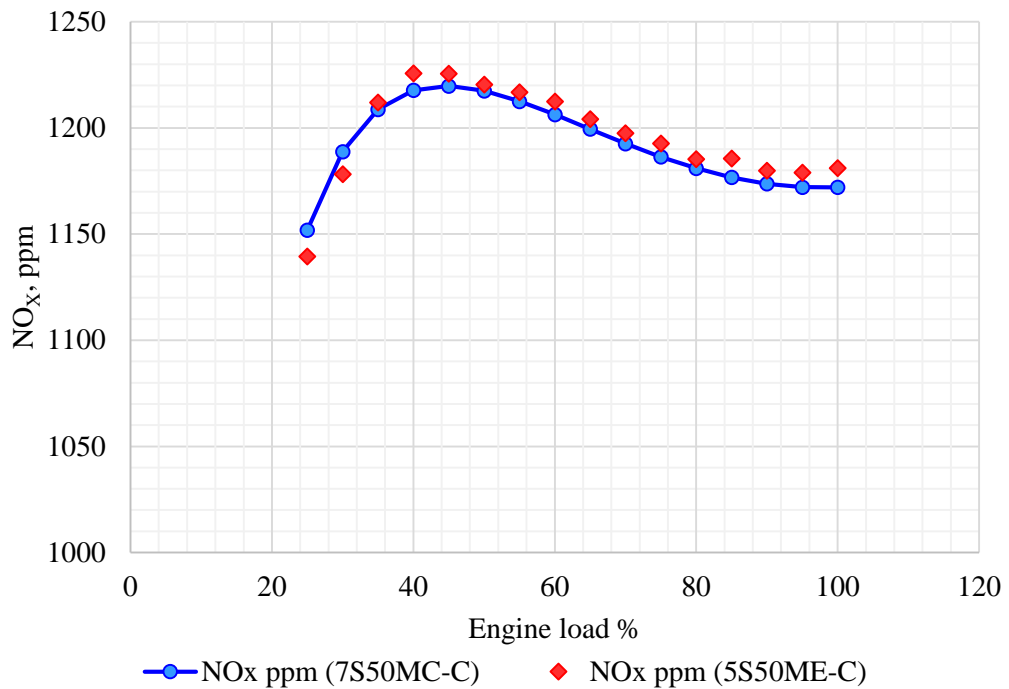


Figure 5.18 Resulted  $NO_x$  concentrations of 5S50MC-C engine compared to initial  $NO_x$  concentrations of 7S50MC-C engine.

In accordance with the obtained regression formula, the  $NO_x$  concentrations for the reference 5S50ME-C engine have been estimated and compared with the original (expanded)  $NO_x$  dataset of 7S50MC-C as shown in Figure 5.18. Notably, the resulting  $NO_x$

concentrations of the 5S50ME-C engine are slightly higher than of 7S50MC-C engine due to generally increased exhaust gas temperatures  $T_{OUT}$  as shown in Figure 5.19 caused by minor changes in the ratio of the intake air flow to the fuel flow.

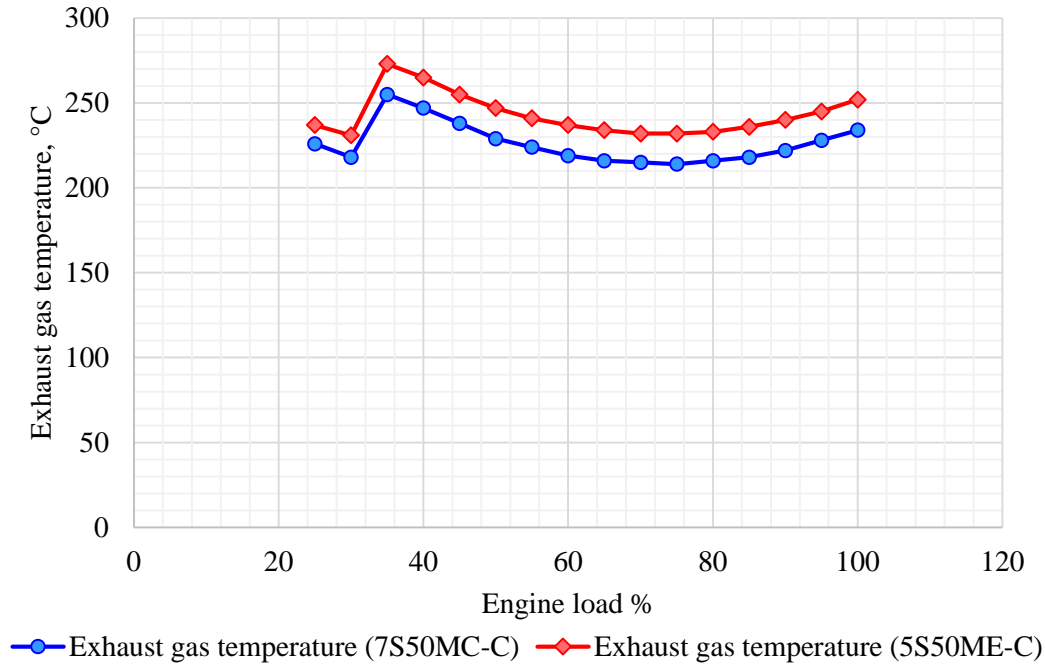


Figure 5.19 The comparison of exhaust gas temperatures of 7S50MC-C and 5S50ME-C engines.

After the  $NO_x$  concentrations on a dry basis for the reference engine 5S50ME-C have been obtained using the multi-linear regression, the  $NO_x$  concentrations on a wet basis as well as the  $NO_x$  mass flow rate and  $NO_x$  specific can be calculated. The results are tabulated in Table 5.16.

The  $NO_x$  concentrations on a wet basis  $c_{wNO_x}$  are estimated by multiplying the  $NO_x$  concentrations on a dry basis by the dry/wet correction factor  $k_w$ , which has been previously calculated using the equation (5.20).  $NO_x$  humidity factor  $k_{hd}$  has been interpolated for each load using the cubic spline interpolation, based on the available points from the 7S50MC-C engine shop tests documentation. It is important to emphasise, that the  $k_{hd}$  values have been kept constant in the following case studies since the ambient conditions are considered to be unchanged. Hence, based on the obtained  $k_{hd}$  values, the  $NO_x$  mass flow rate  $q_{mNO_x}$  can be estimated for each engine load as follows:

$$q_{mNO_x} = u_{NO_x} c_{wNO_x} q_{mew} k_{hd} \quad 5.43$$

where  $u_{NO_x}$  is the IMO exhaust gas  $NO_x$  coefficient ( $u_{NO_x} = 0.001586$ ) and  $q_{mew}$  is the exhaust gas mass flow rate in kg/h.

Table 5.16  $NO_x$  calculation results for the reference engine 5S50ME-C.

Engine load	Engine power	RPM SMCR	Rotational speed	Specific fuel oil consumption	Exhaust gas temperature	Lambda	$NO_x$ concentration dry (regression)	Exhaust gas mass flow rate (wet)	Fuel mass flow rate	Intake air mass flow rate dry	Absolute humidity of intake air	Dry/wet correction factor	$NO_x$ concentration wet	IMO exhaust gas component coefficient	$NO_x$ humidity factor	$NO_x$ mass flow rate	$NO_x$ specific
%	$P_B$	%	$RPM$	$SFOC$	$T_{OUT}$	$\lambda$	$c_{dNO_x}$	$q_{mew}$	$q_{mf}$	$q_{mad}$	$H_a$	$k_W$	$c_{wNO_x}$	$u_{NO_x}$	$k_{hd}$	$q_{mNO_x}$	-
	$kW$		$r/min$	$g/kWh$	$^{\circ}C$	-	$Ppm$	$kg/h$	$kg/h$	$kg/h$	$g/kg$	-	$ppm$	-	-	$kg/h$	$g/kWh$
100	7150	100	127	166.8	252	3.39	1181	57600	1193	56407	0.520	0.972	1138	0.001586	0.873	91	13.44
95	6793	98	125	165.6	245	3.49	1179	55800	1125	54675	0.548	0.974	1140		0.871	88	13.68
90	6435	97	123	164.6	240	3.56	1180	53640	1059	52581	0.562	0.975	1142		0.869	84	13.96
85	6078	95	120	163.9	236	3.66	1186	51840	996	50844	0.567	0.976	1146		0.867	82	14.23
80	5720	93	118	163.3	233	3.71	1185	49320	934	48386	0.565	0.976	1151		0.865	78	14.55
75	5363	91	115	162.9	232	3.80	1193	47160	874	46286	0.560	0.977	1157		0.864	75	14.85
70	5005	89	113	162.8	232	3.86	1198	44640	815	43825	0.554	0.977	1163		0.863	71	15.19
65	4648	87	110	163.5	234	3.90	1204	42120	760	41360	0.551	0.978	1171		0.862	67	15.58
60	4290	84	107	164.4	237	3.95	1212	39600	705	38895	0.554	0.978	1178		0.862	64	15.84
55	3933	82	104	165.5	241	3.97	1217	36720	651	36069	0.566	0.978	1184		0.863	59	16.23
50	3575	79	101	166.7	247	4.00	1220	33840	596	33244	0.590	0.978	1189		0.864	55	16.45
45	3218	77	97	168.0	255	4.03	1226	30960	541	30419	0.629	0.978	1192		0.866	51	16.67
40	2860	74	94	169.4	265	4.03	1226	27720	484	27236	0.687	0.978	1190		0.869	45	16.75
35	2503	70	90	170.8	273	4.03	1212	24480	428	24052	0.765	0.978	1181		0.873	40	16.75
30	2145	67	85	171.8	231	4.82	1178	25200	369	24831	0.869	0.983	1167		0.879	41	19.83
25	1788	63	80	173.8	237	4.82	1139	21240	311	20929	1.000	0.983	1131	0.885	34	19.65	

- Sulphur Dioxide ( $SO_2$ )

The formation of sulphur dioxide  $SO_2$  in the exhaust gas is caused by the oxidation of sulphur content in fuel during the combustion process, where the concentration level of  $SO_2$  is directly connected with the fuel consumption rate and the concentration of sulphur in the burning fuel. It is important to outline that a fraction of the sulphur is further oxidized beyond  $SO_2$  to form  $SO_3$ , while both are referred as  $SO_x$ . However, because the concentrations of  $SO_3$  are generally low and their formation is directly influenced by the  $SO_2$  emissions, for the purpose of this study only the  $SO_2$  component was considered.

Although the initial concentrations of  $SO_2$  have not been provided in the  $NO_x$  technical file of 7S50MC-C engine, it is still possible to predict the concentrations of  $SO_2$  in the exhaust gas flow using the  $SO_2(ppm)/CO_2(\%)$  ratio method outlined in (MEPC.184(59) Annex 9 2010). In this method, the relationship within the  $SO_2/CO_2$  ratio has been determined by simple examination of the respective carbon contents per unit mass of distillate and residual fuel. Since for this group of hydrocarbon fuels the carbon content as a percentage of mass remains closely similar, whereas the hydrogen content differs, it has been concluded that for a given carbon consumption by combustion there will be a consumption of sulphur in proportion to the sulphur content of the fuel, or, in other words, a constant ratio between carbon and sulphur adjusted for the molecular weight of oxygen from combustion. Based on that the fuel oil sulphur contents correspond to the emissions ratio (Table 5.17).

Table 5.17 Fuel oil sulphur contents and corresponding emissions level.

Fuel oil sulphur content	% (mass)	4.50	3.50	1.50	1.00	0.50	0.10
Emission ratio	$SO_2(ppm)/CO_2(\%)$	195.0	151.7	65.0	43.3	21.7	4.3

Since the concentrations of  $CO_2$  on a dry basis have been previously calculated, while the sulphur concentration in the reference fuel is 0.23 percent (Table 5.3), the  $SO_2$  concentrations in the dry exhaust can be estimated by interpolation of the correct emission ratio to the fuel oil sulphur content and further multiplication by the  $CO_2$  concentrations on a dry basis for each engine load (5.44).

$$c_{d_{SO_2}} = 9.9811c_{d_{CO_2}} \quad 5.44$$

where 9.9811 is the  $SO_2(ppm)/CO_2(\%)$  emission ratio interpolated in accordance with the fuel sulphur content (0.23 percent).

Similarly to the previous calculations, the  $SO_2$  concentrations on a wet basis were estimated by applying the dry/wet correction factor  $k_w$ . To estimate the  $SO_2$  mass flow rate and  $SO_2$

specific rate, the total exhaust gas density, in other words, the molecular weights  $MW_{WET}$  of all previously estimated exhaust gas products on wet basis for a range of loads were calculated using simple chemical stoichiometry (Flagan & Seinfeld 1988). Hence, by applying the same calculation principle as in (MEPC.177(58) Annex 14 2010), the  $SO_2$  mass flow rates in  $g/h$  were estimated for each load as follows:

$$q_{m_{SO_2}} = c_{w_{SO_2}} q_{mew} \frac{MW_{SO_2}}{MW_{WET}} / 1000 \quad 5.45$$

where

- $c_{w_{SO_2}}$  is the concentration of  $SO_2$  on a wet basis ( $ppm$ );
- $q_{mew}$  is the exhaust gas flow rate ( $kg/h$ );
- $\frac{MW_{SO_2}}{MW_{WET}}$  is the ratio  $u_{SO_2}$  between density of exhaust component and density of exhaust gas, calculated the same way as in (MEPC.177(58) Annex 14 2010);
- $MW_{SO_2}$  is equal to 64.064 ( $g/mol$ ).

The  $SO_2$  calculation results for the reference engine 5S50ME-C are listed in Table 5.18.

Table 5.18  $SO_2$  prediction results for the reference engine 5S50ME-C.

Engine load	Engine power	Specific fuel oil consumption	Exhaust gas mass flow rate (wet)	Fuel mass flow rate	$SO_2$ (ppm)/ $CO_2$ (%)	$SO_2$ concentration dry	Dry/wet correction factor	$SO_2$ concentration wet	Exhaust gas density	Exhaust gas ratio	$SO_2$ mass flow rate	$SO_2$ specific
%	$P_B$ $kW$	$SFOC$ $g/kWh$	$q_{mew}$ $kg/h$	$q_{mf}$ $kg/h$		$c_{d_{SO_2}}$ $ppm$	$k_W$ -	$c_{w_{SO_2}}$ $ppm$	$MW_{WET}$ $kg/kmol$	$u_{SO_2}$ -	$q_{m_{SO_2}}$ $kg/h$	- $g/kWh$
100	7150	166.8	57600	1193	9.9811	43.50	0.972	42.30	28.94	0.002184	5.39	0.75
95	6793	165.6	55800	1125		42.44	0.974	41.31	28.73	0.002184	5.14	0.76
90	6435	164.6	53640	1059		41.34	0.975	40.27	28.33	0.002186	4.89	0.76
85	6078	163.9	51840	996		40.57	0.976	39.55	28.36	0.002185	4.63	0.76
80	5720	163.3	49320	934		39.79	0.976	38.81	28.36	0.002186	4.32	0.76
75	5363	162.9	47160	874		39.22	0.977	38.28	28.38	0.002186	4.08	0.76
70	5005	162.8	44640	815		38.66	0.977	37.76	28.39	0.002186	3.80	0.76
65	4648	163.5	42120	760		38.09	0.978	37.21	28.39	0.002187	3.54	0.76
60	4290	164.4	39600	705		37.91	0.978	37.06	28.42	0.002186	3.31	0.77
55	3933	165.5	36720	651		37.46	0.978	36.62	28.41	0.002187	3.03	0.77
50	3575	166.7	33840	596		37.44	0.978	36.60	28.42	0.002187	2.79	0.78
45	3218	168.0	30960	541		37.37	0.978	36.55	28.43	0.002186	2.55	0.79
40	2860	169.4	27720	484		37.53	0.978	36.70	28.44	0.002186	2.29	0.80
35	2503	170.8	24480	428		37.69	0.978	36.85	28.45	0.002185	2.03	0.81
30	2145	171.8	25200	369		31.68	0.983	31.14	28.53	0.002189	1.76	0.82
25	1788	173.8	21240	311		31.49	0.983	30.95	28.52	0.002190	1.48	0.83

## 5.4 Module 4: Energy Efficiency Design Index (EEDI) Calculator

The EEDI calculator module can be divided into two general sectors. The first sector is focused on the estimation of the attained EEDI index for the particular vessel, in this case, the reference oil products tanker. However, the developed program is multifunctional and is able to predict the attained EEDI index of any vessel that is covered by the latest guidelines (IMO 2014a). In addition, this sector includes an optional prediction of the weather correction factor  $f_w$  and the  $EEDI_{Weather}$  for bulk carriers, tankers and container ships in accordance with the (MEPC.1/Circ.796 2012). The second sector is designed to verify if the attained EEDI index complies with the reference (required) EEDI value for the particular time phase under the MEPC 65 guidelines, Annex 14 (IMO 2013). Figure 5.20 illustrates the program output reflecting the relationship between the attained and required EEDIs for the reference products tanker.

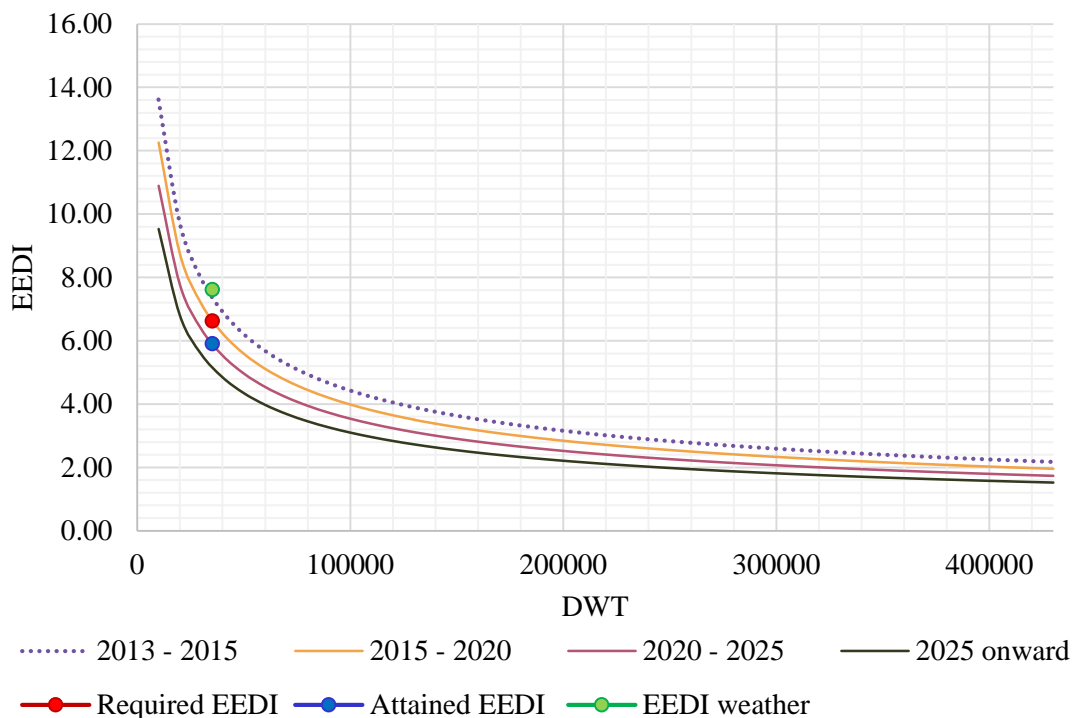


Figure 5.20 Attained and required EEDIs for the reference oil products tanker.

The actual attained EEDI of the reference ship equals to  $5.91 \text{ gCO}_2/tNm$ , while the current (2015 - 2020) required EEDI for such a ship's type and size is  $6.63 \text{ gCO}_2/tNm$ . Despite further reference line reductions by 10 percent every 5 years, the actual EEDI index of this products tanker satisfies the IMO recommendations for the current period. However, following the stringent regulations, such ship design arrangements are only permitted until 2020 and then will have to be improved.

## 6 Time Domain Voyage Simulation

Since the power requirements significantly increase in poor weather conditions influenced by both waves and wind, it is useful, at the design stage, to initially simulate the ship performance at sea as well as to predict changes of power in accordance with the potential fluctuations of weather. This will help to obtain a clear picture of what to expect in terms of fuel consumption and emissions footprint during a voyage.

The wind conditions are usually defined by the Beaufort number (*BN*), which was initially proposed by Admiral Beaufort in 1806. This scale has also been extended to give an indication of sea conditions for fully developed seas (Carlton 2012). This scale is not sufficiently accurate for detailed research; however it provides an understanding of the observed weather conditions. The Beaufort scale of wind speeds with respect to approximate wave heights, is shown in Table 6.1 (Molland et al. 2011).

Table 6.1 Beaufort scale (Molland et al. 2011).

Beaufort number <i>BN</i>	Description	Speed limits		Approximate wave height ( <i>m</i> )
		<i>knots</i>	<i>m/s</i>	
0	Calm	1	0.3	-
1	Light air	1-3	0.3-1.5	-
2	Light breeze	4-6	1.6-3.3	0.7
3	Gentle breeze	7-10	3.4-5.4	1.2
4	Moderate breeze	11-16	5.5-7.9	2.0
5	Fresh breeze	17-21	8.0-10.7	3.1
6	Strong breeze	22-27	10.8-13.8	4.0
7	Near gale	28-33	13.9-17.1	5.5
8	Gale	34-40	17.2-20.7	7.1
9	Strong gale	41-47	20.8-24.4	9.1
10	Storm	48-55	24.5-28.4	11.3
11	Violent storm	56-63	28.5-32.6	13.2
12	Hurricane	64 and over	32.7 and over	-

Generally, ships may adopt the following operational regimes under poor weather conditions. The common way is to reduce speed in order to prevent structural and slamming damage or excessive accelerations (Molland et al. 2011). Alternatively, if the ship is operating on scheduled services, it is possible to maintain its speed at the required constant value while increasing the engine power. In such a case, a sufficient engine power sea-margin is required. However, many ships operate at their NCR while trying to maintain

their nominal service speed as high as possible to compensate the average speed losses associated with the rough weather conditions.

As such, the effects of waves and wind in service can be negotiated either by increasing the engine power to operate at the required ship's service speed as shown in the right diagram in Figure 6.1 or by reducing the ship's speed to keep the engine power and fuel consumption at a constant rate as shown on the left side of Figure 6.1.

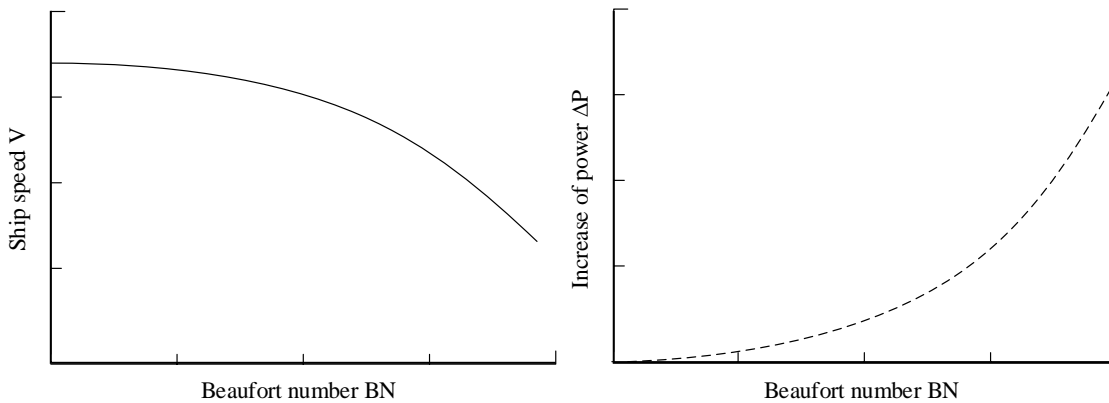


Figure 6.1 Typical service data relationships (Molland et al. 2011).

The influence of wind and waves on a ship's speed and power can be estimated by both theoretical and experimental approaches. The latter one may include wind tunnel tests performed for a particular ship type aiming to predict the impact of wind, while the effect of waves can be simulated via tank tests in a sea-keeping basis. Alternatively, typical voyage data can be analysed for a particular ship type.

From the theoretical side, the following numerical methods can be used to evaluate the potential ship behaviour at sea. For instance, the Aertssen's (Aertssen 1963) and Townsin and Kwon's (Townsin et al. 1980) regression-based approaches are designed to estimate the reduction rate of ship's speed influenced by a particular sea state condition. However, in this research "N.S.M.B Trial Allowances 1976" (de Jong & Fransen 1976) are used for ship performance simulation at realistic sea conditions. The N.S.M.B method has been selected mainly because it predicts the changes in engine power in accordance with changing Beaufort number, rather than reductions in ship's speed as in (Aertssen 1963) and (Townsin et al. 1980). The changes in power requirements due to changing Beaufort number are found to be more convenient for the estimation of the differences in fuel consumption and emissions footprint due to energy saving technologies.

The calculation procedure, based on the “N.S.M.B Trial Allowances 1976” (de Jong & Fransen 1976) method, begins with the estimation of the reference coefficient  $C_{P_{ref}}$  in accordance with the equation 6.1. In this case the coefficient  $C_{P_{ref}}$  corresponds to calm weather namely Beaufort number 0.

$$C_{P_{ref}} = 5.75 - 0.793\Delta^{\frac{1}{3}} + 12.3BN_{ref} + (0.0129L_{PP} - 1.864BN_{ref})\left(\frac{L_{PP}}{7}\right)^{\frac{1}{2}} \quad 6.1$$

where  $\Delta$  is the ship’s displacement tonnage,  $L_{PP}$  is the length between perpendiculars representing the length between the foreside of the stem and the aft of the rudder post at the vessel’s summer load,  $BN_{ref}$  is the reference Beaufort number (in this case  $BN_{ref} = 0$ ).

Then the coefficient  $C_{P_{BN_i}}$  has to be calculated for each  $BN$  in a similar way.

$$C_{P_{BN_i}} = 5.75 - 0.793\Delta^{\frac{1}{3}} + 12.3BN_i + (0.0129L_{PP} - 1.864BN_i)\left(\frac{L_{PP}}{7}\right)^{\frac{1}{2}} \quad 6.2$$

As such, the correction factor should be estimated as follows:

$$C_{P_{corr_{BN_i}}} = \frac{(1 + C_{P_{BN_i}}/100)}{(1 + C_{P_{ref}}/100)} \quad 6.3$$

Finally, the correction factor is applied to the engine power.

$$P_{B_{BN_i}} = C_{P_{corr_{BN_i}}} P_B \quad 6.4$$

The service power requirements for selection of operational speeds ranging from 12.5 – 16 knots based on the design load conditions have been simulated in accordance with the Beaufort numbers 1 – 5 as illustrated in Figure 6.2. In this case, the differences in power requirements for calm weather conditions at  $BN = 0$  and, for instance, fresh breeze  $BN = 5$  at the design speed of 14.6 knots is approximately 16 percent indicating that a sufficient engine service margin has to be reserved to operate in such conditions. It should be noted that the engine service margin for this study has been set at 15 percent as stated above in the engine simulation module and which is normal practice for many shipowners.

As such, the voyage simulation model will predict the power increase due to changes of Beaufort number ( $BN$ ) using the trial allowances approach. However, in order to simulate the voyage as close to reality as possible, the following uncertainties should be taken into account: the distribution of weather fluctuations, the duration of voyage as well as

corresponding ship service speeds. To achieve these, it was decided to incorporate the ship's service data covering the period from January 2005 until October 2009. The data set includes the information about changing sea states with corresponding speed and engine power. However, first, it is necessary to conduct a voyage analysis to assess the influence of wind and waves on propulsive power while filtering the data points to avoid uncertainties in trends.

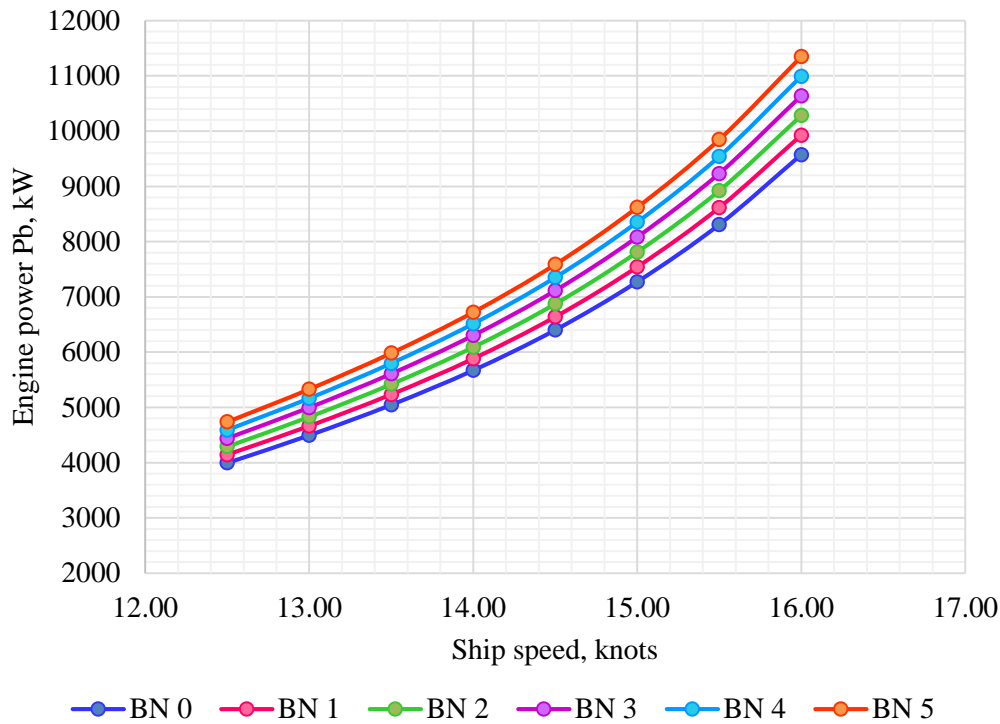


Figure 6.2. The effect of weather on ship's power requirements based on the trial allowances simulation model.

Only whole days are usually considered in the service analysis, while days during which large variations in speed, power or revolutions occur should be neglected. In addition, since the reference service data only contains the sea states up to Beaufort number 5, making it unclear whether the higher values were excluded or not, the final data has been filtered in accordance with the following criteria:

- Beaufort scale equals to or lower than 5;
- Period observed is in range of 22 – 27 hours;
- Water depth equals to or higher than 80m;
- Displacement corresponds to loaded conditions since the number of ballast points was too insignificant.

Changes of displacement were obtained via the regression analysis of the measured mean draughts compared with the draughts available in the model test report and associated with them displacements. In addition, since the ship's speed measured through water using shipborne logs can be inaccurate due to the influence of the boundary layer, ship motions or tide (Molland et al. 2011), only the speeds observed via the Global Positioning System (GPS) are considered.

As outlined in (Carlton 2012), by analysing the relationship between the Admiralty coefficient  $A_C$  (equation 6.5) and the apparent slip  $S_a$  (equation 6.6) as shown in Figure 6.3, it is possible to detect potential outliers among the observations as well as to assess the data quality, since  $A_C - S_a$  relationship represents a convergence in the data.

$$A_C = \frac{\Delta^{2/3} V_S^3}{P_B} \quad 6.5$$

where  $\Delta$  is the displacement,  $V_S$  is the speed and  $P_B$  is the engine power.

$$S_a = 1 - 30.86 \left( \frac{V_S}{PN} \right) \quad 6.6$$

where  $P$  is the propeller pitch,  $N$  is the rotational speed, while  $V_S$  is defined in m/s.

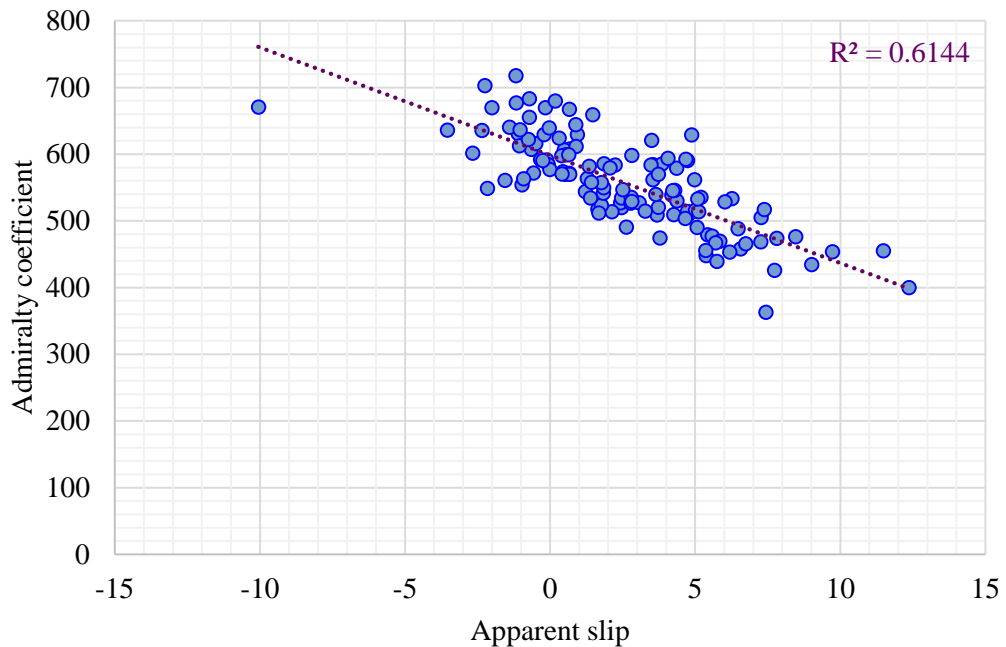


Figure 6.3 Unfiltered Admiralty coefficient versus apparent slip.

Several data points from the observations, that weren't fitting well into the convergence, were carefully examined and, if a discrepancy detected, the outliers were removed from the

dataset. In this case, it was frequently deemed that the outliers were due to misprints, such as unrealistically high speed or power values. The finalised sample is shown in Figure 6.4.

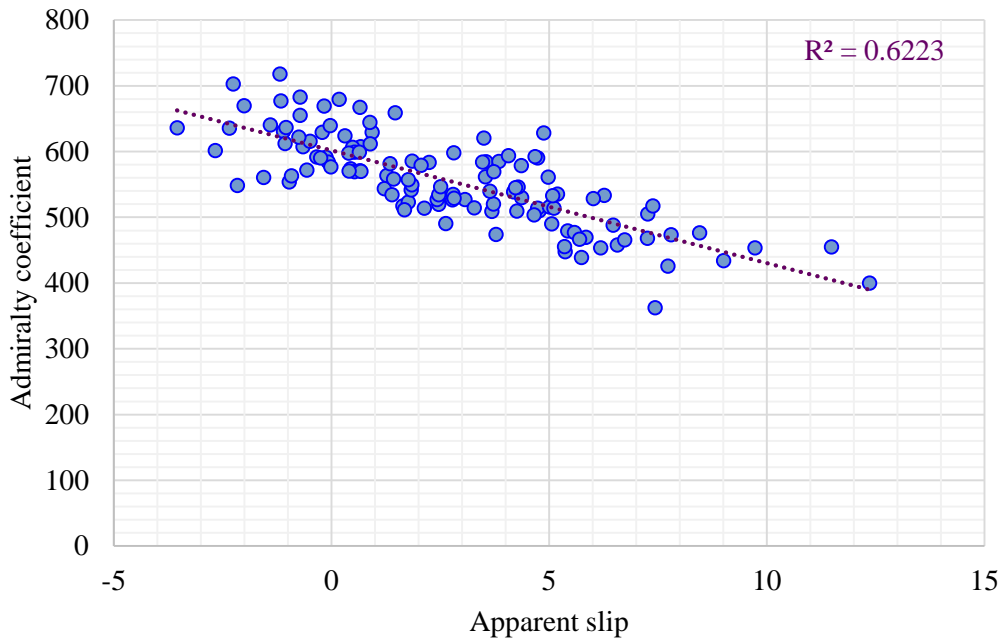


Figure 6.4 Filtered Admiralty coefficient versus apparent slip.

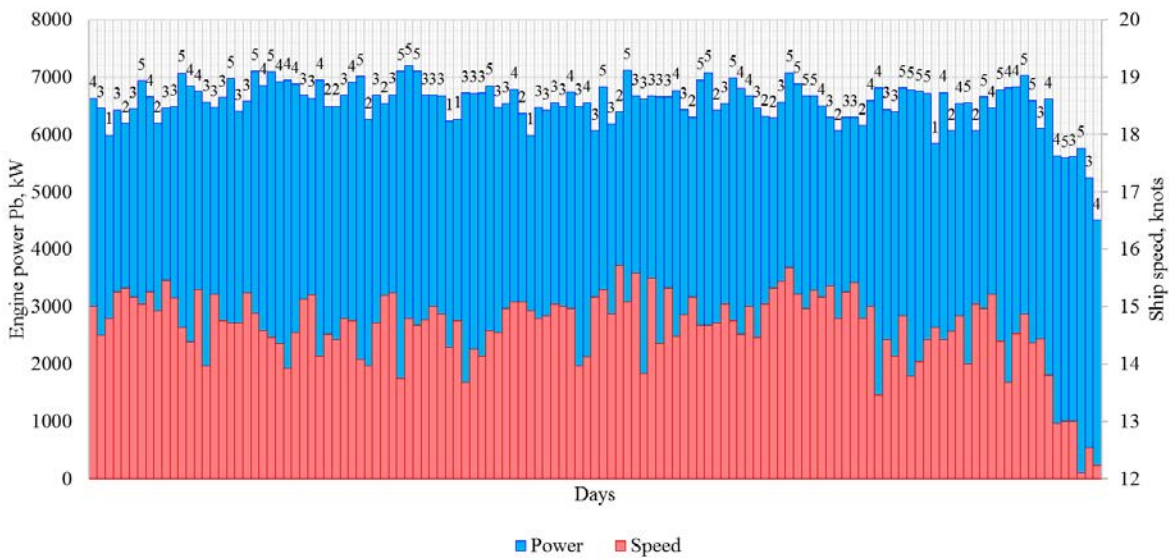


Figure 6.5 Filtered service data in time domain. Numbers at the top of the graph are Beaufort numbers.

After the initial filtration, the Admiralty coefficient versus the apparent slip analysis has shown slightly better correlation with  $R^2 = 0.6223$ . However, this distribution still indicates a presence of noise among the data set and, therefore, a power – speed analysis was also undertaken. Figure 6.5 represents the filtered engine power (blue) with corresponding service speed (red) in the time domain and Beaufort number (the little numbers at the top of the graph).

In order to obtain a more accurate power – speed analysis, it is important to correct the power to mean displacement using the expression 6.7.

$$P_2 = \left(\frac{\Delta_2}{\Delta_1}\right)^{2/3} P_1 \quad 6.7$$

where  $\Delta_2$  is the mean displacement, whilst  $\Delta_1$  and  $P_1$  are the initial displacement and engine power respectively at each service interval (Molland et al. 2011). Hence, in Figure 6.6 the power – speed relationships over time-domain have been updated with the corrected engine power range.

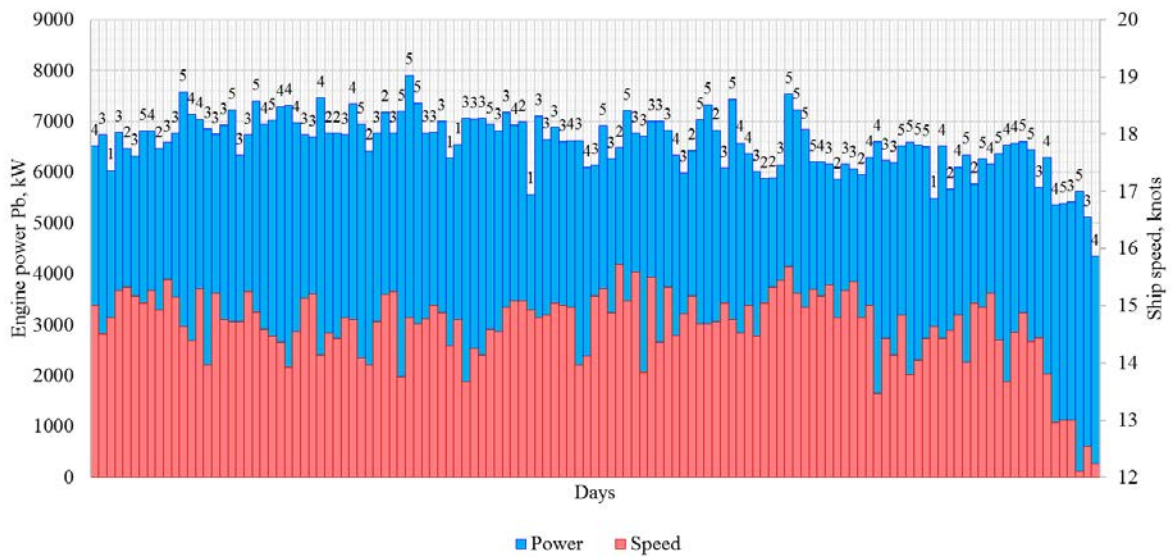


Figure 6.6 Filtered service data with engine power corrected to the mean displacement.

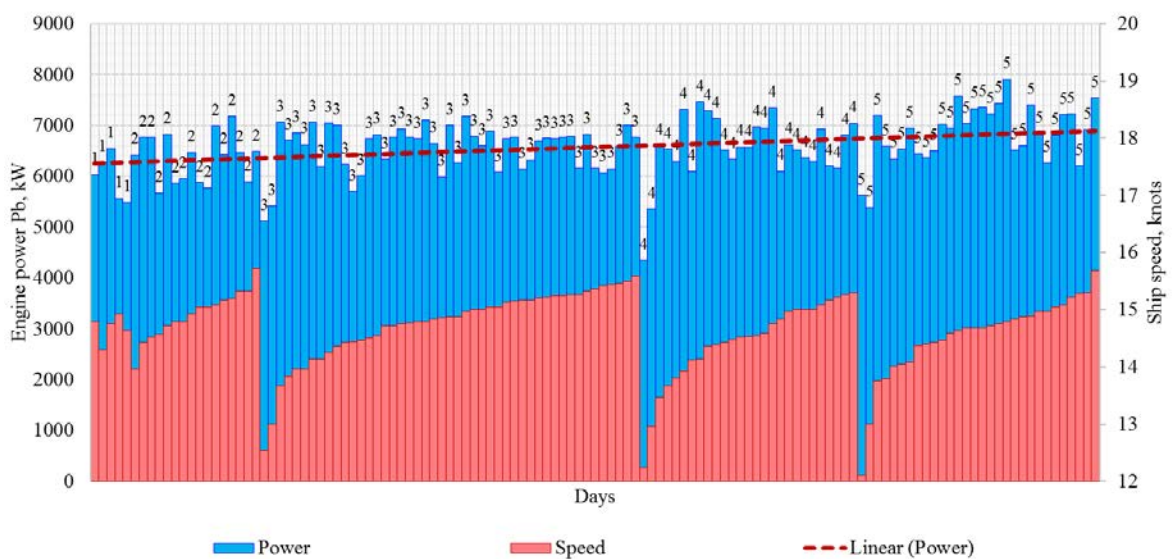


Figure 6.7 Filtered service data sorted by Beaufort number and speed.

In accordance with the cubic propeller law, the power fluctuations should have the similar pattern to changing speed, assuming power to vary as  $V^3$ . As such, the speed and power points first were sorted by Beaufort number and then by speed in ascending order for each Beaufort number. The results of the analysis are illustrated in Figure 6.7. Unfortunately, the data have shown poor power – speed correlation, where power almost does not reflect the speed behaviour pattern. The primary reason for this is likely to be the influence of the relative direction of the sea, fluctuations of which are unknown.

By applying linear regression analysis, it has been noticed that the engine power has an increasing trend over the Beaufort number. Therefore, for time-domain simulation purposes the changing sea states, defined as Beaufort numbers with corresponding service speeds, can be considered as a reference ship/sea behaviour in service.

By obtaining the set of engine powers in accordance with the relevant service speeds using the Module 1 and Module 2 of the Ship Power Simulation model and then correcting them to the suitable Beaufort number by applying the trial allowances correction factors, the realistic ship performance can be obtained. Figure 6.8 illustrates the artificial time-domain performance of the reference ship based on the observed displacements, while Figure 6.9 indicates the expected power – speed correlation by representing the same data points in ascending order by Beaufort number, the service speed for each Beaufort number and corresponding load condition. The load conditions from the filtered service data were conditionally divided into two segments: design load (< 40,000 tonnes) and fully loaded condition (> 40,000 tonnes).

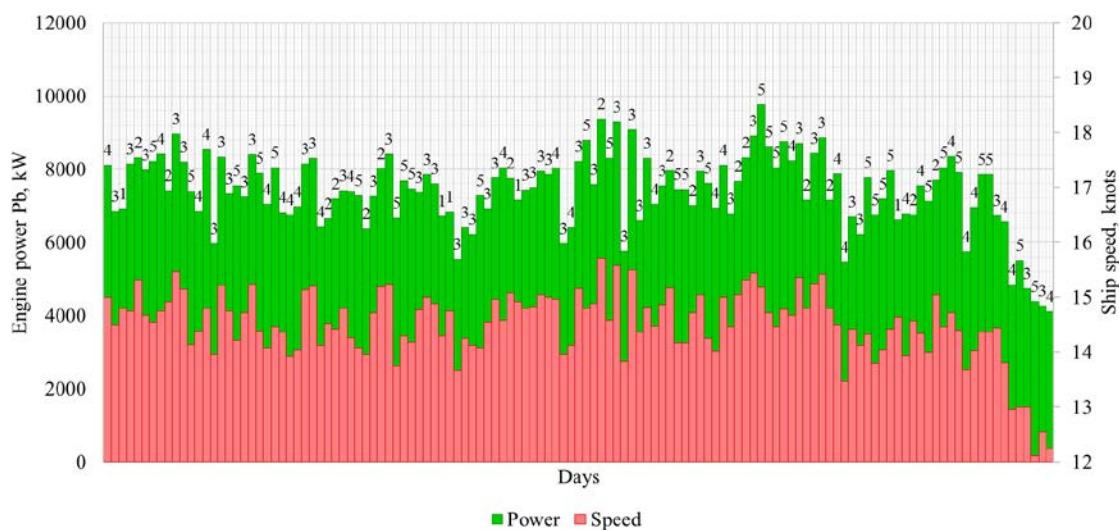


Figure 6.8 Artificial time-domain ship performance simulation. Numbers at the top of the graph are Beaufort numbers.



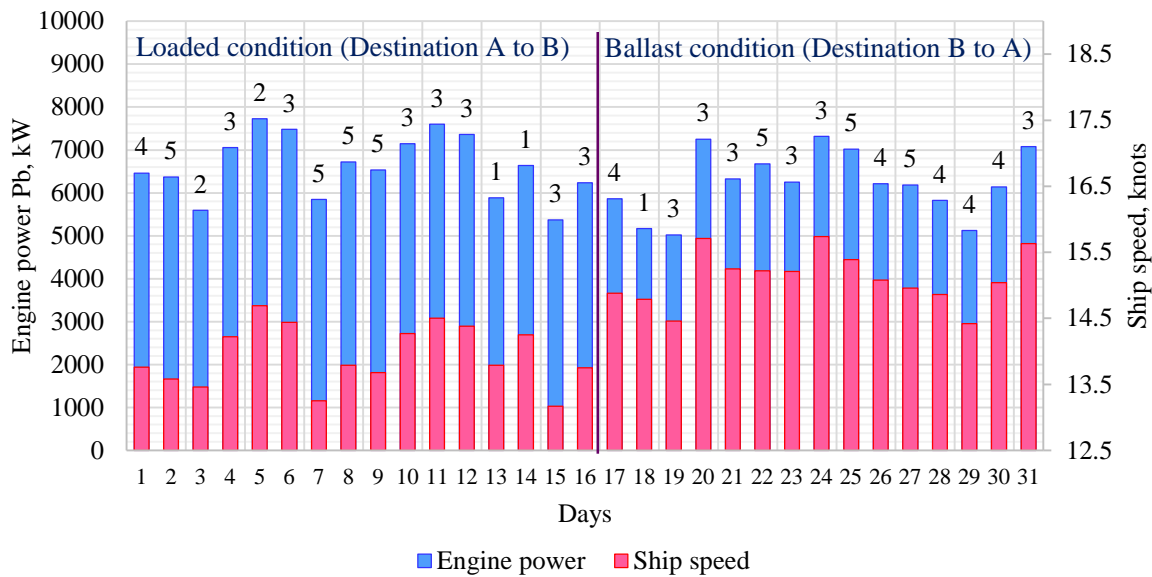


Figure 6.10 The reference ship time-domain voyage simulation. Numbers at the top of the graph are Beaufort numbers.

Table 6.2 The overall results of the reference ship voyage simulation.

Total per voyage (31 days)			Average per voyage			
Fuel consumption	791.4	tonnes per voyage		<i>Loaded</i>	<i>Ballast</i>	
$CO_2$	2527	tonnes per voyage	Engine load	92.6	87.1	%
$NO_x$	63.6	tonnes per voyage	SFOC	165.8	164.8	g/kWh
$SO_2$	3.84	tonnes per voyage				
$CO$	2.16	tonnes per voyage				
$HC$	1.44	tonnes per voyage				

In a similar way, the theoretical roundtrip voyage simulations will be performed and the results compared for each energy efficiency-enhancing technology/method in the following chapters.

## 7 Energy Efficient Propellers

The first case study is dedicated to the comparative analysis of four different types of propulsion systems and aims to explore their effect on the overall ship efficiency performance by means of holistic ship performance simulation as well as to find the best propeller match for the medium size tanker/bulk carrier ship types.

Since the Wake Equalising Duct (WED) was initially installed with the conventional FP propeller on the reference vessel, the first part of this case study is targeted to assess the energy benefits of the propulsion system with WED for this ship type.

The original fixed pitch propeller has been replaced with the Contracted and Loaded Tip (CLT) Propeller while keeping the wake equalising duct. The reference ship's current propulsion system arrangement is illustrated in Figure 7.1. Therefore, to estimate the contribution of the CLT propeller alone for this application, this propulsion system has been compared with the original fixed pitch propeller system with WED in the second part of this case study.



Figure 7.1 Current propulsion system of the reference products tanker fitted with a CLT propeller.

Another propulsor type potentially applicable to the reference products tanker is the ducted propeller, which has been designed and extensively analysed in the third part of this case study. Finally, all these propeller systems have been compared with each other by means of the Energy Efficiency Indicators (EEIs), namely fuel consumption, EEDI, exhaust emissions footprint and changing weather voyage performance. The outlined research

subjects are listed in Table 7.1 along with their description, reference labels and principle characteristics.

Table 7.1 The list of the researched propeller systems.

Reference label	Propeller description	Principle characteristics			
		$D$ (m)	$P/D$	$BAR$	$Z$
FPP	Conventional FP propeller without WED based on Wageningen B-screw series	5.65	0.65	0.56	4
FPP_WED	Conventional FP propeller with WED based on model test report and corrected to Wageningen B-screw	5.65	0.65	0.56	4
CLT_WED	FP CLT propeller with WED based on provided open water diagram	5.25	-	0.49	4
DUCT	Ducted propeller designed by means of Ka 4 – 70 screw series with nozzle no. 19 A	4.75	1.056	0.68	4

It should be noted that conventional FPP, FPP with WED and CLT with WED propeller dimensions have been provided in the model test report, while the ducted propeller dimensions are calculated via the propeller design procedure explained in subsection 7.3.

## 7.1 The Effect of a Wake Equalising Duct

Introduced by Schneekluth, the Wake Equalising Duct is the energy saving device claimed to increase propulsion efficiency by accelerating the inflow of the upper region of the propeller, since the flow in this region is normally relatively slow compared to the lower part of the propeller, as well as to improve the uniformity of the wake over the propeller disk. In addition, the WED is generating an additional thrust (similar to the accelerating ducted propeller) and reducing the possible vibrations by harmonising the wake field at the upper part of the disk. Therefore, the mean wake fraction and thrust deduction coefficients are expected to decrease, resulting in a moderate increase of the hull and open water efficiency components (Carlton 2012).

Most of the studies related to the estimation of the effect of the wake equalizing duct on propulsion efficiency have been carried out by means of model tests or CFD numerical flow computations. The CFD methods are normally based on the Reynolds averaged Navier–Stokes (RANS) equations applied to the ship hydrodynamics aiming to predict their propulsion performance. The CFD analyses have been performed in several independent studies such as (Ok 2004; Çelik 2007) while showing contrary outcomes.

The (Ok 2004) study is dedicated to the effect of the WED installed on the tanker with a higher block coefficient while the numerical computations are performed using the CFD code based on finite volume method. In (Ok 2004), the Reynolds number effects have been investigated for various ship speeds without the propeller presence at the after body. The results have shown a moderate frictional resistance increase and, thus, additional power requirements for propulsion due to the presence of the WED, compared to the naked hull. In (Çelik 2007), a numerical investigation based on RANS method has been carried out to find the most appropriate wake equalizing duct arrangement for a chemical tanker. The computations are carried out for the ship alone, the ship with a propeller, the ship with a wake equalizing duct alone and the ship with a wake equalizing duct and a propeller for the speed range of 10 – 16 knots. As a result, it was found that the differences in the frictional and the viscous pressure resistances between ships with and without WED were insignificant for all the cases. It was also found that the maximum efficiency gain obtained with the relevant WED design is about 10 percent mainly due to additionally generated thrust. It is likely, however, that the results of both studies were highly influenced by the turbulence model used in the computations.

Regarding the WED studies based on model tests, it is difficult to accurately extrapolate the powering performance to the actual full scale, especially for larger vessels, due to the Reynolds number scale effects. The reason is that WED installations are normally fitted to very large ships, which results in a relatively low towing speed in the tank to comply with Froude number scaling of the full-scale ship speed. To address these issues further reliable correlations are needed including tests done in large cavitation tunnels at higher speeds; towing tank tests performed for some equivalent speeds at the lower end of the cavitation tunnel range; and full-scale trials results (ITTC 1999).

For this study, the reference ship's model test report contains self-propulsion tests of the system with a WED for design, loaded and ballast conditions extrapolated to the full scale. These full-scale powering performance results, of course, might be less accurate than the full-scale trials. However, since the reference ship is rather on the smaller side of the spectrum of ship sizes suitable for the WED installation, this analysis may shed some further information into the potential efficiency benefits that could be expected with the installation of a WED for ships of the reference type and size. This, however, recognises the difference in local Reynolds number between the WED and a hull: the former working within the boundary layer of the latter.

To estimate the effect of the wake equalizing duct on the propulsion efficiency alone, it has been decided to predict the full-scale performance of the reference ship without the wake equalizing duct (conventional fixed pitch propeller alone) using the Ship Performance Simulation model described in Chapter 5 and then to compare obtained results with the self-propulsion data from the model test report (fixed pitch propeller with the wake equalizing duct).

First, the effect of the wake equalizing duct on the ship total resistance has been estimated and presented in form of the effective power  $P_E$  for a range of speeds under loaded, design and ballast conditions as shown in Figure 7.2. As a result, the comparison analysis of the resistance performance has not detected any significant changes of the ship resistance due to presence of wake equalizing duct.

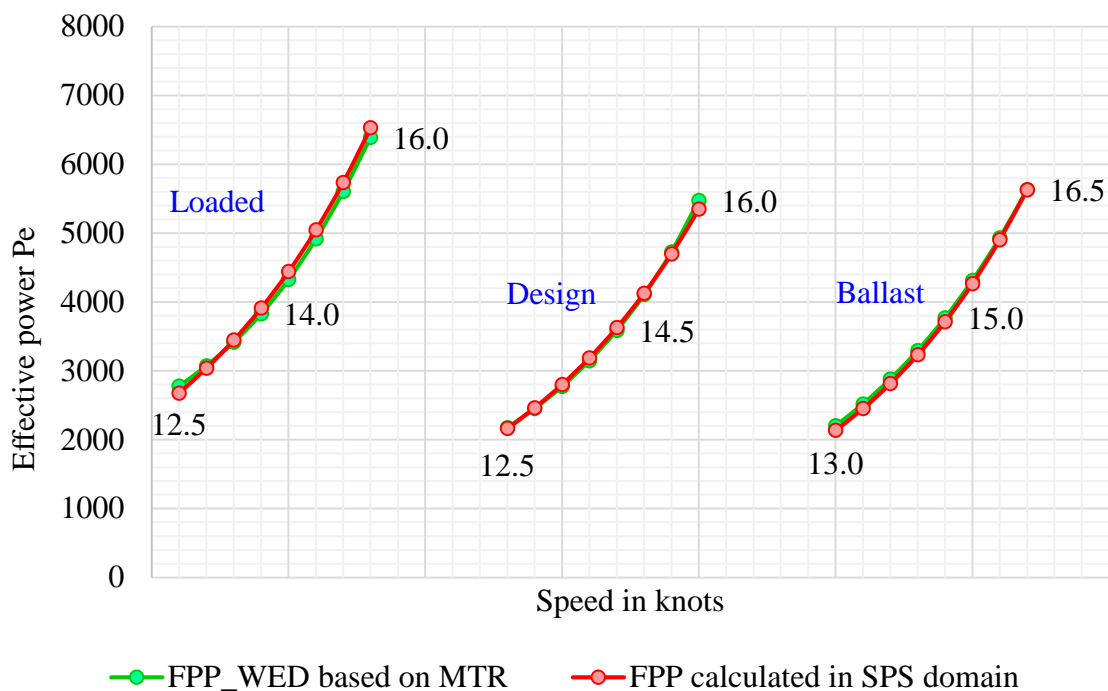


Figure 7.2 Effective power comparison between the propulsion systems with and without the wake equalizing duct. (Fixed pitch propeller with the wake equalizing duct (FPP\_WED) based on the model test report (MTR) versus conventional fixed pitch propeller (FPP) calculated using the Holtrop and Mennen approach in the SPS domain).

It was expected that the wake equalizing duct will have a negative effect on the frictional resistance component due to an additional wetted surface area while positively influencing the wave-making resistance component as a beneficial feature of the decreasing effect on the flow separation behind the hull. However, in the first case the actual size of wake equalizing duct is relatively small in comparison with the actual ship's hull, hence it is likely not to affect the frictional resistance significantly, while the flow separation

reduction might be insufficient to influence of the viscous resistance component, as it has been previously observed during the CFD simulations in (Çelik 2007).

For further propulsion analysis, the open water efficiency performance of the fixed pitch propeller with the wake equalizing duct (initially provided in the model test report) has been corrected to the Wageningen propeller series. The reason for this is to equalize the propulsion performance of two propellers: the original fixed pitch propeller with wake equalizing duct provided in the model test report and the standard conventional fixed pitch propeller of the Wageningen series based on the Ship Performance Simulation model. This will help to estimate the effect of the wake equalizing duct alone without the influence of the original fixed pitch propeller series, which, as already stated in Chapter 5.1, is unknown. The updated open water efficiency ( $\eta_o$ ) values have been calculated based on the  $K_Q$  and  $K_T$  coefficients provided in the model test report using the Wageningen regression based method. As a result, the open water efficiency values of the initial propeller with a wake equalizing duct are slightly increased over a range of speeds as shown in Figure 7.3.

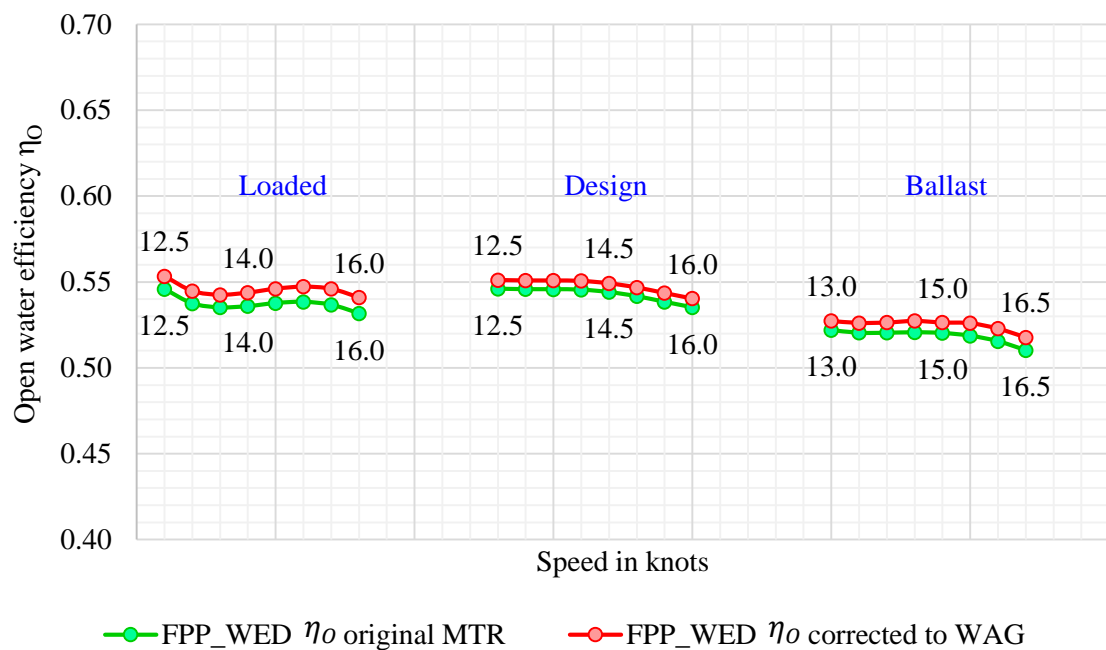


Figure 7.3 The open water efficiency correction to the Wageningen standards. (The fixed pitch propeller with the wake equalizing duct (FPP\_WED) based on the model test report (MTR) versus the fixed pitch propeller with the wake equalizing duct (FPP\_WED) corrected to the Wageningen standards (WAG)).

Table 7.2 comprises the comparison results of the conventional fixed pitch propeller and the original fixed pitch propeller with wake equalizing duct under design condition and operational speed of 14.6 knots, whereas components marked with \* represent the values provided in the model test report, that have been used as initial data for the propulsion

analysis calculations, while the remaining entries have been predicted using the ship performance simulation model outlined in Chapter 5.

Table 7.2 The comparison results of the conventional fixed pitch propeller (FPP) and the fixed pitch propeller with the wake equalizing duct (FPP\_WED) performance at the design condition (14.6 knots).

Parameter	Symbol	FPP	FPP_WED	Metric
Propeller diameter	$D$	5.65*	5.65*	$m$
Pitch to diameter ratio	$P/D$	0.65*	0.65*	-
Blade area ratio	$BAR$	0.56*	0.56*	-
Number of blades	$Z$	4*	4*	-
Wake fraction coefficient	$w$	0.39	0.38*	-
Thrust reduction coefficient	$t$	0.23	0.2217*	-
Relative-rotative efficiency	$\eta_R$	1.01	1.03*	-
Hull efficiency	$\eta_H$	1.25	1.26	-
Open-water efficiency	$\eta_o$	0.54	0.55	-
Propeller torque coefficient	$K_Q$	0.017	0.016	-
Propeller thrust coefficient	$K_T$	0.14	0.14	-
Hull surface pressure	$p_z$	1.89	1.91	$kN/m^2$
Quasi-propulsive coefficient	$QPC$	0.69	0.71	-
Delivered power	$P_D$	5400	5166	$kW$

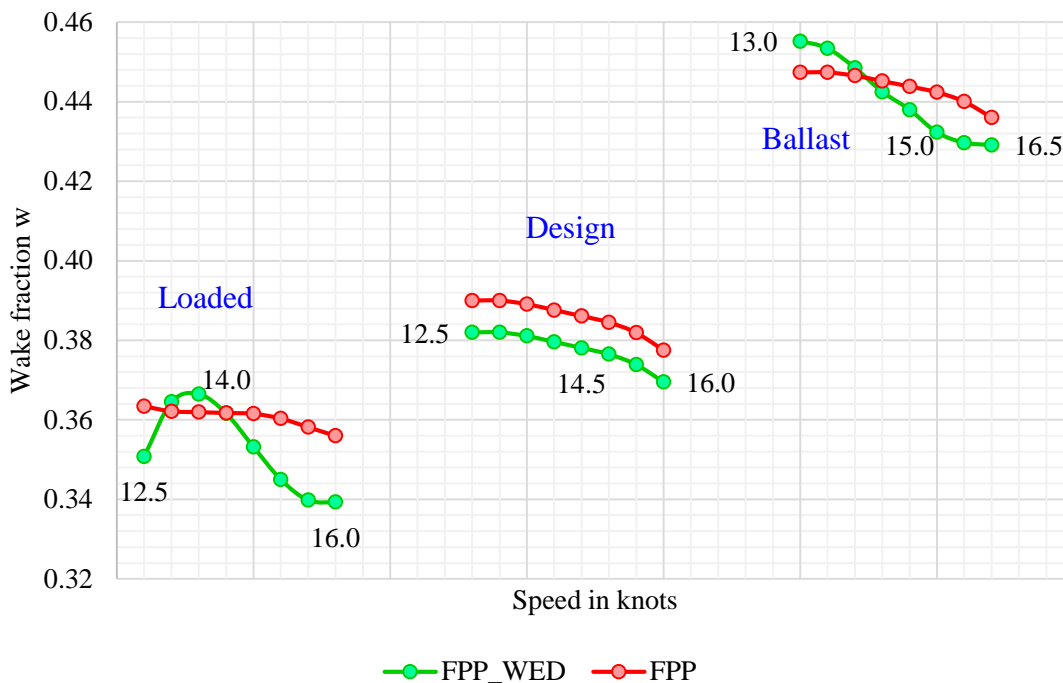


Figure 7.4 The wake fraction comparison results of the fixed pitch propeller with the wake equalizing duct (FPP\_WED) based on the model test report versus the conventional fixed pitch propeller (FPP) calculated using the Holtrop and Mennen approach.

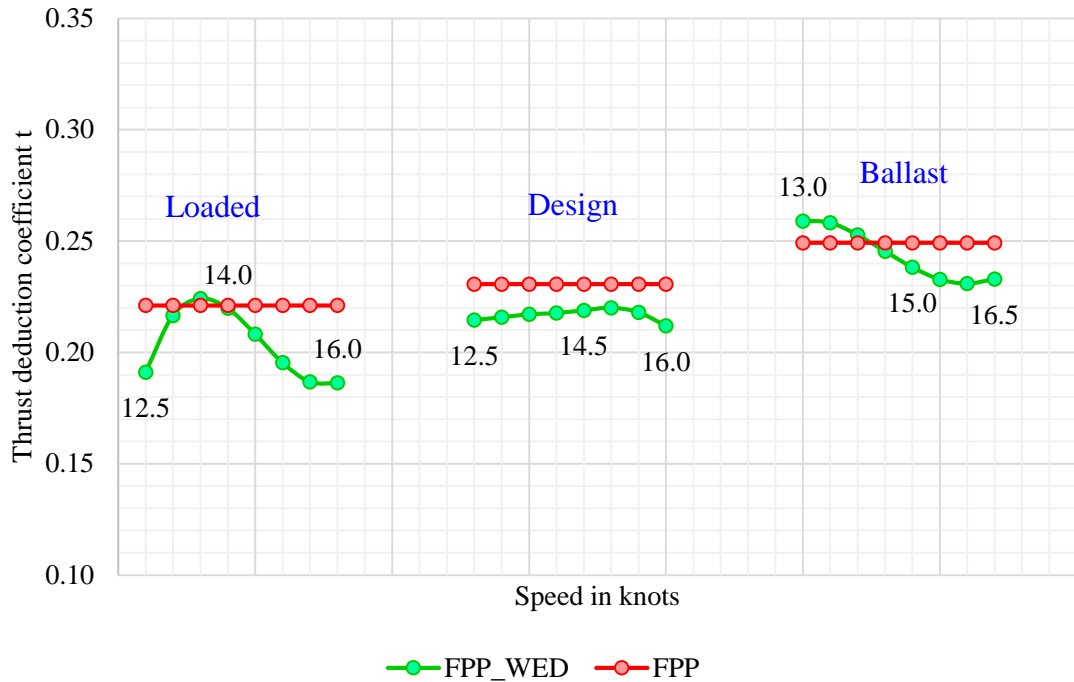


Figure 7.5 The thrust deduction comparison results of the fixed pitch propeller with the wake equalizing duct (FPP\_WED) based on the model test report versus the conventional fixed pitch propeller (FPP) calculated using the Holtrop and Mennen approach.

The results of the propulsion analysis of the conventional fixed pitch propeller and the original fixed pitch propeller with wake equalizing duct over the range of operational speeds, namely a comparison of the wake fractions ( $w$ ) and thrust deduction coefficients ( $t$ ), are shown in Figure 7.4 and Figure 7.5 respectively.

Due to specifics of the regression-based methodologies used for the calculations of the thrust deduction coefficients (Holtrop and Mennen for design and loaded conditions and Moor for ballast condition, see Chapter 5.1), which do not reflect the changes of thrust deduction over the range of speeds, the obtained thrust deduction coefficients for the conventional fixed pitch propeller without wake equalizing duct are only influenced by the ship's operational conditions and the hull form. Nevertheless, both, the wake fractions and thrust deduction coefficients, have demonstrated overall greater values for the conventional fixed pitch propeller system without the wake equalizing duct.

The principal reason for this is that the wake equalizing duct appendage is designed to influence the wake field to make it more homogenous, resulting in a reduction of the wake fraction and enhancement of the open water efficiency. In addition, a reduction of the flow separation area and changes in the afterbody pressure distribution due to wake equalizing duct act as a trigger for the reduction of the thrust deduction coefficient, which has a positive effect on the hull efficiency.

However, there are pronounced peaks in the wake fraction and thrust deduction coefficient distributions in the model test report data of the original fixed pitch propeller with the wake equalizing duct among the off-design conditions (Figure 7.4 and Figure 7.5). A rational explanation for this could be that at lower speeds the wake equalizing duct was unable to capture entire wake current while allowing some of the flow to pass non-homogenised. Although, at higher speeds the performance of wake equalizing duct at off-design conditions, in particular fully loaded, was significantly improved.

As to the standard series conventional fixed pitch propeller system without the wake equalizing duct, the increasing trends of both the wake fraction and thrust deduction coefficients had a negative influence on the hull efficiency ( $\eta_H$ ) values (Figure 7.6), while the increase of the wake fraction ( $w$ ) has also slightly affected the open water efficiency ( $\eta_o$ ) (Figure 7.7), showing that the system with the wake equalizing duct appears to be hydrodynamically more efficient.

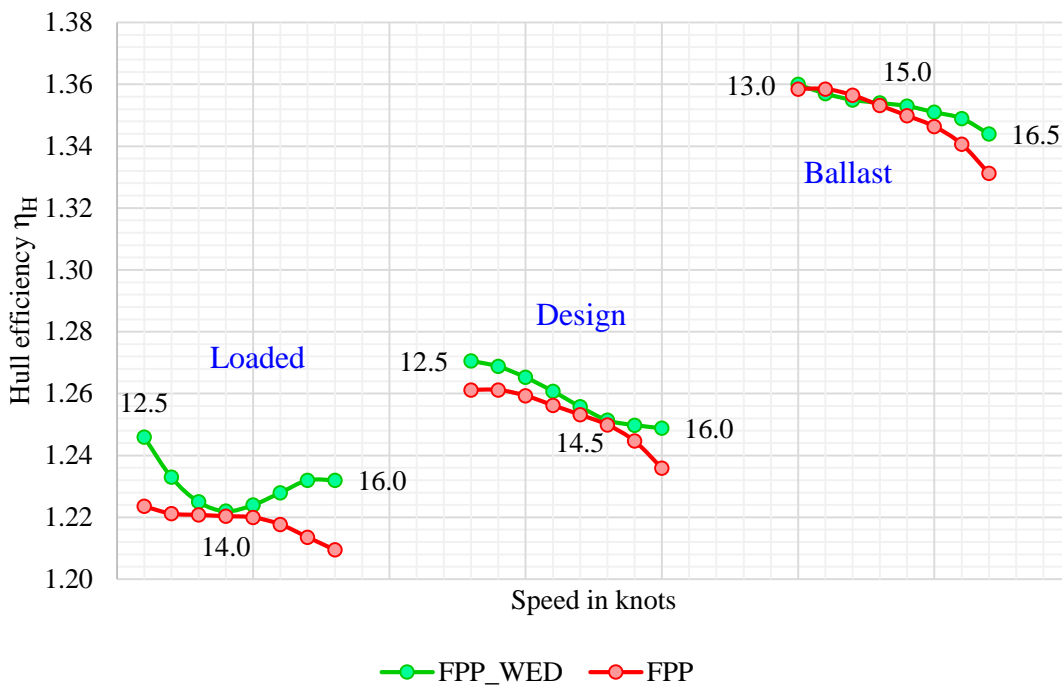


Figure 7.6 The hull efficiency comparison results of the fixed pitch propeller with the wake equalizing duct (FPP\_WED) based on the model test report versus the conventional fixed pitch propeller (FPP) calculated using the Holtrop and Mennen approach.

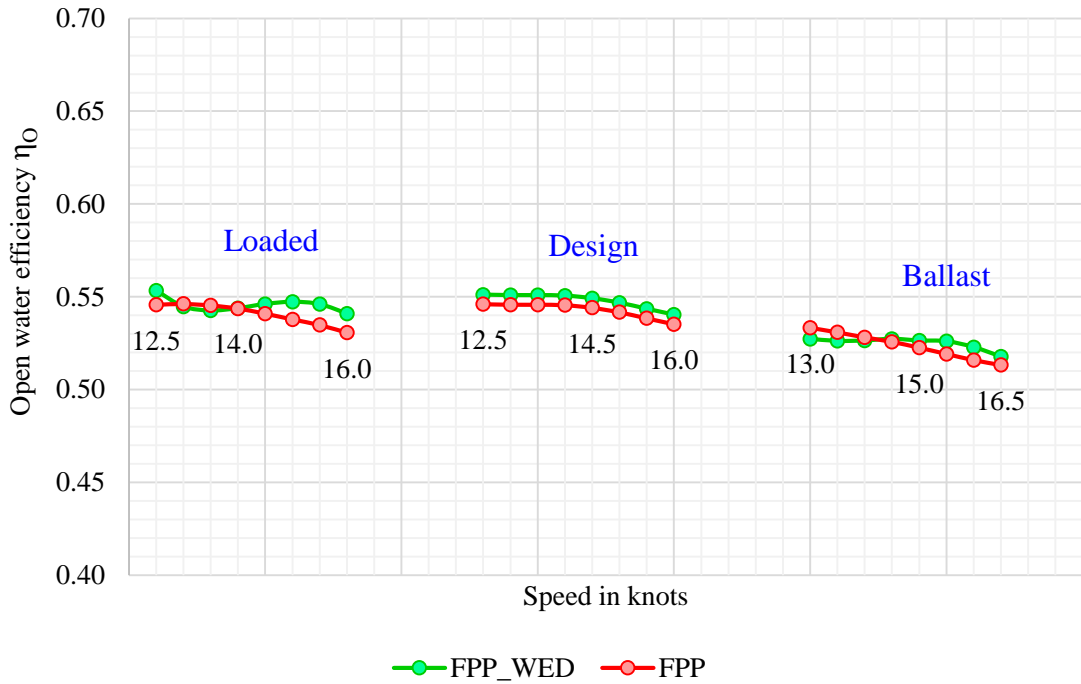


Figure 7.7 The open water efficiency comparison results of the fixed pitch propeller with the wake equalizing duct (FPP\_WED) based on the model test report and corrected to the Wageningen standards versus the conventional fixed pitch propeller (FPP) calculated using the Holtrop and Mennen approach.

The overall propulsion performance is illustrated in Figure 7.8, while Figure 7.9 demonstrates the effect of wake equalizing duct on the power absorption requirements.

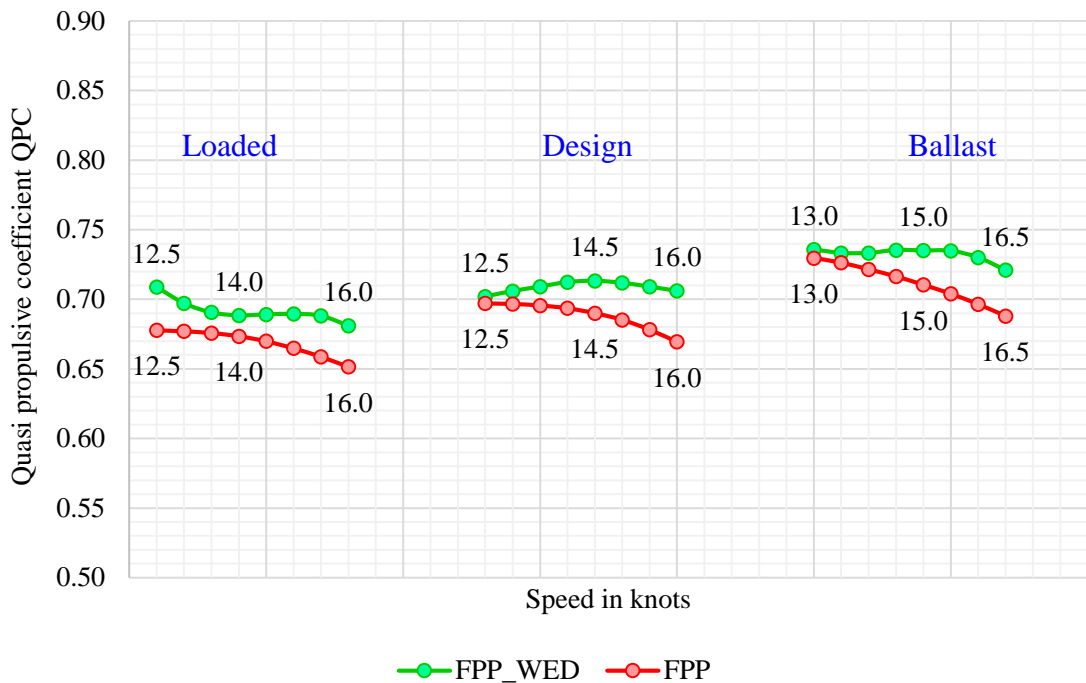


Figure 7.8 The QPC comparison results of the fixed pitch propeller with the wake equalizing duct (FPP\_WED) based on the model test report and corrected to the Wageningen standards versus the conventional fixed pitch propeller (FPP) calculated using the Holtrop and Mennen approach.

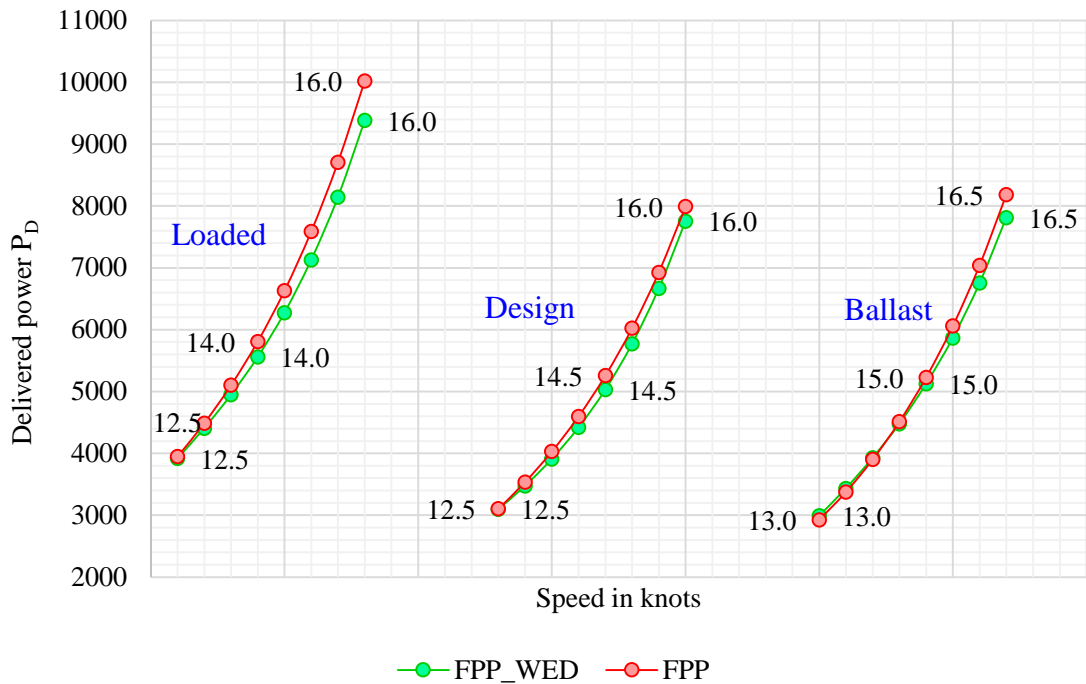


Figure 7.9 The power absorption requirements of the fixed pitch propeller with the wake equalizing duct (FPP\_WED) based on the model test report and corrected to the Wageningen standards versus the conventional fixed pitch propeller (FPP) calculated using the Holtrop and Mennen approach.

Both of these figures are showing an interesting trend of the wake equalizing duct being the more beneficial at higher ship speeds. This could be due to several reasons. One of them is the influence of the angle of duct section as the different angle arrangements of the WED system have shown significantly different trends in propulsion efficiency in (Çelik 2007). Another reason is simply the uncertainty due to the full-scale extrapolation from the self-propulsion tests. Notwithstanding, it is difficult to justify this trend without further analysis. In addition, according to the simulation results, the wake equalizing duct has the most beneficial impact under the loaded conditions rather than ballast. However, the free surface effects in ballast were not considered and this conceivably could influence the result. The mean percentage reductions of the delivered power requirements for all operational conditions are listed in Table 7.3. As such, at the ship recommended speed, the maximum increase of the propulsive efficiency due to the effect of wake equalizing duct amount for 4.49 percent at the fully loaded (scantling) condition.

Table 7.3 Delivered power reductions due to effect of the wake equalizing duct.

Condition	<i>Ballast</i>	<i>Designed</i>	<i>Loaded</i>	Metric
Speed	15.02	14.6	14.07	knots
Reduction of $P_D$	1.98	4.33	4.49	%

## 7.2 CLT Propellers

The Contracted and Loaded Tip (CLT) propellers, both fixed pitch and controllable pitch, are designed according to a principle, known as “New Momentum Theory”, where the thrust generated on a propeller blade continuously increases from a boss to the tip resulting in a significant increase of the propeller efficiency (Perez Gomez & Gonzalez-Adalid 1998). Generally, the CLT propellers are designed to have a lower level of vibration, noise, cavitation and hull pressure pulses. The CLT propellers have been installed on approximately 280 vessels of different ship types, including tankers, cargo ships, bulk carriers, RO/RO ships and etc. This amounts to around 0.5 percent of the total world fleet over 100 GT.

In this study, the original fixed pitch propeller of 5.65m in diameter has been replaced with the fixed pitch CLT propeller of 5.25 m in diameter on the reference products tanker, while keeping the wake equalizing duct (Figure 7.1). This subsection is dedicated towards the comparison analysis of the CLT propeller against the fixed pitch propeller systems both with wake equalizing duct.

Since there appear to be only negligible differences in the ship resistance performance with and without the wake equalizing duct, the effective power  $P_E$  estimation results, previously conducted using the Ship Performance Simulation model for the fixed pitch propeller without the wake equalizing duct, are used as a basis for the CLT propeller with the wake equalizing duct, providing some additional (unknown from the model test report) data necessary for further efficiency estimations.

The initially provided data for the CLT propeller with the WED data includes diameter ( $D$ ), the blade area ratio ( $BAR$ ), the wake fraction ( $w$ ) and thrust deduction coefficient ( $t$ ). These values are listed in Table 7.4 and marked with (\*) symbol. Based on these information, the relative-rotative efficiency ( $\eta_R$ ), the hull efficiency ( $\eta_H$ ) and the advanced coefficient ( $J$ ) have been calculated using the Module 2 of the Ship Performance Simulation suite.

The full-scale propeller open water diagram of the Hamburg Ship Model Basin (HSVA) origin, has been provided for this CLT propeller and demonstrated in Table 7.5. Based on these full-scale open water tests, the thrust ( $K_T$ ) and torque ( $K_Q$ ) propeller coefficients as well as the open water efficiency have been interpolated to the previously calculated set of advanced coefficients corresponding to the reference products tanker rotational and operational speeds. The extrapolated full scale CLT propeller and the conventional fixed

pitch propeller curves are illustrated below in Figure 7.10. This diagram clearly suggests a much greater propeller efficiency of the CLT propeller.

Table 7.4 The comparison results of CLT propeller with wake equalizing duct (CLT\_WED) and fixed pitch propeller with wake equalizing duct (FPP\_WED) performance at design condition and 14.6 knots.

Parameter	Symbol	<i>CLT_WED</i>	<i>FPP_WED</i>	Metric
Propeller diameter	$D$	5.25*	5.65*	$m$
Pitch to diameter ratio	$P/D$	-	0.6523*	-
Blade area ratio	$BAR$	0.4900*	0.5628*	-
Number of blades	$Z$	4*	4*	-
Wake fraction coefficient	$w$	0.377*	0.378*	-
Thrust reduction coefficient	$t$	0.217*	0.217*	-
Relative-rotative efficiency	$\eta_R$	1.016	1.030*	-
Hull efficiency	$\eta_H$	1.258	1.262	-
Open-water efficiency	$\eta_o$	0.628	0.549	-
Propeller torque coefficient	$K_Q$	0.0208	0.0164	-
Propeller thrust coefficient	$K_T$	0.1880	0.1391	-
Hull surface pressure	$p_z$	1.55	1.91	$kN/m^2$
Quasi-propulsive coefficient	$QPC$	0.803	0.713	-
Delivered power	$P_D$	4636	5166	$kW$

Table 7.5 CLT propeller open water performance at the full scale based on the Hamburg Ship Model Basin (HSVA) tests.

Advance coefficient	CLT full-scale HSVA		
	$K_{Ts}$ CLT HSVA	$K_{Qs}$ CLT HSVA	$\eta_{Os}$ CLT HSVA
0.1	0.3188	0.3284	0.1545
0.2	0.2828	0.2952	0.3049
0.3	0.2446	0.2605	0.4483
0.4	0.2039	0.2234	0.5810
0.5	0.1605	0.182	0.7015
0.6	0.1143	0.1354	0.8059
0.7	0.0653	0.0837	0.8703
0.8	0.014	0.0261	0.6850

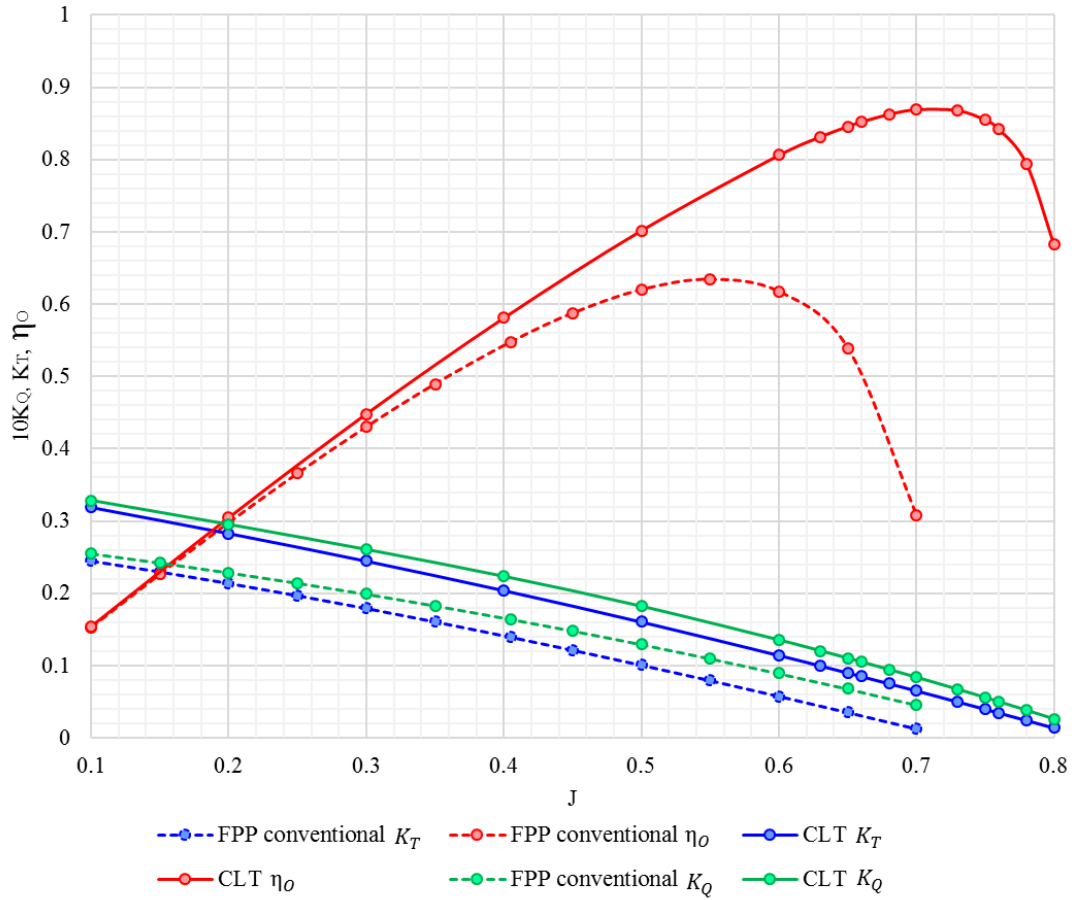


Figure 7.10 The full-scale CLT propeller and the conventional fixed pitch (FP) propeller curves.

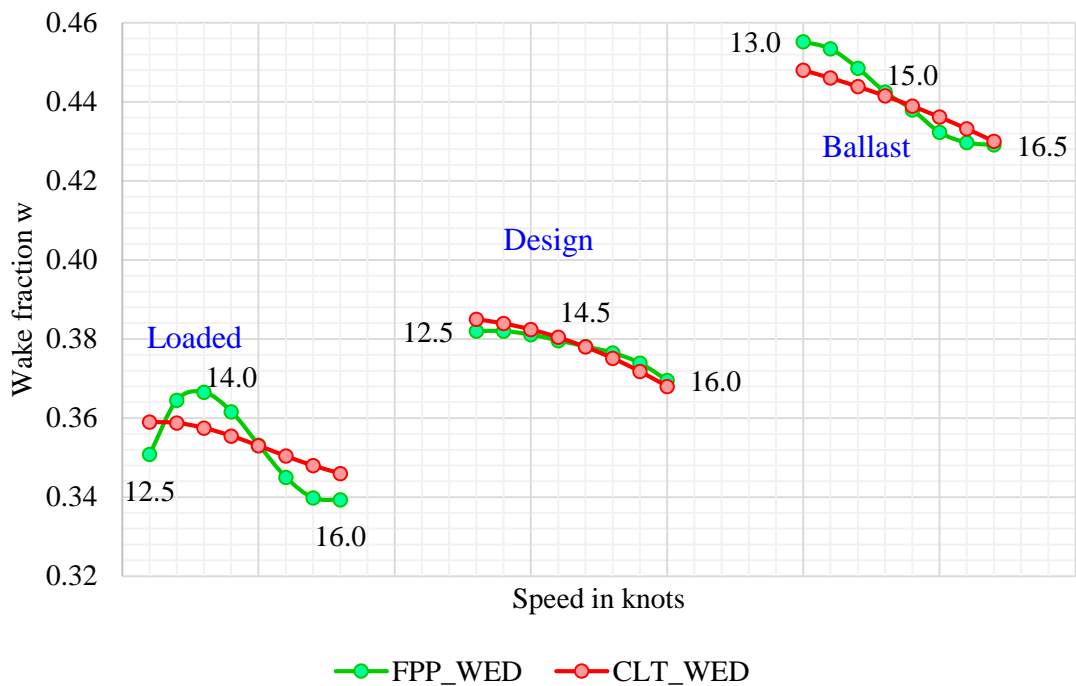


Figure 7.11 The wake fraction comparison results of the fixed pitch propeller (FPP\_WED) and the CLT propeller (CLT\_WED) both with the wake equalising duct.

The propulsion analysis results of the CLT propeller with the wake equalizing duct at the design speed of 14.6 knots and the design draught are tabulated in Table 7.4. It is found that the changes of the wake fraction and thrust deduction coefficients at the design condition are marginal and, therefore, the hull efficiency is almost not affected by the CLT propeller. This effect could be due to the wake equalising duct influence is more dominant than the effect of the increased thrust loading coefficient ( $C_T$ ) of the CLT propeller on the after body flow (Figure 7.11, Figure 7.12).

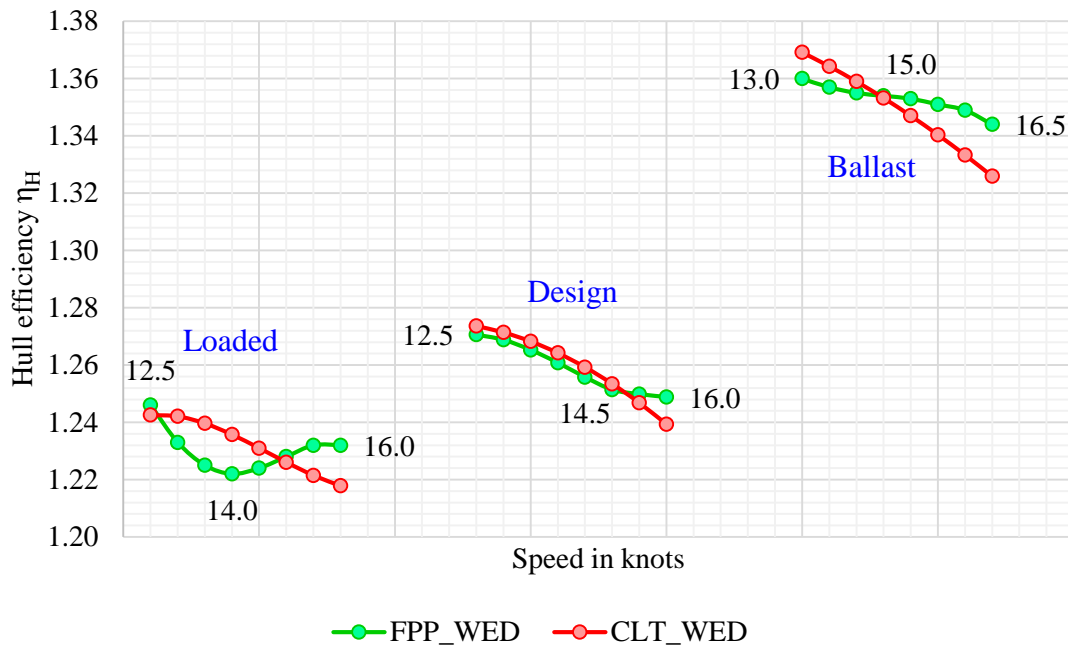


Figure 7.12 The hull efficiency comparison results of the fixed pitch propeller (FPP\_WED) and the CLT propeller (CLT\_WED) both with the wake equalising duct.

The open water efficiency values of the CLT propeller are much greater in all cases, making the average increase of about 14 percent (Figure 7.13). Such an increase in the open water efficiency values is clearly influenced by the propeller open water characteristics listed in Table 7.5 and plotted in Figure 7.10. However, the accuracy of this full-scale open water prediction is questionable since it was extrapolated to the full scale from the model tests. Nevertheless, while the absolute magnitude of this efficiency enhancement the overall effect of the CLT propeller on the power absorption requirements for all load conditions would appear beneficial as demonstrated in Figure 7.14.

The final power reductions due to the CLT propeller under different loads and corresponding recommended ship speeds are tabulated in Table 7.6, making the average reductions of about 10 percent which is high, but is likely to be influenced by a scaling from model to full scale propeller results as yet, further scaling procedures for the CLT

propeller, analogous to those developed by Lerbs for conventional propellers, need to be introduced.

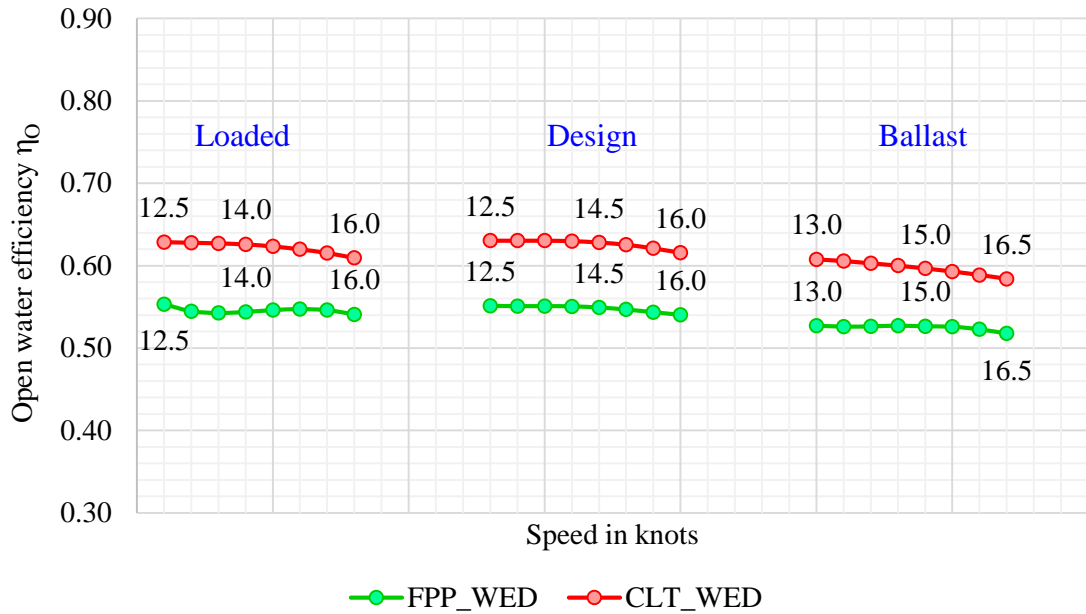


Figure 7.13 The open water efficiency comparison results of the fixed pitch propeller (FPP\_WED) and the CLT propeller (CLT\_WED) both with the wake equalising duct.

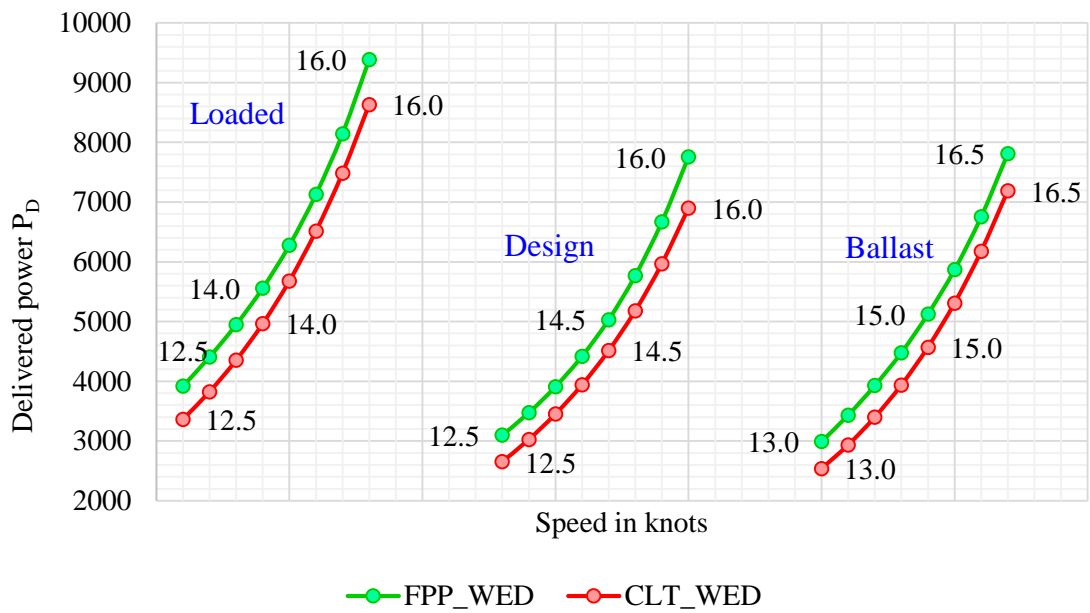


Figure 7.14 The power absorption results of the fixed pitch propeller (FPP\_WED) and the CLT propeller (CLT\_WED) both with the wake equalising duct.

Table 7.6 Delivered power reductions due to the CLT propeller.

Condition	<i>Ballast</i>	<i>Designed</i>	<i>Loaded</i>	Metric
Speed	15.02	14.6	14.07	knots
Reduction of $P_D$	9.53	10.3	10.73	%

### 7.3 Ducted Propellers

This subsection considers the design and analysis of FP ducted propellers based on the Wageningen 19A ducted propeller series, fitted with a Ka 4-70 propeller: that is, a four-bladed propeller having a blade area ratio of 0.70. The 19A duct series uses an accelerating nozzle combining hydrodynamic advantage with manufacturing ease. This together with associated ducted propeller series has been applied to the reference medium size products tanker and further comparison of this propeller performance with the conventional FP propeller without a nozzle.

The main purpose of an accelerating duct system in this type of application is to enhance the propeller efficiency by creating an additional thrust stipulated by the circulation induced around the duct at high thrust loading conditions (Carlton 2012). Alternatively, ducts can give a negative contribution at low thrust loading conditions due to the skin friction effects over the duct surface.

In the early 1970s, (Veenman & Zonen 1970) conducted tests with a model of 95,000 DWT tanker of a conventional hull design and propeller coupled with a range of ducted systems. Analysis of the reductions in power absorption due to the application of the different ducts in comparison with the conventional screw propeller was performed for the ship speed of 16.5 knots under loaded and ballast operational conditions. It was found that for both, loaded and ballast conditions, the most accelerating nozzle provides the largest levels of power reduction. It was also found that the percentage of delivered power reduction is generally higher by 2 – 3 percent in the case of ballast condition.

A more recent study by (Koronowicz et al. 2010) is dedicated to the design and analysis of the ducted propeller performance with the Wageningen 19A nozzle using the computer-based numerical simulation. The system is claimed to significantly facilitate the process of design of ducted propellers using the built-in database with a range of the duct geometry suitable for a wide range of the operating conditions. The comparative analysis has shown that the ducted propellers may offer competitive performance to open propellers and they may be successfully applied on ships with high speed.

However, from experience gained in the 1970s where potential efficiency benefits were predicted from model tests and theoretical modelling, several full-scale comparative trials were undertaken with tankers and bulk carriers. Full-scale practice did not show that such prediction was achievable from the analysis of the service data over the course of two years. Subsequently, the ducts were cut off and the conventional propellers were fitted. The one

underlying reason for this was that the predicted efficiency benefits lay within a statistical error of the measured service data (RINA 1973).

Generally, a properly designed ducted propeller would aim to have the highest possible propeller efficiency at its design condition, acceptable levels of vibration, noise and cavitation not leading to erosion and maintaining suitable hull pressure pulses. The optimum diameter of the ducted propeller itself is normally smaller than the diameter of the open propeller, while the overall propulsor diameter including ducts usually has a comparable size or, perhaps, slightly larger.

The algorithm for the design of ducted propellers differs from the algorithm for the design of open propellers presented in Appendix II in only a few details. The main difference is that a regression-based method for the estimation of the propeller efficiency and propulsion coefficients is specially designed to reflect the performance of the duct. In this approach, the thrust and torque coefficients  $K_T$ ,  $K_{TN}$  and  $K_Q$  are expressed as polynomials of advance coefficient  $J$  and pitch to diameter ratio  $P/D$  (7.1 – 7.3), while the relevant coefficients  $A_{i,j}$ ,  $B_{i,j}$  and  $C_{i,j}$  are listed in (Veenman & Zonen 1970).

$$\begin{aligned}
K_T = & A_{0,0} + A_{0,1} * J + \dots + A_{0,6} * J^6 \\
& + A_{1,0} * (P/D) + A_{1,1} * (P/D) * J + \dots + A_{1,6} * (P/D) * J^6 \\
& + A_{2,0} * (P/D)^2 + A_{2,1} * (P/D)^2 * J + \dots + A_{2,6} * (P/D)^2 * J^6 \\
& + \dots \\
& + A_{6,0} * (P/D)^6 + A_{6,1} * (P/D)^6 * J + \dots + A_{6,6} * (P/D)^6 * J^6
\end{aligned} \tag{7.1}$$

$$K_{TN} = B_{0,0} + B_{0,1} * J + \dots + B_{6,6} * (P/D)^6 J^6 \tag{7.2}$$

$$K_Q = C_{0,0} + C_{0,1} * J + \dots + C_{6,6} * (P/D)^6 J^6 \tag{7.3}$$

The propeller design program is able to design one of the following conventional Kaplan series propellers: Ka 3–65, Ka 4–55, Ka 4–70 and Ka 5–75 with the Wageningen 19a nozzle. The Ka 4–70 has been selected over the Ka 4–55 mainly due to the scaling corrections for Reynolds effects which in the original Ka 4-55 screw series were considered to be less reliable than the Ka 4-70. While many of these irregularities were smoothed out in the regression analysis but some errors still remain and, therefore, it was considered prudent for the major parts of the calculation to use the more reliable Ka 4-70 basis to minimise any errors that may remain.

The detailed ducted propeller design procedure is illustrated in Figure 7.16, while similar design procedure for an open water non-ducted Wageningen propeller (also relevant for the next two chapters) is explained in Appendix II. The algorithm solves the most widely encountered design problem of finding the optimum propeller characteristics by means of a provided speed of advance ( $V_A$ ), power to be absorbed by the screw ( $P_D$ ), and the number of revolutions ( $RPM$ ), which have been chosen in accordance with the reference ship design characteristics. The optimum propeller dimensions including diameter ( $D$ ), pitch to diameter ratio ( $P/D$ ) and blade area ratio ( $BAR$ ) were calculated and interpolated in order to obtain the maximum propeller efficiency. The propeller diameter interpolation diagram from Figure 7.16, generated as a part of the design procedure, was enlarged for better observation in Figure 7.15. The blade area ratio ( $BAR$ ) estimation procedure is described in Appendix III.

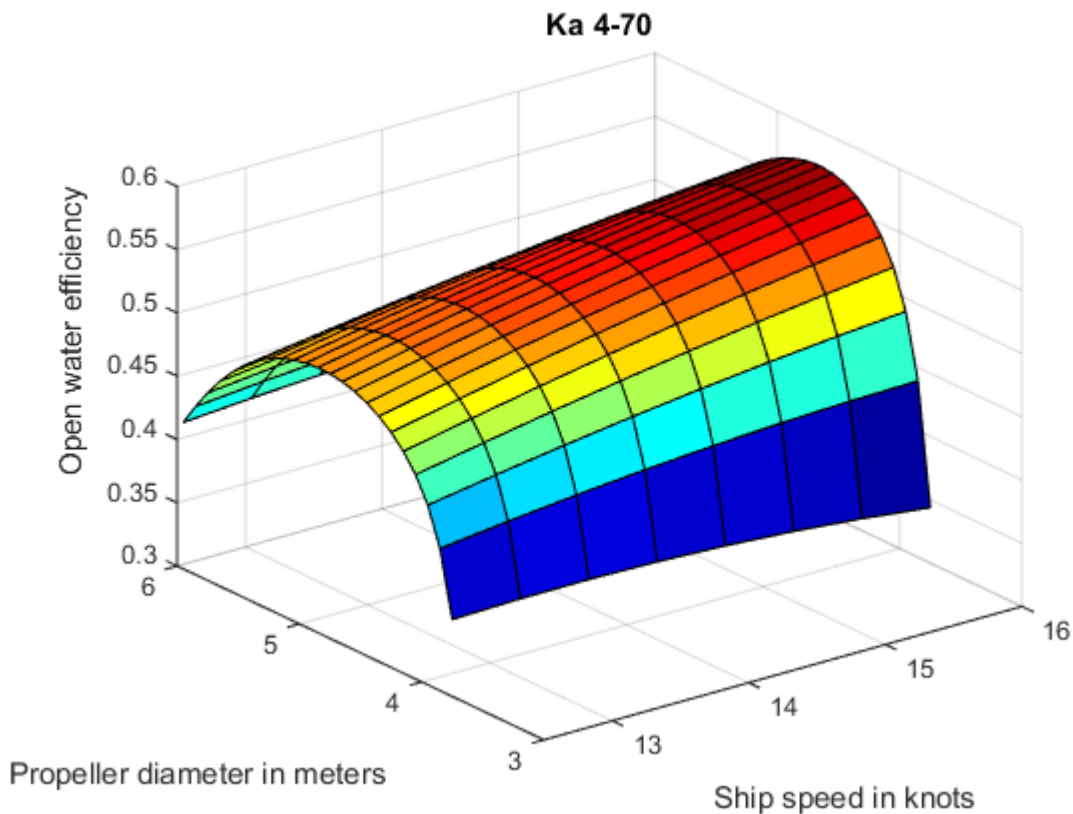


Figure 7.15 The Ka 4-70 propeller diameter interpolation diagram as part of the propeller design procedure.

Therefore, this design procedure was used for designing the optimum Ka 4-70 propeller for the given rate of rotation  $RPM = 122.14$  rpm operating at the design speed of 14.6 knots with initial power absorption  $P_D = 5400$  kW.

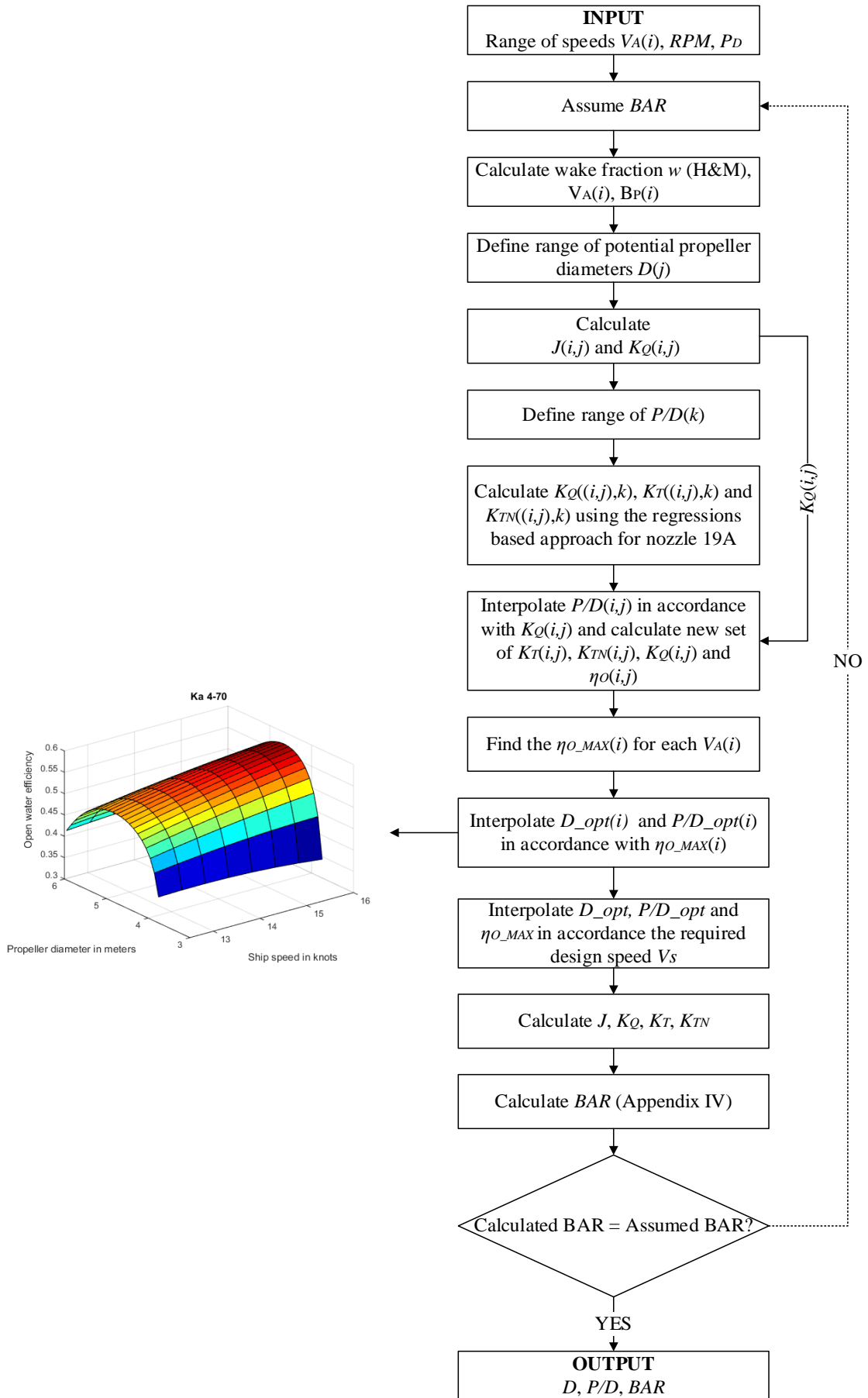


Figure 7.16. Ducted propeller design procedure.

The diameter of the resulting propeller equals to 4.75 m, while the original non-ducted propeller has a diameter of 5.65 m. The remaining propeller characteristics are listed in Table 7.7. The additional propeller analyses for the ship design speed and load were performed using the Ship Performance Simulation model and are also shown in Table 7.7.

Table 7.7 The comparison results of the 19A ducted propeller (DUCT) and the conventional fixed pitch propeller (FPP) at the design load condition and speed of 14.6 knots.

Parameter	Symbol	<i>FPP</i>	<i>DUCT</i>	Metric
Propeller diameter	$D$	5.65	4.75	$m$
Pitch to diameter ratio	$P/D$	0.65	1.056	-
Blade area ratio	$BAR$	0.56	0.68	-
Number of blades	$Z$	4	4	-
Wake fraction coefficient	$w$	0.386	0.370	-
Thrust reduction coefficient	$t$	0.231	0.207	-
Relative-rotative efficiency	$\eta_R$	1.012	1.012	-
Hull efficiency	$\eta_H$	1.253	1.258	-
Open-water efficiency	$\eta_O$	0.544	0.557	-
Propeller torque coefficient	$K_Q$	0.0166	0.0411	-
Propeller thrust/nozzle coefficient	$K_T$	0.1411	0.294	-
Hull surface pressure	$p_z$	1.89	1.16	$kN/m^2$
Quasi-propulsive coefficient	$QPC$	0.689	0.710	-
Delivered power	$P_D$	5400	5246	$kW$

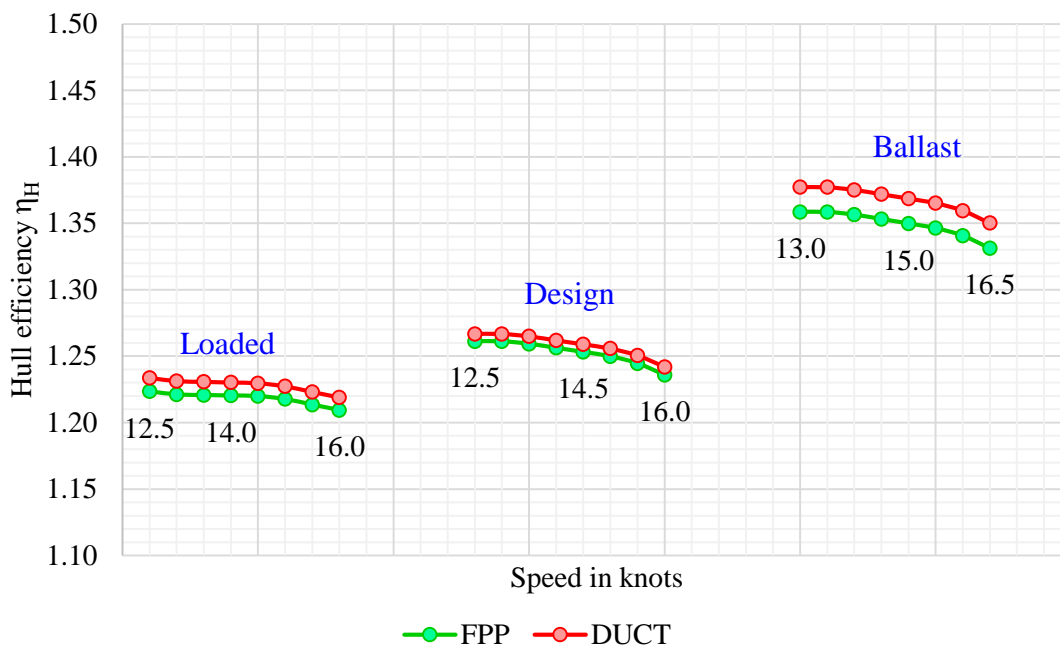


Figure 7.17 The comparison results of the hull efficiency of the 19A ducted propeller (DUCT) and the conventional fixed pitch propeller (FPP).

The propulsion analyses have also been conducted for loaded (scantling), design and ballast conditions. The mutual interference of propeller and hull is represented by the hull efficiency, which is found to have a slightly better performance in case of a ducted propeller, especially at off-design conditions (Figure 7.17). The reason is that the wake fraction and thrust deduction coefficients are slightly decreased, reproducing a similar trend as to the fixed pitch propeller with the effect of wake equalizing duct. The open-water efficiency of the ducted propeller is also relatively better than of the conventional fixed pitch propeller (Figure 7.18).

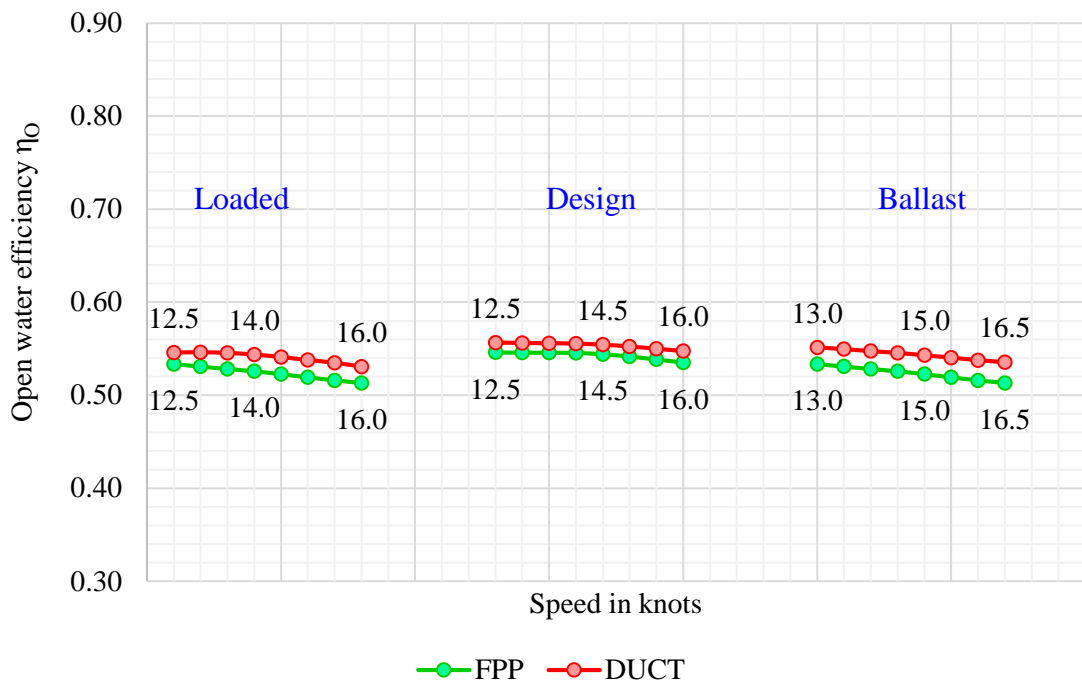


Figure 7.18 The comparison results of the propeller efficiency of the 19A ducted propeller (DUCT) and the conventional fixed pitch propeller.

The Quasi Propulsive Coefficient (*QPC*) of the ducted propeller system and, hence, the power absorption performance at different operational conditions are found to be more beneficial in comparison with the conventional fixed pitch propeller. The ducted propeller performance at the ballast condition was slightly better (more beneficial) than at design and loaded, which resembles the results obtained in (Veenman & Zonen 1970).

The final power reductions due to the ducted propeller under different loads and the corresponding recommended ship speeds are tabulated in Table 7.8, making the maximum reductions of approximately 5 percent.

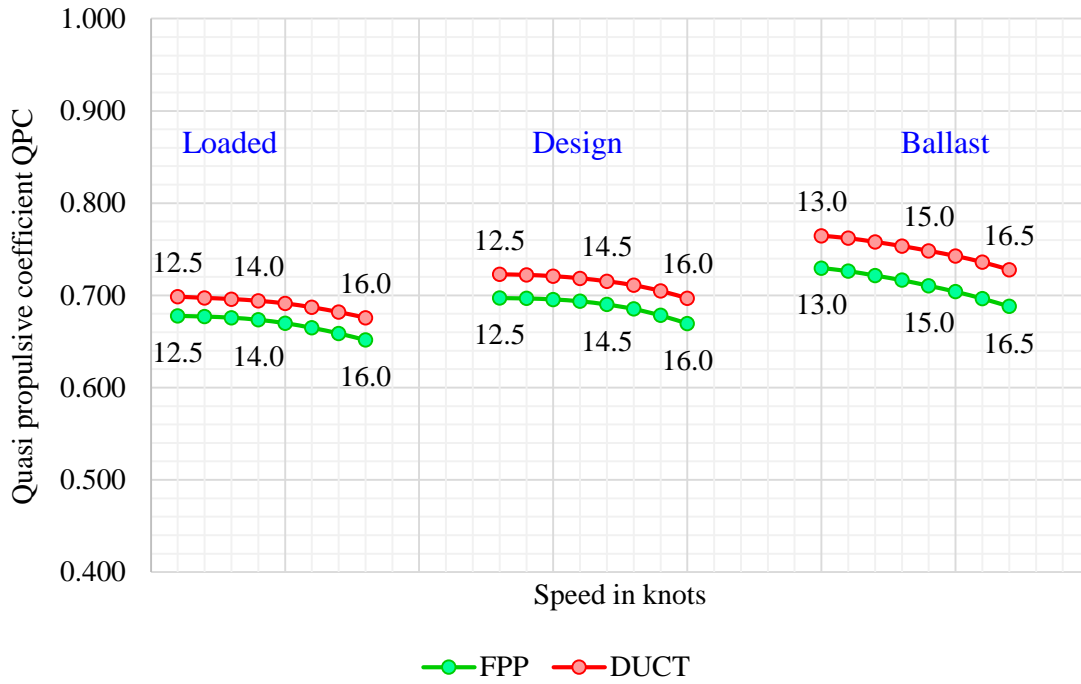


Figure 7.19 The comparison results of the propulsive efficiency (QPC) of the 19A ducted propeller (DUCT) and the conventional fixed pitch propeller (FPP).

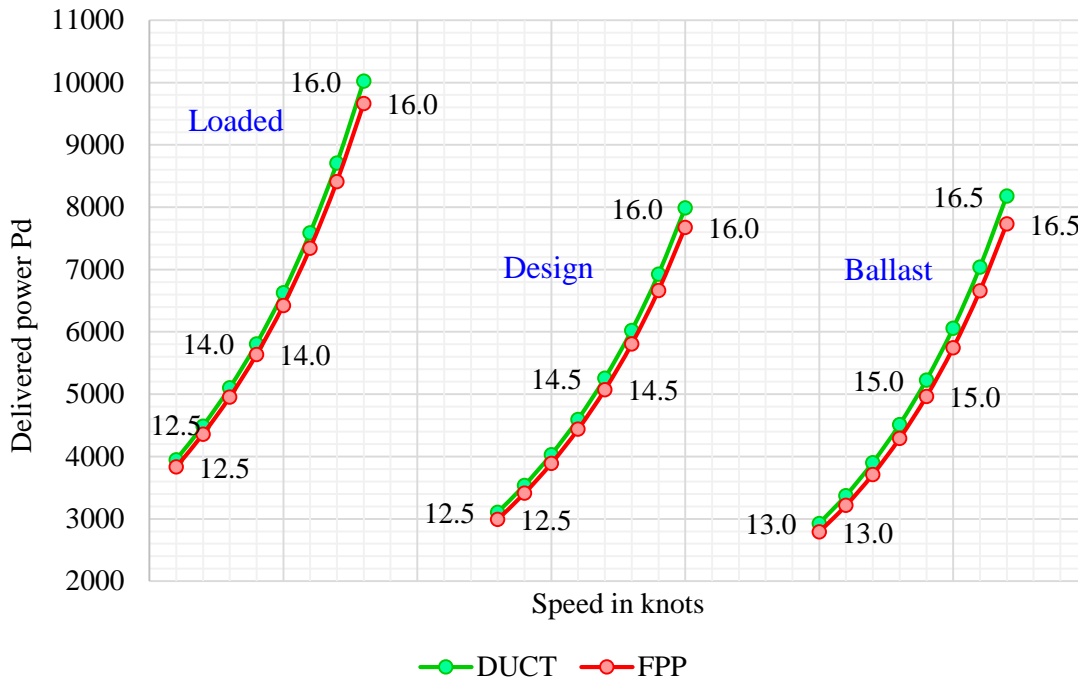


Figure 7.20 The power absorption of the 19A ducted propeller system (DUCT) and the conventional fixed pitch propeller (FPP).

Table 7.8 Delivered power reductions due to the ducted propeller.

Condition	Ballast	Designed	Loaded	Metric
Speed	15.02	14.6	14.07	knots
Reduction of $P_D$	5.05	2.94	2.95	%

## 7.4 Impact on the Energy Efficiency Indicators

Since four energy efficient propeller combinations were analysed in this chapter, this subsection is focused on the comparative analysis of these propeller systems in terms of the energy efficiency indicators (EETs) covering the fuel consumption, the emissions footprint and the EEDI index.

First, the delivered power results of all the cases were compared with each other under the fully loaded, design and ballast conditions in accordance with the designed speed of 14.07 knot at loaded, 14.6 knots at design and 15.02 knots at ballast conditions. The results are summarised in Figure 7.21. The most beneficial propeller performance is suggested by the CLT propeller system with the wake equalizing duct and discussed earlier but with reservations expressed in section 7.2. The ducted and the original fixed pitch propeller system with the wake equalizing duct performed relatively similarly, although the ducted propeller has shown by 3.2 percent better results at the ballast condition than the fixed pitch propeller system with the wake equalizing duct.

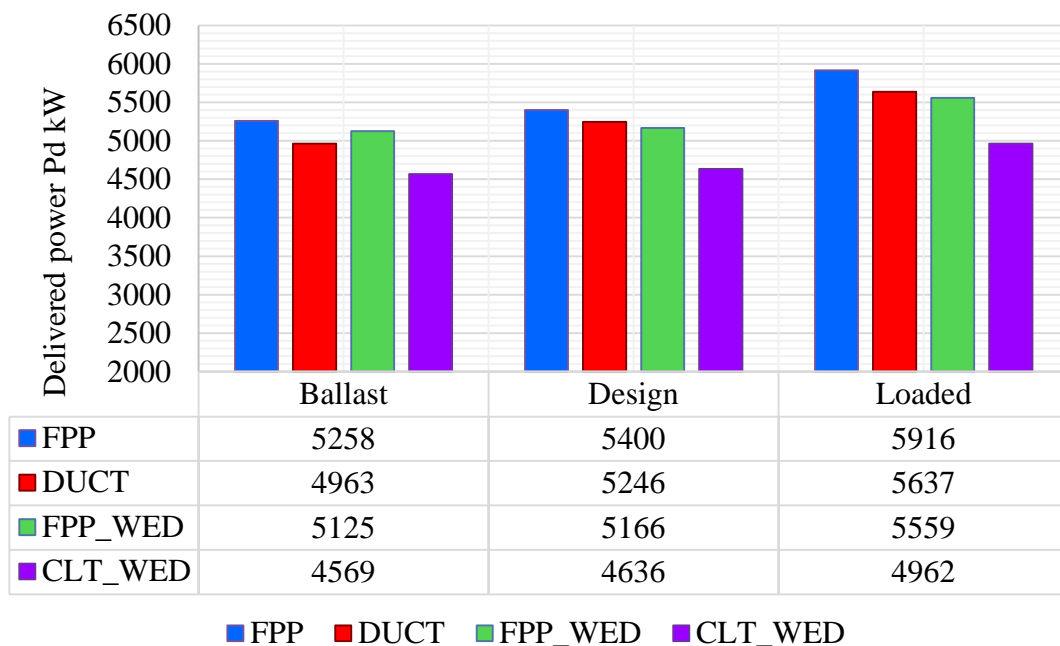


Figure 7.21 The comparative analysis of the required delivered power under different loads and corresponding operational speed (FPP – the convention fixed pitch propeller, DUCT – the 19A ducted propeller system, FPP\_WED – the original fixed pitch propeller with the wake equalizing duct, CLT\_WED – the CLT propeller with the wake equalizing duct).

For the conventional fixed pitch propeller, the original fixed pitch propeller with the wake equalizing duct and the ducted propeller systems an engine has been kept constant and the same as assumed for the reference vessel (5S50ME-C), while the SMCR were changed to

maintain integrity of the engine operating diagram and also in accordance with the propeller performance at 15 knots with the 15 percent sea margin. In the case of the CLT propeller, since its performance has exceeded the minimum margin of the reference engine, the smaller engine from the ME-B range, 5S46ME-B, has been selected for this case. The list of engines with their SMCR power and SMCR speed are summarised in Table 7.9.

Table 7.9 The range of selected engines and their SMCR (FPP – the convention fixed pitch propeller, DUCT – the 19A ducted propeller, FPP\_WED – the original fixed pitch propeller with the wake equalizing duct, CLT\_WED – the CLT propeller with the wake equalizing duct).

15 knots	<i>FPP</i>	<i>FPP_WED</i>	<i>CLT_WED</i>	<i>DUCT</i>	
SMCR	7371	7061	6338	7153	kW
RPM	127	127	127	127	rpm
Engine	5S50ME-C	5S50ME-C	5S46ME-B	5S50ME-C	

In addition, Figure 7.22 demonstrates the load diagrams for both engines together with the engine service curves for each propeller system and their Normal Continuous Ratings (NCR) at 90 percent SMCR corresponding to the 14.6 knots operational speed.

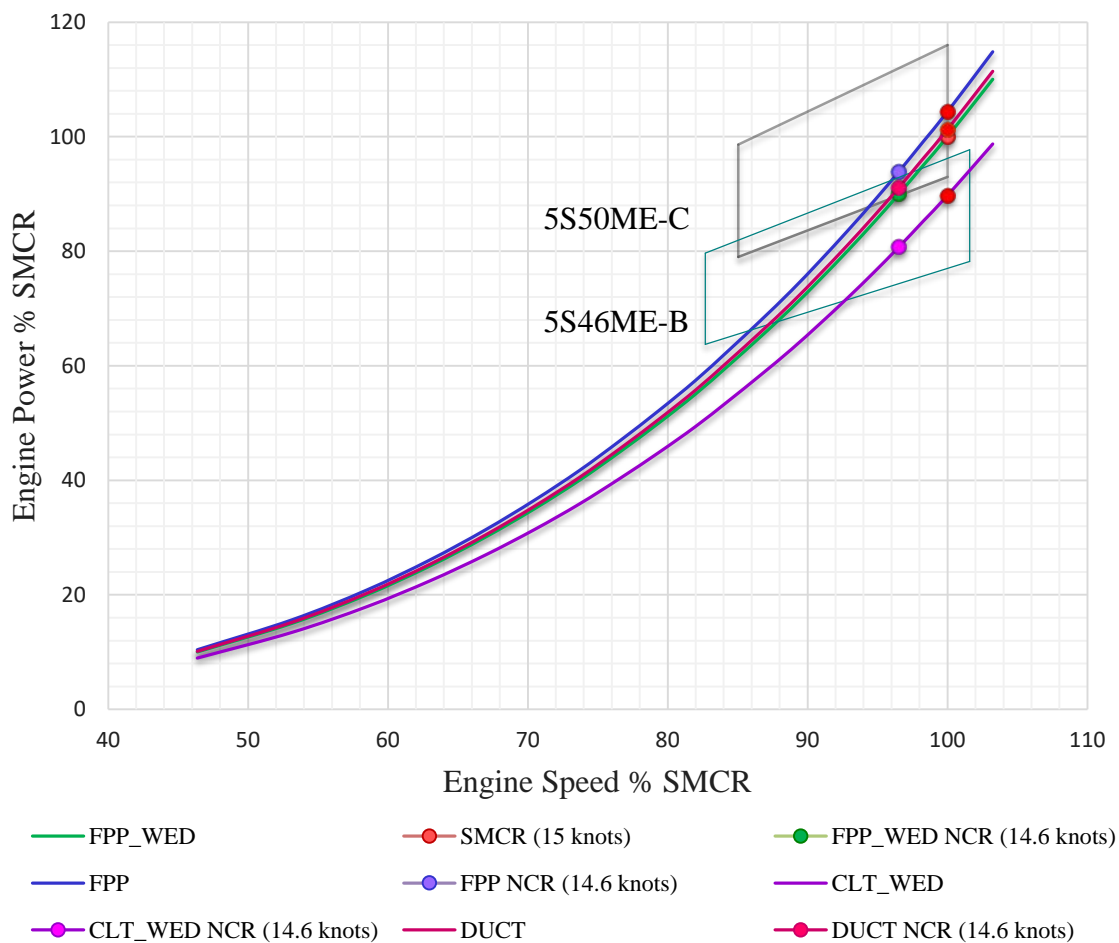


Figure 7.22 Engines service curves for all the propeller systems (FPP – the convention fixed pitch propeller, DUCT – the 19A ducted propeller, FPP\_WED – the original fixed pitch propeller with the wake equalizing duct, CLT\_WED – the CLT propeller with the wake equalizing duct).

The resulting fuel consumption and pollutants mass flow rates as well as their specific values at Normal Continuous Rating operational condition are summarised in Table 7.10. The SFOC values have been additionally corrected by 2 percent to account actual fuels in comparison to test fuels according to ISO.

The results show that the lowest fuel consumption, as expected, is achieved by the CLT propeller with the WED (CLT\_WED), which is on 140 kg/h lower than the conventional fixed pitch propeller (FPP) requirements. However, since a general rate of the specific fuel oil consumption of the 5S46ME-B engine is slightly higher than of 5S50ME-C engine, the SFOC of the CLT propeller at NCR is by 1.39 percent exceeding the conventional fixed pitch propeller system (FPP). The lowest SFOC rate of 164.3 g/kWh is attained by the fixed pitch propulsion system with the wake equalizing duct (FPP\_WED).

Table 7.10 The summary table of propellers performance at the normal continuous rating (NCR) (FPP – the convention fixed pitch propeller, DUCT – the ducted propeller, FPP\_WED – the original fixed pitch propeller with the wake equalizing duct, CLT\_WED – the CLT propeller with the wake equalizing duct).

\* Note comments in section 7.2 when considering this table.

Fuel Consumption	Symbol/Unit		<i>FPP</i>	<i>FPP_WED</i>	<i>CLT_WED</i> *	<i>DUCT</i>
	FC	kg/h	1097	1044	957	1060
SFOC	g/kWh	165.4	164.3	167.7	164.6	
Mass Flow Rate	<i>NO<sub>x</sub></i>	kg/h	88	84	75	85
	<i>CO</i>		3.15	3.01	2.68	3.05
	<i>HC</i>		2.03	1.94	1.73	1.97
	<i>CO<sub>2</sub></i>		3503	3334	3054	3383
	<i>SO<sub>2</sub></i>		5.20	4.95	4.54	5.03
Specific	<i>NO<sub>x</sub></i>	g/kWh	13.3	13.2	13.13	13.22
	<i>CO</i>		0.47	0.47	0.47	0.47
	<i>HC</i>		0.31	0.31	0.30	0.31
	<i>CO<sub>2</sub></i>		528	525	535	526
	<i>SO<sub>2</sub></i>		0.78	0.78	0.80	0.78
EEDI	gCO <sub>2</sub> /tnm	6.12	5.82	5.36	5.91	

Regarding the exhaust emissions footprint, it is possible to reduce the *CO<sub>2</sub>* emissions by 12.8 percent by adopting the CLT propeller with the WED, by 4.8 percent by applying the FPP with the WED (FPP\_WED) and by 3.4 percent with the ducted propeller (DUCT) in comparison to the conventional FPP. It is also possible to reduce *NO<sub>x</sub>* emissions by 14.8

percent with the CLT propeller with the WED, by 4.5 percent with the FPP with the WED and by approximately 3.4 percent with the ducted propeller system.

In terms of the EEDI index, the lowest value is dedicated to the CLT propeller with the WED, followed by the FPP with the WED and the ducted propeller as shown in Figure 7.23. The application of the FPP with the WED and the ducted propellers for such ship types and design will satisfy the EEDI requirements up to 2020, while the reference ship design arrangements with the application of the CLT propeller with the WED will almost meet the 2025 EEDI expectations.

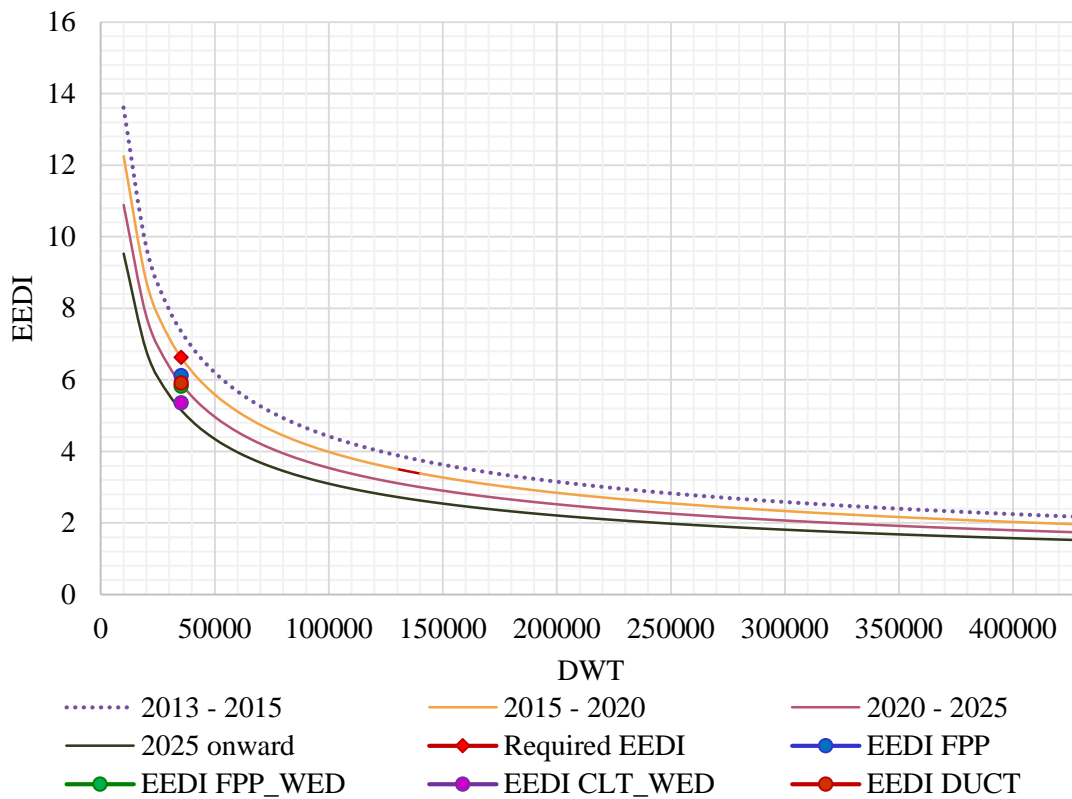


Figure 7.23 The EEDI results for all propeller systems (FPP – the convention fixed pitch propeller, DUCT – the ducted propeller, FPP\_WED – the original fixed pitch propeller with the wake equalizing duct, CLT\_WED – the CLT propeller with the wake equalizing duct).

After completing a month-long theoretical voyage simulation under realistic weather conditions (described in Chapter 6), the results have been plotted and illustrated in Figure 7.24 as well as summarised in Table 7.11 and Table 7.12. Since the ducted propeller (DUCT) is more beneficial at ballast condition, its voyage performance is found to be more advantageous when competing with the original propeller system with the wake equalizing duct (FPP\_WED) with the possible savings of 4 tonnes of fuel per voyage, while application of the CLT propeller with the WED resulted in savings of 93 tonnes of fuel per voyage compared to the conventional fixed pitch propeller (FPP).

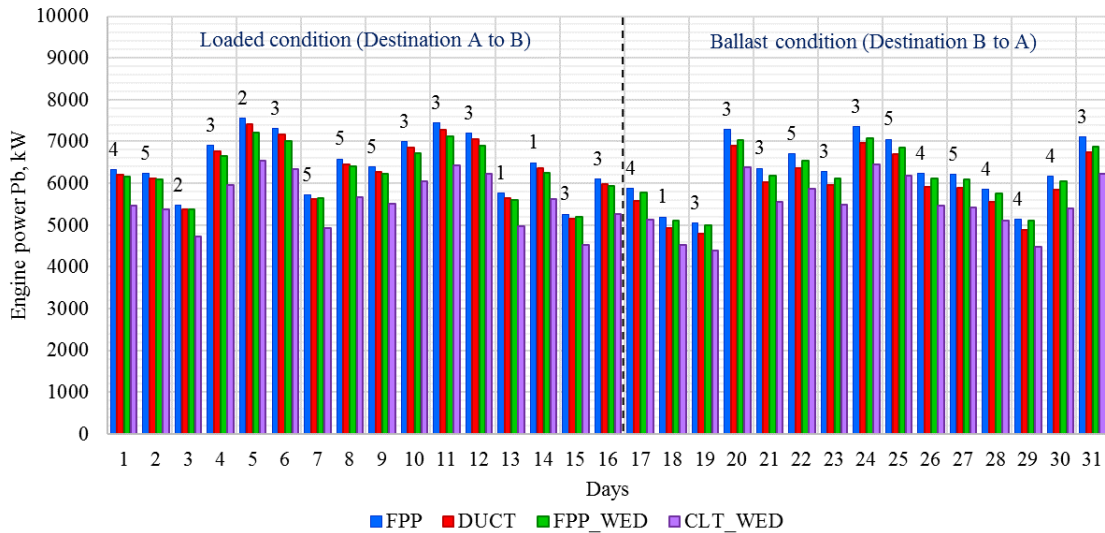


Figure 7.24 The voyage simulation results of all propeller systems: FPP – the convention fixed pitch propeller, DUCT – the ducted propeller, FPP\_WED – the original fixed pitch propeller with the wake equalizing duct, CLT\_WED – the CLT propeller with the WED. Numbers at the top of the graph are Beaufort numbers.

Table 7.11 The fuel consumption and emissions footprint performance per voyage (FPP – the convention fixed pitch propeller, DUCT – the ducted propeller, FPP\_WED – the original fixed pitch propeller with the wake equalizing duct, CLT\_WED – the CLT propeller with the wake equalizing duct).

	<i>FPP</i>	<i>FPP_WED</i>	<i>CLT_WED</i>	<i>DUCT</i>	
Fuel	785	758	692	754	tonnes per voyage
$CO_2$	2506	2422	2210	2407	tonnes per voyage
$NO_x$	64.1	61.4	54.2	61.7	tonnes per voyage
$SO_2$	3.7	3.6	3.3	3.6	tonnes per voyage
$CO$	2.2	2.2	1.9	2.1	tonnes per voyage
$HC$	1.4	1.4	1.2	1.4	tonnes per voyage

Table 7.12 The average SFOC and engine load per voyage. (FPP – the convention fixed pitch propeller, DUCT – the ducted propeller, FPP\_WED – the original fixed pitch propeller with the wake equalizing duct, CLT\_WED – the CLT propeller with the wake equalizing duct).

	<i>FPP</i>		<i>FPP_WED</i>		<i>CLT_WED</i>		<i>DUCT</i>		
	Loaded	Ballast	Loaded	Ballast	Loaded	Ballast	Loaded	Ballast	
LOAD	88.0	85.4	88.9	85.8	88.4	85.4	88.9	85.4	%
SFOC	165.6	165.2	164.6	164.2	168.1	167.9	165.0	164.2	g/kWh

Based on the ship performance analysis it is considered that the most beneficial propeller system is a combination of the CLT propeller with the wake equalizing duct, followed by the conventional fixed pitch propeller with the wake equalizing duct and the ducted propeller. It has also been discovered that during the voyage simulation the ducted propeller has performed better than the original fixed pitch propeller with the wake equalizing duct since the ducted propeller is found to be more efficient at the ballast condition.

## 8 Propeller Optimisation

Besides the energy efficient propeller designs, examined in the previous chapter, there are also a number of propeller design characteristics that can be further optimised to potentially provide a positive impact on the overall propulsion efficiency. Namely, propulsion efficiency improvements may be achieved by increasing the propeller diameter or decreasing the blade area ratio (or both). However, the scale of changes is restricted by the hull dimensions and the level of generated hull surface pressure pulses, in the case of an artificially increased propeller diameter, while governed by cavitation avoidance margins when decreasing the propeller blade area ratio.

The cavitation phenomenon occurs when the local fluid pressure drops to the vapour pressure level or below causing the formation of cavities. When these cavitation structures collapse, mostly in times considerably less than one second, this gives rise to significant pressure fluctuations induced by a variety of collapse mechanisms. The presence of cavitation disturbs the flow around the propeller surface, which can in extreme cases negatively affect the propulsion characteristics, namely, give rise to deteriorations in thrust and torque performance resulting in the reduction of the propulsion efficiency and, potentially, in erosion on the propeller blade surface due to the collapsing cavitation bubbles (Molland et al. 2011). In addition, hydrodynamic pressure fluctuations, also caused by the cavitation bubbles, may result in an unacceptable level of noise and vibration in the ship.

To limit the harmful effects of cavitation, it is important to carefully select the blade area ratio ensuring that the global thrust loading, in other words, the ratio of the delivered thrust to the total blade area of the propeller, lies within the acceptable cavitation limits. The cavitation limits are normally estimated for each propeller case individually during the detailed design stage by applying the Gutsche or Walcher “bucket” type diagrams or by implementing cavitation tunnel tests and detailed flow analysis.

For the preliminary cavitation predictions as well as for the calculation of a suitable *BAR*, as already mentioned in Chapter 2.3, there are two widely used empirical methods, namely, those derived by Burrill and Keller. Both the Burrill and Keller methods have been extensively used by propeller designers for preliminary estimations of the required *BAR* to avoid excessive cavitation (Carlton 2012), while according to (Trodden & Woodward 2013), the Burrill’s method has shown more conservative results than the Keller’s formula. It is important to emphasize that according to the Burrill’s method an acceptable upper limit

of back cavitation for merchant vessels is in the region of 5 percent, while the thrust breakdown does not usually occur before approximately 20 percent back cavitation has been developed. The actual level of the breakdown limit is a matter for the propeller designer in terms of the ship's operational profile.

In case a smaller *BAR* is desired, the control of cavitation appearance may also be achieved by increasing the propeller diameter, which helps to distribute the excessive thrust loading across the propeller disk while smoothing out the fluctuating pressure peaks. In addition, as already outlined above, the application of bigger propeller diameters is more hydrodynamically efficient. However, there are certain constraints and rules that have to be observed when increasing the propeller diameter artificially, while keeping the rotational speed constant.

The first one is to keep sufficient clearances between the propeller and the hull, which are important to minimise the risk of on-board noise and vibration. Secondly, a larger propeller diameter could give rise to the wake fluctuations causing the reduction in hull efficiency due to a decrease in the average value of the wake fraction (Ghose & Gokarn 2009). It is also important to take into account the propeller and the hull interactions, namely hull surface pressure pulses being transmitted from the propeller through the water and also the global system of forces and moments transmitted through the bearing system to the hull. The hull surface pressure depends upon the ship type, shape of the stern and the propeller size.

In summary, the reduction of the propeller blade area ratio will most likely result in improvements of the propeller performance in terms of energy efficiency, while also may increase the risk of cavitation and attendant erosion. However, from the current research and development in this area, we see a rising interest from the industry to minimise the damage from the cavitation phenomenon not only by implementing cavitation safe propeller designs but also by finding innovative composite materials or coatings with robust anti-cavitation properties.

For example, in (Yamatogi et al. 2009) the authors have examined the cavitation erosion resistance of the Aramid Fibre Reinforced Polymer (AFRP) and found that the fibrils covered over the surface tend to absorb the impact of impulses during the cavitation collapse making it difficult for erosion to progress. Other work done by (Bregliozzi et al. 2005) is focused on the examination of the cavitation erosion behaviour of AISI 304 steel and high nitrogen containing austenitic stainless steel as a function of the grain size. It has

been found that the fine grain structure of austenitic stainless steels leads to an increase in the surface density of grain boundary, which provides a dominant supporting action against cavitation compared to the medium and coarse grain steel samples.

Therefore, should the robust anti-cavitation materials and propeller coatings substitute the present propeller compositions prone to cavitation in the near future, this will also influence the current cavitation margins used in the design procedures as well as the requirements for the propeller blade area sizes providing the possibility for its potential reductions for the efficiency gaining purposes. Even with existing materials, (Moulijn et al. 2006) showed if we understood the cavitation margins adequately than the propeller efficiency could rise by 5 percent or more.

This chapter explores the potential effect caused by the artificially decreased propeller blade area ratios and artificially increased propeller diameters on the overall propulsion efficiency as well as the evaluations of risks in terms of cavitation and hull surface pressures for the reference ship type and design.

## 8.1 The Effect of BAR on Ship Efficiency

Since the minimum blade area ratio used in the Wageningen B-screw series regression-based method for a 4-bladed propeller is equal to 0.4, the effect of the blade area ratios on ship propulsion performance ranging from 0.4 to 0.7 has been investigated in this section and compared with the initial *BAR* value of 0.56. A list of considered propeller design combinations is presented in Table 8.1, where the highlighted area indicates the original propeller characteristics.

Table 8.1 Considered propeller design characteristics.

<i>BAR</i>	0.4	0.45	0.5	0.5628	0.6	0.65	0.7
Diameter	5.65	5.65	5.65	5.65	5.65	5.65	5.65
<i>P/D</i>	0.65	0.65	0.65	0.65	0.65	0.65	0.65
<i>Z</i>	4	4	4	4	4	4	4

The effect of *BAR* on three efficiency components, namely the hull efficiency ( $\eta_H$ ), the relative-rotative efficiency ( $\eta_R$ ) and the open water efficiency ( $\eta_O$ ) has been estimated using the Ship Performance Simulation model.

### **Hull efficiency**

Since the hull efficiency ( $\eta_H$ ) is a function of the wake fraction ( $w$ ) and thrust deduction coefficient ( $t$ ) which, in the Holtrop and Mennen analysis depend upon the propeller

diameter ( $D$ ) and a number of different hull design parameters, the blade area ratio values do not affect the hull efficiency performance neither included in the hull efficiency calculation process.

### ***Relative-rotative efficiency***

Generally, relative-rotative efficiency describes the relationship between the torque absorbed by the propeller when operating in a uniform flow field (an open water) at a particular speed and that absorbed when working in a mixed wake field with the same mean velocity. An analysis of the relative-rotative efficiency  $\eta_R$  changes for the range of  $BAR$ s, using the Holtrop and Mennen formulation (8.1), has shown the proportional but moderate increase in  $\eta_R$  of approximately 0.5 percent on average with decreasing  $BAR$ . The  $\eta_R$  results are presented in Figure 8.1

$$\eta_R = 0.9922 - 0.05908BAR + 0.07424(C_p - 0.0225lcb) \quad 8.1$$

where  $C_p$  is the prismatic coefficient,  $lcb$  is the longitudinal position of centre of buoyancy.

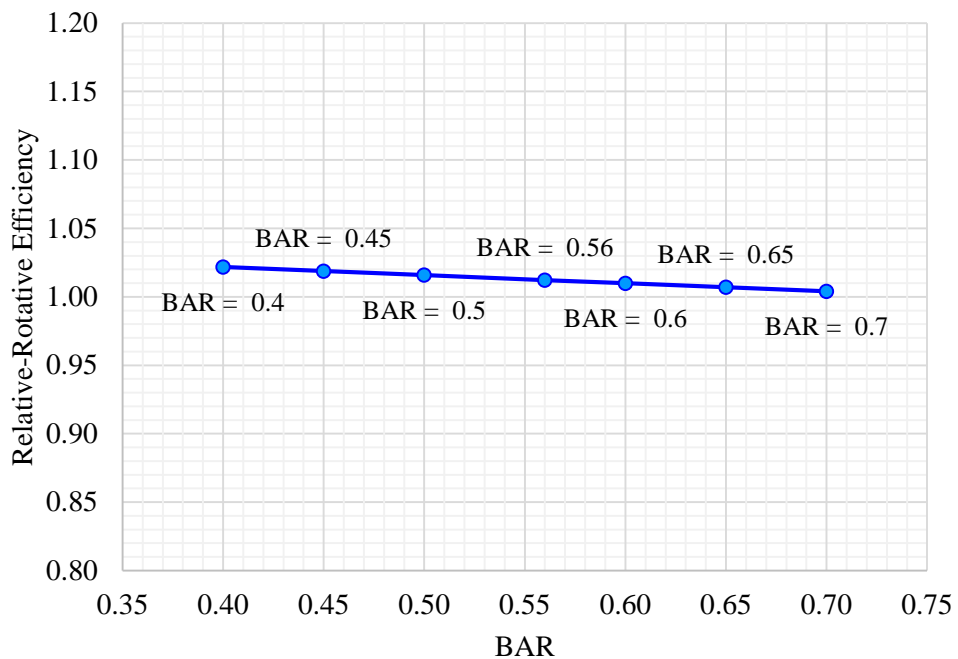


Figure 8.1 Effect of  $BAR$  on the relative-rotative efficiency  $\eta_R$ .

### ***Open water efficiency***

The open water efficiency values have been estimated for the range of blade area ratios using the Wageningen B-screw series regression-based approach. The results have shown an increase in  $\eta_O$  with decreasing  $BAR$ s, as demonstrated in Figure 8.2. According to the calculation results, the scale of impact of  $BAR$  on the open water efficiency is gradually decreasing, being almost negligible between  $BAR = 0.45$  and  $BAR = 0.4$ .

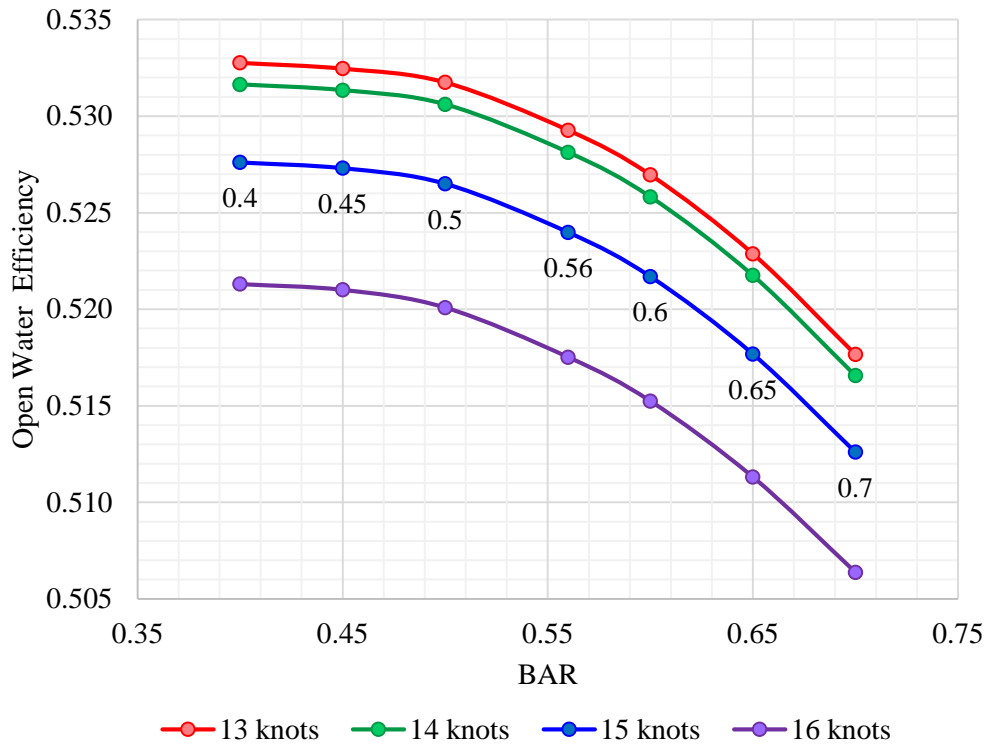


Figure 8.2 Effect of *BARs* on the open water efficiency for the 4-bladed propeller.

The difference in the open water efficiency performance between the original  $BAR = 0.56$  and the minimum for this case study  $BAR = 0.4$  is found to be approximately 0.5 percent in case of the 4-bladed propeller. Alternatively, the reduction in efficiency with the increase of the  $BAR$  up to 0.65 is equal to 1.2 percent on average as a result of increased skin friction over the larger blade area. Finally, the effect of  $BARs$  on ship delivered power  $P_D$  is demonstrated in Figure 8.3.

For an analysis of the potential cavitation occurrence associated with the reduction of  $BAR$ , the Burrill’s method has been used in this work. The 2.5 and 5 percent back cavitation curves on Burrill’s diagram, acting as thresholds for the reference products tanker cavitation allowance, have been reproduced and plotted in Figure 8.4. The thrust loadings  $\tau_c$  and cavitation numbers  $\sigma$  for a range of blade area ratios ( $BAR = 0.4, 0.45 \dots 0.7$ ) have been estimated using Burrill’s approach under different ship speeds and plotted in Figure 8.4 for comparative reasons.

As can be seen from Figure 8.4, the original propeller  $BAR = 0.56$  (the green line) is located much below the 2.5 percent back cavitation Burrill’s curve ensuring that the original propeller cavitation performance even at the maximum speeds nominally lies within 2.5 percent back cavitation limits.

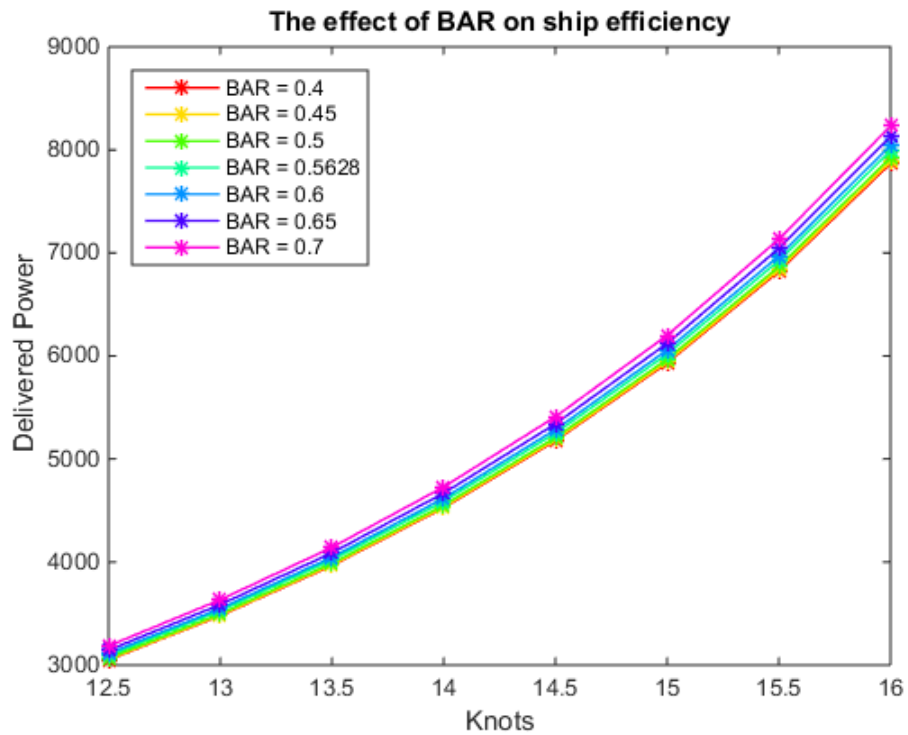


Figure 8.3 Effect  $BARs$  on ship delivered power  $P_D$  over a range of speeds.

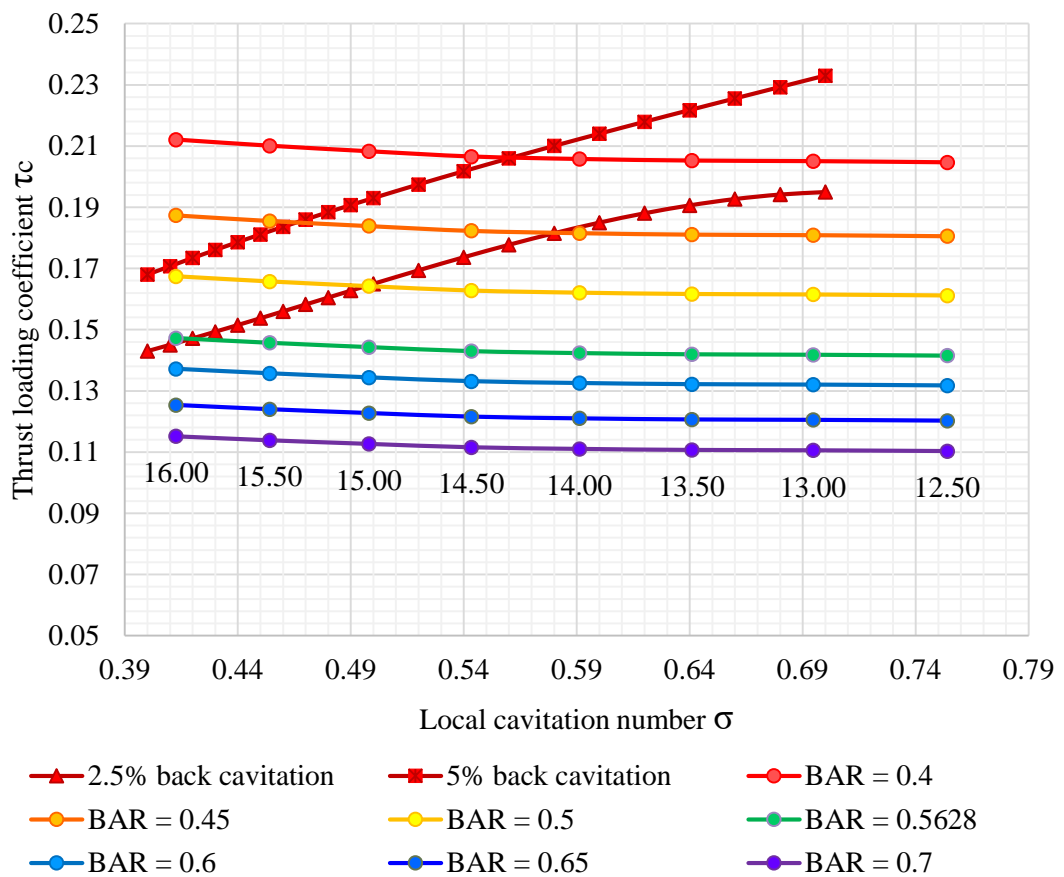


Figure 8.4 Artificial  $BAR$  cavitation performance based on Burrill's curves.

The artificially decreased blade area ratio performances of up to  $BAR = 0.45$  have shown the acceptable limits of cavitation in open water within the 5 percent cavitation margin, whereas in the case of the lowest  $BAR = 0.4$ , the cavitation performance slightly exceeds the recommended factors.

The comparison results for the propellers with the original  $BAR = 0.56$ ,  $BAR = 0.5$  and  $BAR = 0.4$  are listed in Table 8.2 for the ship design condition at the recommended service speed of 14.6 knots, indicating the reductions in the delivered power requirements of 0.92 percent when the  $BAR$  is decreased to 0.5 and by 1.54 percent when the  $BAR$  is minimised to 0.4.

Table 8.2 Comparison results of fixed pitch performance with reduced  $BAR$ s at design condition and operational speed of 14.6 knots.

Parameter	Symbol	$BAR = 0.5628$	$BAR = 0.5$	$BAR = 0.4$	Metric
Propeller diameter	$D$	5.65	5.65	5.65	$m$
Pitch to diameter ratio	$P/D$	0.6523	0.6523	0.6523	-
Number of blades	$Z$	4	4	4	-
Wake fraction coefficient	$w$	0.386	0.386	0.386	-
Thrust reduction coefficient	$t$	0.231	0.231	0.231	-
Relative-rotative efficiency	$\eta_R$	1.012	1.016	1.022	-
Hull efficiency	$\eta_H$	1.253	1.253	1.253	-
Open-water efficiency	$\eta_o$	0.5442	0.5466	0.5468	-
Propeller torque coefficient	$K_Q$	0.0166	0.0167	0.0169	-
Propeller thrust coefficient	$K_T$	0.1411	0.1427	0.1449	-
Thrust loading coefficient	$\tau_C$	0.1432	0.1630	0.2068	-
Local cavitation number	$\sigma$	0.5342	0.5342	0.5342	-
Hull surface pressure	$p_z$	1.89	1.89	1.89	$kN/m^2$
Quasi-propulsive coefficient	$QPC$	0.689	0.696	0.700	-
Delivered power	$P_D$	5400	5351	5319	$kW$
Power reduction	-	-	0.92	1.54	%

In addition, calculations have been performed for the ballast and loaded conditions. The results in the form of delivered power versus ship speed are illustrated in Figure 8.5 for the original and minimum  $BAR$ s of 0.56 and 0.4 respectively, while the average power reductions are listed in Table 8.3 showing that the maximum benefit has been achieved with the minimum  $BAR = 0.4$  under the ballast operational condition.

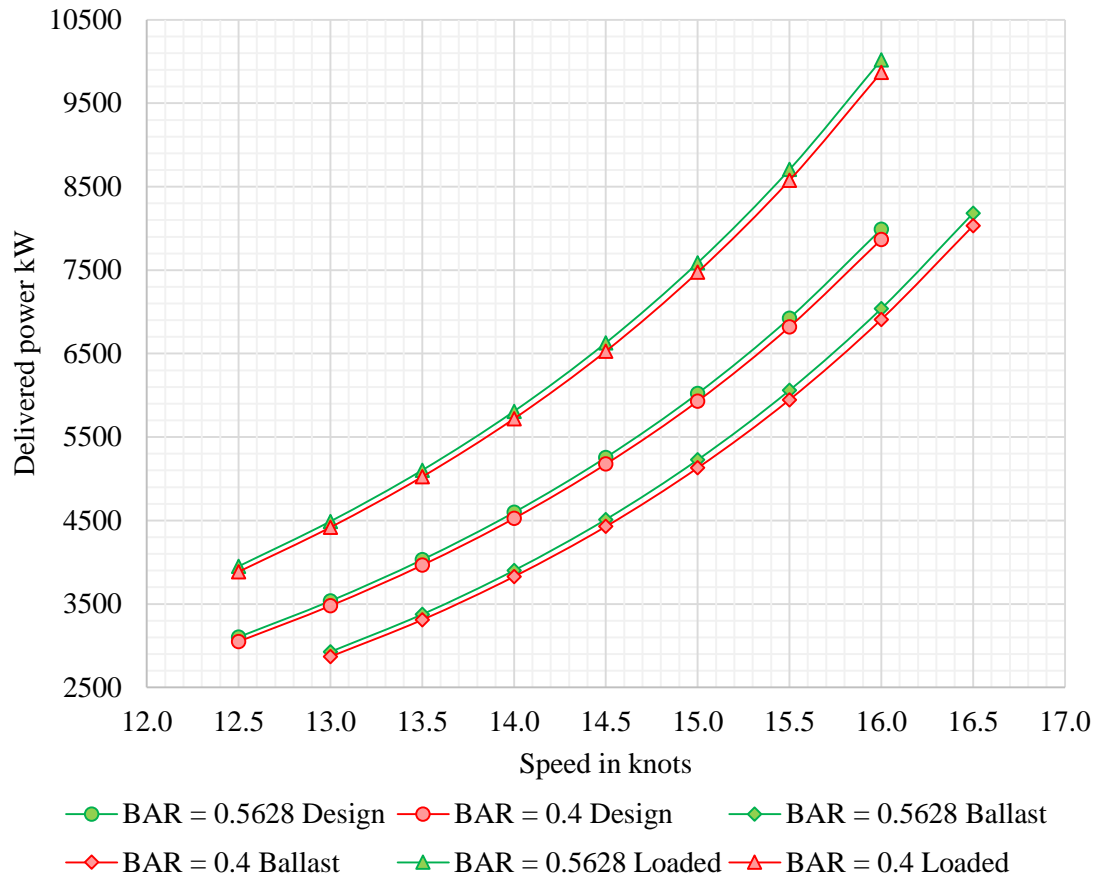


Figure 8.5 Power absorption of the conventional fixed pitch propeller with the original  $BAR = 0.5628$  vs  $BAR = 0.4$  under design, ballast and loaded conditions.

Table 8.3 Delivered power reductions due to  $BAR = 0.5$  and  $BAR = 0.4$ .

Condition	<i>Ballast</i>	<i>Designed</i>	<i>Loaded</i>	Metric
Reduction of $P_D$ for $BAR = 0.5$	1.06	0.93	0.88	%
Reduction of $P_D$ for $BAR = 0.4$	1.88	1.58	1.55	%

## 8.2 The Effect of Artificially Increased Propeller Diameters

In this section, a range of the artificially increased propeller diameters has been selected in order to analyse the effect of the increased/decreased diameters on propeller characteristics and the propulsion efficiency while keeping the rotational speed constant. The diameters were selected by means of the original propeller acting as a midpoint of the spectrum surrounded by the artificially increased and decreased by 2.5 and 5 percent diameters as shown in Table 8.4. It should be noted that the resulting largest propeller, namely the original diameter increased by 5 percent, is found to be 5.93 m, which is not the maximum possible diameter for the reference stern shape according to the normally acceptable clearances recommendations. The maximum possible propeller diameters for the reference ship along with the clearances calculations are covered in the next chapter.

Table 8.4 Results of the design procedure: the artificial propellers characteristics.

Parameter	Symbol	5.0%	2.5%	0.0%	-2.5%	-5.0%	Metric
Propeller diameter	$D$	5.93	5.79	5.65	5.51	5.37	$m$
Pitch to diameter ratio	$P/D$	0.586	0.619	0.655	0.695	0.74	-
Blade area ratio	$BAR$	0.48	0.52	0.56	0.61	0.66	-
Number of blades	$Z$	4	4	4	4	4	-

For prediction of the optimum propeller characteristics associated with the selected diameters, the standard design procedure has been performed starting from the point of calculation of the optimum propeller diameter being substituted by the artificial diameters range, as outlined in Figure 8.7. Hence, the range of the optimum  $P/D$  ratios and  $BAR$ s has been further estimated by following the standard propeller design procedure described in Appendix II.

It is important to emphasize that in order to keep the initial blade area ratio within the original cavitation limits, first the thrust loading coefficient along with the cavitation number have been estimated for the original propeller and then, based on the resulted values, interpolated for other diameters keeping them in line with the original thrust loading factor as shown in Figure 8.6. The resulted propeller characteristics are tabulated in Table 8.4.

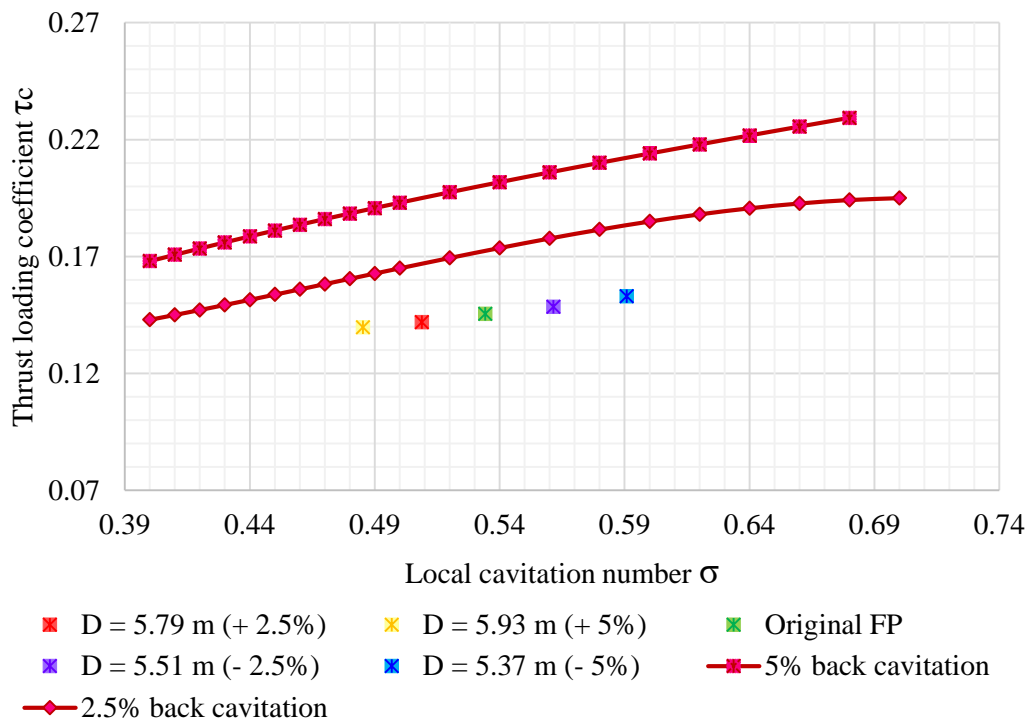


Figure 8.6 Thrust loading distribution for the artificial propeller diameters.

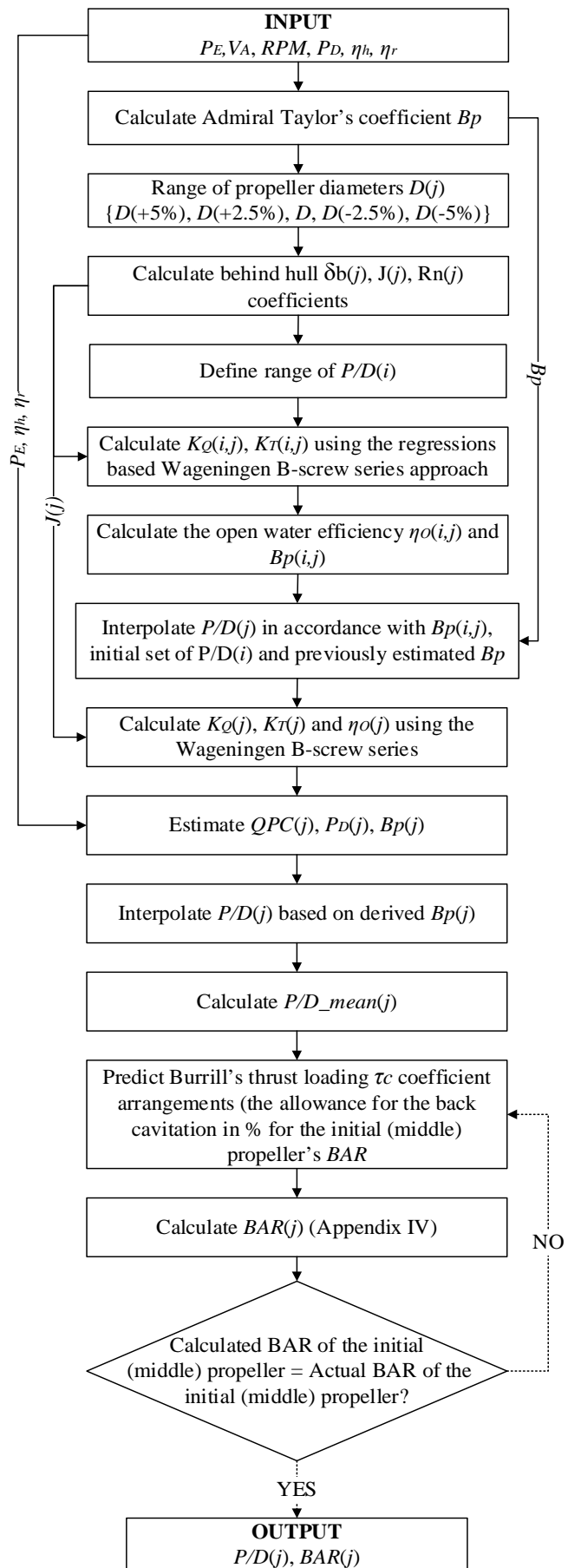


Figure 8.7 Propeller design process based on the artificially selected propeller diameters.

Similarly to the previously analysed *BARs*, all three components of the quasi propulsive coefficient (*QPC*), namely hull efficiency ( $\eta_H$ ), relative rotative efficiency ( $\eta_R$ ) and the open water efficiency ( $\eta_o$ ) have been analysed for each artificial propeller design as described below.

### ***Hull efficiency***

Since “the mean circumferential wake at any radius is greater at the inner radii in a single screw ship” (Ghose & Gokarn 2009), the increase of the propeller diameter results in a decrease in the average wake fraction, resulting in the overall decrease in the hull efficiency ( $\eta_H$ ). Such pattern, also observed in (Kim & Fraas 1992), in many cases may significantly reduce or even cancel out the beneficial effects of the bigger propeller diameter on the propulsive efficiency. It should be noted that such efficiency behaviour is mostly relevant to full form ships that do not suffer from the separation effects on the upper part of the propeller aperture and this is not always true in the case of V-form ships. However, in this case the scale of decrease in the hull efficiency with the artificially increasing propeller diameter is relatively insignificant. The resulted hull efficiency pattern is demonstrated in Figure 8.8.

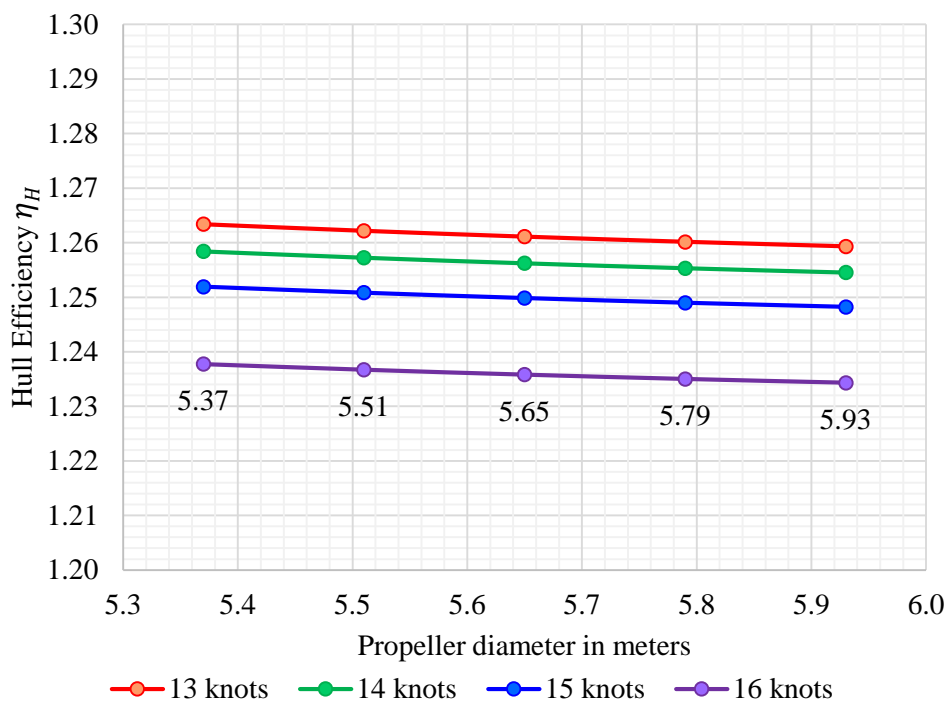


Figure 8.8 Hull efficiency behaviour with the artificially changing propeller diameters.

### ***Relative-rotative efficiency***

The relative-rotative efficiency ( $\eta_R$ ) is moderately increasing with the increasing propeller diameter due to decreasing *BAR*s. The relative-rotative efficiency results are shown in Figure 8.9.

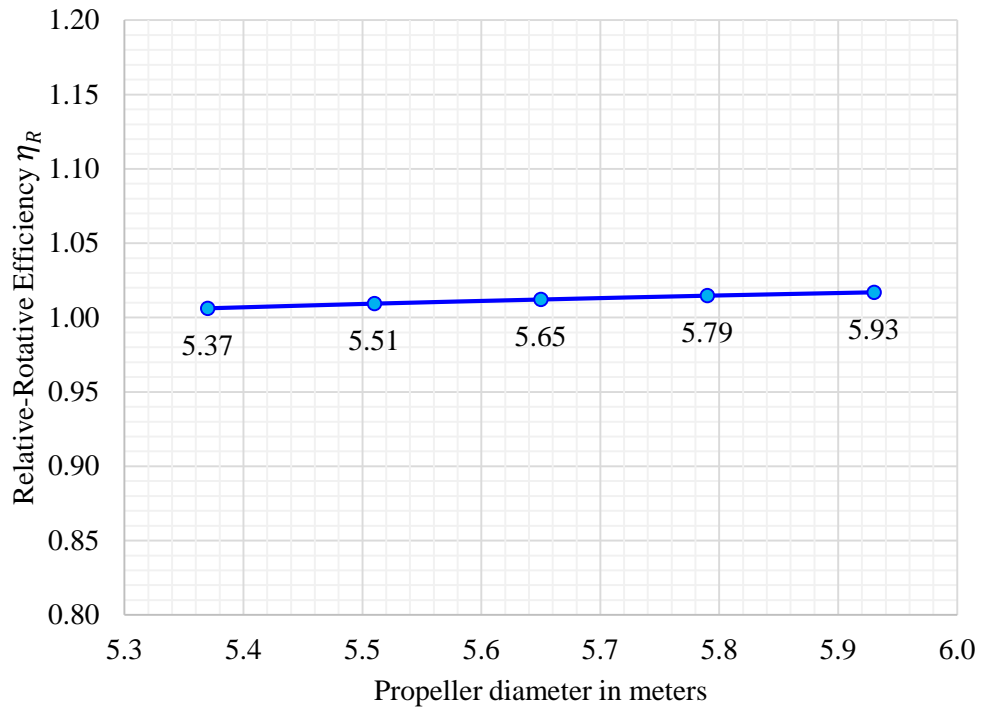


Figure 8.9 Relative-rotative efficiency behaviour with changing propeller diameters.

### ***Open water efficiency***

The open water efficiency has been estimated using the Wageningen B-screw series regression-based method. The resulted  $\eta_o$  pattern is represented in Figure 8.10 showing that the open water efficiency is increasing with the increasing propeller diameter/decreasing *BAR* but at a much lower scale after the original (optimum) diameter point. However, even slight decrease of the propeller diameter by 2.5 percent would have noticeable negative impact onto the open water efficiency performance while the application of the bigger propeller diameter (for example by 5 percent in this case) resulted in the open water efficiency improvement by 0.7 percent.

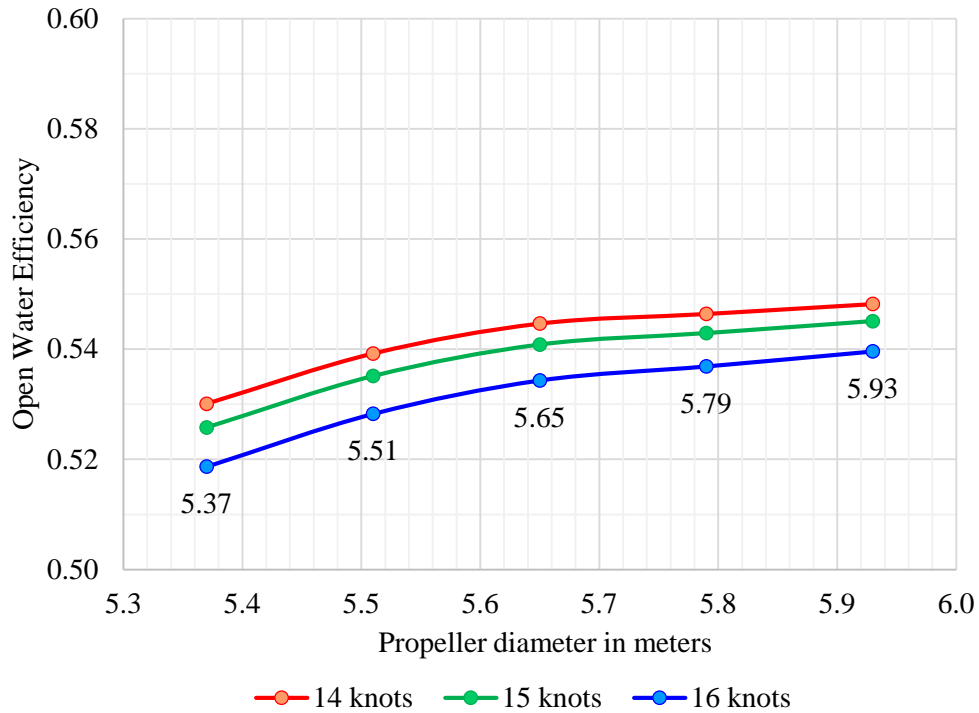


Figure 8.10 Open water efficiency behaviour with changing propeller diameters.

Lastly, the impact of the artificially increased/decreased diameters on ship delivered power  $P_D$  is demonstrated in Figure 8.11.

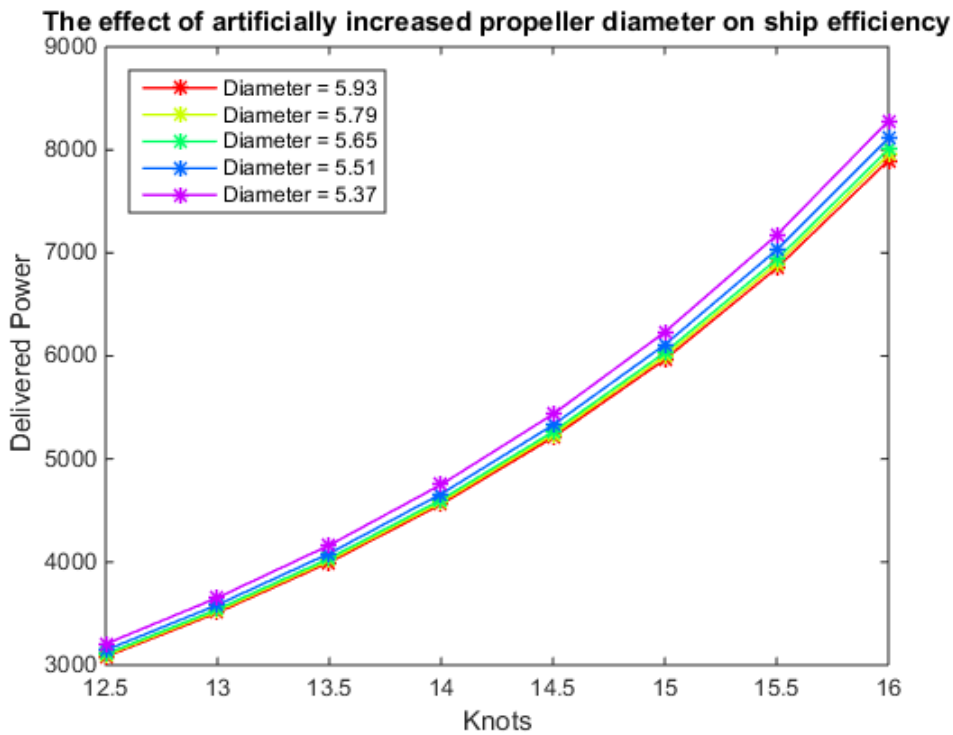


Figure 8.11 Effect of the artificially increased propeller diameters on ship delivered power  $P_D$  over a range of speeds.

The cavitation performance analysis has also been evaluated and plotted to compare with the Burrill's cavitation reference lines as illustrated in Figure 8.12. As expected, the increased propeller diameters have cancelled out the potential increase of the back cavitation due to a decrease of the *BARs* and helped to keep the potential cavitation occurrence within the acceptable limits for all of the operational ship speeds (2.5 percent back cavitation). In fact, the thrust loadings for bigger propeller diameter/lower *BAR* are found to be even lower than the original values.

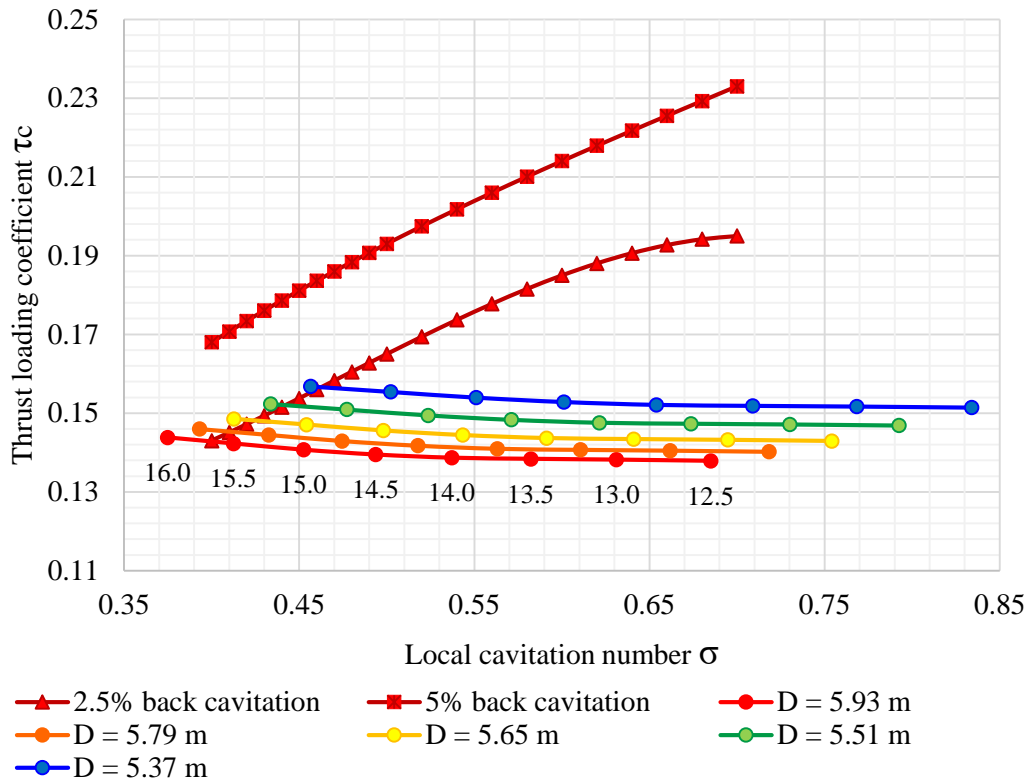


Figure 8.12 Cavitation performance due to the artificial diameters based on Burrill's curves.

As outlined previously, a too large propeller may cause unwanted on-board vibration and noise due to the rise of the hull surface pressure pulses. As such, the corresponding hull blade rate surface pressures  $p_z$  have also been estimated using Holden's hull surface pressure prediction method identified in (Carlton 2012, pp.281–282). Since a standard value of the acceptable hull surface pressures  $p_z$  is around  $2 \text{ kN/m}^2$ . The resulting  $p_z$  associated with the biggest propeller diameter in the artificial range ( $D = 5.93 \text{ m}$ ) equals  $2.17 \text{ kN/m}^2$ , showing that the installation of this propeller with the original rotational speed may marginally already have a negative effect on the level of vibration and noise, while making it difficult to further increase the propeller diameter without optimising the rotational speed even if the sufficient hull clearances are available. Alternatively, some minor re-design of the ship's after-body might be helpful.

Table 8.5 Comparison results of the fixed pitch propeller with artificial propeller diameters ad design condition and speed of 14.6 knots.

Parameter	Symbol	5.0%	2.5%	0.0%	-2.5%	-5.0%	Metric
Propeller diameter	$D$	5.93	5.79	5.65	5.51	5.37	$m$
Pitch to diameter ratio	$P/D$	0.5856	0.6186	0.6550	0.6951	0.7395	-
Blade area ratio	$BAR$	0.4804	0.5189	0.5628	0.6099	0.6635	-
Number of blades	$Z$	4	4	4	4	4	-
Wake fraction coefficient	$w$	0.383	0.384	0.386	0.387	0.389	-
Thrust reduction coefficient	$t$	0.228	0.229	0.231	0.232	0.233	-
Relative-rotative efficiency	$\eta_R$	1.017	1.015	1.012	1.009	1.006	-
Hull efficiency	$\eta_H$	1.251	1.252	1.253	1.254	1.255	-
Open-water efficiency	$\eta_O$	0.547	0.545	0.543	0.537	0.528	-
Propeller torque coefficient	$K_Q$	0.1194	0.1300	0.1424	0.1570	0.1741	-
Propeller thrust coefficient	$K_T$	0.0134	0.0149	0.0167	0.0191	0.0220	-
Thrust loading coefficient	$\tau_C$	0.1397	0.1420	0.1446	0.1485	0.1530	-
Local cavitation number	$\sigma$	0.4853	0.5088	0.5342	0.5614	0.5908	-
Hull surface pressure	$p_z$	2.17	2.03	1.89	1.75	1.63	$kN/m^2$
Quasi-propulsive coefficient	$QPC$	0.695	0.692	0.688	0.68	0.667	-
Delivered power	$P_D$	5351	5380	5409	5475	5584	$kW$
Power reduction	-	1.07	0.54	0.00	-1.22	-3.14	%

In addition, calculations have been performed for the ballast and loaded conditions. The results in the form of delivered power versus ship speed are illustrated in Figure 8.13 for the original, minimum and maximum diameters of 5.65m, 5.37m and 5.93m respectively, while the average power reductions are listed in Table 8.6. The results have indicated that the maximum efficiency benefit has been achieved with the  $D = 5.93m$  under the ballast operational condition when compared with the original fixed pitch propeller diameter of 5.65m.

Table 8.6 Average fluctuations of the delivered power  $P_D$  due to artificially changing diameters.

Condition	<i>Ballast</i>	<i>Designed</i>	<i>Loaded</i>	Metric
Reduction of $P_D$ for $D = 5.37 m$	-3.57	-3.18	-3.26	%
Reduction of $P_D$ for $D = 5.51 m$	-1.46	-1.24	-1.29	%
Reduction of $P_D$ for $D = 5.65 m$	0.00	0.00	0.00	%
Reduction of $P_D$ for $D = 5.79 m$	0.81	0.56	0.62	%
Reduction of $P_D$ for $D = 5.93 m$	1.66	1.13	1.25	%

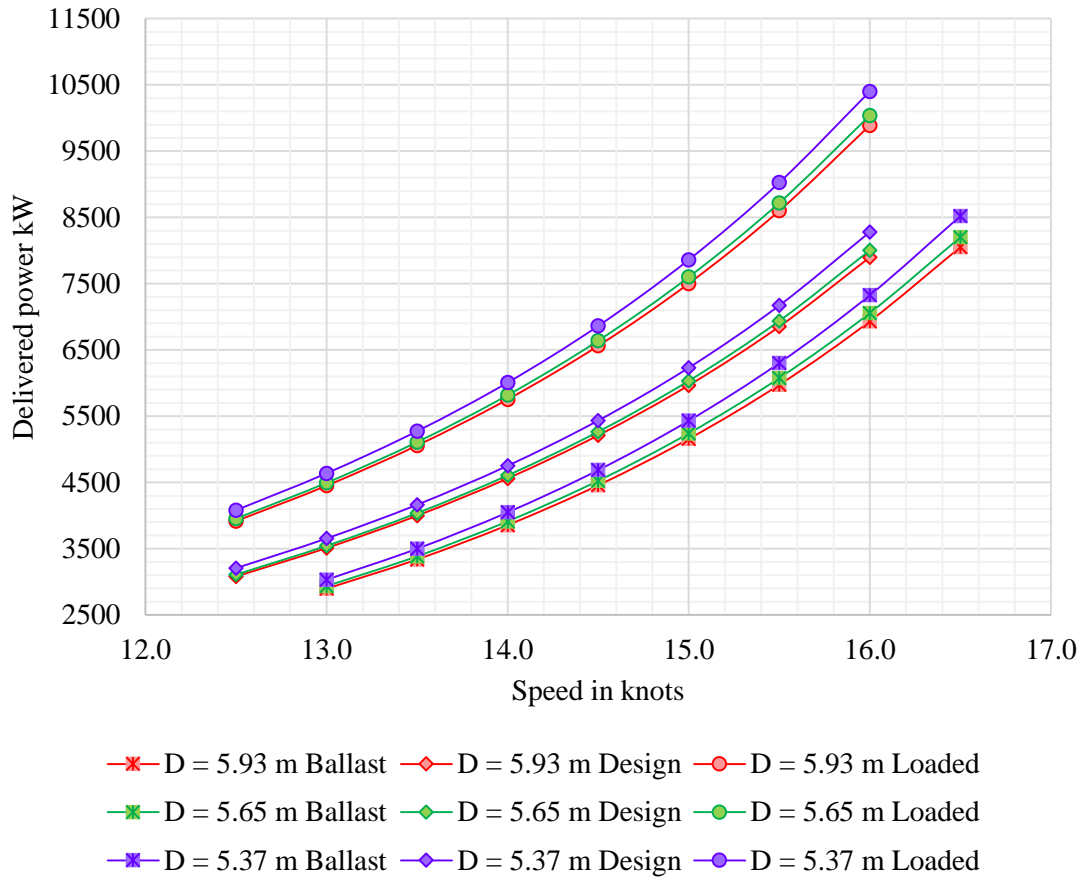


Figure 8.13 Comparison plot of the power absorption requirements of the fixed pitch propeller with the original  $D = 5.65\text{m}$  and the artificially increased and decreased diameters by 5 percent under design, ballast and loaded conditions.

### 8.3 Impact on the Energy Efficiency Indicators

This subsection is dedicated to the comparative analysis of the optimised propeller designs described in this chapter, namely the fixed pitch propeller with the artificially reduced blade area ratio ( $BAR = 0.4$ ) and the fixed pitch propeller with the artificially increased diameter by 5 percent. These designs are compared with the original fixed pitch propeller in the form of the Energy Efficiency Indicators (EEIs) covering the fuel consumption, the emissions footprint and the EEDI index.

First, the delivered power results of all cases were compared with each other under load, design and ballast conditions in accordance with the designed ship speeds of 14.07 knots at loaded, 14.6 knots at design and 15.02 knots at ballast conditions. The results are summarised in Figure 8.14. The most beneficial propeller performance has been achieved by the fixed pitch propeller with reduced blade area ratio ( $BAR = 0.4$ ), following by the fixed pitch propeller with the artificially increased diameter by 5 percent, however the

differences between their performances are marginal, while the most noticeable impact was achieved under the ballast condition for both cases.

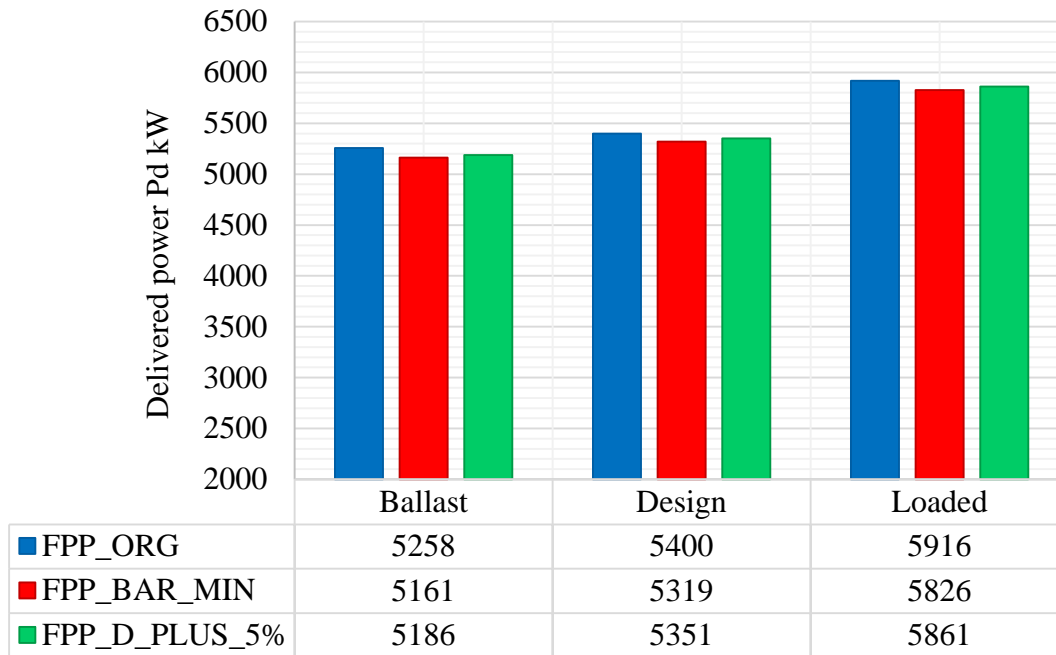


Figure 8.14 Comparative analysis of the required delivered power under different loads and corresponding operational speed. (FPP\_ORG - the original fixed pitch propeller, FPP\_BAR\_MIN - the fixed pitch propeller with the artificially reduced blade area ratio ( $BAR = 0.4$ ), FPP\_D\_PLUS\_5% - the fixed pitch propeller with the artificially increased diameter by 5 percent).

Both propulsive systems were coupled to the original 5S50ME-C engine, while the SMCRs in each case were changed in accordance with the propeller performance at 15 knots with added 15 percent of the sea margin and compared with the original propeller performance. The list of selected SMCR power points along with SMCR speed (which is constant in all cases) are summarised in Table 8.7.

Table 8.7 List of SMCRs for each propeller case (FPP\_ORG - the original fixed pitch propeller, FPP\_BAR\_MIN - the fixed pitch propeller with the artificially reduced blade area ratio ( $BAR = 0.4$ ), FPP\_D\_PLUS\_5% - the fixed pitch propeller with the artificially increased diameter by 5 percent).

15 knots	FPP_ORG	FPP_BAR_MIN	FPP_D_PLUS_5%	
SMCR	7347	7259	7301	kW
RPM	127	127	127	rpm
Engine	5S50ME-C	5S50ME-C	5S50ME-C	

In addition, Figure 8.15 along with its enlarged version for easier reading Figure 8.16 demonstrate the load diagram of the original 5S50ME-C together with the engine service curves for each propeller system and their Normal Continuous Ratings (NCR) at 90 percent SMCR corresponding to 14.6 knots operational speed.

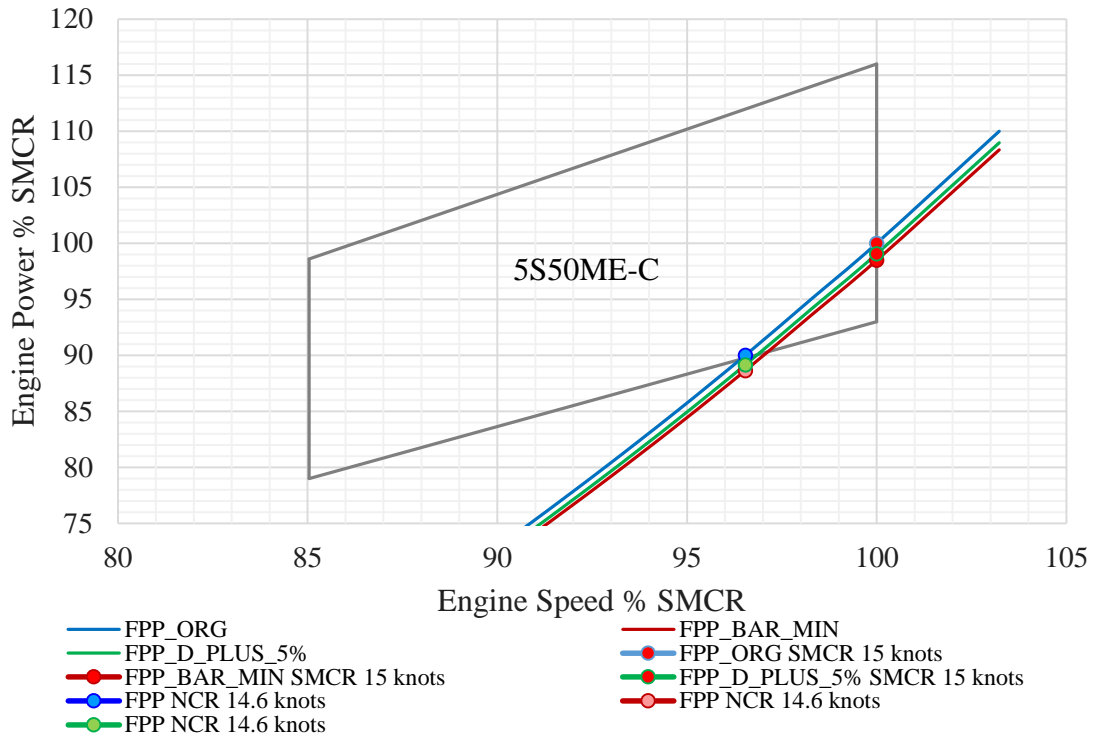


Figure 8.15 Engines service curves for FPP\_ORG, FPP\_BAR\_MIN, FPP\_D\_PLUS\_5% propeller systems. (FPP\_ORG - the original fixed pitch propeller, FPP\_BAR\_MIN - the fixed pitch propeller with the artificially reduced blade area ratio ( $BAR = 0.4$ ), FPP\_D\_PLUS\_5% - the fixed pitch propeller with the artificially increased diameter by 5 percent).

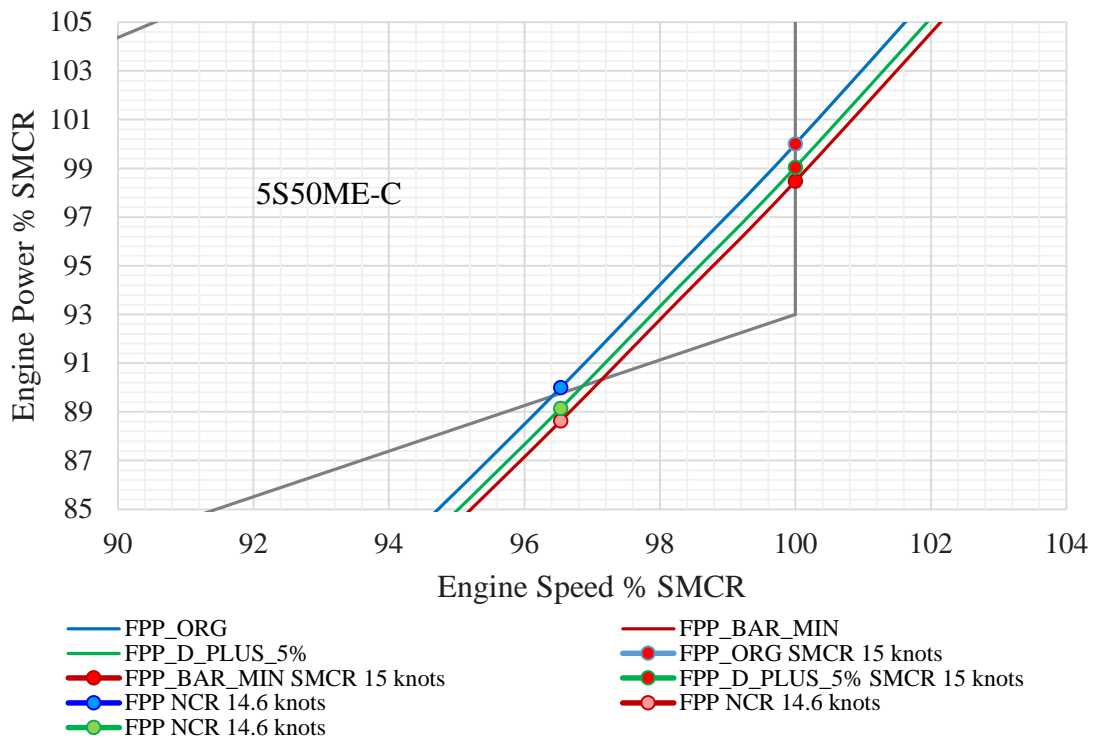


Figure 8.16 Enlarged version of Figure 8.15. Engines service curves for FPP\_ORG, FPP\_BAR\_MIN, FPP\_D\_PLUS\_5% propeller systems. (FPP\_ORG - the original fixed pitch propeller, FPP\_BAR\_MIN - the fixed pitch propeller with the artificially reduced blade area ratio ( $BAR = 0.4$ ), FPP\_D\_PLUS\_5% - the fixed pitch propeller with the artificially increased diameter by 5 percent).

After the engine performance and exhaust emissions simulations were performed, the resulted fuel consumption and pollutants mass flow rates as well as their specific values at NCR operational condition were summarised in Table 8.8.

Table 8.8 Summary table of propellers performance at NCR condition (FPP\_ORG - the original fixed pitch propeller, FPP\_BAR\_MIN - the fixed pitch propeller with the artificially reduced blade area ratio ( $BAR = 0.4$ ), FPP\_D\_PLUS\_5% - the fixed pitch propeller with the artificially increased diameter by 5 percent).

Fuel	Symbol/Metric		<i>FPP_ORG</i>	<i>FPP_BAR_MIN</i>	<i>FPP_D_PLUS_5%</i>
		FC	kg/h	1097	1078
	SFOC	g/kWh	165.4	165	165.2
Mass Flow Rate	$NO_x$	kg/h	88	87	88
	$CO$		3.15	3.11	3.13
	$HC$		2.03	2.01	2.02
	$CO_2$		3503	3442	3466
	$SO_2$		5.20	5.11	5.15
Specific	$NO_x$	g/kWh	13.3	13.3	13.3
	$CO$		0.47	0.48	0.48
	$HC$		0.31	0.31	0.31
	$CO_2$		528	527	527
	$SO_2$		0.78	0.78	0.78
	EEDI	gCO <sub>2</sub> /tnm	6.12	6.01	6.05

The results have shown that the lowest fuel consumption, as expected, is achieved by the propeller with reduced  $BAR$  ( $BAR = 0.4$ ), which is on 19 kg/h lower than the conventional fixed pitch propeller requirements. However, this achievement is relatively insignificant in comparison, for example, with the effect of the different propeller types such as CLT or the application of wake equalizing duct, since the SFOC values for in these cases are rather constant (around 165 g/kWh).

Regarding the exhaust emissions footprint, it is possible to reduce the  $CO_2$  emissions by 1.8 percent by adopting the propeller with reduced  $BAR$  ( $BAR = 0.4$ ) and by about 1 percent by artificially increasing the propeller diameter by 5 percent. However, almost no changes were found in level of  $NO_x$  emissions footprint in both cases.

In terms of the EEDI index, the lowest value is dedicated to the propeller with reduced  $BAR$  ( $BAR = 0.4$ ), followed by the propeller with artificially increased diameter by 5 percent as shown in Figure 8.17 and listed in Table 8.8. The scale of EEDI fluctuations due to the propeller optimisation for both cases is small and does not have any significant impact on the EEDI certification process.

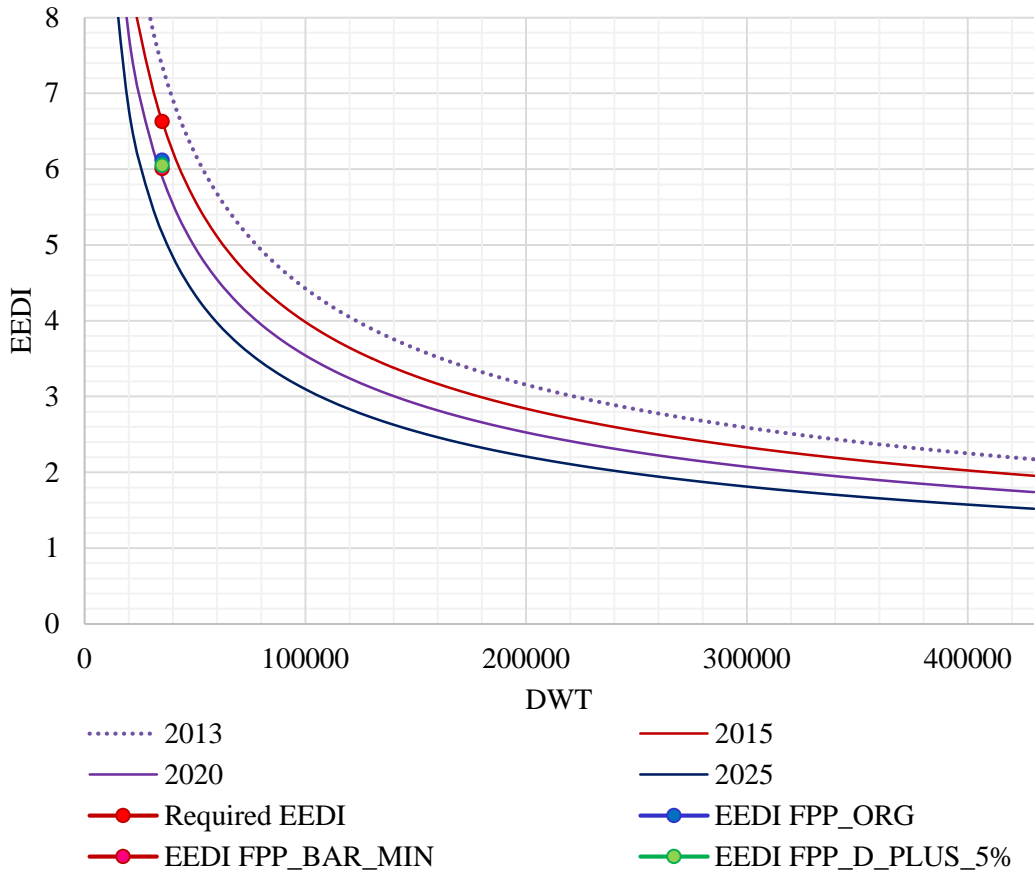


Figure 8.17 EEDI results for FPP\_ORG, FPP\_BAR\_MIN, FPP\_D\_PLUS\_5% propeller systems. (FPP\_ORG - the original fixed pitch propeller, FPP\_BAR\_MIN - the fixed pitch propeller with the artificially reduced blade area ratio ( $BAR = 0.4$ ), FPP\_D\_PLUS\_5% - the fixed pitch propeller with the artificially increased diameter by 5 percent).

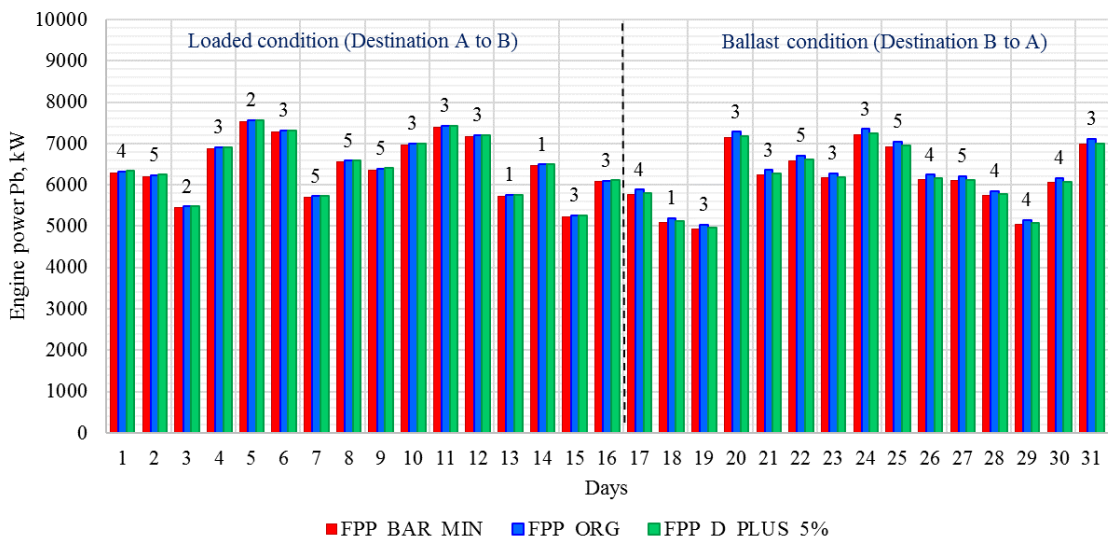


Figure 8.18 Voyage simulation results for FPP\_ORG, FPP\_BAR\_MIN, FPP\_D\_PLUS\_5% propeller systems. (FPP\_ORG - the original fixed pitch propeller, FPP\_BAR\_MIN - the fixed pitch propeller with the artificially reduced blade area ratio ( $BAR = 0.4$ ), FPP\_D\_PLUS\_5% - the fixed pitch propeller with the artificially increased diameter by 5 percent). Numbers at the top of the graph are Beaufort numbers.

After completing a month-long theoretical voyage simulation under realistic weather conditions (described in Chapter 6), the results have been plotted and illustrated in Figure 8.18 as well as summarised in Table 8.9 and Table 8.10. It is found that the possible savings of 6 tonnes of fuel per voyage could be achieved by increasing the propeller diameter by 5 percent, while the installation of the fixed pitch propeller with reduced BAR ( $BAR = 0.4$ ) would contribute to the fuel reduction of 11 tonnes per voyage. Such savings might look unimpressive when compared to the fuel reductions associated with the energy efficient propeller types but might be a useful bonus when applied in combination with the energy saving devices.

Table 8.9 The fuel consumption and emissions footprint performance. (FPP\_ORG - the original fixed pitch propeller, FPP\_BAR\_MIN - the fixed pitch propeller with the artificially reduced blade area ratio ( $BAR = 0.4$ ), FPP\_D\_PLUS\_5% - the fixed pitch propeller with the artificially increased diameter by percent).

	<i>FPP_ORG</i>	<i>FPP_BAR_MIN</i>	<i>FPP_D_PLUS_5%</i>	
Fuel	785	774	779	tonnes per voyage
$CO_2$	2506	2472	2486	tonnes per voyage
$NO_x$	64.1	63.1	63.6	tonnes per voyage
$SO_2$	3.7	3.6	3.7	tonnes per voyage
$CO$	2.2	2.2	2.2	tonnes per voyage
$HC$	1.5	1.5	1.5	tonnes per voyage

Table 8.10 Average SFOC and engine load per voyage. (FPP\_ORG - the original fixed pitch propeller, FPP\_BAR\_MIN - the fixed pitch propeller with the artificially reduced blade area ratio ( $BAR = 0.4$ ), FPP\_D\_PLUS\_5% - the fixed pitch propeller with the artificially increased diameter by percent).

	<i>FPP_ORG</i>		<i>FPP_BAR_MIN</i>		<i>FPP_D_PLUS_5%</i>		
	Loaded	Ballast	Loaded	Ballast	Loaded	Ballast	
LOAD	88.0	85.4	88.9	84.6	88.5	85.4	%
SFOC	165.6	165.2	165.4	164.8	165.0	164.2	g/kWh

In conclusion, two propeller optimisation techniques, a reduction of the blade area ratio and an artificial increase of the propeller diameter, were analysed in this chapter. As a result, both cases have shown advantageous elements but are unlikely to be applied outcomes.

In case of reduction of the blade area ratio to its possible minimum as recommended for a 4-bladed Wageningen propeller, the beneficial impact onto the power absorption is found to be slightly higher than in case of the artificially increased propeller diameter, however this would significantly increase the chance of development of the back cavitation on the propeller blades. Nevertheless, with growing research interests in developing of the anti-cavitation materials and coatings, a chance to incorporate more hydrodynamically efficient

propellers with reduced blade area ratio without the fear of cavitation will significantly increase. The foregoing results suggest that further work is necessary for understanding the margins against cavitation erosion.

In turn, the artificially increased propeller diameter has also shown a positive influence on the overall propulsive efficiency, although slightly lower than in the case of the reduction of blade area ratio. Nevertheless, the increase of the propeller diameter (with decreasing *BAR*) will not affect the cavitation performance since the excessive thrust loading would be evenly distributed along a larger surface of the propeller disk. However, even 5 percent increase of the optimum diameter will give a minor rise to the hull surface pressure pulses, resulting in potential intensification of the inboard noise and vibration.

The analysis of the energy efficiency indicators (EElS) has shown that the application of such propeller systems alone will not significantly affect the emissions footprint and the EEDI index, however, will provide some fuel savings which might be a useful bonus when combined with other energy saving devices.

## 9 Maximum Propeller Diameter

In recent years, maximising the propeller diameter while allowing the rotational speed to fall for large merchant vessels became a popular trend, which allows an increase in the propulsive efficiency while reducing fuel oil consumption. Indeed, for many ships, the installation of bigger propeller diameters also became possible due to an introduction of the longer stroke marine diesel engines into the market which enable a higher power output with a lower rate of revolutions.

Generally, the scale of the propeller diameter maximisation depends not only on the *RPM* range of the selected power plant but also upon a shape of the ship stern, namely the availability of the sufficient clearances that should be kept to minimise the possible risks associated with the vibration and noise. In some retrofitting cases, a further increase of the propeller diameter to maximise the propulsion efficiency might be restricted by the position of the shaft, even if the sufficient space is available. In this case the position of the shaft may be relocated, for example lifted, allowing to fit a bigger propeller, while satisfying the propeller clearances. A shaft relocation itself might be expensive since it involves the extension (or reduction in size) of the supporting bearings as well as general remodelling and alignment of the engine and transmission system including the stern tube bearing housing.

As such, this chapter focuses on an exploration by means of design and analysis of the efficiency benefits due to an increase of the propeller diameter to its maximum size based on the conventional shafting system design in comparison with the maximum possible propeller, which requires shaft relocation (lifting), while keeping the noise and vibration to its minimum. In addition, these propellers have been compared with the original fixed pitch propeller as well as their effects on the EEDI, emissions and possible fuel savings have also been estimated.

### 9.1 The Estimation of the Optimum Diameter-RPM Combinations

The propeller design procedures in the previous case studies (Chapter 7 and Chapter 8) have been performed for the recommended rotational speed at the design conditions, while the corresponding propeller analyses were also based on the relevant *RPM* range for the particular ship speeds provided in the model test report.

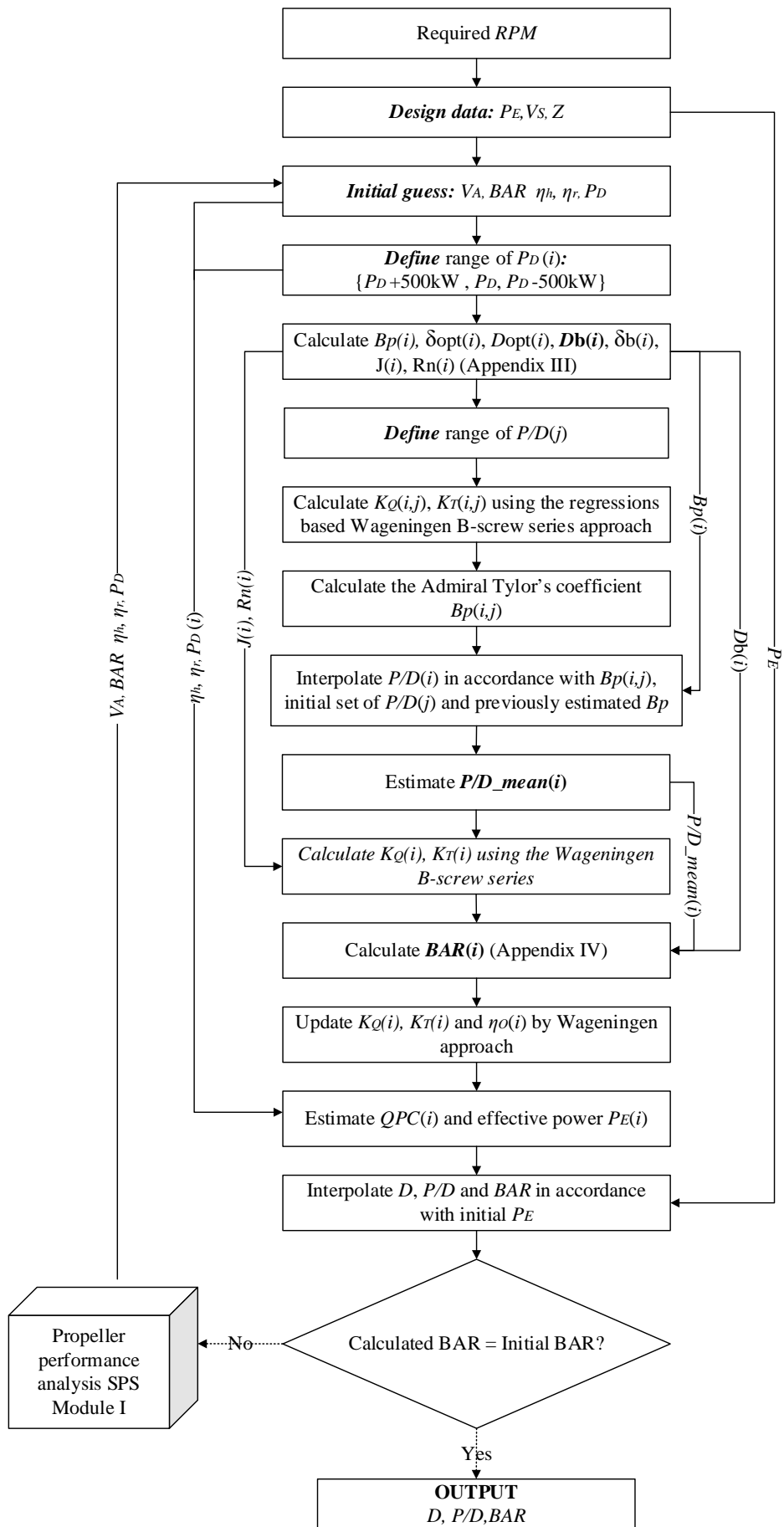


Figure 9.1 Optimum RPM – diameter range design process.

In this case, only principal ship design dimensions, together with the previously estimated resistance curve and effective power range, are available. As such, in order to design larger propeller diameter with lower *RPM*, a range of optimum diameter – *RPM* combinations were predicted for the ship design speed. In this regard, at first, a range of rotational speeds has been selected as follows:

$$RPM = \{80, 85, 90, \dots, 120, 125, 130\} \quad 9.1$$

The next step was to perform the propeller design procedure, illustrated in Figure 9.1 above, for each *RPM* value. This design process is similar to the original design method, described in Appendix II. However, since in this case the initial delivered power has been guessed with a lower accuracy, the propeller self-propulsion analysis was also conducted in each cycle. The design process was repeated until the main propeller characteristics converged. As a result, a range of propeller diameters with corresponding *BAR* and *P/D* ratios has been designed for each rotational speed as graphically shown in Figure 9.2. In fact, the resulting propeller characteristics, which correspond to the optimum rotational speed of 122.14 *RPM* for the reference tanker (and marked with the red colour) are very similar to the original FP propeller confirming the accuracy level of the design approach used.

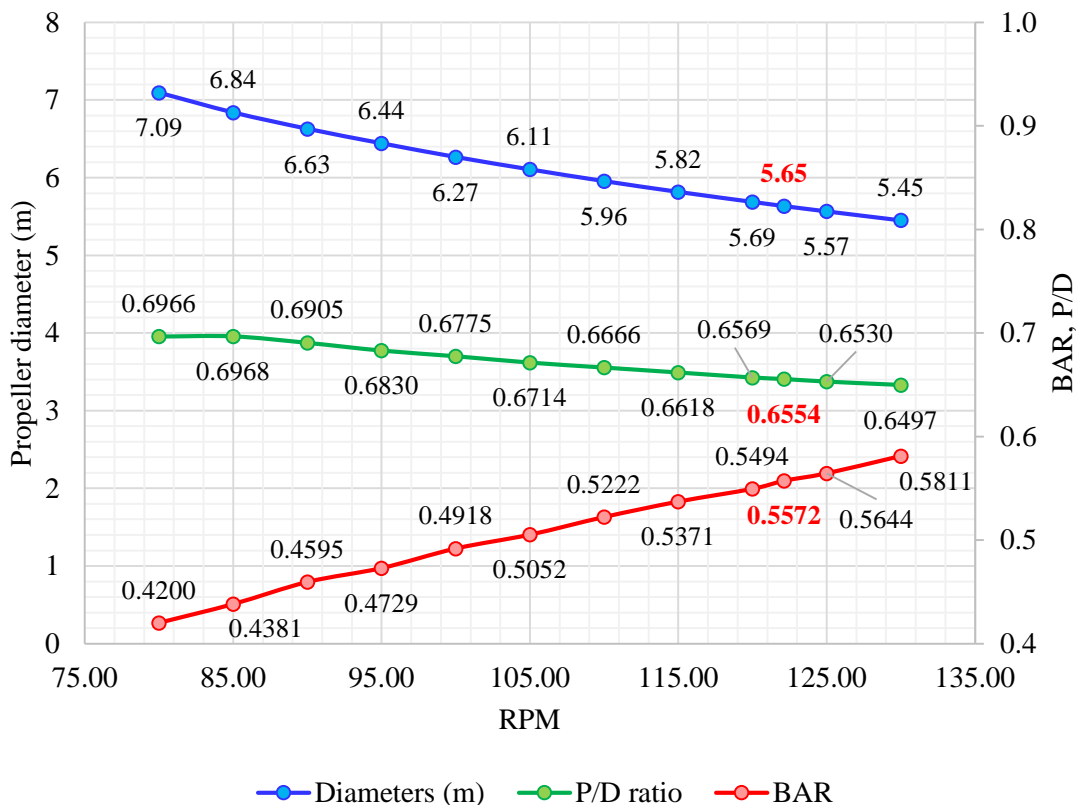


Figure 9.2 Resulted optimum RPM – diameter range.

For the selection of an optimum *BAR* in the design process, the cavitation allowance was kept at the same level as for the original propeller (slightly lower than 2.5 percent of back cavitation).

The hull surface pressures at the design speed of 14.6 knots have also been predicted using the Holden’s approach. As shown in Figure 9.3, the resulted pressures in each case are lower than the recommended limit of  $2 \text{ kN/m}^2$  for this type of ship, meaning that the level of noise and vibration due to the propeller hull and shaft interactions is likely to lay within the acceptable limits.

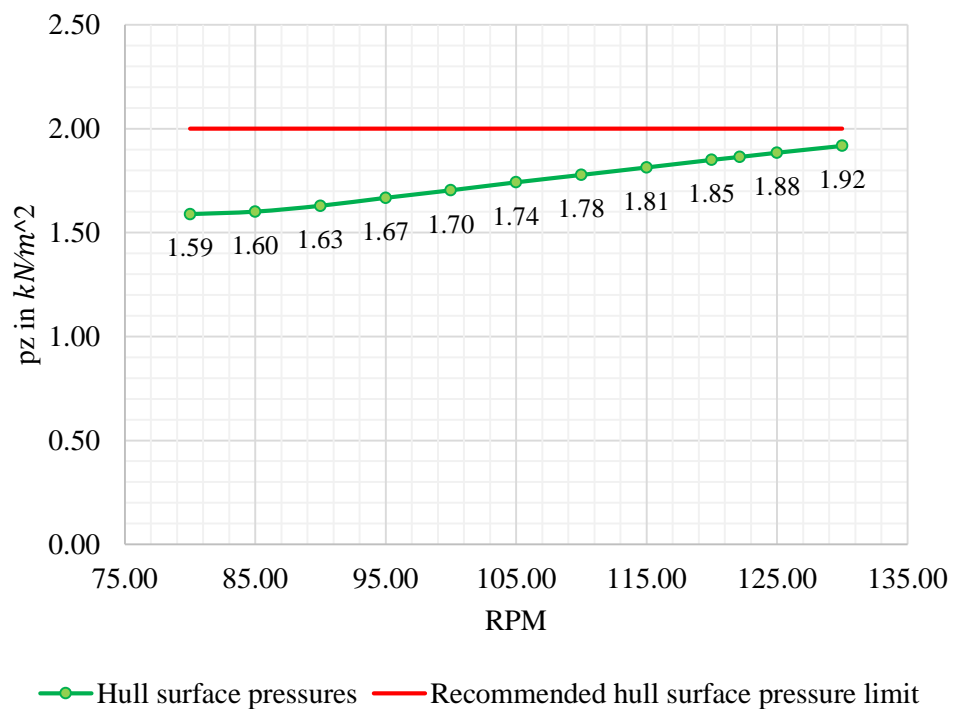


Figure 9.3 Hull surface pressure distribution.

## 9.2 Propeller Clearances

The next step was to define the maximum propeller diameters for each case. This is done by allowing for reasonable propeller clearances in order to reduce the likelihood of unwelcomed blade rate pressure pulse vibrations being induced in the local hull structure. For the reference ship, the minimum distance between the hull baseline and the tips and the outer section leading edges of the propeller blade equals to 0.15m while the recommended upper limit for the propeller diameter is the ballast draught. Schematic representation of both, the maximum propeller with the original stern arrangement and the maximum possible propeller with the lifted shaft is shown in Figure 9.4. In this figure, the hull

structure is reproduced in accordance with the reference ship blueprints. A restriction was placed on this changes that the propeller blade tips should not protrude below the baseline of the ship which is in contrast to some naval practices.

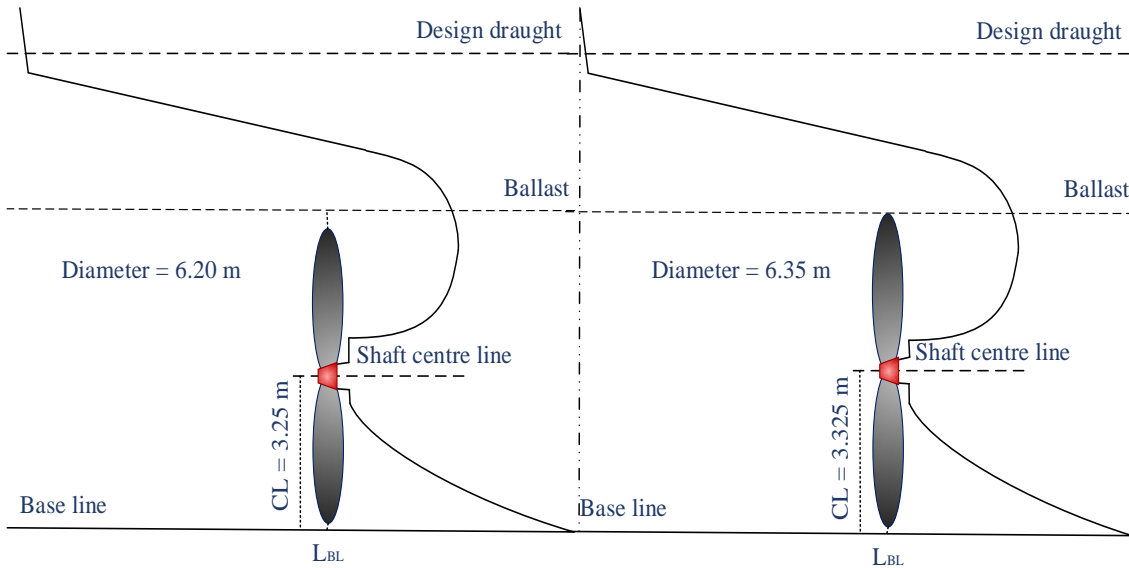


Figure 9.4 FPP\_MAX (left) and FPP\_MAX\_SHAFT (right) applied to the reference stern design with the lifted shaft on the latter case. (FPP\_MAX - the maximum propeller with the original stern arrangement, FPP\_MAX\_SHAFT - the maximum possible propeller with the lifted shaft).

Table 9.1 FPP\_MAX and FPP\_MAX\_SHAFT diameter calculation procedure (FPP\_MAX – the maximum propeller with the original stern arrangement, FPP\_MAX\_SHAFT – the maximum possible propeller with the lifted shaft).

Parameter	FPP_MAX			
	Symbol	Source/Equation	Value	Metric
Ballast draught	$T_{Ballast}$	Ship documentation	6.50	<i>m</i>
Depth of the centre line	$CL$	Ship documentation	3.25	<i>m</i>
Stern wave	$SW$	Recommended	1	<i>m</i>
Minimum length to the baseline	$L_{BL}$	Recommended	0.15	<i>m</i>
MAX Radius	$r_{MAX}$	$r_{MAX} = CL - L_{BL}$	3.10	<i>m</i>
MAX Diameter	$D_{MAX}$	$D_{MAX} = 2 * r_{MAX}$	6.20	<i>m</i>
Rotational speed	$RPM$	Interpolated	101	<i>RPM</i>
Parameter	FPP_MAX_SHAFT			
	Symbol	Source/Equation	Value	Metric
Distance btw shaft and ballast	$L_{SB}$	$L_{SB} = T_{Ballast} - CL$	3.25	<i>m</i>
MAX possible diameter	$D_{MAX\_SHAFT}$	$D_{MAX\_SHAFT} = r_{MAX} + L_{SB}$	6.35	<i>m</i>
MAX possible radius	$r_{MAX\_SHAFT}$	$r_{MAX\_SHAFT} = D_{MAX\_SHAFT} / 2$	3.175	<i>m</i>
Shaft relocation (lift)	$L_{SHAFT}$	$L_{SHAFT} = r_{MAX\_SHAFT} - r_{MAX}$	0.075	<i>m</i>
MAX depth of the centre line	$CL_{MAX\_SHAFT}$	$CL_{MAX\_SHAFT} = CL + L_{SHAFT}$	3.325	<i>m</i>
Rotational speed	$RPM$	Interpolated	96.5	<i>RPM</i>

For both, the maximum propeller with the original stern arrangement and the maximum possible propeller with the lifted shaft, the diameter sizes were calculated as described in Table 9.1, while the optimum *RPM* at the design condition for each case was interpolated from the optimum *RPM* – diameter range. Therefore, the resulted maximum diameter suitable with the original stern arrangement is found to be 6.20m with the optimum rotational speed of 101 *RPM*, while the diameter of the maximum possible propeller with the lifted shaft equals to 6.35m with the rotational speed of 96.5 *RPM*. In the latter case, the shaft centre line has been lifted up by 0.075m resulting in the new height of the centre line (*CL*) equal to 3.325m.

The corresponding propeller characteristics (*BAR* and *P/D*) can also be interpolated from those associated with the optimum *RPM* – diameter range (Figure 9.2). However, for a better accuracy, *BAR* and *P/D* have been re-designed using the similar design process as for the artificial propeller diameters in the previous chapter. This is especially important for propeller with the maximum possible diameter with the lifted shaft, since the depth of the centre line has been changed due to the shaft relocation, which will primarily affect the blade area ratio as well as the hull surface pressure.

Resulting characteristics for both, the maximum propeller with the original stern arrangement and the maximum possible propeller with the lifted shaft, along with the original fixed pitch propeller for comparison purposes are listed in Table 9.2 below.

Table 9.2 Final propellers dimensions.

Reference label	Propeller description	Principle characteristics				
		<i>D</i> (m)	<i>P/D</i>	<i>BAR</i>	<i>Z</i>	<i>RPM</i>
<i>FPP</i>	Conventional FP propeller	5.65	0.6523	0.5628	4	122.14
<i>FPP_MAX</i>	The maximum propeller diameter at the current arrangements	6.20	0.6853	0.4997	4	101
<i>FPP_MAX_SHAFT</i>	The maximum propeller possible with the lifted shaft	6.35	0.6919	0.4866	4	96.5

### 9.3 Propellers Performance Analysis

Since the propeller performance analysis is normally executed not only for the recommended ship speed at the design condition but also across a range of speeds and under ballast and scantling loads to predict the realistic ship behaviour in a seaway, it is necessary to define a suitable *RPM* rate for each ship speed at various operational conditions. In this

regard, the  $RPM$  – diameter range for a number of ship speeds (12.5 knots – 16 knots) has been created using the same design procedure (Figure 9.1) as for the 14.6 knots at design condition.

Namely, an individual propeller has been designed for a range of rotational speeds (80 - 130) at different ship speeds (12.5 knots – 16 knots) based on the corresponding effective power  $P_E$  and total ship resistance  $R_T$  values under the design condition. The resulted  $RPM$  – diameter ranges at different ship speeds are demonstrated in Figure 9.5.

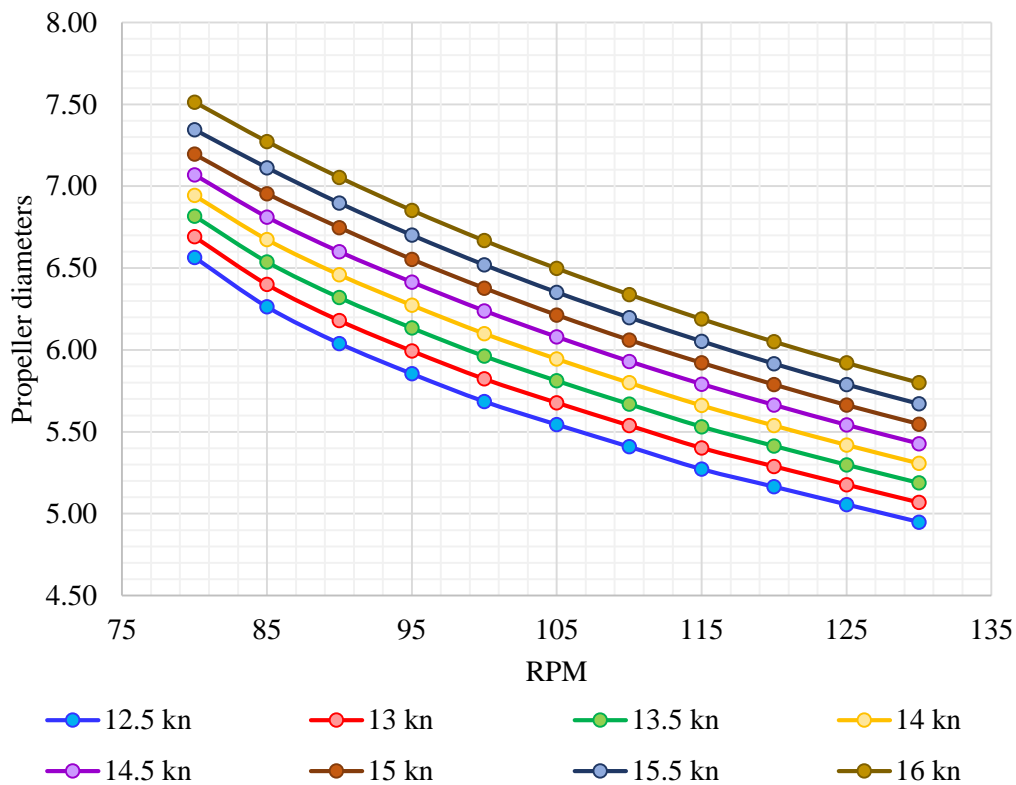


Figure 9.5  $RPM$  – diameter ranges at different ship speeds (design conditions).

Then, to obtain the  $RPM$  ranges for both propeller systems, their diameters were used to get an appropriate  $RPM$  value at respective ship speed from the resulted  $RPM$  – diameter ranges (Figure 9.5) by means of interpolation. The  $RPM$  ranges for ballast and loaded conditions were also interpolated in accordance with the relevant  $RPM$  distributions from the model test report. The resulted  $RPM$  distributions for ballast, design and loaded conditions are illustrated in Figure 9.6

The propeller propulsion analysis has been performed using the Ship Performance Simulation model described in Chapter 5. The results for both propellers, the maximum diameter with the original stern arrangement and the maximum possible diameter with the lifted shaft, at the design condition (14.6 knots) are listed in Table 9.3.

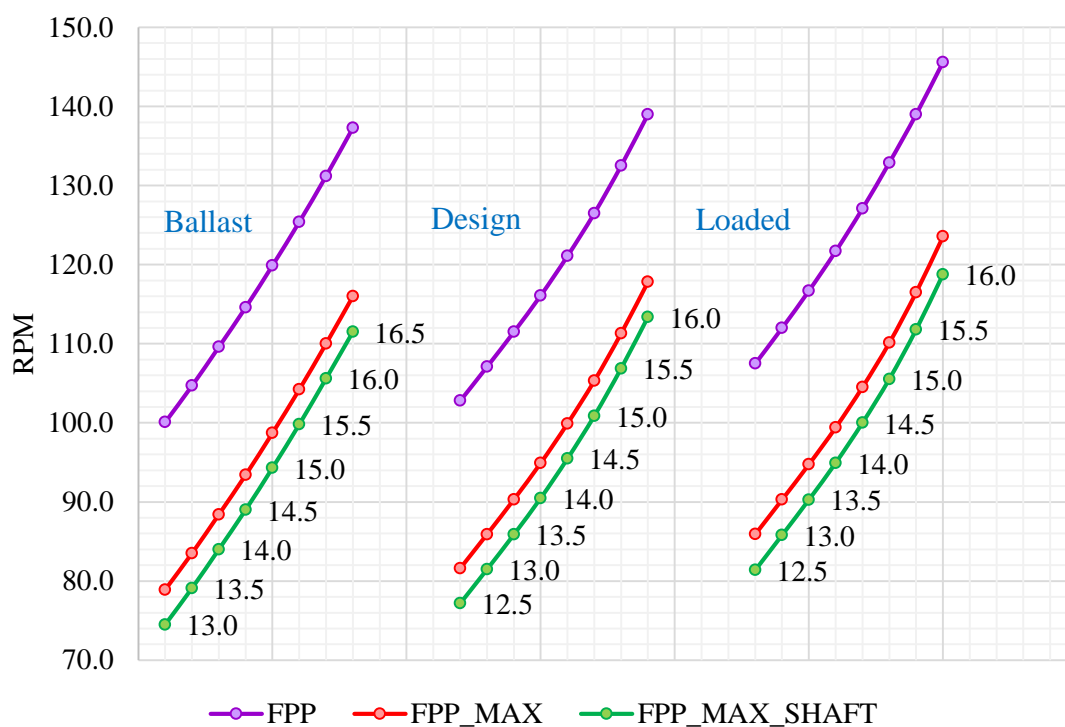


Figure 9.6 Resulted *RPM* distributions at different loads.

Table 9.3 Comparison results of the *FPP*, *FPP\_MAX*, and *FPP\_MAX\_SHAFT* performance at design condition and speed of 14.6 knots. (*FPP* – original fixed pitch propeller, *FPP\_MAX* – the maximum propeller with the original stern arrangement, *FPP\_MAX\_SHAFT* – the maximum possible propeller with the lifted shaft).

Parameter	Symbol	<i>FPP</i>	<i>FPP_MAX</i>	<i>FPP_MAX_SHAFT</i>	Metric
Propeller rotational speed	<i>RPM</i>	122.14	101	96.5	
Propeller diameter	<i>D</i>	5.65	6.20	6.35	<i>m</i>
Pitch to diameter ratio	<i>P/D</i>	0.6523	0.6853	0.6919	-
Blade area ratio	<i>BAR</i>	0.5628	0.4997	0.4866	-
Number of blades	<i>Z</i>	4	4	4	-
Wake fraction coefficient	<i>w</i>	0.386	0.381	0.380	-
Thrust reduction coefficient	<i>t</i>	0.231	0.226	0.225	-
Relative-rotative efficiency	$\eta_R$	1.012	1.016	1.017	-
Hull efficiency	$\eta_H$	1.253	1.249	1.249	-
Open-water efficiency	$\eta_o$	0.544	0.573	0.580	-
Propeller torque coefficient	$K_Q$	0.0166	0.1415	0.1407	-
Propeller thrust coefficient	$K_T$	0.1411	0.0175	0.0176	-
Hull surface pressure	$p_z$	1.89	1.69	1.66	<i>kN/m<sup>2</sup></i>
Quasi-propulsive coefficient	<i>QPC</i>	0.689	0.727	0.736	-
Delivered power	$P_D$	5400	5115	5058	<i>kW</i>

The propulsion analyses have also been conducted for loaded, design and ballast conditions. The hull efficiency  $\eta_H$  for both propellers and at all loads, as expected, is found to be slightly lower than that of the original fixed pitch propeller since the increase of the propeller diameter results in a decrease in the average wake fraction, resulting in the overall decrease in the hull efficiency (Figure 9.7). The scale of the hull efficiency reduction is more evident at the ballast condition while almost negligible when fully loaded. The hull efficiency difference between maximum propeller and maximum possible propeller with the lifted shaft are minimal, while the reduction trend for the latter case has been retained as its diameter is larger than of the maximum propeller.

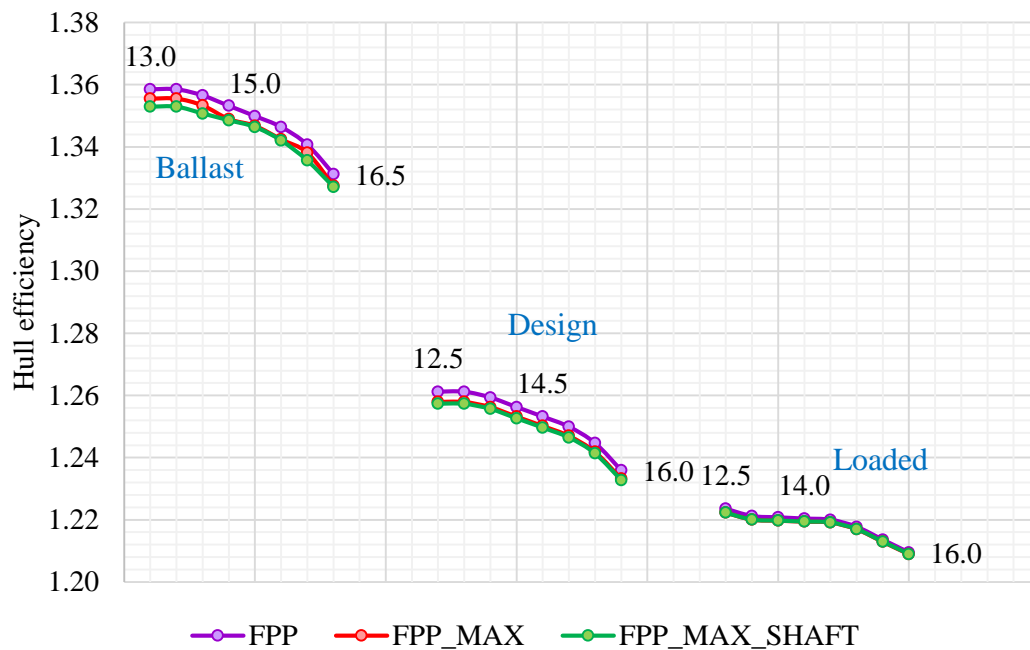


Figure 9.7 Hull efficiency results for FPP, FPP\_MAX and FPP\_MAX\_SHAFT at the ballast, design and loaded conditions. (FPP – original fixed pitch propeller, FPP\_MAX – the maximum propeller with the original stern arrangement, FPP\_MAX\_SHAFT – the maximum possible propeller with the lifted shaft).

The relative-rotative efficiency  $\eta_R$  (Figure 9.8) and the open water efficiency  $\eta_o$  (Figure 9.9) are proportionally higher for both propellers since increasing with the propeller diameter.

The required power absorption for original fixed pitch propeller, the maximum propeller for the original stern arrangement and the maximum possible propeller with the lifted shaft have also been estimated in accordance with the relevant effective power  $P_E$  at different loads as shown in Figure 9.10.

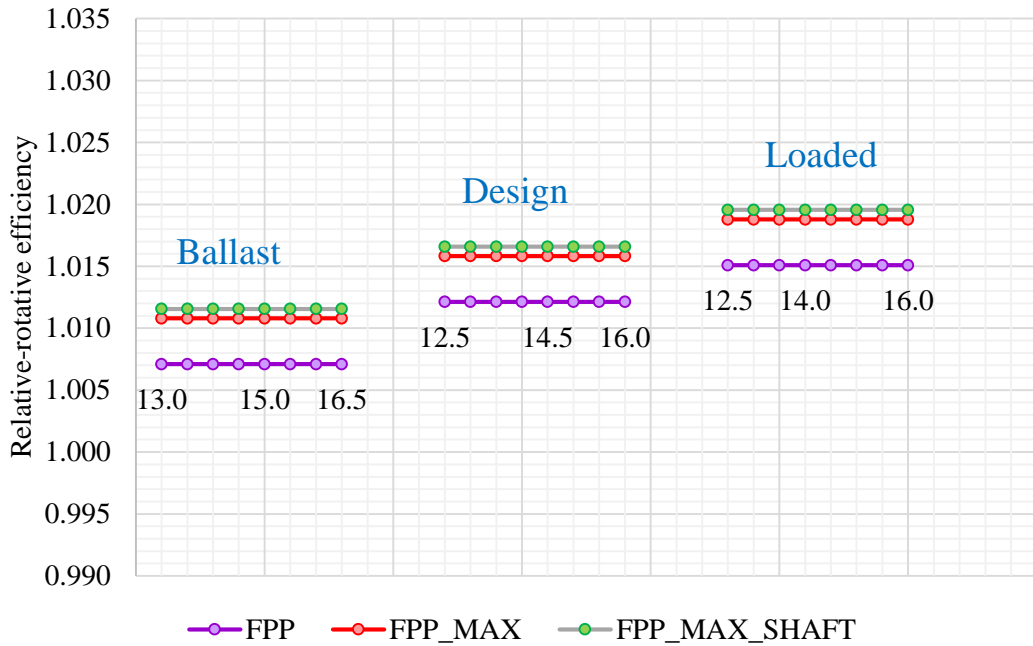


Figure 9.8 Relative-rotative efficiency results for FPP, FPP\_MAX and FPP\_MAX\_SHAFT at the ballast, design and loaded conditions. (FPP – original fixed pitch propeller, FPP\_MAX – the maximum propeller with the original stern arrangement, FPP\_MAX\_SHAFT – the maximum possible propeller with the lifted shaft).

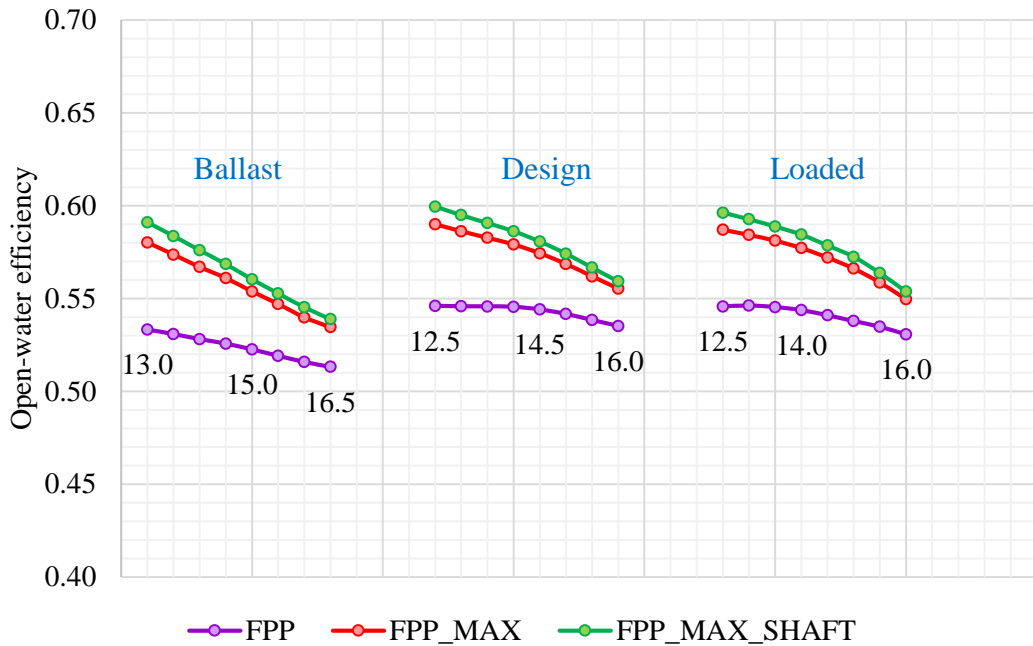


Figure 9.9 Open water efficiency results for FPP, FPP\_MAX and FPP\_MAX\_SHAFT at the ballast, design and loaded conditions. (FPP – original fixed pitch propeller, FPP\_MAX – the maximum propeller with the original stern arrangement, FPP\_MAX\_SHAFT – the maximum possible propeller with the lifted shaft).

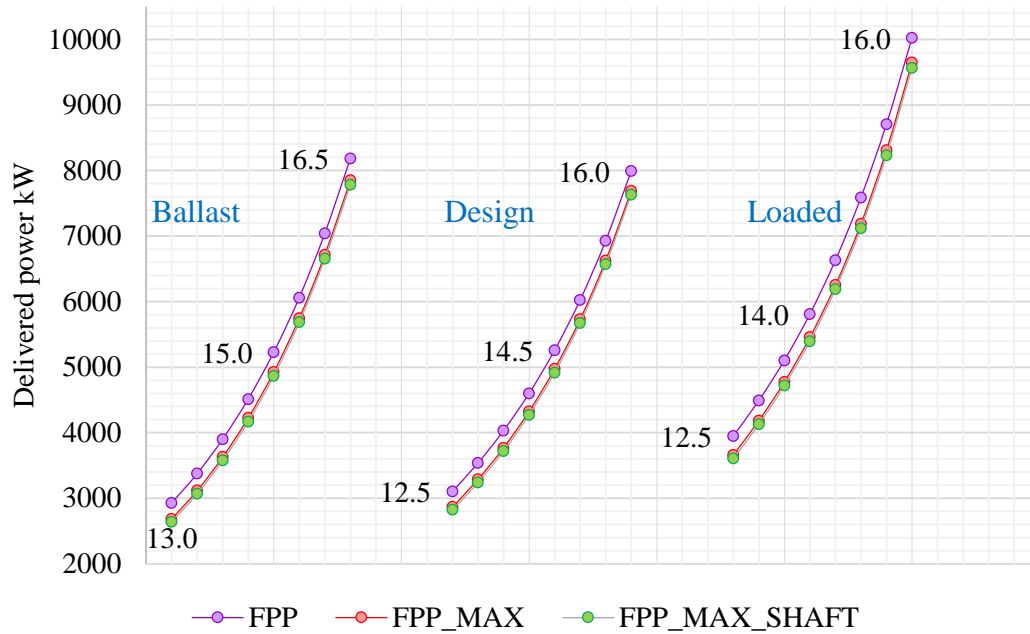


Figure 9.10 Delivered power results for FPP, FPP\_MAX and FPP\_MAX\_SHAFT at the ballast, design and loaded conditions. (FPP – original fixed pitch propeller, FPP\_MAX – the maximum propeller with the original stern arrangement, FPP\_MAX\_SHAFT – the maximum possible propeller with the lifted shaft).

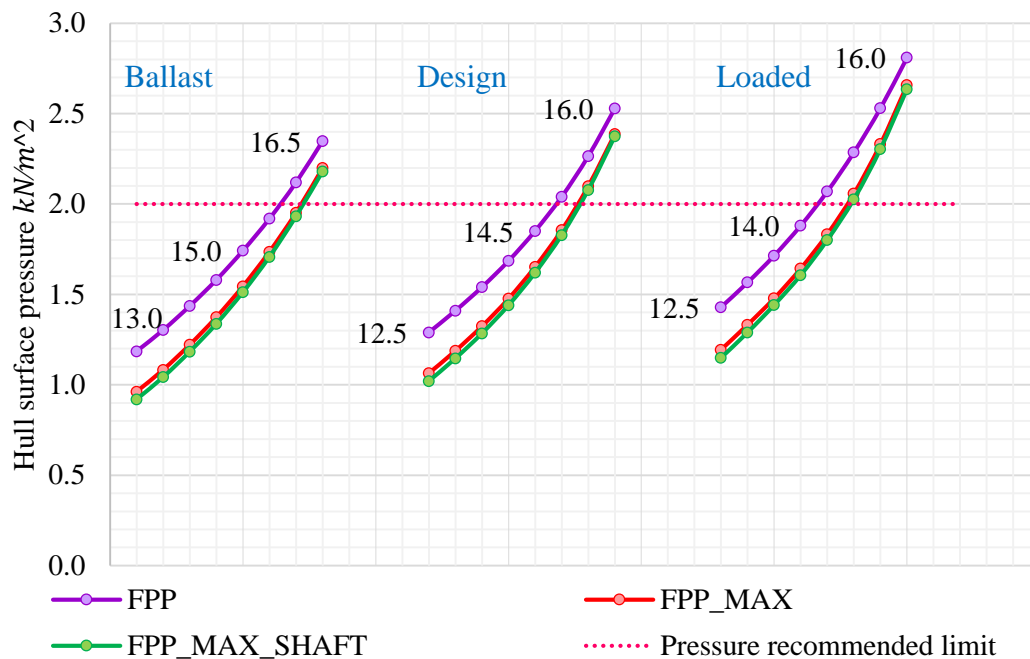


Figure 9.11 Hull surface pressures for FPP, FPP\_MAX and FPP\_MAX\_SHAFT at the ballast, design and loaded conditions. (FPP – original fixed pitch propeller, FPP\_MAX – the maximum propeller with the original stern arrangement, FPP\_MAX\_SHAFT – the maximum possible propeller with the lifted shaft).

The hull surface pressures at different loads and speeds have been estimated by Holden’s approach to evaluate the level of vibration and noise. The hull surface pressure results are demonstrated in Figure 9.11. It has been found that the risk of vibration and noise tend to decrease with increasing propeller diameter mostly influenced by the reduction of the *RPM*,

thereby making the maximum possible propeller with the lifted shaft the most valuable on this matter. However, for all cases the hull surface pressures are exceeding the pressure limits at higher speeds (mostly 15.5 and 16 knots), although these speeds are rarely used in operation.

Table 9.4 Delivered power reductions at design ship speeds. (FPP – original fixed pitch propeller, FPP\_MAX – the maximum propeller with the original stern arrangement, FPP\_MAX\_SHAFT – the maximum possible propeller with the lifted shaft).

Condition	<i>Ballast</i>	<i>Designed</i>	<i>Loaded</i>	Metric
Speed	15.02	14.6	14.07	knots
FPP vs FPP_MAX	6.12	5.57	6.46	%
FPP vs FPP_MAX_SHAFT	7.44	6.75	7.67	%
FPP_MAX vs FPP_MAX_SHAFT	1.24	1.12	1.14	%

The delivered power reductions at different loads in accordance with their recommended ship speed have been evaluated in percentage as listed in Table 9.4, being the most significant at off-design conditions. Therefore, the average reduction due to maximising the propeller diameter while minimising its rotational speed accounts for 6 percent in the case of the maximum propeller with the original stern arrangement and 7.3 percent for the maximum possible propeller with the lifted shaft. The actual difference between the maximised propeller and the maximised propeller with lifted shaft are less significant and accounts for 1.17 percent on average.

#### 9.4 Impact on the Energy Efficiency Indicators

According to the simulation results conducted in this chapter, the efficiency benefits of maximising the propeller diameter are clearly coherent. However, the question that has to be answered is whether it would be reasonable for a ship owner to invest into the shaft relocation in order to obtain the maximum possible fuel savings from the propeller itself. Therefore, this subchapter is dedicated not only to the estimation of the energy efficiency indicators (EEIs) covering the fuel consumption, emissions footprint and the EEDI index but also aimed to explore if there is a merit in shaft relocation.

Since the rotational speed required for the maximised propeller operation is significantly lower than in the case of the conventional propeller, the application of bigger propellers will require an installation of an alternative diesel engine. For the purpose of this study, the innovative G-type diesel engine by MAN has been selected. The G-type is an ultra-long-stroke engine, which is designed to reduce engine speed, thereby paving the way for ship

designs with bigger propeller and higher efficiency. According to the manufacturer brochure (MAN Diesel and Turbo 2011), G-type engine also achieves low SFOC and better overall performance due “to variable, electronically controlled timing of fuel injection and exhaust valves at any engine speed and load”. As such, the selected engine for both propeller cases is the G45ME-C with 6 cylinders providing the MCR of 8340 kW with the maximum rotational speed of 111 RPM. The list of SMCR powers and SMCR speeds for both propellers together with the conventional engine arrangement comparison reasons are summarised in Table 9.5.

Table 9.5 Range of selected engines and their SMCR. (FPP – original fixed pitch propeller, FPP\_MAX – the maximum propeller with the original stern arrangement, FPP\_MAX\_SHAFT – the maximum possible propeller with the lifted shaft).

15 knots	<i>FPP</i>	<i>FPP_MAX</i>	<i>FPP_MAX_SHAFT</i>	
SMCR	7347	7013	6943	kW
RPM	127	106	102	rpm
Engine	5S50ME-C	6G45ME-C	6G45ME-C	

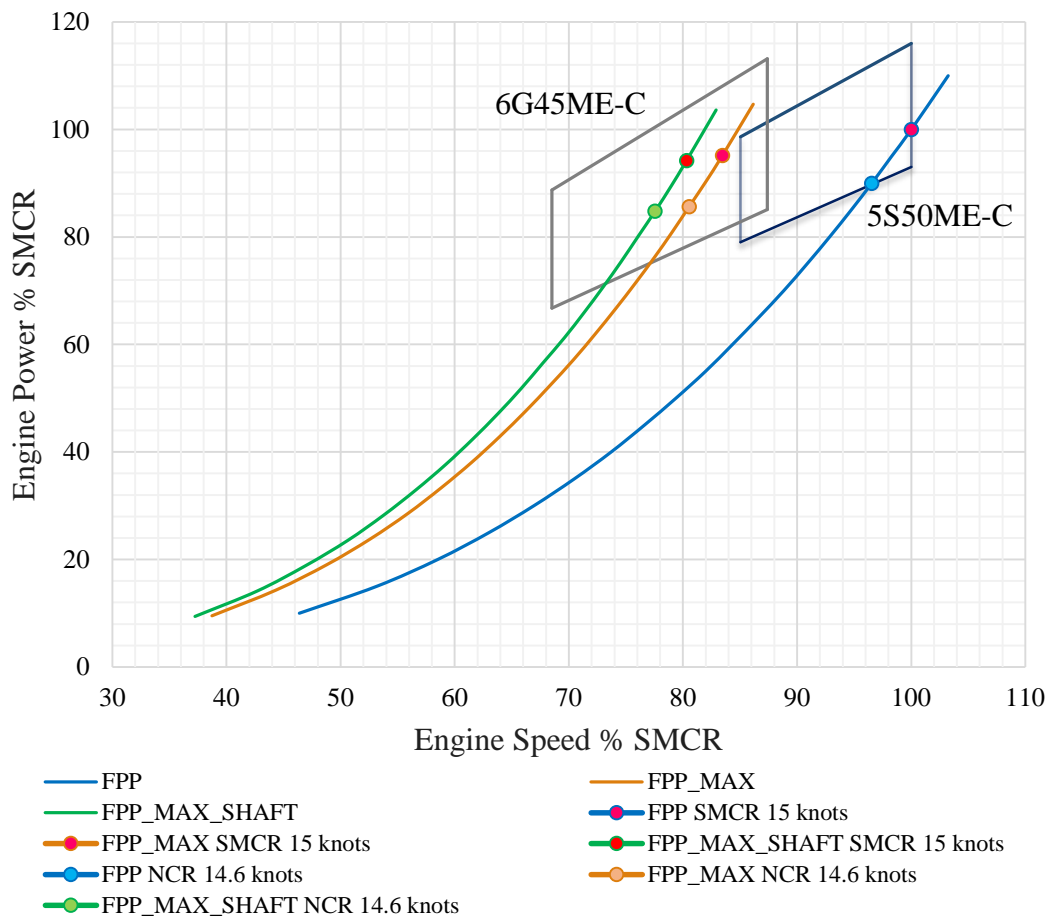


Figure 9.12 Engines service curves for all propeller systems (FPP – original fixed pitch propeller, FPP\_MAX – the maximum propeller with the original stern arrangement, FPP\_MAX\_SHAFT – the maximum possible propeller with the lifted shaft).

Figure 9.12 demonstrates the load diagrams for both engines, the 6G45ME-C and the conventional 5S50ME-C, together with the engine service curves for each propeller system and their Normal Continuous Ratings (NCR) at 90 percent SMCR corresponding to 14.6 knots operational speed.

After the engine performance and exhaust emissions simulation modules of the Ship Performance Simulation model were conducted, the resulting fuel consumption and emissions mass flow rates as well as their specific values at the NCR operational condition are summarised in Table 9.6.

Table 9.6 Summary table of propellers performance at the NCR condition. (FPP – original fixed pitch propeller, FPP\_MAX – the maximum propeller with the original stern arrangement, FPP\_MAX\_SHAFT – the maximum possible propeller with the lifted shaft).

Fuel	Symbol/Metric		<i>FPP</i>	<i>FPP_MAX</i>	<i>FPP_MAX_SHAFT</i>
	FC	kg/h	1097	1043	1037
SFOC	g/kWh	165.4	165.3	166	
Mass Flow Rate	<i>NO<sub>x</sub></i>	kg/h	88	72	71
	<i>CO</i>		3.15	2.67	2.65
	<i>HC</i>		2.03	1.73	1.72
	<i>CO<sub>2</sub></i>		3503	3331	3311
	<i>SO<sub>2</sub></i>		5.20	4.96	4.93
Specific	<i>NO<sub>x</sub></i>	g/kWh	13.28	11.34	11.37
	<i>CO</i>		0.47	0.42	0.42
	<i>HC</i>		0.31	0.27	0.27
	<i>CO<sub>2</sub></i>		528	528	530
	<i>SO<sub>2</sub></i>		0.78	0.79	0.79
EEDI	gCO <sub>2</sub> /tnm	6.12	5.82	5.78	

The results have shown that the lowest fuel consumption is achieved by performance of the maximum possible propeller with the lifted shaft, which is on 60 kg/h lower than the conventional fixed pitch propeller requirements, following by the maximum propeller with the original stern arrangement, where the fuel savings equal to 54 kg/h. In turn, the differences between the maximum propeller with the original stern arrangement and the maximum possible propeller with the lifted shaft are small and account for 6 kg of fuel per hour, although the SFOC at NCR of the of the maximum possible propeller with the lifted shaft is higher than in other cases.

Regarding the exhaust emissions footprint, when compared with the conventional fixed pitch propeller, it is possible to reduce the  $CO_2$  emissions by 172 kg/h in case of the maximum propeller with the original stern arrangement and by 192 kg/h with of the maximum possible propeller with the lifted shaft. In turn, the difference between them accounts for 20 kg of  $CO_2$  per hour. The  $NO_x$  reductions due to the maximum propeller with the original stern arrangement and the maximum possible propeller with the lifted shaft are quite significant and equal to 16 kg/h and 17 kg/h respectively.

In the matter of the obtained EEDI values, the introduction of both propeller systems alone will satisfy the EEDI requirements up to the year of 2020, while no significant differences in the EEDI perspective were detected if compared to each other. The EEDI values for both propellers are also presented in Table 9.6 as well as outlined in Figure 9.13.

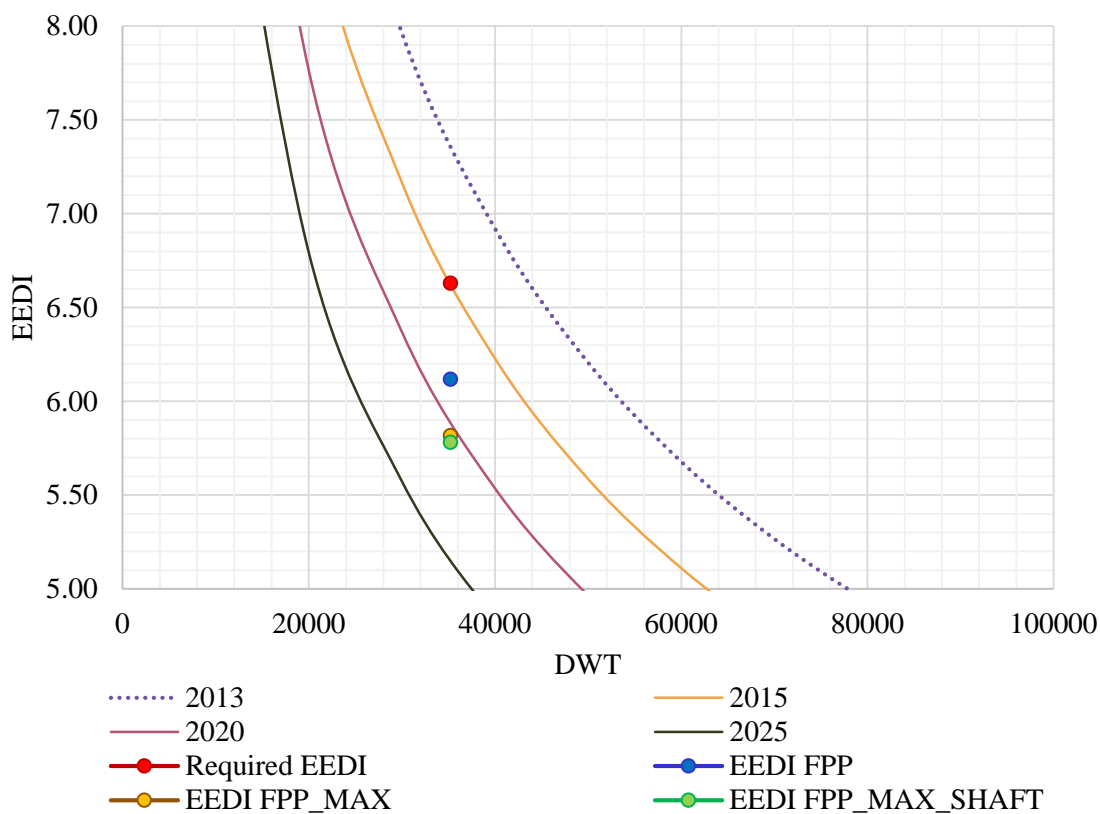


Figure 9.13 EEDI results for all propeller systems. (FPP – original fixed pitch propeller, FPP\_MAX – the maximum propeller with the original stern arrangement, FPP\_MAX\_SHAFT – the maximum possible propeller with the lifted shaft).

After completing a month-long theoretical voyage simulation under realistic weather conditions (described in Chapter 6), the results have been plotted and illustrated Figure 9.14 as well as summarised in Table 9.7 and Table 9.8. The fuel savings obtained with the maximum propeller with the original stern arrangement and the maximum possible

propeller with the lifted shaft account for 43 and 48 tonnes per voyage respectively, while the benefits due to the shaft relocation save up to 5 tonnes of fuel per voyage.

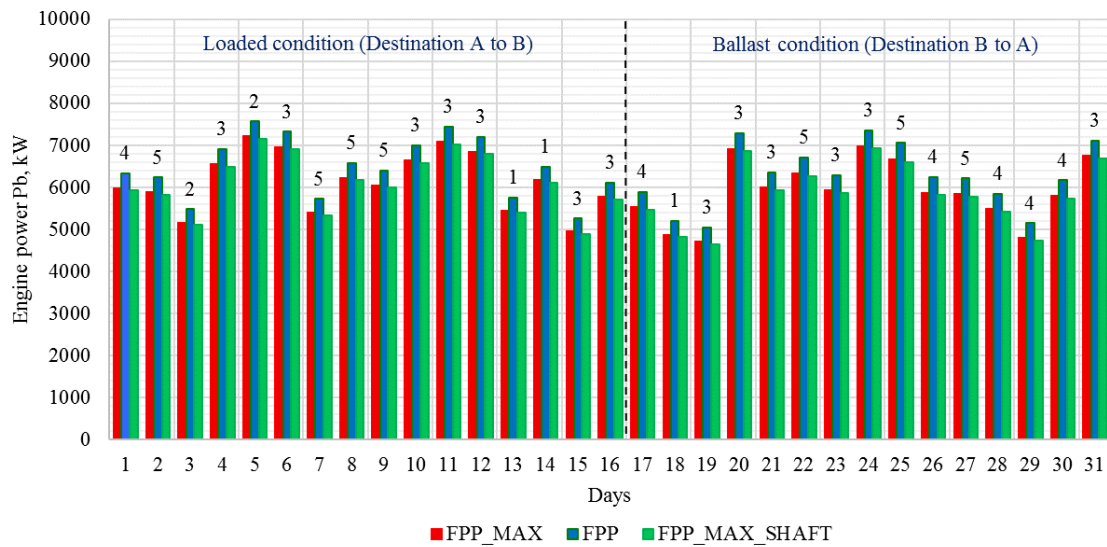


Figure 9.14 Voyage simulation results of all propeller systems. (FPP – original fixed pitch propeller, FPP\_MAX – the maximum propeller with the original stern arrangement, FPP\_MAX\_SHAFT – the maximum possible propeller with the lifted shaft). Numbers at the top of the graph are Beaufort numbers.

Table 9.7 Fuel consumption and emissions footprint performance per voyage. (FPP – original fixed pitch propeller, FPP\_MAX – the maximum propeller with the original stern arrangement, FPP\_MAX\_SHAFT – the maximum possible propeller with the lifted shaft).

	<i>FPP</i>	<i>FPP_MAX</i>	<i>FPP_MAX_SHAFT</i>	
Fuel	785	742	737	tonnes per voyage
CO <sub>2</sub>	2506	2369	2352	tonnes per voyage
NO <sub>x</sub>	64.1	51.4	51.4	tonnes per voyage
SO <sub>2</sub>	3.7	3.5	3.5	tonnes per voyage
CO	2.2	1.8	1.8	tonnes per voyage
HC	1.5	1.2	1.2	tonnes per voyage

Table 9.8 Average SFOC and engine load per voyage. (FPP – original fixed pitch propeller, FPP\_MAX – the maximum propeller with the original stern arrangement, FPP\_MAX\_SHAFT – the maximum possible propeller with the lifted shaft).

	<i>FPP</i>		<i>FPP_MAX</i>		<i>FPP_MAX_SHAFT</i>		
	Loaded	Ballast	Loaded	Ballast	Loaded	Ballast	
LOAD	88.0	85.4	87.8	84.2	87.7	85.4	%
SFOC	165.6	165.2	165.4	165.0	166.2	165.7	g/kWh

As a final remark, in case of retrofitting, both, the maximum propeller with the original stern arrangement and the maximum possible propeller with the lifted shaft systems will require a significant financial effort to provide new propeller, super slow diesel engine as well as to modify the transmission system for the latter case. However, for new builds, maximising the propeller diameter is a good option to save up to 50 tonnes of fuel per voyage and being especially profitable should fuel prices increase; again reduce the  $CO_2$  emissions by almost 200 kg per hour and  $NO_x$  by 17 kg per hour while complying with the EEDI index requirements up to 2020. In addition, there is no need for the shaft relocation should the propeller size be confirmed prior the power plant selection making the preliminary ship performance simulation an important part of the efficient ship design.

## 10 Energy Efficient Trim Optimisation

In addition to hull and propulsor design improvements leading to a reduction in fuel consumption, exhaust emissions and EEDI index, even relatively simple changes in ship operational profile may offer significant gains in the energy efficiency. As already stated in the introduction, the efficiency benefits achieved by modifying an operational profile will not affect the EEDI index. Instead, the EEOI (Energy Efficiency Operational Indicator) may be voluntarily calculated by the operator in order to estimate the impact of fuel consumption for IMO data tracking or personal purposes. Although an optimised operational profile doesn't have an immediate effect onto the ship environmental certification, in reality, it may significantly contribute to the level of  $CO_2$  and other atmospheric emissions and even cancel the positive effects of the energy efficiency technologies (and EEDI) should the operational profile not be properly established.

Trim optimisation is one of the easiest and cheapest methods for ship performance optimisation since it does not normally require any hull or engine modifications, while the optimisation is normally performed by an adaptation of the loading plan. It can be made by means of model tests or using computational fluid dynamics (CFD). For instance, in the work by (Hansen et al. 2012), a trim matrix is built using the potential flow code for ship performance prediction while validated by means of the RANS flow code. The results have shown that in this case the overall ship efficiency can be increased by 8.7 percent through sailing with the optimum trim. Another research tool in this field has been developed by FORCE Technology (Reichel et al. 2014), where trim tests are performed for approximately 300 vessels with a primary focus on the container vessels. Testing has shown possible savings of up to 15 percent at an optimum trim compared to even keel.

The efficiency gain due to an optimised trim is a function of the ship resistance mainly resulting from changes in flow behaviour around the bulbous bow. However, as outlined in (Reichel et al. 2014), fluctuations in the propulsive efficiency could also contribute to the ship performance improvements or energy losses. In addition, there is no universal optimum trim for a ship, since the optimum value depends on the individual operating parameters such as speed, displacement, specific hull shape and cargo carried.

Therefore, this chapter is dedicated to an exploration of the effect of trim on the reference oil products tanker resistance components and propulsive efficiency by means of the Ship Performance Simulation (SPS) model. The effect on  $CO_2$  and other atmospheric emissions as well as voyage performance behaviour due to changing trim have also been predicted.

## 10.1 Trim Definition

Generally, trim is defined as the difference between the draught at stern ( $T_A$ ) and the bow draught ( $T_F$ ) (Reichel et al. 2014):

$$Trim = T_A - T_F$$

10.1

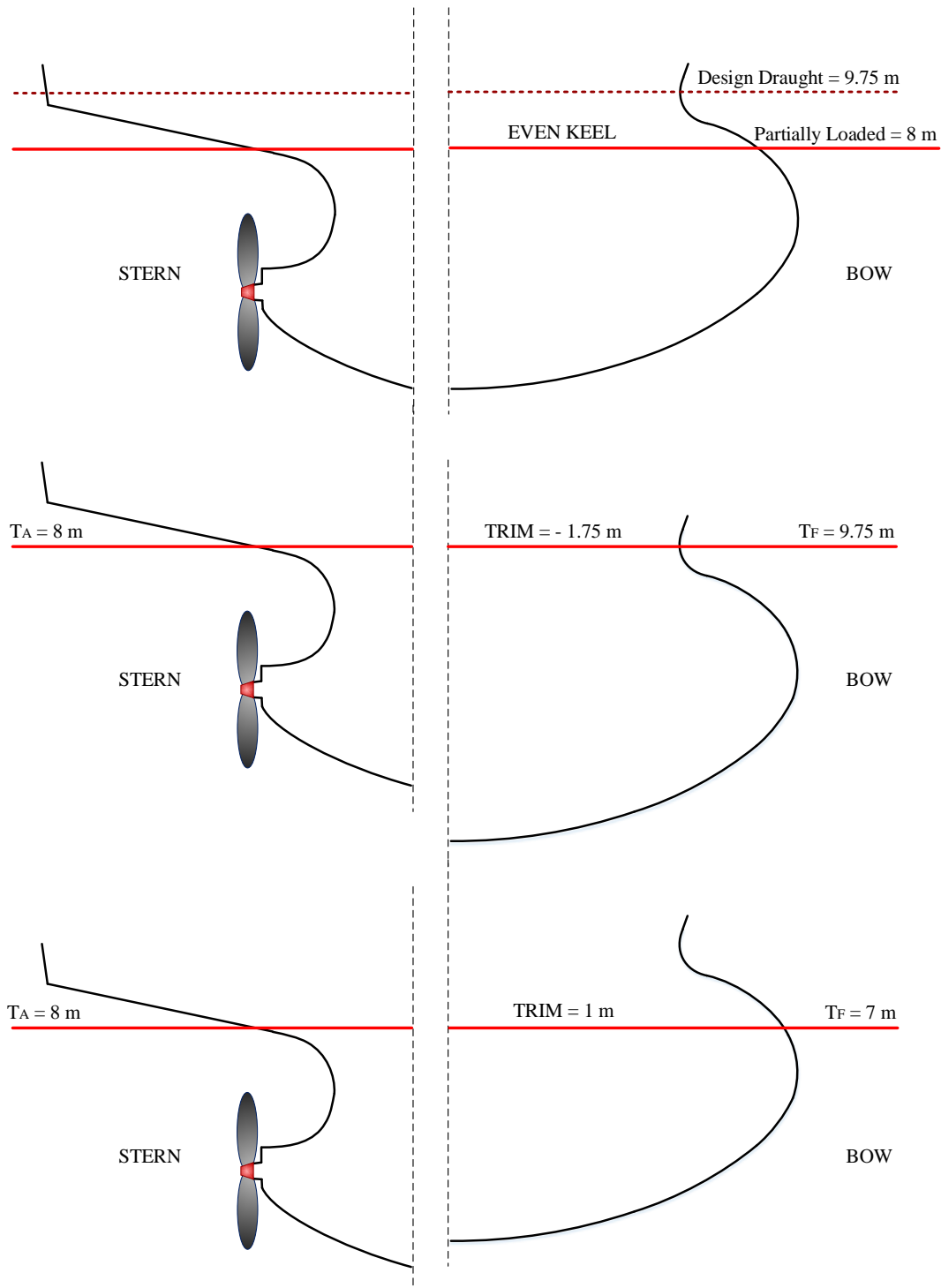


Figure 10.1 Schematic representation of considered trim conditions.

This case study is performed with the reference to -1.75m and 1.0m trim conditions representing a partially loaded draught of 8 m at an even keel. These trims have been selected in accordance with the waterline fluctuations around the bulbous bow while the variations around the stern are kept constant.

As illustrated in Figure 10.1, at the even keel the bulbous bow is slightly above the water level, at forward trim -1.75m the bulbous bow is submerged, while at the 1m trim, the bulbous bow is situated approximately one-third above the water line. Changes at the stern are modest and have been neglected. The initial hull dimensions for both trim conditions and even keel are listed in Table 10.1

Table 10.1 Initial hull dimensions at different trim conditions.

Parameters	Symbol	<i>Trim = -1.75 m</i>	<i>Even keel</i>	<i>Trim = 1 m</i>	Metric
Length of the ship	$L$	171.2	171.2	171.2	$m$
Length btw perpendiculars	$L_{PP}$	162	162	162	$m$
Length of the waterline	$L_{WL}$	159.2	161.7	162.5	$m$
Draught	$T$	8.875	8	7.5	$m$
Draught aft	$T_A$	8	8	8	$m$
Draught forward	$T_F$	9.75	8	7	$m$
Moulded breadth	$B$	27.4	27.4	27.4	$m$
Displacement volume	$\nabla$	27801	27801	27801	$m^3$
Displacement tonnage	$\Delta$	28496	28496	28496	tonnes

For each trim case, the length of the waterline  $L_{WL}$  has been manually measured from the reference vessel blueprints and scaled up to a full size. The displacement is kept constant for both trim conditions since no extra ballast is added and corresponds to the 8m draught at even keel, which has been interpolated in accordance with the provided values in the model test report for fully loaded, design and ballast conditions.

## 10.2 Hull Design Parameters

Updated hull design parameters were calculated by means of the Ship Performance Simulation model and summarised in Table 10.2. Hull wetted surface area is estimated in accordance with the formulas proposed in (Holtrop 1984), as described in Chapter 5.1, while wetted bulbous bow area is calculated using the first Simpsons rule based on the reference ship hull offset table provided. The fluctuations in the hull wetted surface due to changing trim conditions are stipulated by a changing immersion of the bulbous bow, since the bulbous bow wetted area is included into the wetted surface area formulation in the Holtrop and Mennen resistance prediction method.

Table 10.2 Changing hull parameters due to trim.

Parameters	Symbol	<i>Trim = -1.75m</i>	<i>Even keel</i>	<i>Trim = 1m</i>	Metric
Longitudinal position of centre of buoyancy	$lcb$	8.9	8.2	8.1	$m$
		5.6	5.1	5.0	%
Waterplane area at $L_{WL}$	$A_{WPL}$	3809	3749	3773	$m^2$
Midship section area	$A_M$	242	218	204	$m^2$
Wetted surface area	$WSA$	6052.8	5741.7	5562.6	$m^2$
<i>Design coefficients</i>					
Block coefficient	$C_B$	0.718	0.784	0.833	-
Midship section coeff	$C_M$	0.994	0.993	0.993	-
Waterplane coefficient	$C_W$	0.873	0.846	0.847	-
Prismatic coefficient	$C_P$	0.723	0.789	0.838	-
<i>Bulbous bow</i>					
Bulbous bow centre above the keel line	$hb$	4.061	3.236	2.736	$m$
Wetted bulbous bow area	$A_{BB}$	28.80	26.5	24.6	$m^2$

## 10.3 Ship Resistance

The total resistance components and, hence, the effective power  $P_E$  for both trim conditions and the even keel have been calculated by means of the Ship Performance Simulation model for the ship reference speed of 14.6 knots as listed in Table 10.3 as well as for a range of speeds 13 – 16 knots as demonstrated in Figure 10.2 – Figure 10.5.

Table 10.3 Ship resistance components under changing trim conditions (Design condition at 14.6 knots).

Ship Geometry	Symbol	<i>Trim = -1.75m</i>	<i>Even keel</i>	<i>Trim = 1m</i>	Metric
Form factor	$(k + 1)$	1.223	1.267	1.321	-
Frictional coefficient	$C_F$	0.0015296	0.0015266	0.0015257	-
Frictional resistance	$R_F$	267.90	253.63	245.58	<i>kN</i>
Appendage resistance	$R_{APP}$	4.09	4.08	4.08	<i>kN</i>
Wave-making resistance	$R_W$	50.62	84.40	164.84	<i>kN</i>
Bulbous bow resistance	$R_{BB}$	1.11	2.79	3.79	<i>kN</i>
Immersed transom resistance	$R_{TR}$	0.00	0.00	0.00	<i>kN</i>
Correlation resistance	$R_A$	72.84	68.46	66.14	<i>kN</i>
Total ship resistance	$R_T$	456	481	563	<i>kN</i>
Effective power	$P_E$	3426	3612	4231	<i>kW</i>

As a result, the form factor  $(k + 1)$  is changing in accordance with the waterline length  $L_{WL}$  and, hence is reduced at the forward trim = -1.75 m.

Both the frictional coefficient  $C_F$  and the frictional resistance  $R_F$  are increasing in line with the submerging bulbous bow due to an overall increase of the wetted surface area of the ship's hull. However, a scale of change is not affected by speed since the wetted surface area stays constant with higher speed of the ship of deep water (Figure 10.2).

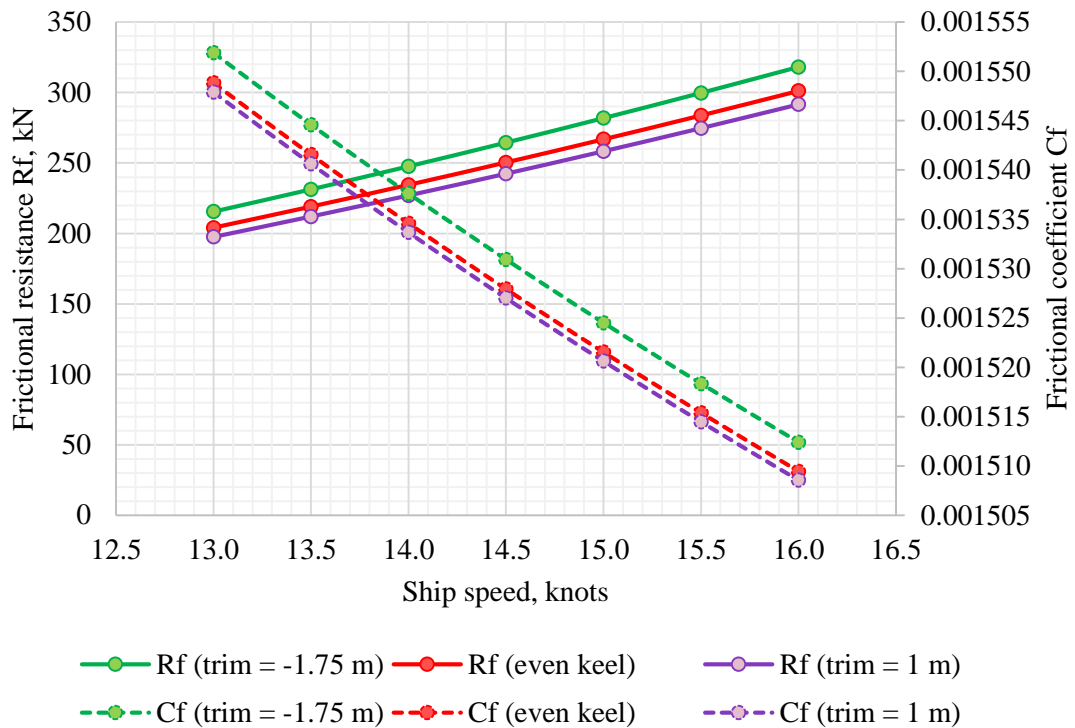


Figure 10.2 Frictional resistance  $R_F$  and frictional coefficient  $C_F$  performance due to changing trim.

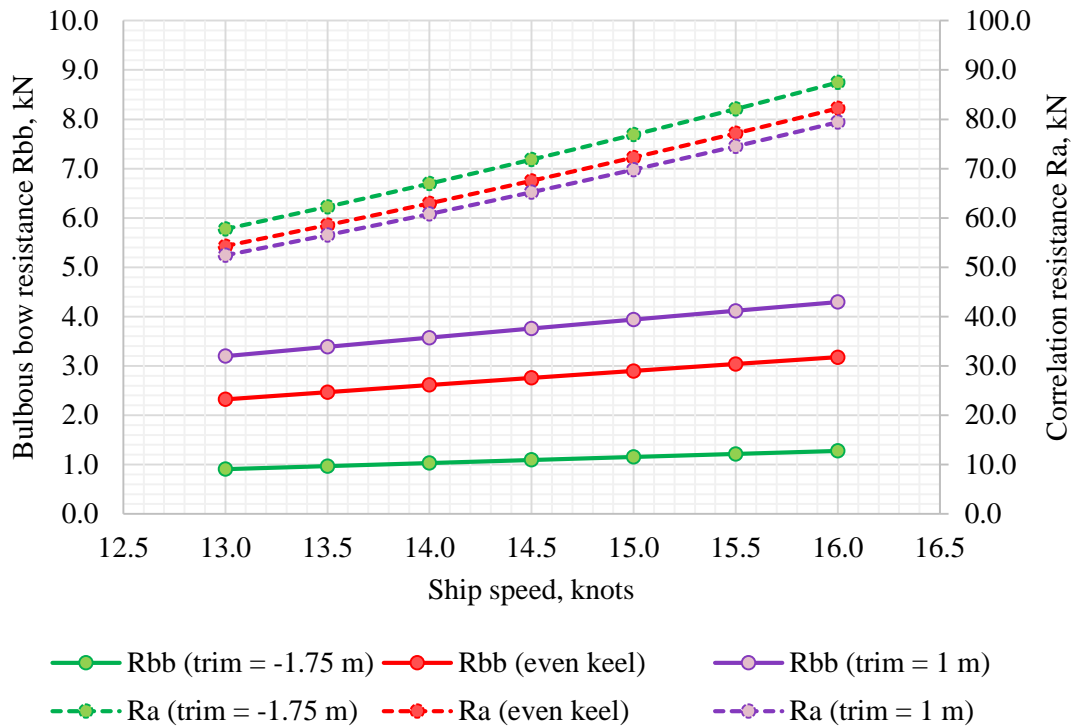


Figure 10.3 Bulbous bow resistance  $R_{BB}$  and correlation resistance  $R_A$  performance due to changing trim.

The bulbous bow resistance is minimised when the bulbous bow is totally submerged as in the case of the forward trim = -1.75m. Alternatively, the model-ship correlation resistance  $R_A$  is slightly reduced at trim = 1m (Figure 10.3), since being a function of a forward trim. In fact, the immersed transom resistance equals to 0 at all cases, since the transom locates much higher than 8 m draught aft and is not reached by water.

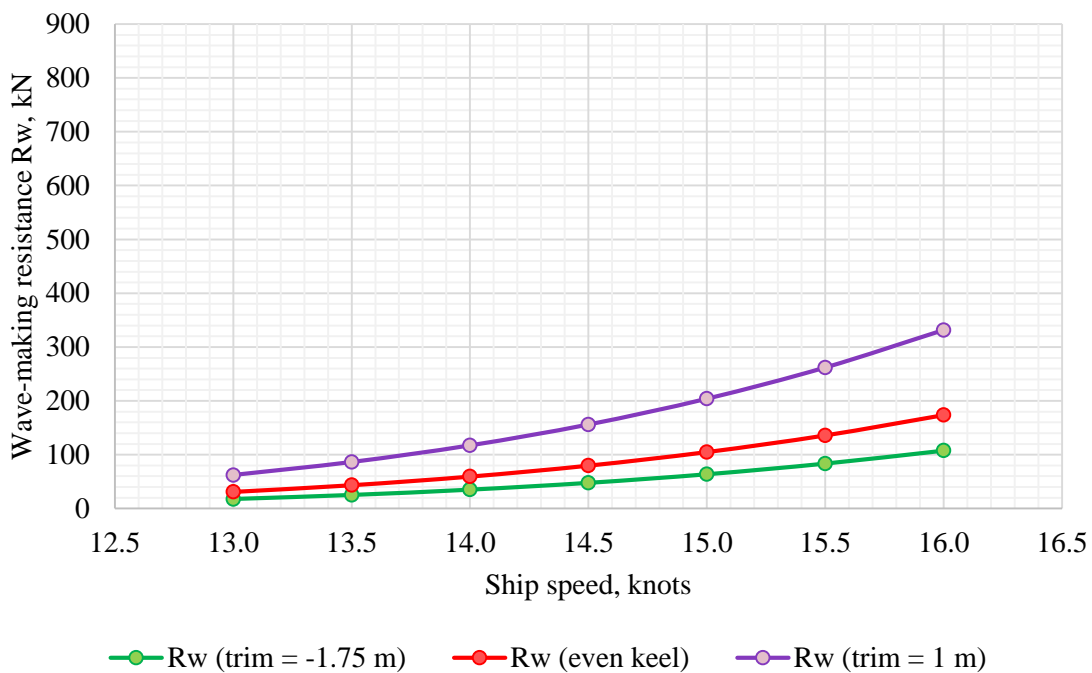


Figure 10.4 Wave-making resistance  $R_W$  performance due to changing trim.

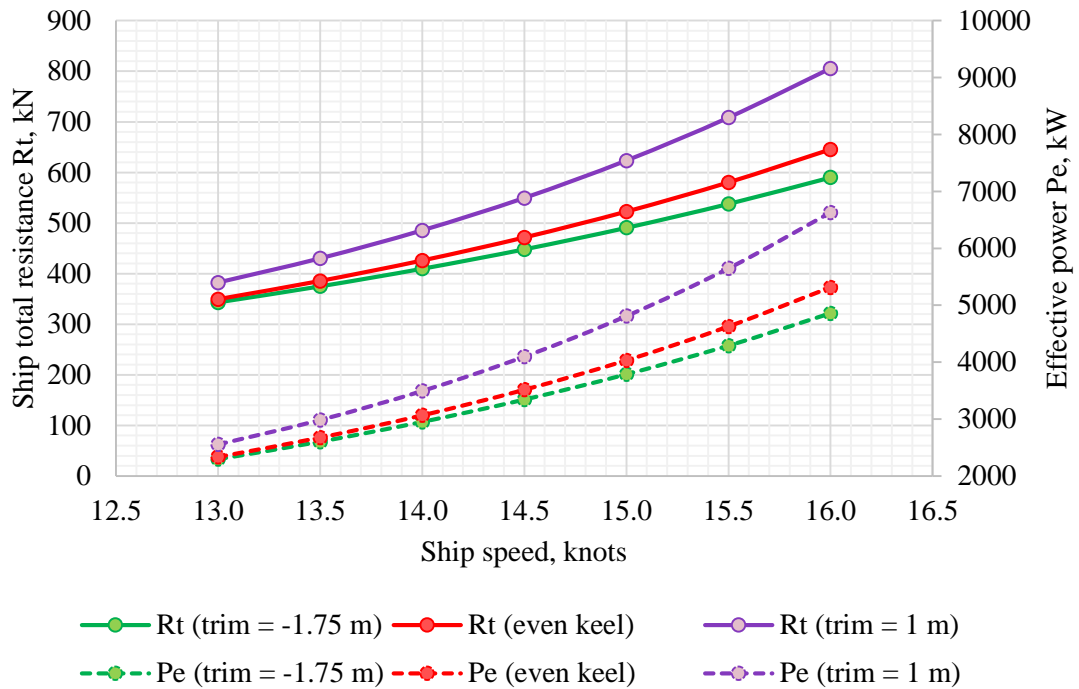


Figure 10.5 Total resistance  $R_T$  and effective power  $P_E$  performance due to changing trim.

As expected, the most significant impact on ship resistance has been achieved due to the wave-making resistance  $R_W$ , which largely depends upon the drag reduction properties of the bulbous bow being the most effective when totally submerged (for example at design draught). Therefore, since the forward draught  $T_F$  at trim = -1.75m equals to the design forward draught ( $T_F = 9.75\text{m}$ ) the wave making resistance  $R_W$  is significantly reduced in comparison with the even keel. Alternatively, the wave making resistance  $R_W$  at trim = 1m is increased, it fact, almost doubled in comparison with the even keel while the level of gain is scaling up as the ship's speed increases.

As a result, the effect of trim on the wave-making resistance  $R_W$  cancels out all other trends, making the total resistance and, hence, the effective power the most beneficial at the trim = -1.75m among the other cases.

## 10.4 Propulsive Efficiency

For the estimation of the propulsive efficiency due to changing trim, a constant range of rotational speeds ( $RPM$ ) corresponding to the mean draught of 8m at even keel is used. The range of  $RPM$  has been calculated by means of regression analysis in accordance with the rotational speeds, provided in the model test report at loaded, design and ballast conditions. The results for the reference ship speed of 14.6 knots are summarised in Table 10.4, while the outcomes for the range of ship speeds are demonstrated in Figure 10.6 and Figure 10.7.

Table 10.4 Propulsive efficiency components under changing trim conditions (Design condition at 14.6 knots).

Ship Geometry	Symbol	<i>Trim = -1.75m</i>	<i>Even keel</i>	<i>Trim = 1m</i>	Metric
Wake fraction	$w$	0.370	0.382	0.390	-
Thrust deduction coefficient	$t$	0.220	0.226	0.228	-
Relative-rotative efficiency	$\eta_R$	1.003	1.009	1.013	-
Hull efficiency	$\eta_H$	1.24	1.25	1.27	-
Open water efficiency	$\eta_O$	0.57	0.56	0.55	-
Thrust coefficient	$K_T$	0.1314	0.1346	0.1369	-
Torque coefficient	$K_Q$	0.0157	0.0160	0.0162	-
Quasi-propulsive coefficient	$QPC$	0.703	0.705	0.710	
Delivered power	$P_D$	4871	5121	5959	

Both the wake fraction  $w$  and thrust deduction  $t$  coefficients are lower at trim = - 1.75m be the head, leading to a reduction of the hull efficiency  $\eta_H$ . According to the regression methods described in Chapter 5, the wake fraction  $w$  is a function of length of the waterline  $L_{WL}$  and the viscous resistance  $C_V$  coefficient, which in turn depends upon the frictional resistance  $C_F$  coefficient and since both are decreasing, the wake fraction has mathematically resembled the same trend. In case of thrust deduction, the reduction is mostly affected by  $L_{WL}$ . In the same manner, the relative-rotative efficiency  $\eta_R$  is also reduced at trim = -1.75m. However, it is difficult to explain these trends hydrodynamically without model tests or CFD simulation.

The reduced wake fraction  $w$  has also affected  $K_Q$  and  $K_T$  coefficients resulting in slightly increased open water efficiency  $\eta_O$  at trim = -1.75m.

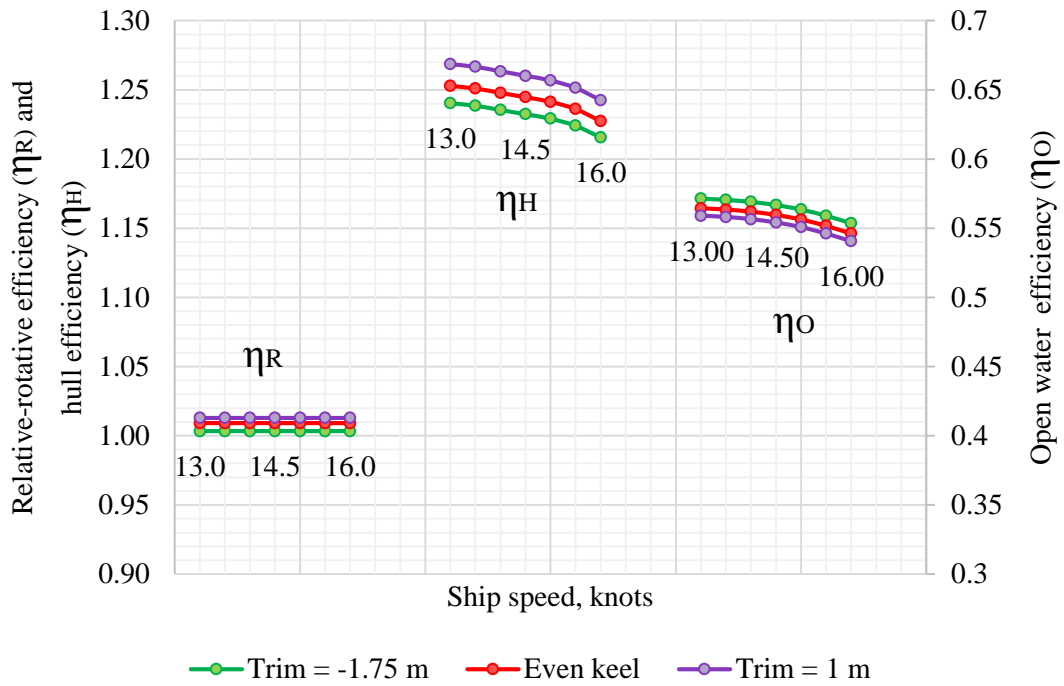


Figure 10.6 Effect on the propulsive efficiency components due to changing trim.

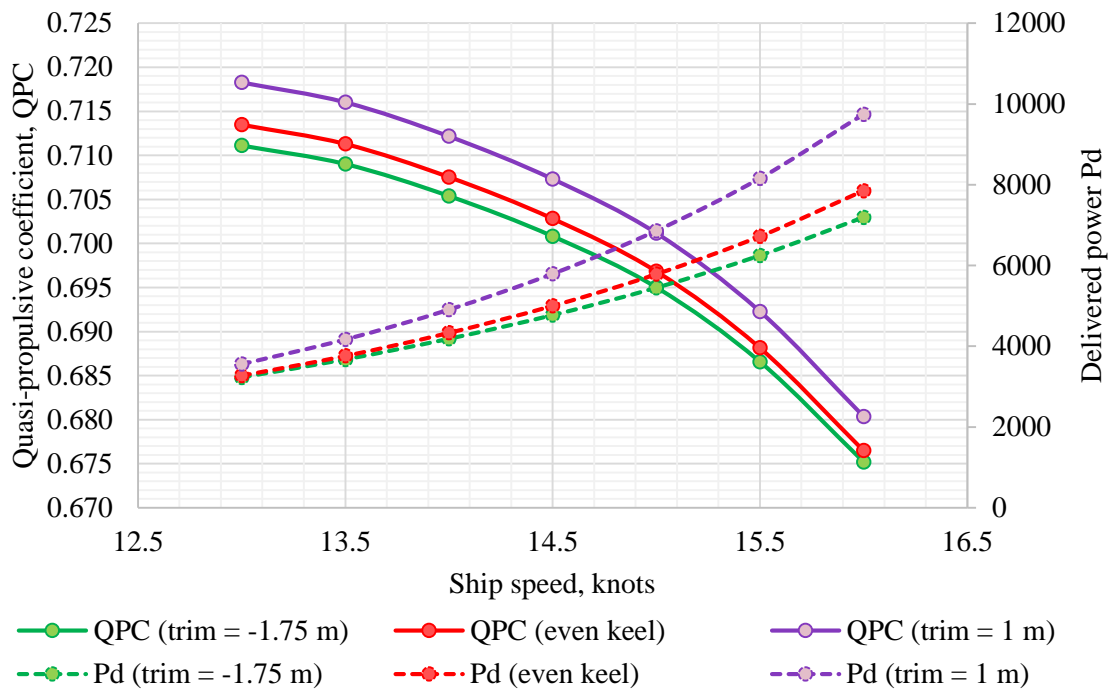


Figure 10.7 Power absorption  $P_D$  and  $QPC$  performance due to changing trim.

As a result, the combined effect of hull  $\eta_H$  and relative-rotative  $\eta_R$  efficiencies has neutralised the positive effect of the open water efficiency  $\eta_O$  at trim = - 1.75m, resulting in the most efficient  $QPC$  at trim = 1m. However, a strong domination of the wave-making resistance  $R_W$  has cancelled out the propulsion efficiency fluctuations due to trim, making the forward trim = - 1.75m the most beneficial option in comparison to the even keel while

the energy losses due to trim = 1m can reach up to 19.4 percent with increasing speed as shown in Figure 10.8.

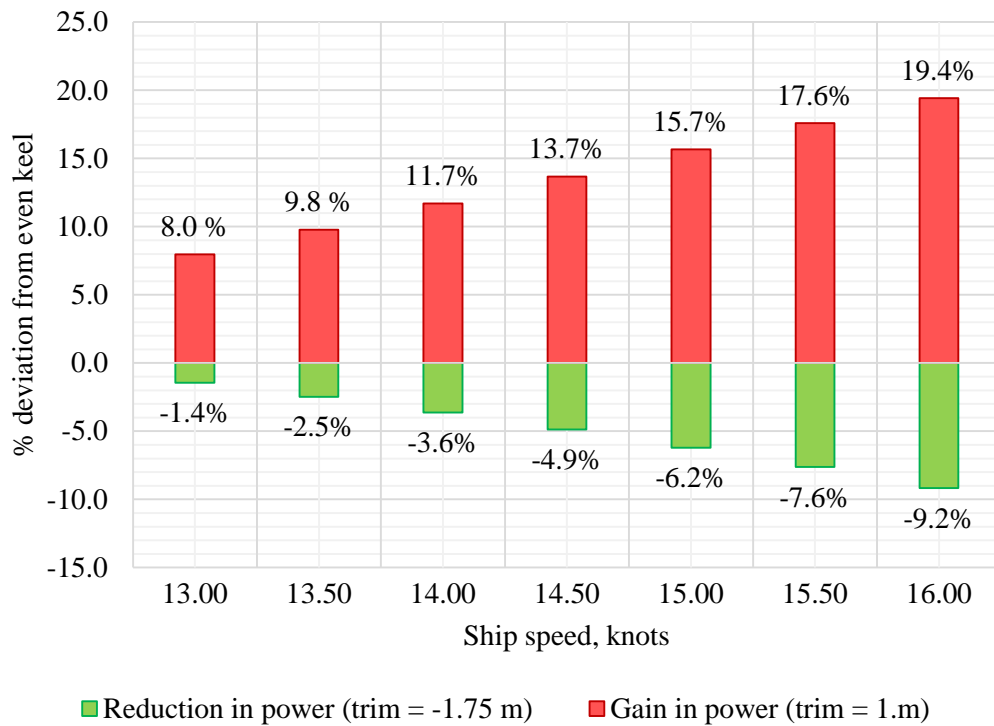


Figure 10.8 Resulting level of gains and reductions of power in percentage due to changing trim.

### 10.5 Impact on the Energy Efficiency Indicators

Since the trim optimisation does not require engine modifications as well as the conventional fixed pitch propeller has been used as a base for the propulsion analysis, the corresponding original 5S50ME-C engine with SMCR power or 7371kW and SMCR speed of 127 rpm is selected for the fuel consumption and exhaust emissions prediction. The engine performance curves at trim = -1.75m, even keel and trim = 1m are illustrated in Figure 10.9.

The engine performance and exhaust emissions simulation results at the reference speed of 14.6 knots are summarised in Table 10.5. The results have shown that it is possible to reduce fuel oil consumption by more than 5 percent when operating at trim = -1.75m compare to the even keel, while if the trim was not properly optimised (trim = 1m), the fuel losses reach up to 15 percent in contrast with the even keel.

Regarding the exhaust emissions footprint, it is possible to reduce the  $CO_2$  emissions by 5.3 percent and the  $NO_x$  emissions by 3.6 percent in case the of the optimised trim (trim = -1.75m), while the  $CO_2$  and  $NO_x$  emissions will increase by 15.3 and 9.3 percent respectively at the poorly optimised trim (trim = 1m).

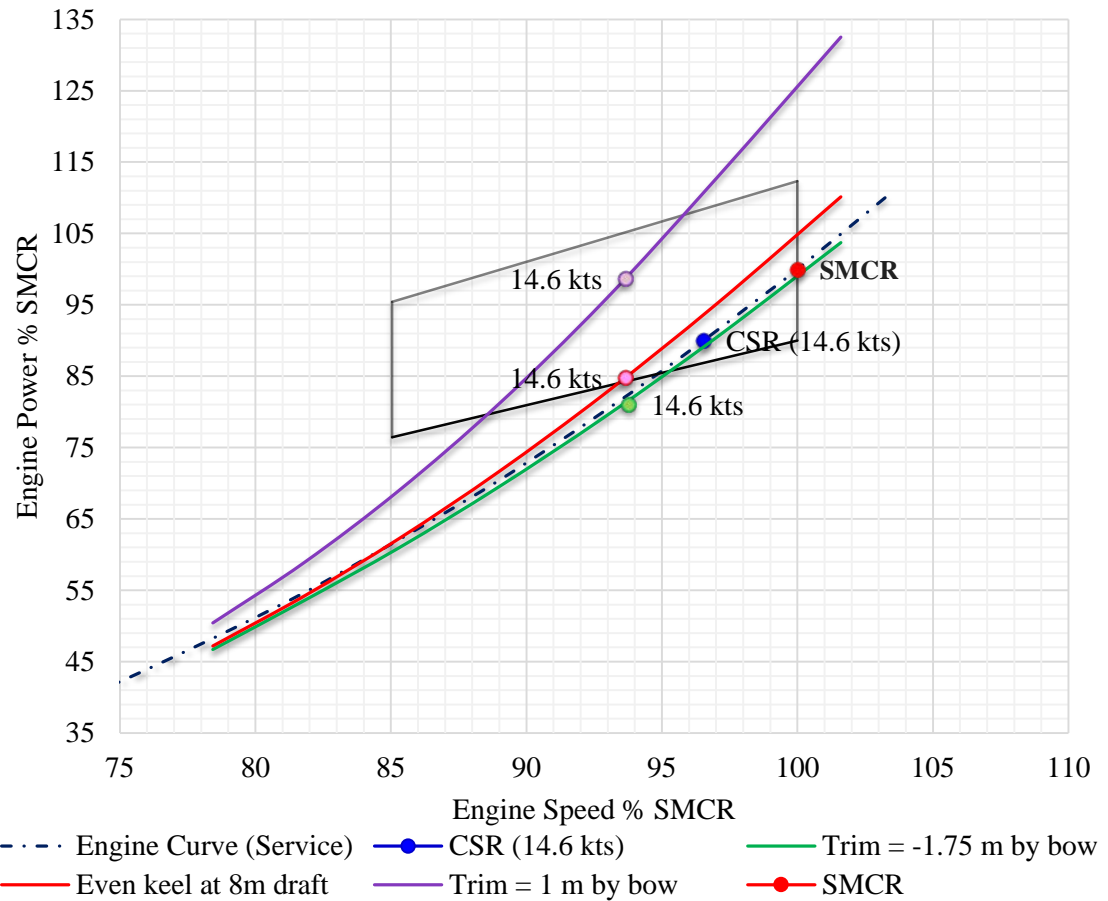


Figure 10.9 Engines service curves for partially loaded operation at both trim conditions and the even keel.

Table 10.5 Summary table of engine performance due to changing trim at 14.6 knots.

		Symbol/Metric	<i>Trim = -1.75</i>	<i>Even keel</i>	<i>Trim = 1m</i>
Speed	<i>V</i>	knots	14.6	14.6	14.6
RPM	% SMCR		94	94	94
Power	% SMCR		81	85	99
Fuel	FC	kg/h	973	1026	1213
	SFOC	g/kWh	163.3	163.7	166.4
Mass Flow Rate	<i>NO<sub>x</sub></i>	kg/h	84	87	96
	<i>CO</i>		2.87	3.07	3.59
	<i>HC</i>		2.01	2.07	2.20
	<i>CO<sub>2</sub></i>		3174	3342	3944
	<i>SO<sub>2</sub></i>		4.71	4.96	5.80

The theoretical voyage simulation for both trim cases and the even keel has also been conducted. In this case, the first part of the voyage, which is normally performed under the

loaded condition, has been substituted with the partially loaded condition under changing trims and the even keel with 8m draught. The second part of the voyage is kept the same as in the previous cases (Chapter 7 – Chapter 9) corresponding to the ballast condition. In addition, for comparison purposes the ship speed distribution for the partially loaded conditions (changing trim) has been kept as fully loaded, which is normally 0.5 – 1 knot lower on average than at ballast conditions. Therefore, the 31-day voyage is still divided as 16/15 days.

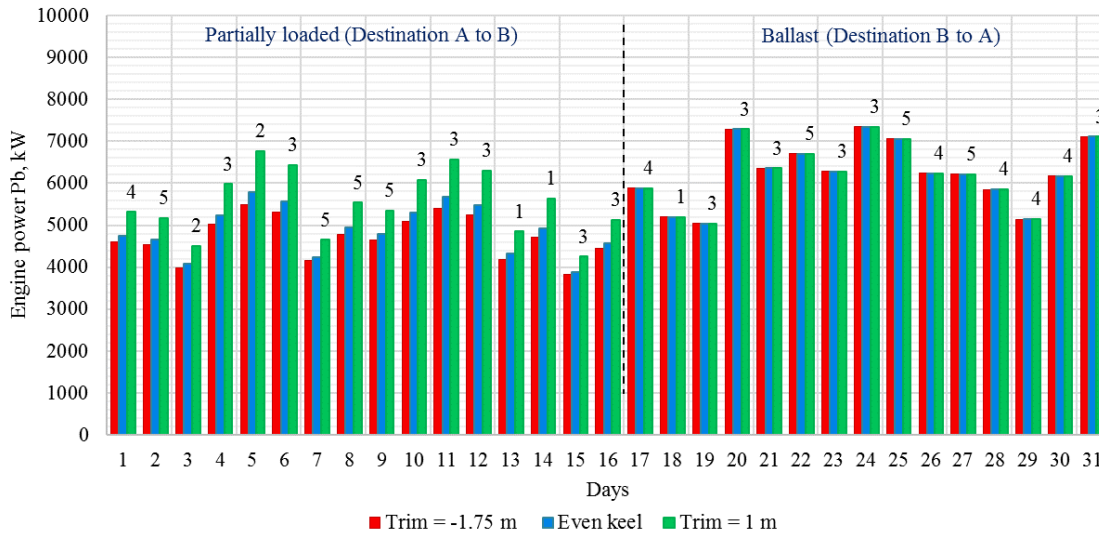


Figure 10.10 Voyage simulation results for both trim conditions and the even keel. Numbers at the top of the graph are Beaufort numbers.

The fuel savings with the optimised trim (trim = -1.75m) account for 11 tonnes of fuel per voyage, while losses due to trim = 1m reach up to 41 tonnes of fuel per voyage. Similar trends occur with the  $CO_2$  and other atmospheric emissions as summarised in Table 10.6.

It should be remembered, that the level of gains/reductions due to trim conditions increase with speed and the impact of trim optimisation could be much more significant if the voyage speed range increased by 0.5 – 1 knot.

Table 10.6 Fuel consumption and emissions footprint performance per voyage.

	<i>Trim = -1.75m</i>	<i>Even keel</i>	<i>Trim = 1m</i>	
Fuel	670	681	722	tonnes per voyage
$CO_2$	2141	2174	2304	tonnes per voyage
$NO_x$	57.6	58.3	60.7	tonnes per voyage
$SO_2$	3.2	3.2	3.4	tonnes per voyage
$CO$	1.8	1.8	2.0	tonnes per voyage
$HC$	1.3	1.3	1.4	tonnes per voyage

Table 10.7 Average SFOC and engine load per voyage.

	<i>Trim = 1.75m</i>		<i>Even keel</i>		<i>Trim = 1m</i>		
	Loaded	Ballast	Loaded	Ballast	Loaded	Ballast	
LOAD	63.7	84.8	66.0	84.8	74.8	84.8	%
SFOC	164.7	165.2	164.5	165.2	164.5	165.2	g/kWh

In Table 10.7, the average engine load and SFOC for both trim conditions and the even keel are summarised. Indeed, the SFOC of trim = -1.75m is slightly higher due to low load. Thus, in order to achieve the most efficient operation, the average ship speed could be slightly increased to operate at about 70 percent load corresponding to the lowest fuel consumption rate for this type of engine.

In conclusion, the results have shown that the impact of trim on ship efficiency is significant and, if not optimised properly, can lead to serious power losses, while minimising the benefits of energy saving devices and high-efficiency propellers as well as the initial purpose of the EEDI certification.

On the other end of the spectrum, the trim optimisation is difficult to be controlled governmentally, since it has to be performed in each individual case depending on load, speed and the hull structure as well as the master's discretion. However, the industry's interests in fuel savings and environmental concerns regarding the exhaust emissions control coupled with the growing trim optimisation CFD based software development could lead to some additional improvements addressed to the EEDI legislation, namely to include the trim optimisation software installation as a mandatory requirement to a ship owner in order to be issued with the EEDI certificate.

## 11 Future Hybrid Propulsion Concepts

By following the discussions in Chapter 2.5, progressive developments in battery and fuel cell technologies as well as hybridisation and complete electrification of a number of smaller ferries and offshore vessels hold a significant promise for more efficient use of propulsion power coupled with the potential reductions in the atmospheric emissions for larger vessels travelling longer distances.

Since, in the case of modern marine diesel engines the energy efficiency and specific emissions depend upon the load, being less beneficial at low and changing loads. The hybrid-based operational profile can help to avoid the operation at these loads by using a battery bank to store the excess energy produced due to load variations and then return it to the system when needed while operating at constant load and potentially producing some extra power by means of renewable energy sources or fuel cells. Such an operational principle is often referred as a load leveling (Whitelegg & Bucknall 2013) or peak-shaving (Pestana 2014).

The benefit of hybrid-based power systems is closely associated with the operational profile and type of vessel. Traditionally, load leveling operational concepts are considered to be especially advantageous when the level of load fluctuations is high, for instance for tugs, vessels based on the dynamic positioning (DP) operations as well as offshore supply vessels. A typical example is the first hybrid offshore supply vessel, Viking Lady, built in 2013 with incorporated fuel cell technology as a part of the propulsion system. According to various industry references, this system provides the primary benefits of 20 percent in reduction of fuel consumption,  $CO_2$  and other atmospheric emissions. However, there is a number of other operational profiles where the frequency and level of load fluctuations is less obvious but undervalued, including the additional fuel consumption due to heavy weather conditions influenced by increased wave-making resistance and fluctuating propeller immersion.

Based on the initial service data and voyage simulation results of the Ship Performance Simulation model, the engine load of the reference oil products tanker is also fluctuating due to changing weather and ship speed as shown in the power-versus-time voyage diagram (Figure 11.1) where the upper labels represent values of the engine load in percentage corresponding to certain engine power (blue) and ship speed (red). Hence, it has been decided to evaluate the potential benefits and savings due to hybridisation of the reference

tanker through the introduction of the load leveling operational profiles for the previously considered 31 days' voyage.

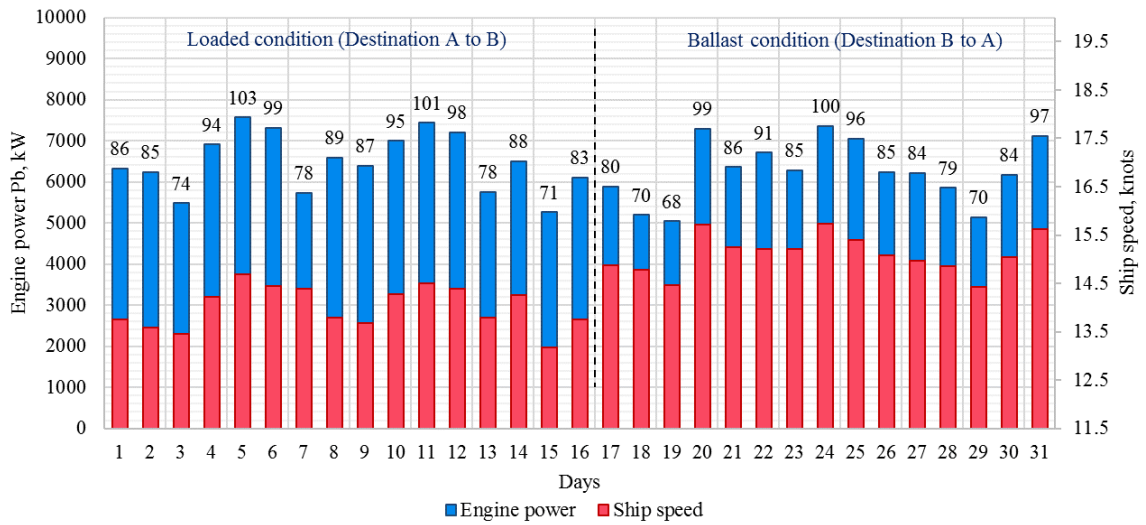


Figure 11.1 Original voyage of the reference oil products tanker. Numbers at the top of the graph are rotational speeds.

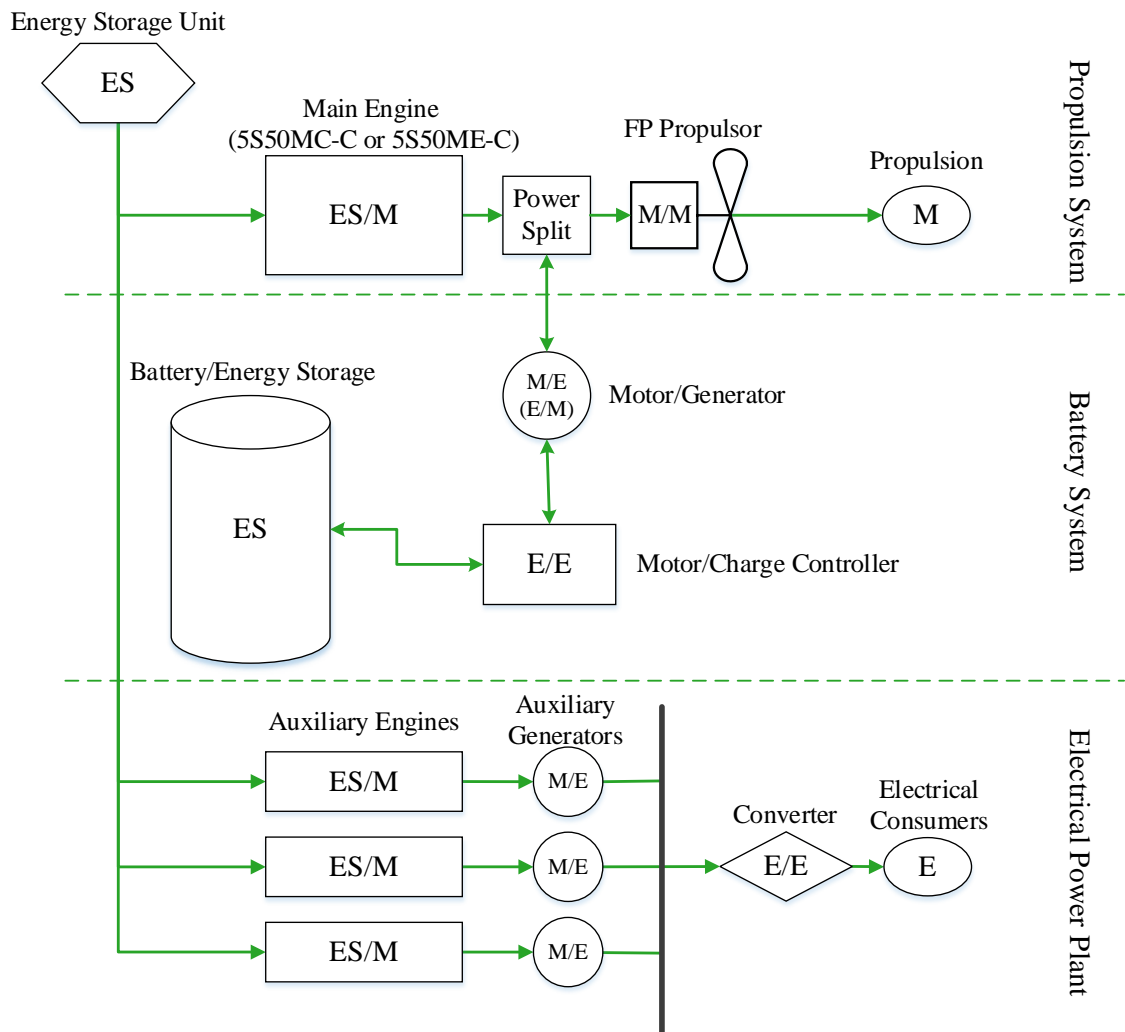


Figure 11.2 Hybrid-based machinery arrangement for the reference vessel.

From a review of recent literature (Whitelegg & Bucknall 2013; DNV GL 2015), the hybrid system developed in Figure 11.2 was produced as being one of the simplest systems could be applied to the modern products tanker. The system includes:

- a power split mechanical device which allows to transfer the power between its connections,
- a battery or energy storage unit that stores an excess power produced by the engine or supplies demanded power to the propeller if needed,
- a motor/generator acting as a driver of the energy from/to shaft/battery while converting the energy from mechanical to electrical state and vice versa.

The system may also be equipped with renewable energy technologies or fuel cells for production and storage of additional power for the battery support purposes. Such a concept allows the propulsion from the engine or from the motor individually as well as from both at the same time. In addition, the propeller can also be disconnected for stand-alone generator functions.

### 11.1 On-Time Voyage Simulation

From the operational perspective, the engine load and fuel consumption depend upon the following factors: required ship speed, ship displacement and weather. In this chapter, two load-leveling-based operation approaches are considered.

The first concept involves the engine operation based on the average operational speed for loaded and ballast conditions aiming to complete the voyage on time (referred as ON\_TIME in this study). Therefore, in order to conduct a hybrid-based voyage simulation, the constant operational engine load and ship speed should be determined.

In this case, a typical 31 days' voyage, consisting of 16 days at loaded and 15 days at ballast operations, is considered. The voyage is based on the original FP propeller connected with the MAN 5S50ME-C marine diesel engine similar to the previous case studies.

The average ship speed for the loaded part of the voyage accounts for 14 knots while in the case of ballast the average ship speed is 15.1 knots. The ship speed distributions for both conditions along with their average lines are demonstrated in Figure 11.3.

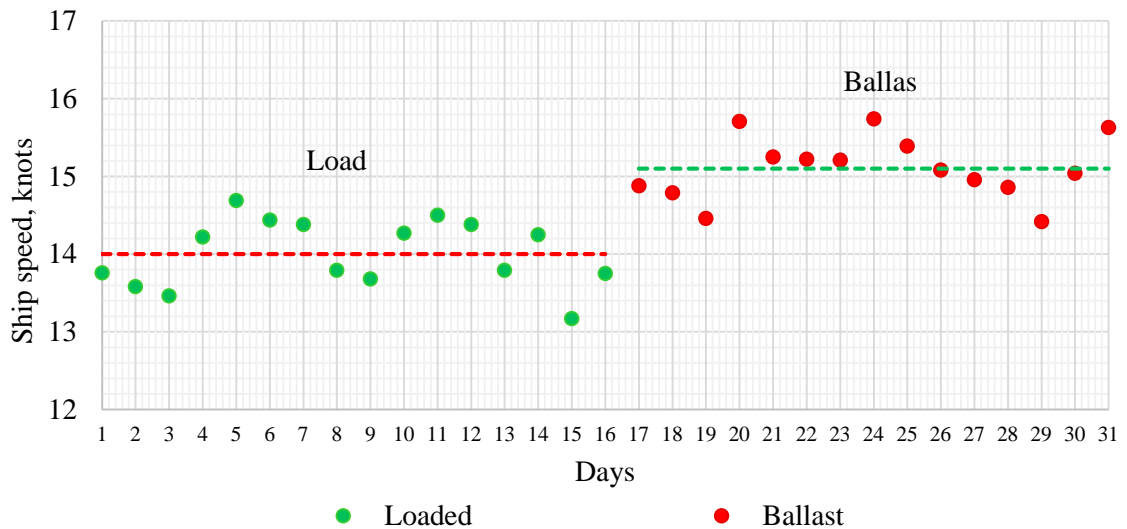


Figure 11.3 Ship speed distribution during the original voyage.

Another important factor is the weather conditions, which should be taken into account. According to the probability analysis of 125 ship service data points, the most common sea state with the probability of 38 percent is related to the Beaufort number 3 described as a gentle breeze in accordance with Table 6.1. The sea state probability analysis results are illustrated in Figure 11.4.

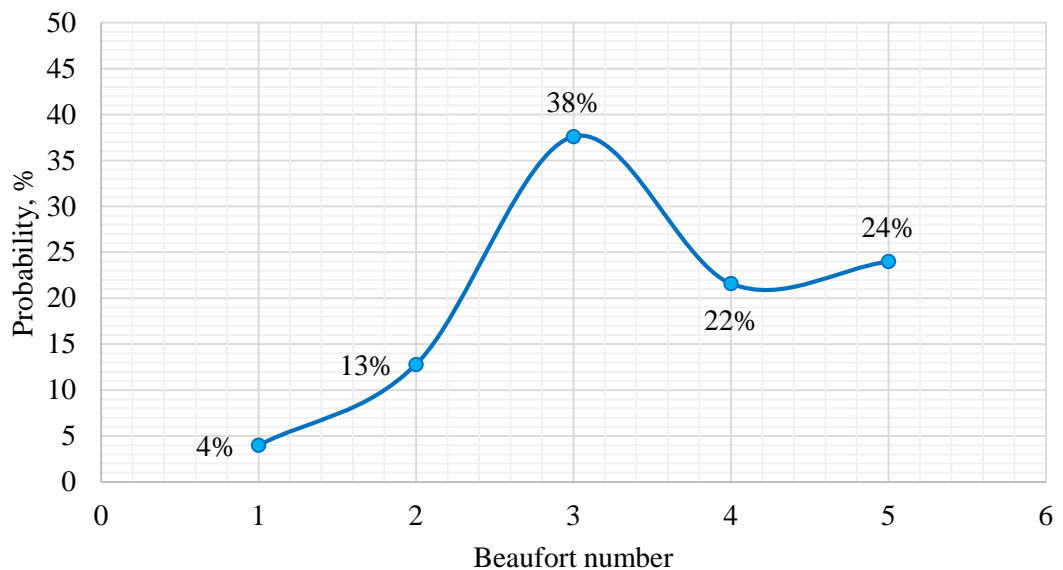


Figure 11.4 Sea state probability analysis results.

As a result, to complete the voyage on time, the hybridised reference tanker should operate with the speed of 14 knots at 88.4 percent load (SFOC = 165.2 g/kWh) under fully loaded condition and with the speed of 15.1 knots at 82.5 percent load (SFOC = 164.4 g/kWh) under ballast condition. Both of these operational requirements are corresponding to the additional power needs associated with the Beaufort number 3 as shown in Figure 11.5.

The resulting ON\_TIME voyage simulation is shown in Figure 11.6 where the blue columns represent the power demand with the upper labels indicating relevant weather conditions, the red columns demonstrate the ship speed while the purple line represents the constant engine power for loaded and ballast draughts.

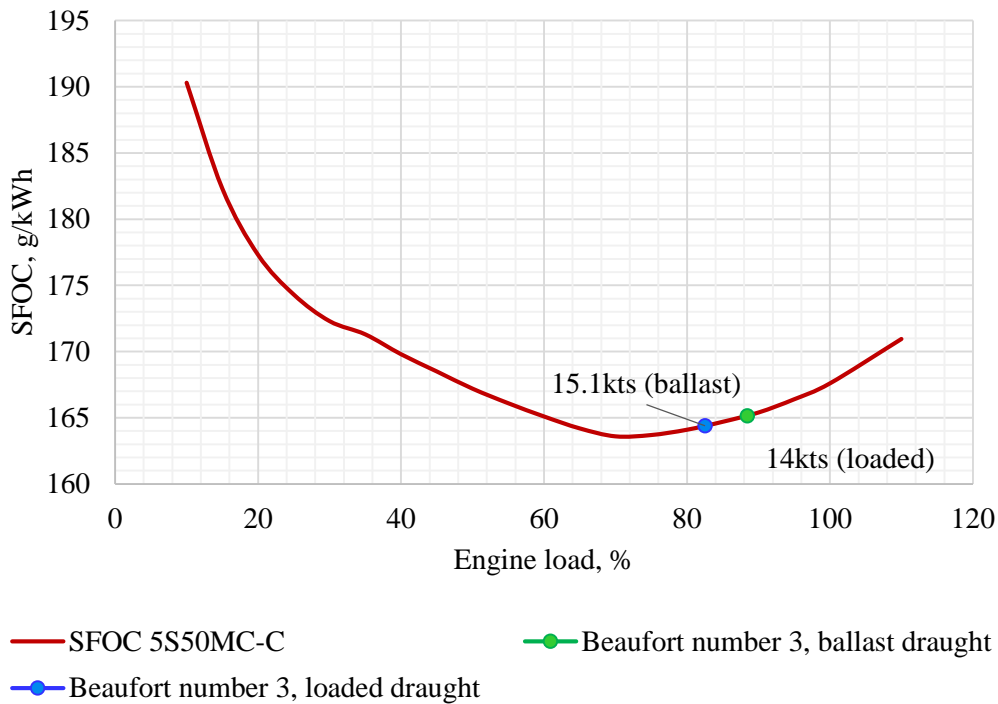


Figure 11.5 Speed, load and SFOC arrangements for the completed voyage on time (ON\_TIME) operation.

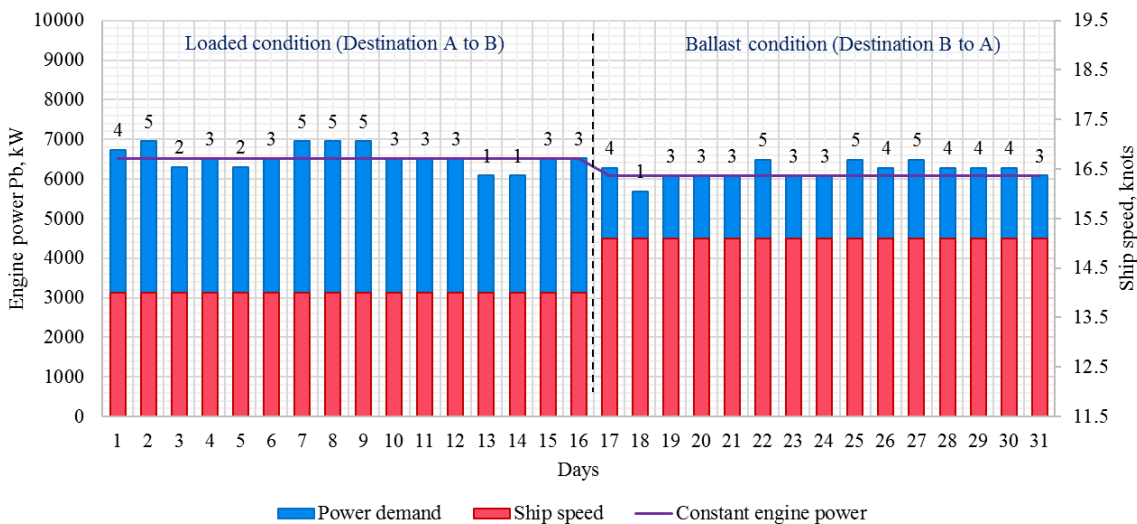


Figure 11.6 ON\_TIME voyage simulation. Numbers at the top of the graph are Beaufort numbers.

In addition, Figure 11.7 illustrates the power demand that should be provided from the battery system (red) while the excess power produced by the engine is shown as green columns. The weather distribution for the voyage simulation is the same as in the previous case studies, which was selected randomly (from the ship service measurements as

described in Chapter 6). Since in this selection “bad weather” of *BN 4* and *5* occurs more often than *BN 1* and *2*, the battery power capacity should be significant (or supported by fuel cells or other sources).

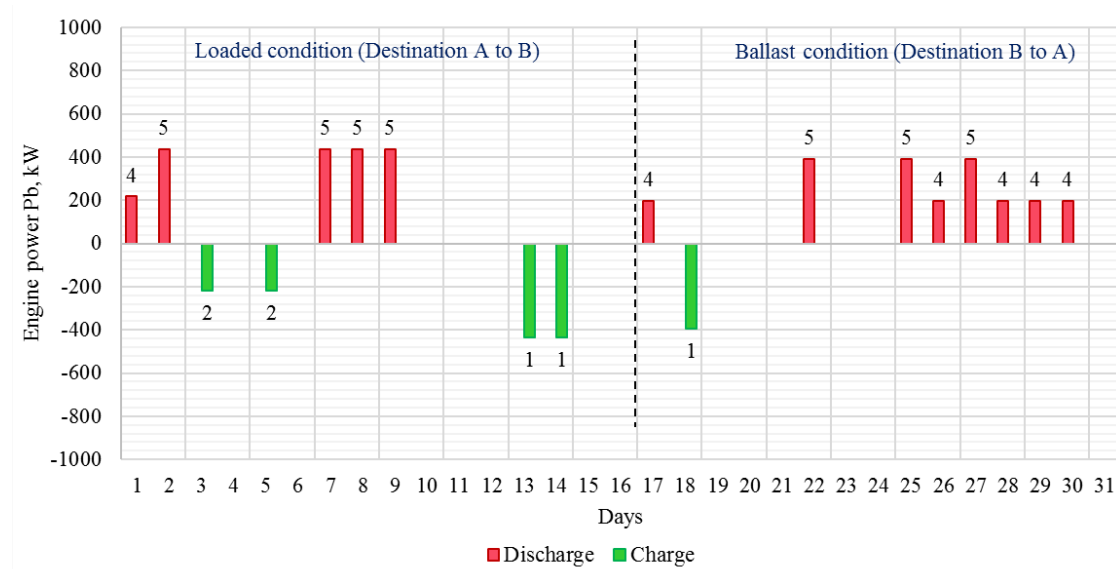


Figure 11.7 ON\_TIME battery charging/discharging diagram.

Namely, it has been estimated that the total battery discharge for the loaded and ballast conditions are 47MW and 52MW while the excessively produced power (battery charge) are 31MW and 9MW respectively making the longest discharge period worth of 47MW of battery power in case of ballast condition. Therefore, it can be assumed that approximate battery capacity of 50MW is required to performed this voyage. The resulting fuel consumption, atmospheric emissions and approximate battery capacity for the ON\_TIME voyage are listed in Table 11.1.

In this case, the battery discharge/charge has been calculated as per 24 hours, since weather forecasting along with ship speed measurements have been performed once a day by the data provider and, therefore, no information regarding the weather and ship speed fluctuations during the 24 hours’ period is known. Perhaps, should the hourly speed and weather fluctuations occur with the same frequency as daily, the total battery capacity would be significantly reduced.

However, in order to decrease the battery size and capacity, it has been decided to slightly reduce the ship speed when operating under heavy weather conditions helping to minimise the amount of power to be consumed from the battery storage while keeping the voyage duration as close to original as possible.

In this case, referred as ON\_TIME\_SPEED, the ship speed has been reduced by 0.1 knots for each load (13.9 for loaded and 15 for ballast) when the Beaufort number reaches the state of 4 or 5. In fact, such voyage optimisation will not affect the main engine performance in terms of emissions and fuel oil consumption but will “cut off” the extra power demand due to bad weather. It has been estimated that the additional voyage time due to the speed reduction accounts for 2 hours 53 minutes at loaded conditions and for 2 hours 24 minutes at the ballast. The resulted delays are considerably small in both cases and have been neglected. But it has to be taken into account in a practical application so as to avoid potential delays rising from the ship being unable to enter a port due to water depth limitations. The ON\_TIME\_SPEED voyage simulation is shown in Figure 11.8 while the ON\_TIME\_SPEED battery charging/discharging performance is illustrated in Figure 11.9.

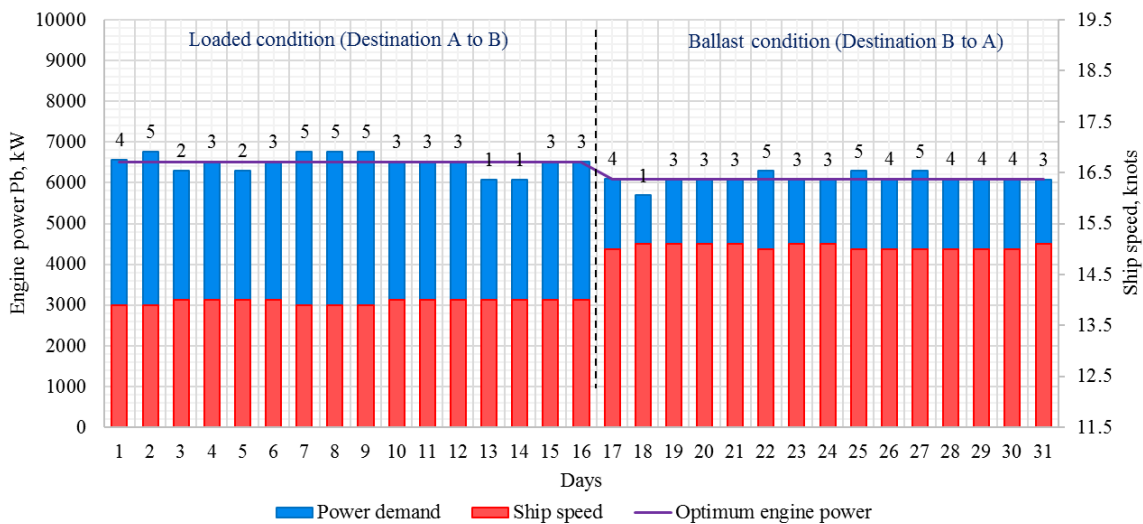


Figure 11.8 ON\_TIME\_SPEED voyage simulation.

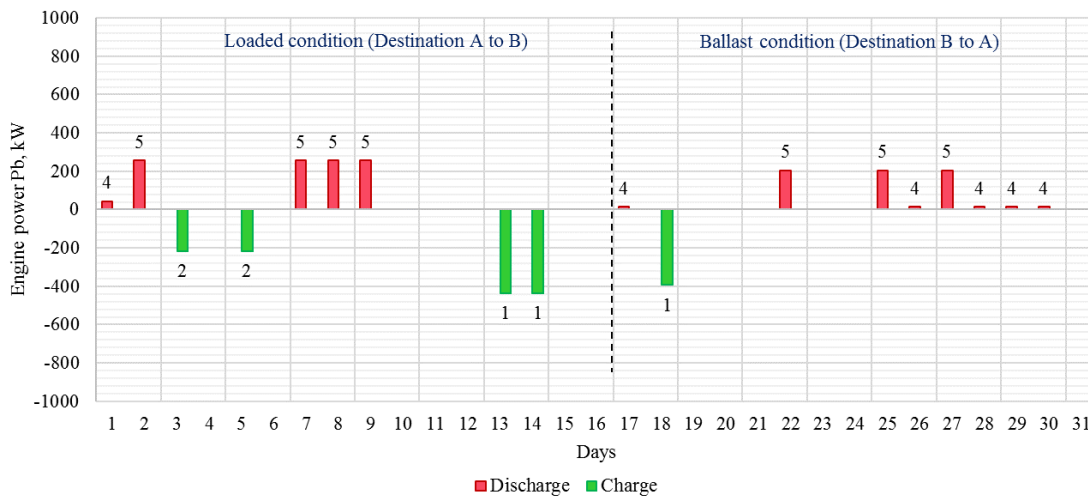


Figure 11.9 ON\_TIME\_SPEED battery charging/discharging diagram.

As a result, the total battery discharge for loaded and ballast conditions is reduced to 26MW and 16MW while the excessively produced power (battery charge) is kept the same making the longest discharge period worth of 18MW of battery power in case of the loaded condition. Therefore, it can be estimated that approximate battery capacity of 20MW is required to performed this voyage. The results of the ON\_TIME\_SPEED voyage are also listed in Table 11.1.

Table 11.1 ON\_TIME and ON\_TIME\_SPEED voyage results.

Parameter	ON_TIME		ON_TIME_SPEED		Metrics
	Loaded	Ballast	Loaded	Ballast	
Speed	14	15.1	14	15.1	Knots
Power	6517	6083	6517	6083	kW
FOC	1076	1000	1076	1000	kg/h
	25832	24001	25832	24001	kg/day
$CO_2$	3437	3193	3437	3193	kg/h
$NO_x$	87.1	83.5	87.1	83.5	kg/h
$SO_2$	5.10	4.74	5.10	4.74	kg/h
$CO$	3.09	2.83	3.09	2.83	kg/h
$HC$	2.02	1.95	2.02	1.95	kg/h
Load	88.4	82.5	88.4	82.5	%
SFOC	165.2	164.4	165.2	164.4	g/kWh
Reduced speed	-	-	13.90	15.00	Knots
Battery performance					
Total discharge	47	52	26	16	MW
Total charge	-31	-9	-31	-9	MW
Longest discharge	31	47	18	16	MW
Battery capacity	50		20		MW
Voyage extension					
Day	-	-	-	-	
Hours	-	-	2	2	
Minutes	-	-	53	24	
Total	-	-	-	-	Days

## 11.2 Optimum Load Voyage Simulation

The second concept, referred as OPTIMUM, is focused on the main engine, constantly operating at the most efficient load, which in the case of 5S50MS-C equals to 70 percent,

and corresponding ship speeds for loaded and ballast conditions while taking into account the sea state associated with the Beaufort number 3. The power excess and demand due to changing weather are covered by the energy storing battery system similar to the previous case.

The corresponding ship speeds are found to be 13.1 knots at the loaded condition and 14.5 knots at ballast condition as shown in Figure 11.10 while for both draughts the vessel will operate at 70 percent load with the most favourable SFOC of 163.6 g/kWh.

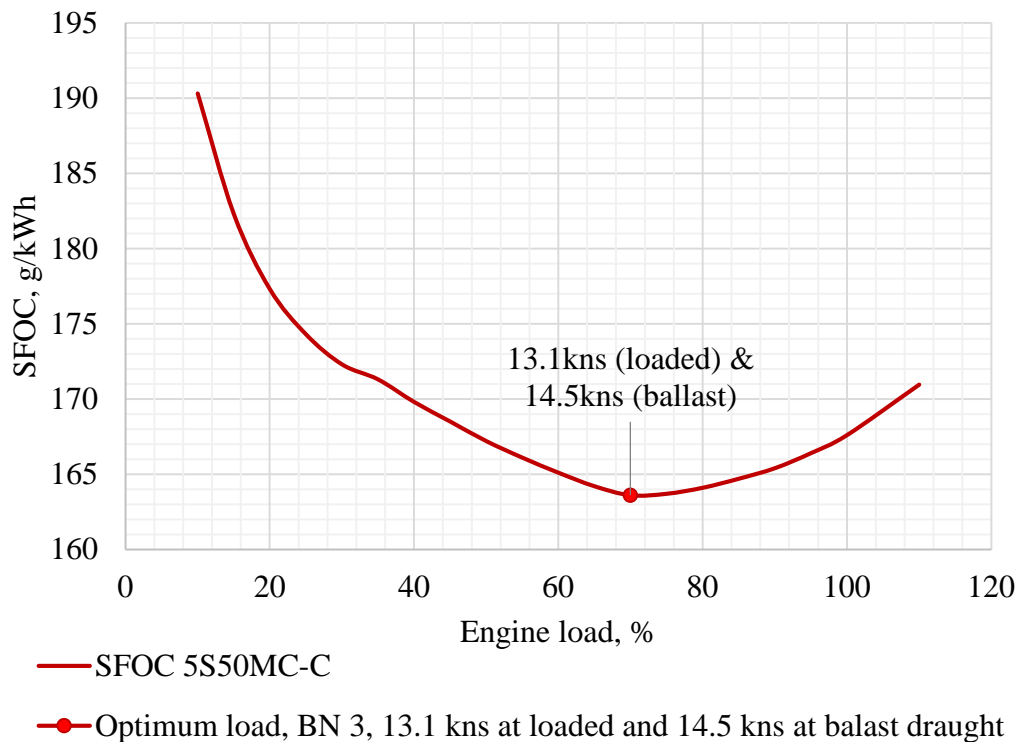


Figure 11.10 Speed, load and SFOC arrangements for the OPTIMUM operation.

Since the ship speed for both draughts has been reduced quite significantly, the duration of the voyage has been re-estimated. In the case of the loaded condition, the voyage has been increased by 1 day, 2 hours and 24 minutes while the ballast part of the voyage has a delay by 14 hours and 52 minutes. Therefore, by approximation both ways were increased by 1 day, making the total voyage of 33 days including 17 days of the loaded trip and 16 days of ballast. The resulting OPTIMUM voyage simulation is illustrated in Figure 11.11 while the battery charging/ discharging demand is shown in Figure 11.12.

It has been estimated that the total battery discharge for loaded and ballast conditions accounts for 37MW and 44MW respectively while the battery charge is expected to be 25MW (loaded) and 8MW (ballast) resulting in the longest discharge period worth of 40MW of battery power in case of ballast condition. Therefore, it can be estimated that

approximate battery capacity of 40MW is required to performed this voyage. The results of OPTIMUM voyage are listed in Table 11.2.

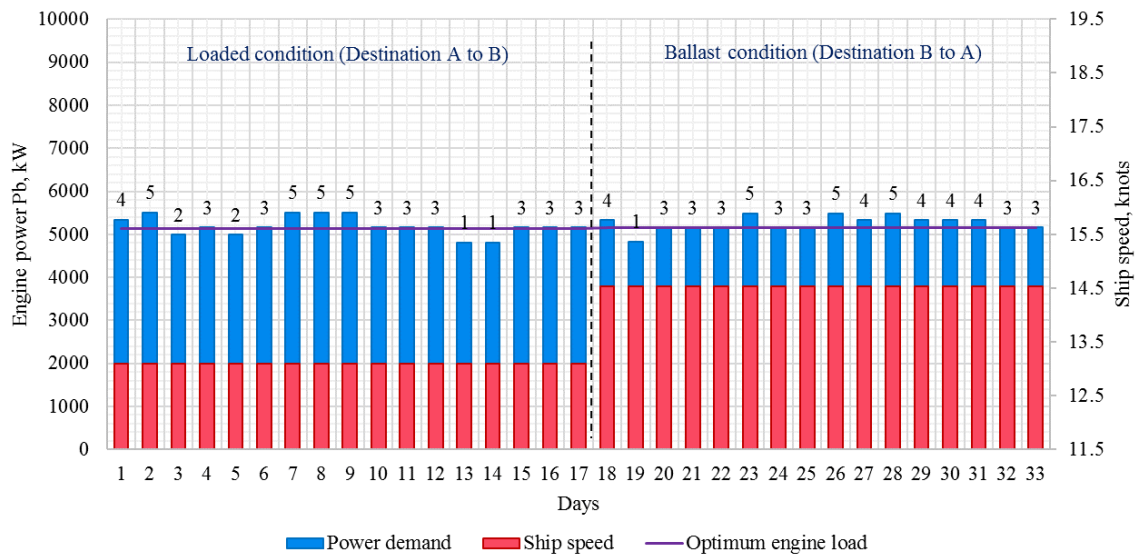


Figure 11.11 OPTIMUM voyage simulation.

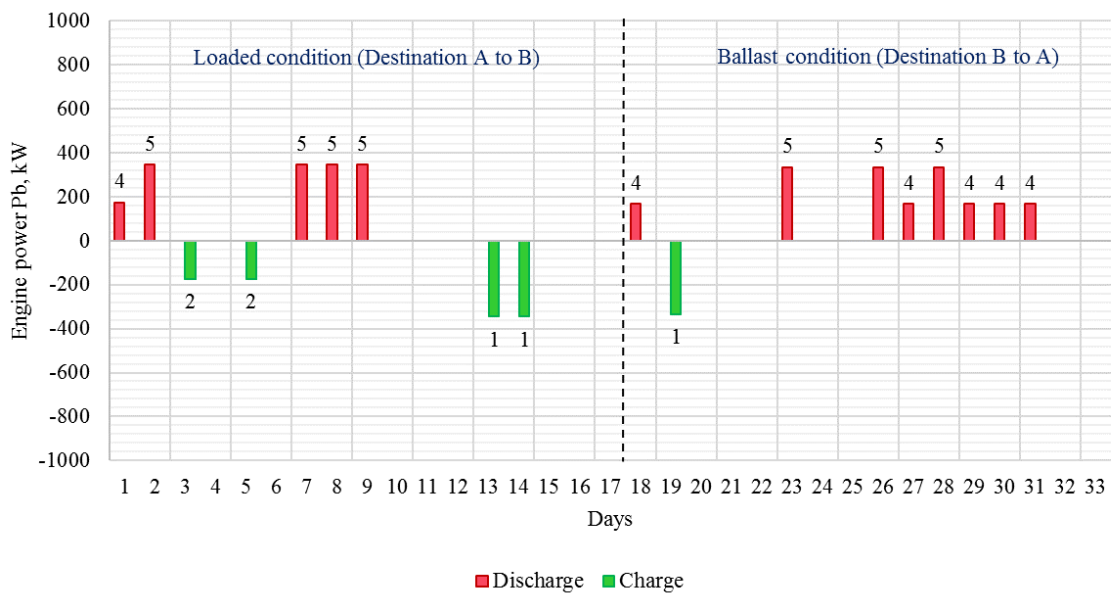


Figure 11.12 OPTIMUM battery charging/discharging diagram.

Therefore, in order to optimise the demand of extra power from the energy storage system, similarly to the previous case, the ship speed at Beaufort number 4 and 5 has been reduced by 0.1 knots for both draughts resulting in the operation at 13 knots (loaded) and 14.4 knots (ballast) when the sea state behaviour exceeds *BN* 3. Such an operational profile, also referred as OPTIMUM\_SPEED, is demonstrated in Figure 11.13 while the updated battery charging/discharging profile is shown in Figure 11.14. In fact, the ballast power demand at

BN 4 has been converted from the positive to negative allowing to store the resulted extra power by the energy storage system.

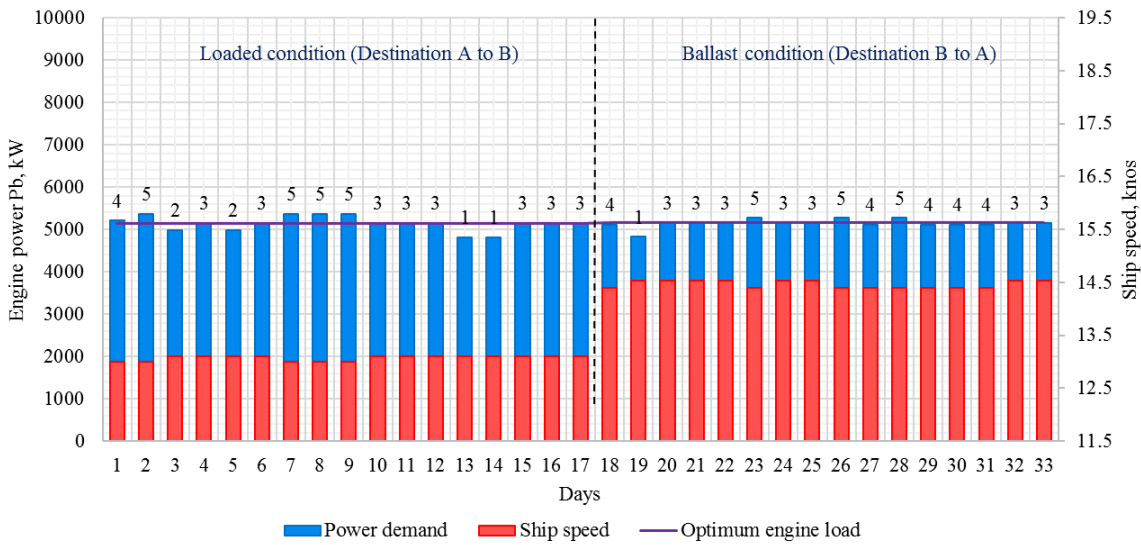


Figure 11.13 OPTIMUM\_SPEED voyage simulation.

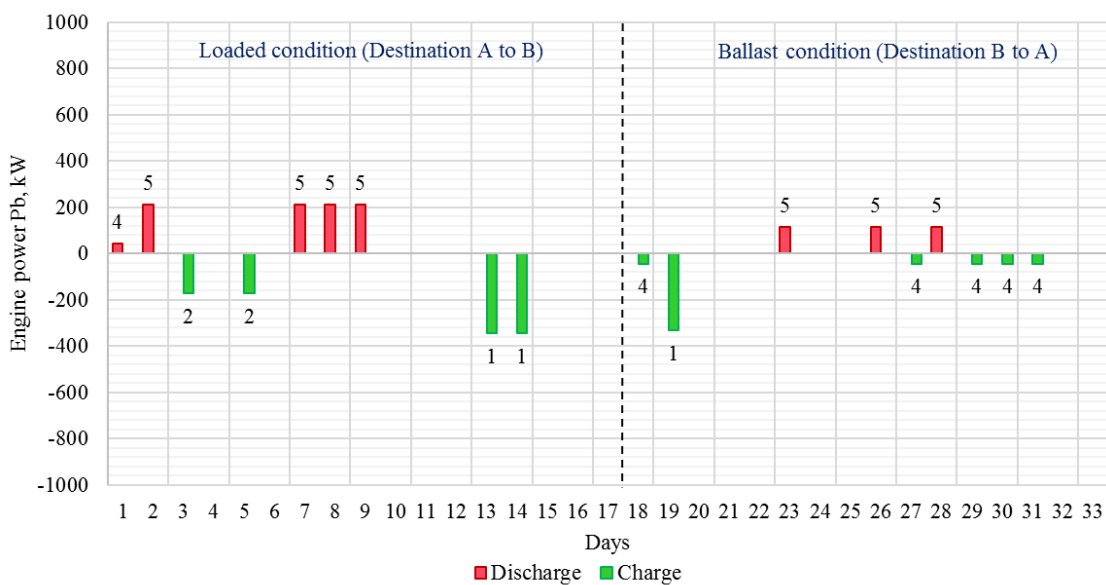


Figure 11.14 OPTIMUM\_SPEED battery charging/discharging diagram.

As a result, the total battery discharge for loaded and ballast conditions has been reduced to 22MW and 8MW while the excessively produced power is also kept the same making the longest discharge period worth of 15MW of battery power in case of the loaded condition. Therefore, it can be estimated that approximate battery capacity of 15MW is required to performed this voyage. The results of the OPTIMUM\_SPEED voyage are listed in Table 11.2.

In addition, the ship speed optimisation due to poor weather resulted in the following delays: 3 hours 07 minutes for loaded and 2 hours 38 minutes for ballast conditions and, since delays are relatively insignificant in comparison to days, they have been neglected.

Table 11.2 OPTIMUM and OPTIMUM\_SPEED voyage results.

Parameter	<i>OPT</i>		<i>OPT_SPEED</i>		Metrics
	Loaded	Ballast	Loaded	Ballast	
Speed	13.1	14.5	13.1	14.5	knots
Power	5160	5160	5160	5160	kW
FOC	844	844	844	844	kg/h
	20261	20261	20261	20261	kg/day
$CO_2$	2696	2696	2696	2696	kg/h
$NO_x$	75.5	75.5	75.5	75.5	kg/h
$SO_2$	4.00	4.00	4.00	4.00	kg/h
$CO$	2.25	2.25	2.25	2.25	kg/h
$HC$	1.77	1.77	1.77	1.77	kg/h
Load	70.0	70.0	70.0	70.0	%
SFOC	163.6	163.6	163.6	163.6	g/kWh
Reduced speed	-	-	13.0	14.4	Knots
Battery performance					
Total discharge	37	44	22	8	MW
Total charge	-25	-8	-25	-13	MW
Longest discharge	25	40	15	6	MW
Battery capacity	40		15		MW
Voyage extension					
Day	1	-	-	-	
Hours	2	14	2	3	
Minutes	24	52	38	39	
Total	1	1	-	-	Days

It should be remembered that the application of the load leveling approach for this type of ship is innovative and considered to be conceptual since there is no suitable commercially-ready energy storing system as well as safety and environmental regulations, including EEDI index, available today for this type of ship and the duration of the voyage. However, for mid-sized tankers of around 35000 DWT the introduction of hybrid system may be possible in the near future, since the power deficit when charging /discharging is relatively

smaller compared to larger vessels and therefore, making it easier to develop a suitable hybrid system by incorporating latest developments in batteries, renewable energy and fuel cells technologies. The fuel consumption and emissions results estimated per voyage are listed in Table 11.3.

Table 11.3 Fuel consumption and emissions footprint performance per voyage.

	<i>ORIGINAL</i>	<i>ON_TIME</i>	<i>OPTIMUM</i>	Metric
FOC	785	773	648	tonnes per voyage
$CO_2$	2506	2470	2071	tonnes per voyage
$NO_x$	64.1	63.6	58.1	tonnes per voyage
$SO_2$	3.7	3.7	3.1	tonnes per voyage
$CO$	2.2	2.2	1.7	tonnes per voyage
$HC$	1.5	1.5	1.4	tonnes per voyage

The calculations have shown that the hybridised voyage simulation based on constant ship speed, *ON\_TIME*, is resulting in reductions in fuel consumption by 12 tonnes per voyage (1.55 percent) and  $CO_2$  by 36 tonnes per voyage, while the reductions of other emissions are insignificant. However, the reductions of fuel due to the operation at the constant optimum load while taking into account the extended voyage duration account for 137 tonnes per voyage (17.45 percent),  $CO_2$  by 435 tonnes per voyage (17.35 percent),  $NO_x$  by 10 percent,  $SO_2$  by 16.2 percent as well as 22.7 percent of  $CO$  and 7 percent of  $HC$ .

In conclusion, the continuous operation at the most optimum load by means of the load leveling concept is found to be very efficient allowing to significantly reduce the consumption of fuel and, which is highly important, the level of atmospheric emissions. However, such operational approach in application to bigger vessels travelling longer distances requires powerful, safe and clean energy storage and generation technologies that are not yet commercially available. Nevertheless, there is currently extensive research and development into alternative and innovative chemistries, including lithium-oxygen and aluminium-graphite technologies making it theoretically possible to develop much more power dense cells in the near future.

## 12 EEDI Amendments Proposal

The case studies were dedicated towards the exploration of methods and technologies to improve the energy efficiency of the medium size oil products tanker while reducing the level of  $CO_2$  and other atmospheric emissions to comply with the Energy Efficiency Design Index (EEDI). However, this chapter focuses on the assessment of the EEDI methodology in terms of its actual impact on the reduction of global  $CO_2$  emissions from shipping as well as providing a proposal on how it may be improved. The EEDI methodology analysis is centred on interactions of the realistic ship service behaviour, based on the example of the reference oil products tanker, and its reflection by the mandatory attained EEDI and voluntary EEDI weather values.

First, it is essential to briefly recall the basic philosophy of the EEDI certification and its effect on the maritime industry at large. Generally, the EEDI index is the main mandatory instrument in determining which new build designs are efficient and should receive an approval for exploitation. The EEDI index represents a ship performance under calm weather conditions, defined as  $gCO_2/tnm$ , and, in a simple form, can be described as follows:

$$EEDI = \frac{CO_2 \text{ emission}}{\text{Transport work}} \quad 12.1$$

The EEDI reference lines are getting more stringent every 5 years aiming to reduce ship produced  $CO_2$  emissions by 30 percent by 2025. Both, the attained EEDI and the EEDI reference line methodologies, are described in details in the Introduction and Appendix I.

Although the mandatory EEDI certification went into force in 2013, it has been occasionally criticised by the industry experts. Namely, as discussed in Chapter 3, the EEDI reference lines were defined based on the reference SFOC associated with the older engine models performing at higher levels of the fuel consumption in comparison with the modern engines. As such, in the most cases, these reference lines are now inconsistent with the modern marine diesel engines capabilities. This results in reductions of the targeted energy efficiency ship design improvements as the majority of vessels, including the reference oil products tanker (Figure 12.1), would already comply with the EEDI requirements in the years to come.

In addition, the question regarding the influence of the weather conditions on the EEDI has been addressed since the EEDI represents a measure that reflects the actual amount of  $CO_2$

emitted per *tonnes nm*, which might differ from when in service due to influence of wind and waves. Hence, the weather correction factors,  $f_w$  has been additionally introduced for indicating the decrease in speed in representative sea conditions of wave height, wave frequency and wind speed associated with Beaufort number 6 (strong breeze). This weather correction factor can be determined by conducting the ship specific simulation on its performance at representative sea conditions. Otherwise, if the simulation is not available,  $f_w$  can be estimated using “standard  $f_w$ ” curve, which is only provided for bulk carrier, tanker and container ship as specified in Appendix I. In case of including this coefficient into the EEDI calculation, which is an optional action and will not affect the EEDI certification process, the index should be specified as  $EEDI_{Weather}$ .

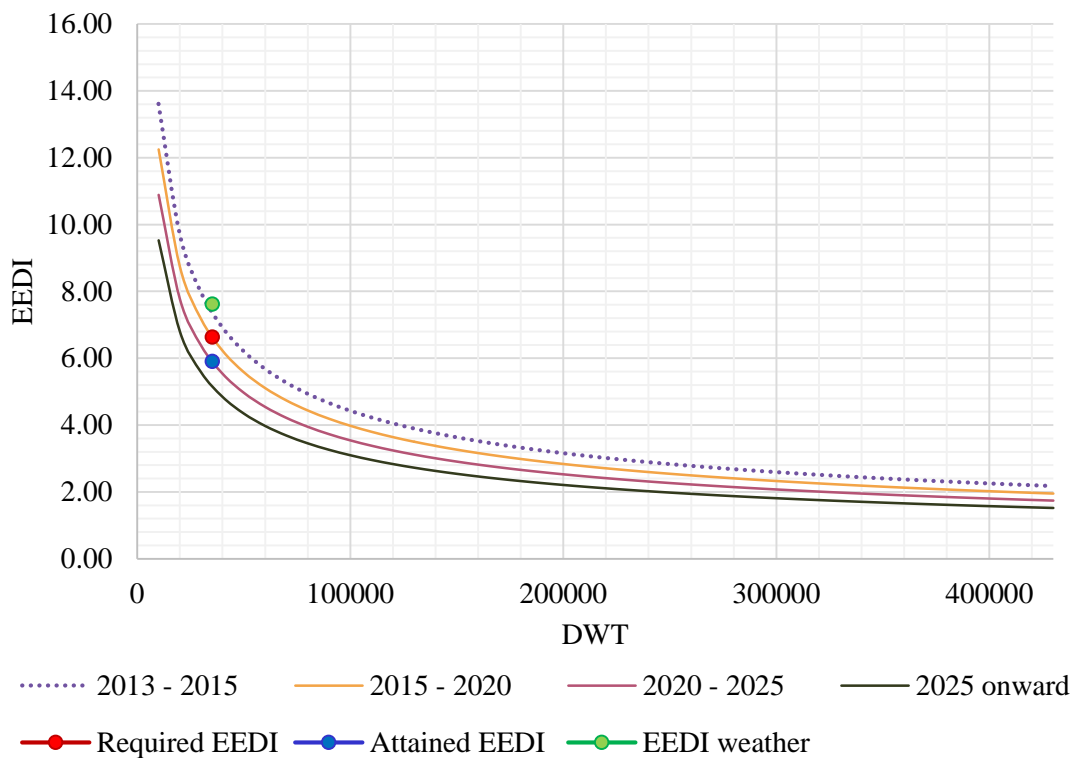


Figure 12.1 Attained EEDI, required EEDI due to 2015 and the EEDI weather of the reference oil products tanker.

As such, it has been decided to analyse the effect of the sea state conditions and other service parameters on the EEDI index. This will help to conclude on whether the EEDI measure is capable of influencing the global GHG reduction targets while acting as a global driver of demand for more energy efficient technologies.

The analysis is based on the realistic ship service data, which has previously been examined and filtered as explained in Chapter 6. The filtered data set includes 125 points measured daily. The captured engine power measurements with corresponding ship speed (observed)

over time domain are shown in Figure 12.2. The EEDI index for each data point has been estimated in accordance with its formulation and the calculation procedure summarised in Appendix I.

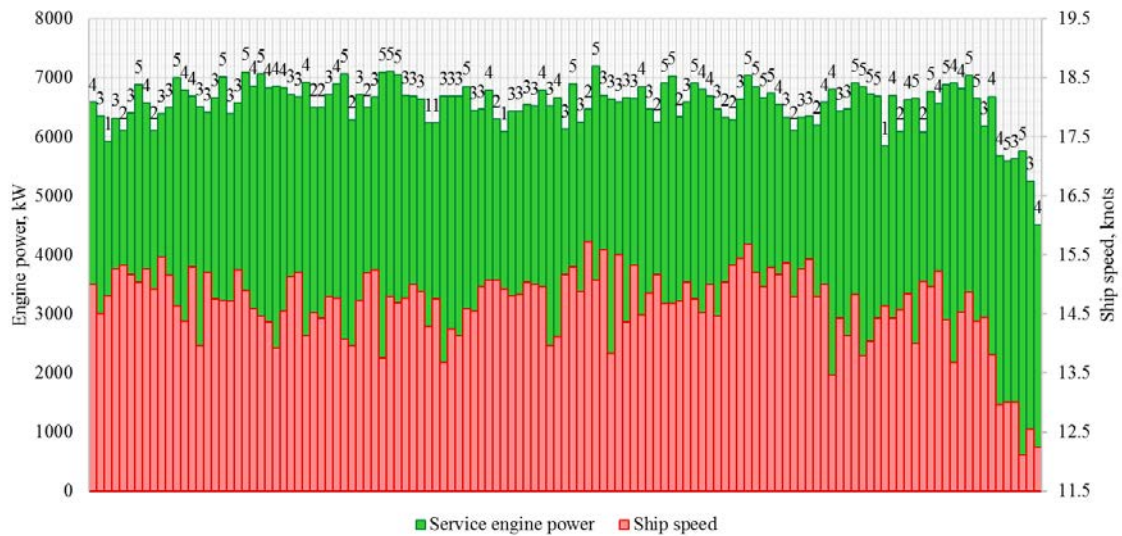


Figure 12.2 Measured ship service engine power and ship speed observed.

The auxiliary engines power  $P_{AE}$  and the fuel consumption  $SFC_{AE}$  as well as the type of fuel (MDO) for both, the auxiliary  $C_{FAE}$  and main engines  $C_{FME}$ , have been kept constant for each data point while the ship speed  $V_{ref}$ ,  $DWT$ , main engine power  $P_{ME}$  and the fuel consumption  $SFC_{ME}$  are fluctuating in accordance with the provided measurements.

Since according to the EEDI calculation guidelines, the main engine power  $P_{ME}$  is 75 percent of the SMCR of the engine measured in kW, the following assumptions have been adopted:

- the provided main engine service power data has been sorted by the Beaufort number and the numerical approach “N.S.M.B Trial Allowances 1976” (de Jong & Fransen 1976) was applied in order to remove the effect of weather on the propulsion power;
- the regression formulas (6.1 – 6.4), listed in Chapter 6, were used for the calculation, although in the inverse order, since the effect of weather has to be removed from the service data but not applied as in the case of the voyage simulation;
- the individual displacement value at each data point has been used for the calculation of the weather coefficients  $C_{p_{BN_i}}$  while for the estimation of the reference correction coefficient  $C_{P_{ref}}$  for the Beaufort number 0, the summer load displacement has been taken into account.

Therefore, the correction factor  $C_{p_{corr_i}}$  to eliminate the effect of weather from the service engine power data has been estimated (12.2) and then applied to each data point (12.3).

$$C_{p_{corr_i}} = \frac{(1 + C_{p_{ref}}/100)}{(1 + C_{p_{BN_i}}/100)} \quad 12.2$$

$$P_{B_i} = C_{p_{corr_i}} P_{B_{BN_i}} \quad 12.3$$

where  $i$  is the data point of the service data set.

The next step is to estimate the implied engine load at each data point without the effect of weather by deducting the resulting power from the original SMCR of 7150 kW and then applying the residual load to the original engine service measurements to obtain the list of service SMCRs where the deviation from the original SMCR of 7150 kW would indicate the effect of weather and the operational deadweight on the engine performance. The initial engine service power together with the resulting service SMCRs are illustrated in Figure 12.3 as green and blue columns respectively.

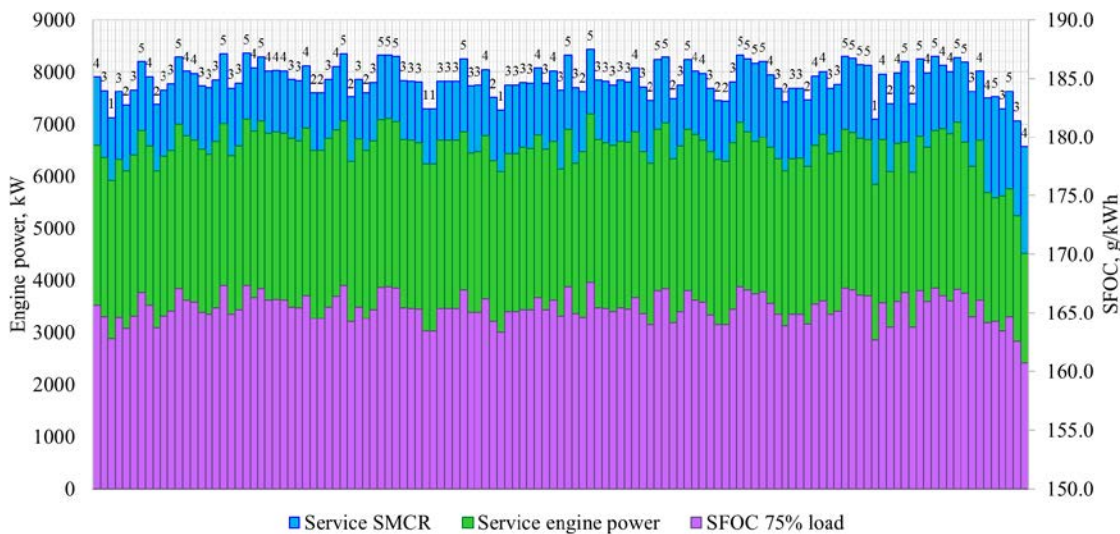


Figure 12.3 Service data used for the EEDI calculation: service SMCR, original engine power measurements and SFOC at 75 percent load corresponding to service SMCR.

The SFOC at 75 percent load for each data point is estimated by the regressions analysis based on the SFOC at 75 percent load obtained for the average service SMCR for each Beaufort number by means of the CEAS engine simulator. The range of DWT tonnage is calculated by deducting the lightweight from the service displacement, while instead of the reference ship speed, the ship service speed observed is used for the estimation of the EEDI indices. The range of DWT and ship speed observed are demonstrated in Figure 12.4 while the resulted EEDI values, sorted by Beaufort number, are shown in Figure 12.5.

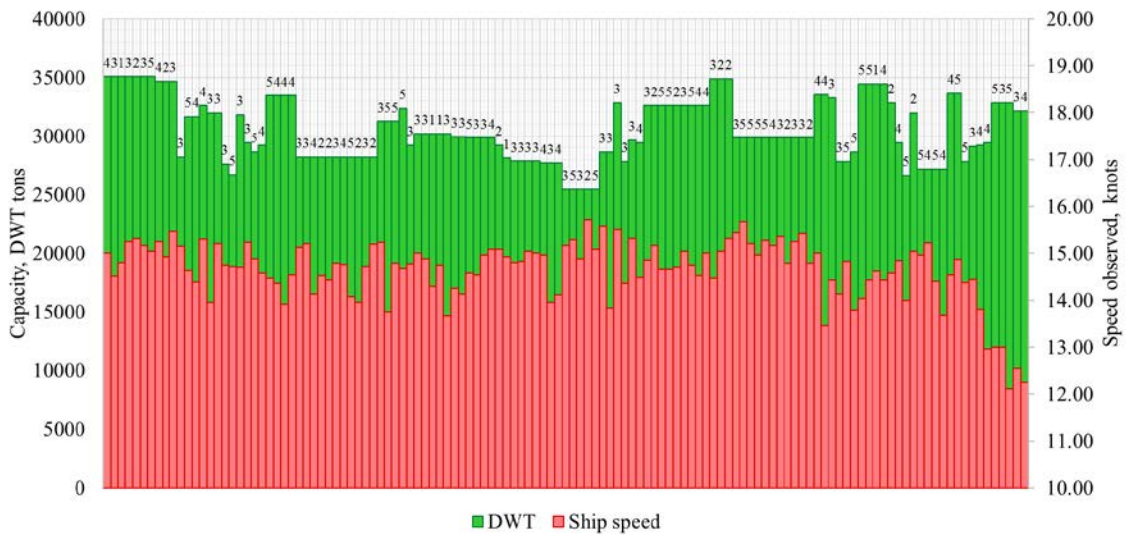


Figure 12.4 Service data used for the EEDI calculation: ship DWT and speed observed.

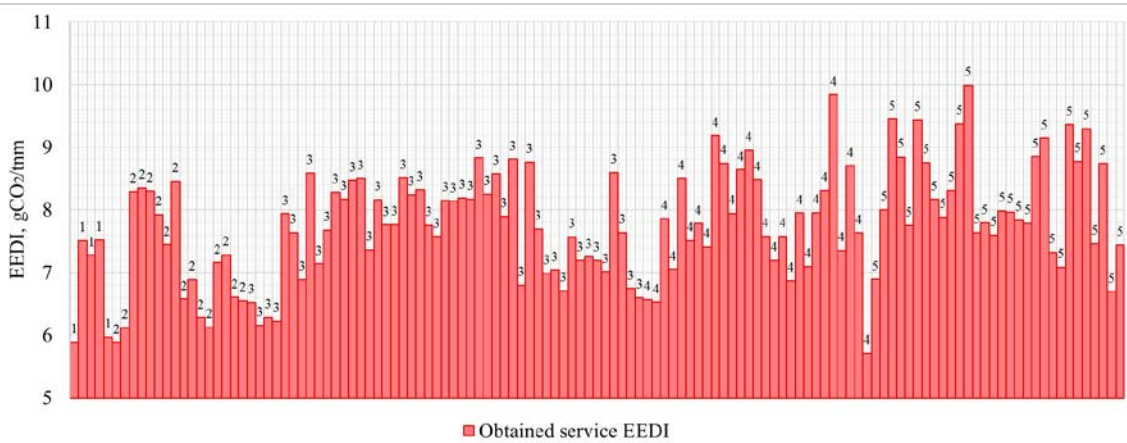


Figure 12.5 Resulting service EEDI distribution sorted by Beaufort number.

The resulting service EEDI values have been grouped by the Beaufort number in order to obtain the average index for each Beaufort number in the range of *BN 1 – BN 5* as shown in Figure 12.6 in comparison with the original attained EEDI, current reference EEDI and the EEDI weather.

The resulting average service EEDI values are considerably greater than the originally attained EEDI and required EEDI index (due in 2015) while definitely laying outside the trend associated with the EEDI weather *BN 6*. Therefore, the most sensible EEDI parameters including DWT, the engine power and the ship speed, used in the calculation process, have been carefully investigated. In addition, since the SFOC values have the same pattern as the SMCR power, they have been excluded from the consideration.

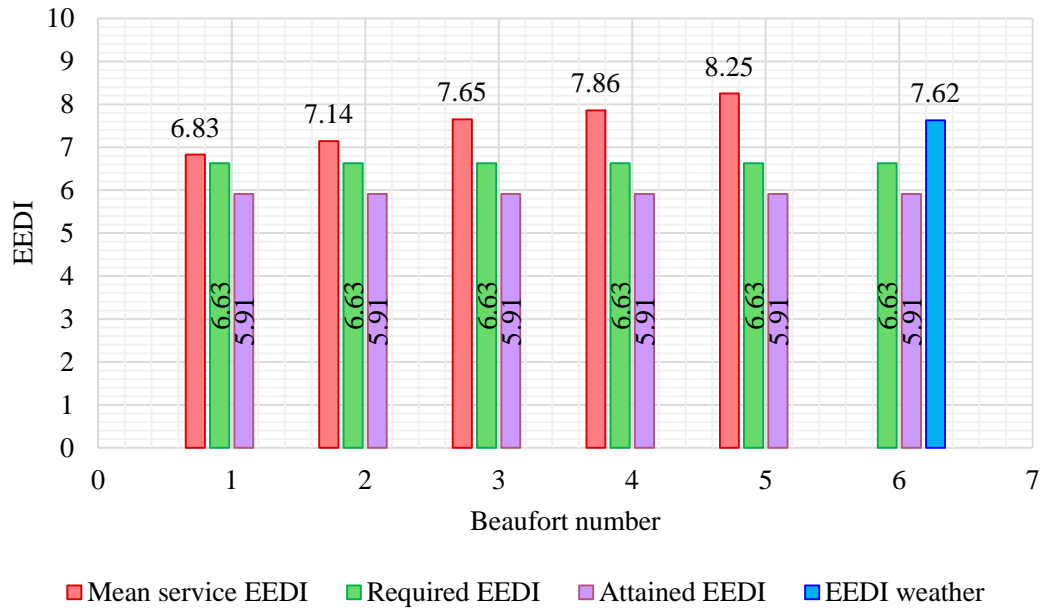


Figure 12.6 Mean service EEDI indexes grouped by Beaufort number in comparison with the original attained EEDI, reference EEDI and the EEDI weather.

First, it becomes evident that the mean service EEDI indices are increasing with the increasing Beaufort number, meaning that the deteriorating weather conditions have a direct effect on the EEDI values. In turn, the weather conditions reflect the ship speed and the engine power performance. The linear regression trend lines, determined by the frequency of the relative power and speed entries for each Beaufort number (Figure 12.7), show that the engine power has an overall increasing and the ship speed has an overall decreasing trend with the Beaufort number increasing.

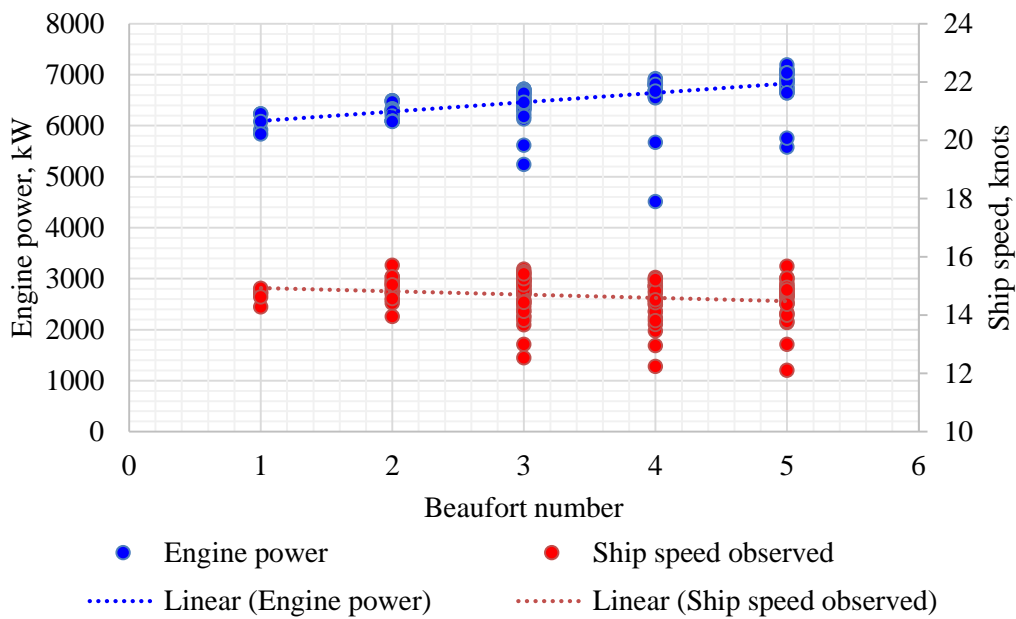


Figure 12.7 The effect of weather on service engine power and ship speed behaviour.

Secondly, it is important to understand why the resulting EEDI values appeared to be considerably higher than the initially obtained EEDI weather *BN* 6. The cause of this phenomenon could originate from the denominator of the EEDI formula, which represents the “benefit to society” while expressed as the DWT times the ship speed. In this case, as presented in Figure 12.8, the ship speed is less likely to be the reason as it fluctuates primarily near its reference value of 14.6 knots, while the mean service DWT tonnage in all cases is considerably smaller than the recommended maximum summer load capacity for the calculation of the attained EEDI as well as the EEDI weather indices. In fact, according to the provided service data measurements, the actual ship displacements at service have never reached its maximum load meaning that less benefit to society has been provided than expected. The load deficiency is fluctuating between 10 – 15 percent being the main reason of significant increase in service EEDI values. However, this phenomenon could also be a consequence of the data quality deficiency and, hence, more data records of this or other similar products tankers have to be analysed on this matter.

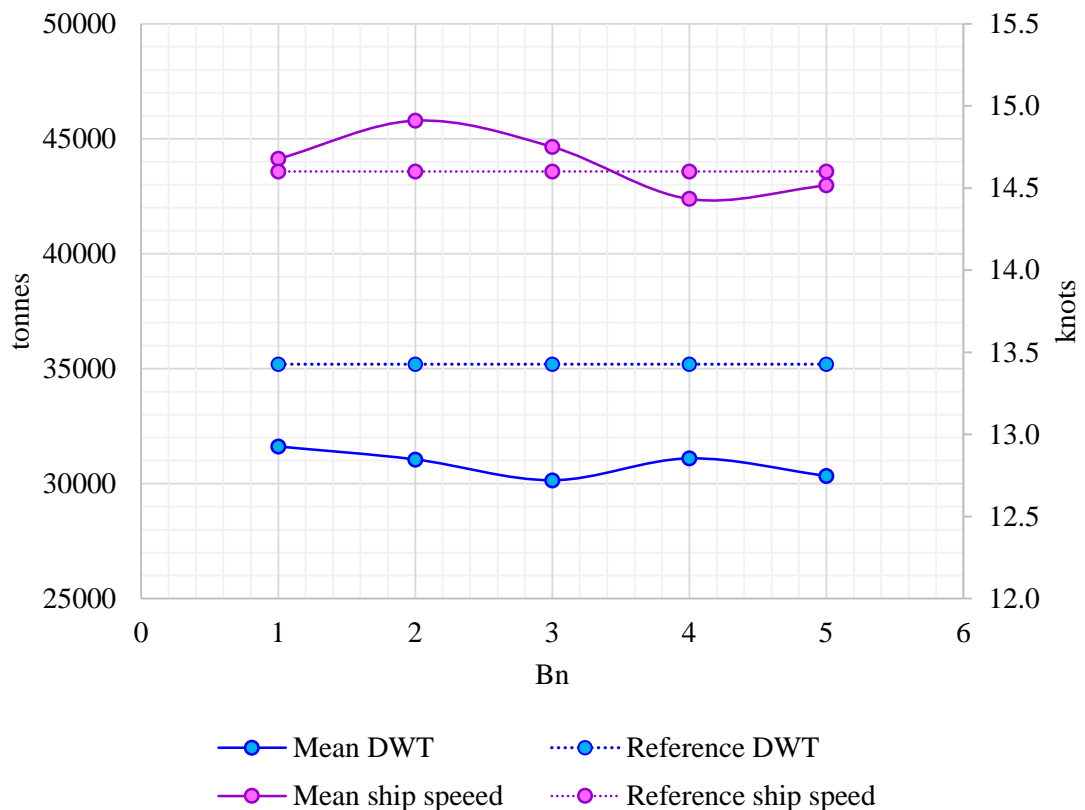


Figure 12.8 Mean service DWT, mean service speeds and their linear trend lines.

The correlation between the Beaufort scale, ship displacement and the EEDI measure is illustrated in Figure 12.9 by means of 3D map clearly indicating that both, the weather

factor and the Beaufort number, have a strong influence on the EEDI index and this should not be underestimated.

Therefore, in order to estimate the actual effect of weather on the EEDI index alone, the service DWT values have been replaced with the originally required maximum summer load DWT capacity of 35,100 tonnes. The similar procedure on determining the service SMCR values was performed although the provided engine service power has been initially corrected to the maximum displacement in accordance with the equation 12.4, as discussed in Chapter 5. The resulting mean EEDI values based on constant DWT are illustrated in Figure 12.10 while the resulting EEDI distribution sorted by Beaufort number in comparison with the original service EEDI are shown in Figure 12.11.

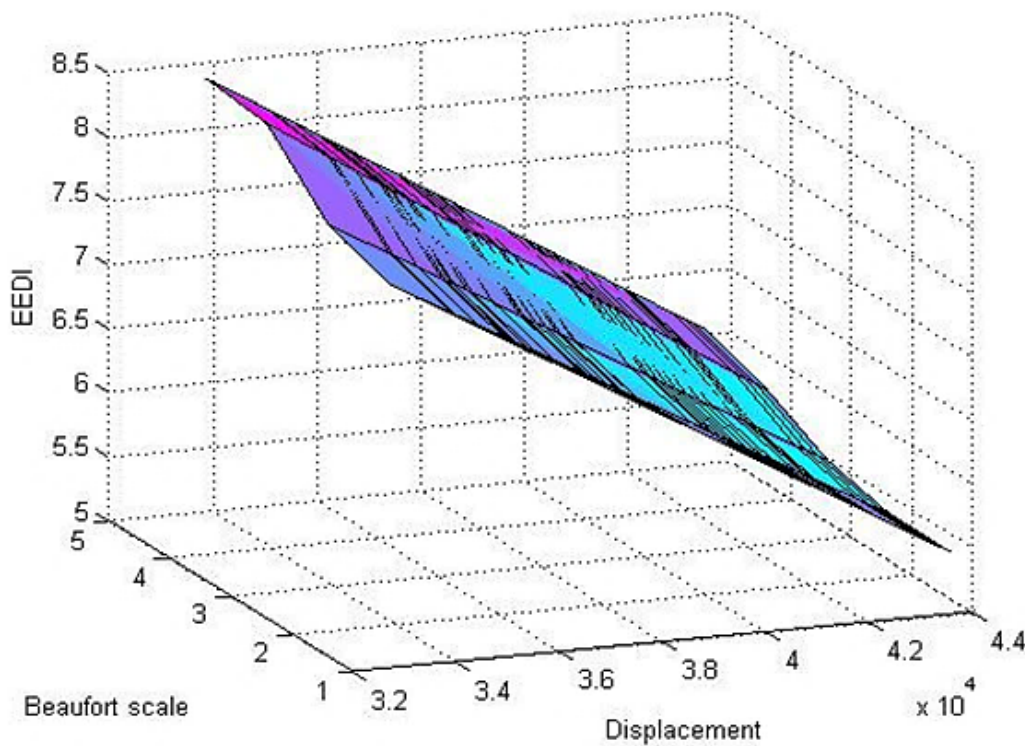


Figure 12.9 3D map correlation between the Beaufort scale, ship displacement and the EEDI measure.

$$P_2 = \left(\frac{\Delta_2}{\Delta_1}\right)^{2/3} P_1 \quad 12.4$$

As such, Figure 12.10 indicates that the increase of the EEDI index due to Beaufort number lies within one trend with the EEDI weather index based on the Beaufort number 6 and calculated in accordance with the IMO guidelines using the same maximum DWT tonnage, while designating that the “N.S.M.B Trial Allowances 1976” (de Jong & Fransen 1976) is an accurate regression method which could be also used for the calculation of the EEDI weather for other Beaufort numbers if needed. However, the obtained service EEDI values

are still greater than the originally attained EEDI index and, starting from the BN 3, than the required EEDI index.

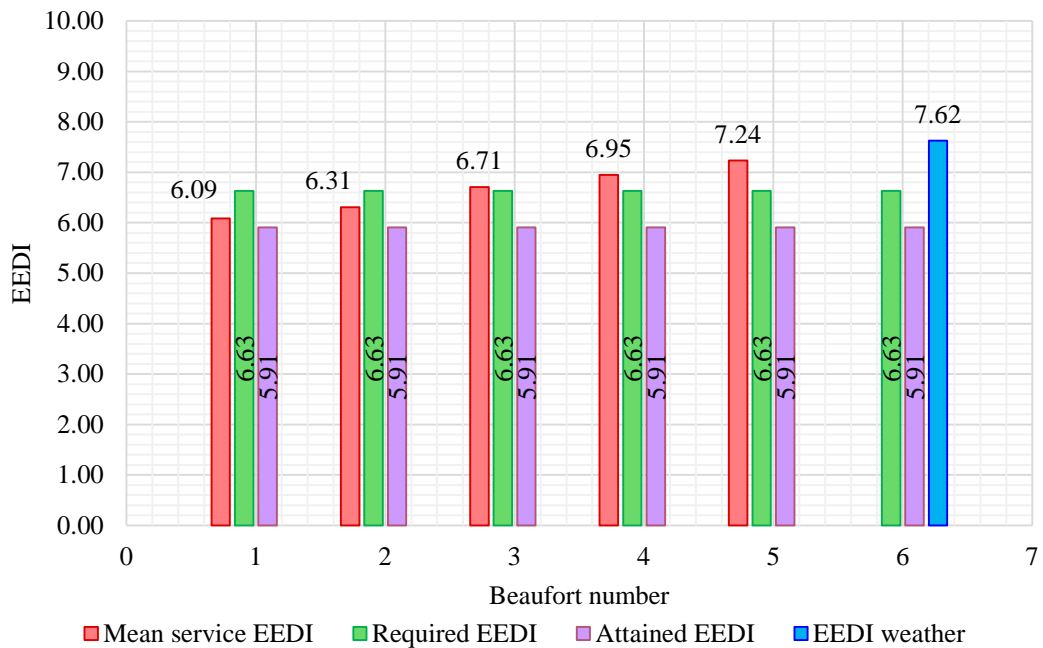


Figure 12.10 Mean service EEDI indexes based on constant DWT grouped by Beaufort number in comparison with the original attained EEDI, reference EEDI and the EEDI weather.

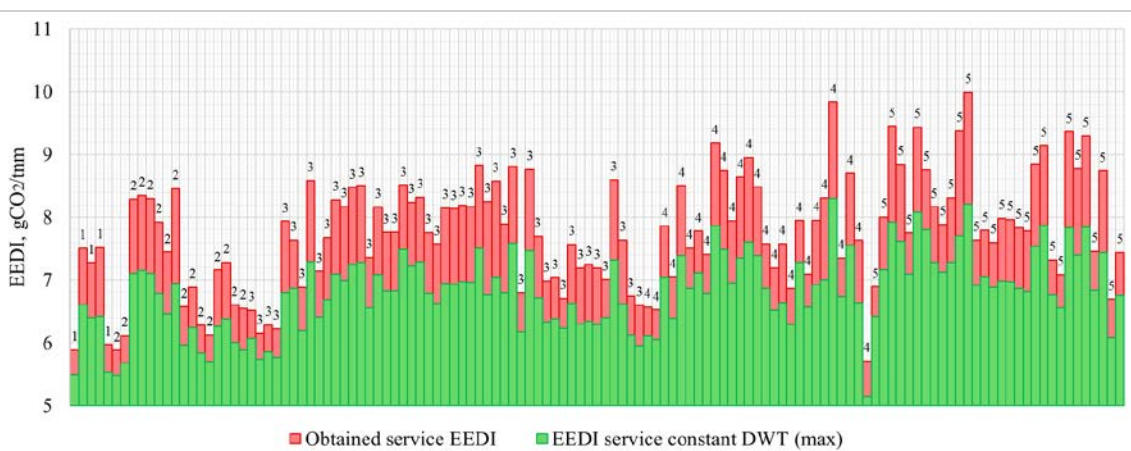


Figure 12.11 Resulting constant DWT EEDI distribution sorted by Beaufort number in comparison with the originally obtained service DWT.

These findings have significant implications on the correctness of the attained EEDI index, namely the ship will never behave at sea in the same manner as it assumed at calm weather conditions which often form the base for a number of assumptions regarding the ship performance including the amount of  $CO_2$  emissions.

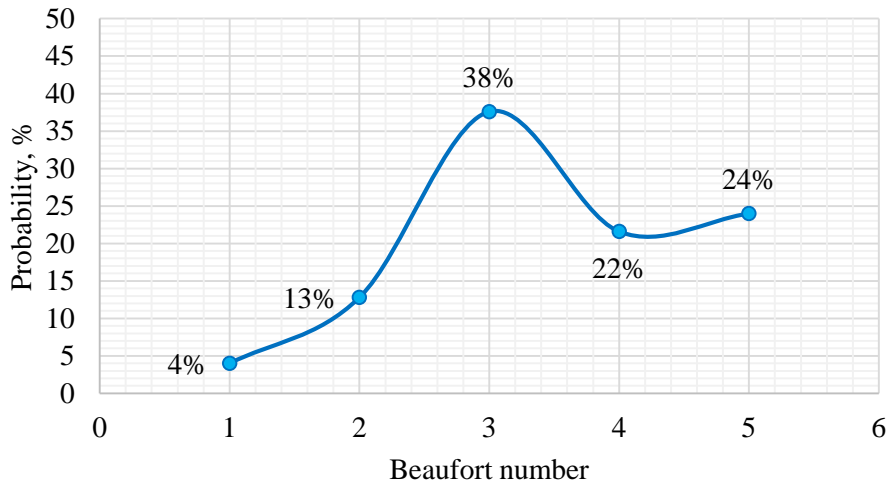


Figure 12.12 Sea state probability analysis results.

According to the probability analysis, the most common sea state with the probability of 38 percent is related to the Beaufort number 3 described as gentle breeze as illustrated in Figure 12.12 above. Therefore, in reality, the ship is more likely to emit  $7.65 \text{ gCO}_2/\text{tnm}$  rather than  $5.91 \text{ gCO}_2/\text{tnm}$ , as predicted by the attained EEDI calculation. This raises a question regarding the sustainability of the attained EEDI index based on the calm weather conditions as well as optional EEDI weather designed to represent ship performance at *BN* 6. Therefore, the EEDI methodology investigation leads to a proposal of the following amendments to the formula:

1. *EEDI\_DWT*. In the denominator of the EEDI formula, instead of maximum capacity, expressed as DWT for tankers, use the DWT reduced by 10 percent, which, according to the calculations, is the lowest level of DWT deficiency among the provided data. However, for a better confidence, more service data points of this and other ships/ship types should be investigated to exclude the possible concerns regarding the quality of the provided data or distinctive features in the operation of this particular vessel.
2. *EEDI\_BN3*. Instead of using the attained EEDI associated with the calm weather conditions and optional EEDI weather representing ship performance at *BN* 6, to employ the attained EEDI, based on the potential vessel behaviour at *BN* 3, for new builds certification process. The index can be calculated by multiplying the main engine power (75% SMCR) by the *BN* 3 correction factor estimated using for example “N.S.M.B Trial Allowances 1976” regression formulas, similar to this research, or, should sufficient data provided, updated regression methods for individual ship types could be developed.

3. EEDI\_DWT\_BN3. The most realistic EEDI solution would be the combination of both.

Table 12.1 Obtained EEDI values.

Attained EEDI	DWT	90% of DWT	Metric
		35190	30827
EEDI original	5.91		$gCO_2/tnm$
EEDI BN 3	6.58		$gCO_2/tnm$
EEDI DWT		6.74	$gCO_2/tnm$
EEDI DWT BN 3		7.50	$gCO_2/tnm$
Required EEDI			
Original required EEDI (2013)	7.37	7.86	$gCO_2/tnm$
Current required EEDI (2015)	6.63	7.07	$gCO_2/tnm$

The EEDI indexes for all proposed solutions, EEDI\_DWT, EEDI\_BN3 and EEDI\_DWT\_BN3 have been calculated and compared with the original value. The obtained values are listed in Table 12.1 as well as graphically represented in Figure 12.13. The impact on the global shipping  $CO_2$  reduction level has also been estimated for each time phase and summarised in Table 12.2

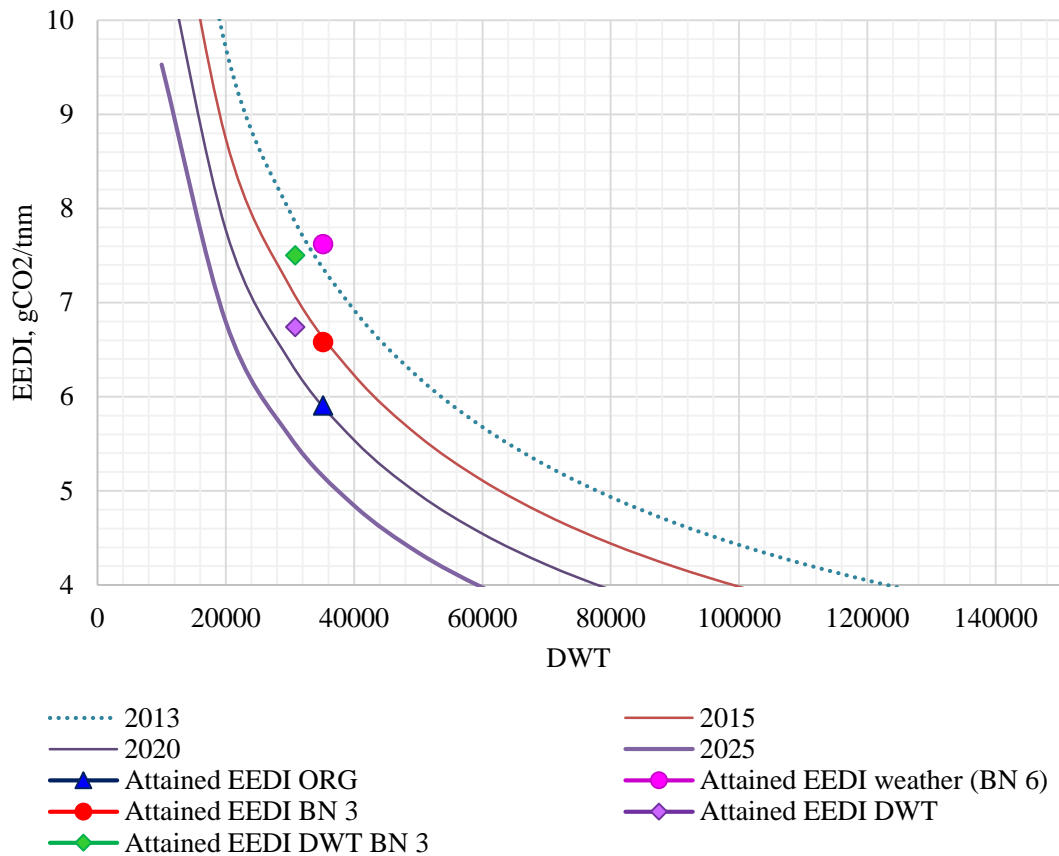


Figure 12.13 Original attained EEDI, EEDI weather and the amended EEDI values.

Table 12.2 Impact of amended EEDI values on global  $CO_2$  reduction level.

Phases	Planned reduction relative to original baseline	Reduction due to Attained EEDI ORG	Reduction due to Attained EEDI BN 3	Reduction due to Attained EEDI DWT	Reduction due to Attained EEDI DWT BN 3
2013	0%	-19.81%	-10.67%	-14.23%	-4.5%
2015	10%	-9.81%	-0.67%	-4.23%	5.5%
2020	20%	0.19%	9.33%	5.77%	15.5%
2025	30%	10.19%	19.33%	15.77%	25.5%

It has been found that the attained EEDI index estimated by means of the conventional procedure, in case of the reference tanker design, will only lead to 10 percent of  $CO_2$  reduction by 2025 instead of targeted 30 percent, while the application of the attained EEDI\_DWT\_BN3, which reflects the realistic ship behaviour at sea, will contribute to some 26 percent of the  $CO_2$  reduction level from shipping, which complies with the original target.

## 13 Conclusion

The primary objective of this PhD project was *to develop an advanced understanding of necessary and realistic performance expectations from full form medium size ship system by means of numerical computer modelling, in order to minimise the harmful environmental signature by increasing its efficiency in compliance with the EEDI requirements while in search of how the EEDI methodology might be enhanced.*

To solve such extensive problem, in the first place, the energy efficient technology market has been analysed in a structured manner while selecting the most favourable fuel consumption reduction methods applicable to the examined ship type.

Next, an integrated computer Ship Performance Simulation model, involving linked engine, propeller and hull analysis programs, has been developed and calibrated with the model tests and sea trial data.

By means of the Ship Performance Simulation model, several case studies have been conducted where the ship system has been analysed under diverse conditions including CLT and ducted propulsion systems, energy efficiency-enhancing wake equalising duct (WED), maximised and optimised propeller designs and trim conditions as well as innovative hybridised machinery arrangements while taking into account changing weather and load conditions.

The evaluation of potential benefits associated with the deployment of innovative technologies, operation profiles and their combination was made by comparing designated Energy Efficiency Indicators (EEI), namely, the propulsive efficiency, fuel oil consumption, exhaust emissions footprint and EEDI, respectively associated with the technical, fuel savings, environmental and legal perspectives.

### *Energy efficient propellers*

The first case study was dedicated to the comparative analysis of four different types of propulsion systems aiming to explore their effect on the overall ship efficiency performance by means of holistic ship performance simulation as well as to find the best propeller match for the medium size tanker/bulk carrier ship types.

- The comparative analysis of fixed pitch propeller with the wake equalizing duct vs. the conventional fixed pitch propeller has shown an interesting trend of the wake equalizing duct being the most beneficial at higher ship speeds. In addition, according to the simulation results, the wake equalizing duct has the most beneficial impact under the

loaded conditions rather than ballast while at the ship design speed the maximum increase of the propulsive efficiency due to the effect of the wake equalizing duct is found 4.5 percent at the fully loaded (scantling) condition.

- The average reductions of the delivered power by approximately 10 percent have been found due to the application of the CLT propeller with the wake equalizing duct over the fixed pitch propeller with the wake equalizing duct system. However, further fundamental research is needed to ensure that the scaling procedures for this type of propeller are realistic.
- The power absorption performance of the ducted propeller at different operational conditions are found to be beneficial in comparison with the conventional fixed pitch propeller while the ducted propeller performance at ballast condition was slightly better than at design and loaded conditions. As a result, the maximum power reductions due to ducted propeller account for approximately 5 percent.
- As a result of the comparative evaluation of the propellers performances between each other, the most beneficial propeller system is found to be a combination of the open CLT with the wake equalizing duct (subject to the reservation expressed above), followed by the open fixed pitch propeller with the wake equalizing duct and the ducted propeller, although the ducted propeller has shown 3.3 percent better performance at ballast condition than the conventional fixed pitch with the wake equalizing duct.
- From the fuel economy point of view, the lowest consumption is expected to be achieved by the CLT propeller performance. However, since a general rate of the specific fuel oil consumption of 5S46ME-B engine is slightly higher than that of 5S50ME-C engine, the SFOC of the CLT propeller at NCR is by 1.4 percent exceeding the conventional fixed pitch propeller, while the lowest SFOC rate of 164.3 g/kWh is achieved by the fixed pitch propulsion system with the wake equalizing duct.
- Regarding the exhaust emissions footprint, it is possible, again taking into account the above reservation, to reduce the  $CO_2$  emissions by 14.7 percent by adopting the CLT propeller and by about 5 percent by applying the wake equalizing duct or ducted propeller. It is also possible to reduce  $NO_x$  emissions by 17.3 percent with the CLT propeller and by approximately 4.8 percent with the ducted propeller or the wake equalizing duct.
- In terms of the EEDI index, the application of wake equalizing duct and ducted propellers for such ship types and design will satisfy the EEDI requirements up to 2020,

while the reference ship design arrangements with the application of the CLT propeller will almost meet the 2025 EEDI expectations.

- Since the ducted propeller is more beneficial at ballast condition, its voyage performance is found to be more advantageous vs. fixed pitch propeller with the wake equalizing duct achieving the possible savings of 4 tonnes of fuel per voyage, while the CLT propeller application resulted in savings of 93 tonnes of fuel per voyage compared to the conventional FPP.

### ***Propeller optimisation***

Two propeller optimisation techniques, a reduction of the blade area ratio and an artificial increase of the propeller diameter, have been analysed in this case study.

- In the case of reduction of the blade area ratio to its possible minimum (0.4), the power absorption is found to be 1.54 percent lower than in the case of the optimum blade area ratio, however, this would significantly increase a chance of development of the back cavitation on the propeller blades. Nevertheless, with growing R&D interests in developing of the anti-cavitation materials and coating, a chance to incorporate more hydrodynamically efficient propellers with reduced blade area ratio without the fear of cavitation will significantly increase.
- In turn, the artificially increased propeller diameter has also shown a positive influence onto the overall propulsive efficiency, although slightly lower than in case of the reduction of the blade area ratio, with achieved reductions in the delivered power requirements by 1.07 percent when increasing the original propeller diameter by 5 percent ( $D = 5.93\text{m}$ ).
- The increase of the propeller diameter (with decreasing blade area ratio) will not affect the cavitation performance since the excessive thrust loading would be evenly distributed along a larger surface of the propeller disc. However, even 5 percent increase of the optimum diameter will give a rise to the hull surface pressure pulses, resulting in a potential intensification of the inboard noise and vibration. In addition, the increase of the propeller diameter results in a decrease in the average wake fraction, resulting in the overall decrease in the hull efficiency.

The Energy Efficiency Indicators analysis has shown that the application of such propeller systems alone will not significantly affect the emissions footprint and the EEDI index, however, they will provide some fuel savings while might be a useful bonus when combined with other energy saving devices.

- The lowest fuel consumption, as expected, is achieved by the propeller with reduced blade area ratio, which is on 19 kg/h lower than the conventional fixed pitch propeller requirements.
- Regarding the exhaust emissions footprint, it is possible to reduce the  $CO_2$  emissions by 1.8 percent by adopting the propeller with reduced blade area ratio and by about 1 percent by artificially increasing the propeller diameter by 5 percent. However, almost no changes were found in case of  $NO_x$  emissions footprint in both cases.
- The scale of EEDI fluctuations due to the propeller optimisation for both cases is small and does not have any significant impact on the EEDI certification process.
- In addition, the possible savings of 6 tonnes of fuel per voyage could be achieved by increasing the propeller diameter by 5 percent, while the installation of the fixed pitch propeller with reduced blade area ratio would contribute to the fuel reduction of 11 tonnes per voyage.

#### ***Maximum propeller diameter***

Two low RPM/increased diameter propeller design concepts based on the conventional fixed pitch propellers, namely the system with the maximum diameter that could be fitted into the current ship arrangement and the system with the maximum possible diameter involving the shaft relocation, have been analysed.

- The average reduction due to maximising the propeller diameter while minimising its rotational speed accounts for 6 percent in the case of maximised propeller with the initial shaft arrangements and 7.3 percent for the maximised propeller with the lifted shaft.
- In the case of retrofitting, both systems will require a significant financial effort to provide new propeller, super slow diesel engine as well as to modify the transmission system to perform the shaft relocation.
- For new builds, maximising the propeller diameter is a good option to save up to 50 tonnes of fuel per voyage, being especially profitable should the fuel prices increase, reducing the  $CO_2$  emissions by almost 200 kg per hour and  $NO_x$  by 17 kg per hour while complying with the EEDI index requirements up to 2020. In addition, there is no need for shaft relocation should the propeller size be confirmed before the power plant selection, making the preliminary ship performance simulation an important part of the efficient ship design.

### *Trim optimisation*

The case study is performed with the reference to -1.75m and 1m trim conditions representing a partially loaded draught of 8 m at an even keel. These trims have been selected in accordance with the waterline fluctuations around the bulbous bow while the variations around the stern are kept constant.

- It has been found that the forward trim = - 1.75m is the most beneficial option with the maximum delivered power reductions by 9.2 percent in comparison to the even keel while the energy losses due to trim = 1m can reach up to 19.4 percent with increasing speed.
- The engine simulation results have shown that it is possible to reduce fuel oil consumption by more than 5 percent when operating at trim = -1.75m compare to the even keel, while if the trim was not properly optimised (trim = 1m), the fuel losses reach up to 15 percent in contrast with the even keel.
- Regarding the exhaust emissions footprint, it is possible to reduce the  $CO_2$  emissions by 5.3 percent and the  $NO_x$  emissions by 3.6 percent in the case of the optimised trim (trim = -1.75m), while the  $CO_2$  and  $NO_x$  emissions will increase by 15.3 and 9.3 percent respectively at the poorly optimised trim (trim = 1m).
- The fuel savings with the optimised trim (trim = -1.75m) account for 11 tonnes of fuel per voyage, while losses due to trim = 1m reach up to 41 tonnes of fuel per voyage.

Therefore, the results have shown that the impact of trim on ship efficiency is significant and, if not optimised properly, can lead to serious power losses, while minimising the benefits of energy saving devices and high-efficiency propellers as well as the initial purpose of the EEDI certification.

On the other end of the spectrum, the trim optimisation is difficult to control governmentally, since it has to be performed in each individual case depending on load, speed and the hull structure. However, the industry's interests in fuel savings and environmental concerns regarding the exhaust emissions control coupled with the growing trim optimisation CFD based software development could lead to some additional improvements addressed to the EEDI legislation, namely to include the trim optimisation software installation as a mandatory requirement to a ship owner in order to be issued with the EEDI certificate.

### ***Future hybrid propulsion concepts***

The case study is dedicated towards the evaluation of the potential benefits and savings due to hybridisation of the reference tanker through the introduction of the load leveling operational profiles for the previously considered 31 days' voyage.

- As a result, the continuous operation at the most optimum load by means of load leveling concept is found to be very efficient allowing to significantly reduce the consumption of fuel and more importantly the level of atmospheric emissions.
- The reductions of fuel due to the operation at the constant optimum load while taking into account the extended voyage duration amount for 137 tonnes per voyage (17.45 percent),  $CO_2$  by 435 tonnes per voyage (17.35 percent),  $NO_x$  by 10 percent,  $SO_2$  by 16.2 percent as well as 22.7 percent of  $CO$  and 7 percent of  $HC$ .

However, such operational approach in the application for bigger vessels travelling longer distances requires powerful, safe and clean energy storage and generation technologies that are not yet commercially available. On the positive note, there is currently extensive research and development into alternative and innovative chemistries, including lithium-oxygen and aluminium-graphite technologies making it theoretically possible to develop much more power dense cells in the near future.

### ***EEDI methodology assessment***

The EEDI methodology's ability to act as a global driver for cleaner shipping has been analysed in this study.

- It has been found that the current EEDI methodology does not fully reflect the realistic ship performance at sea while the attained EEDI estimated by means of the conventional procedure, in case of the reference tanker design, will only lead to 10 percent of  $CO_2$  reduction by 2025 instead of the targeted 30 percent.

Therefore, it has been proposed to enhance the EEDI methodology by applying the following corrections:

- In the denominator of the EEDI formula, instead of maximum capacity, expressed as DWT for tankers, use the DWT reduced by 10 percent, which, according to the calculations, is the lowest level of DWT deficiency among the provided data. However, for a better confidence, more service data points of this and other ships/ship types should be investigated to exclude the possible concerns regarding the quality of the provided data or distinctive features in the operation of this particular vessel.

- Instead of using the attained EEDI associated with the calm weather conditions and optional EEDI weather representing ship performance at *Bn 6*, to employ the attained EEDI, based on the potential vessel behaviour at *Bn 3*, for new builds certification process. The index can be calculated by multiplying the main engine power (75% SMCR) by the *Bn 3* correction factor estimated using for example “N.S.M.B Trial Allowances 1976” regression formulas, as in this research, or, should sufficient data provided, updated regression methods for individual ship types could be developed.

However, the most realistic EEDI solution would be a combination of both.

- As a result, the application of the consistent with reality attained EEDI with reduced DWT and associated with the *Bn 3* will contribute to some 26 percent of the  $CO_2$  reduction level from shipping, which almost perfectly complies with the original target.
- In addition, a stipulation to include the on-board trim optimisation software as a mandatory requirement to a ship owner in order to be issued with the EEDI certificate will help to ensure that the ship is operating with the same environmental signature as it is required by the legal authorities.

## 14 Recommendations

### *Recommendations for the medium size ship system*

The medium size ship system may benefit from:

- the installation of a CLT propeller in combination with the wake equalizing duct;
- the maximised propeller diameter with reduced rotational speed for new build application;
- careful trim optimisation by means of on-board computer simulations will help to maximise the hull design beneficial features and to save more fuel.

In long term perspective:

- the minimisation of propeller's blade area ratio (should the cavitation resistant propeller materials or coatings be introduced to the market);
- the continuous operation at the most optimum load by means of load leveling concept will bring significant reductions in emissions and fuel consumption as well as stabilised engine exploitation.

### *EEDI methodology recommendations*

- to employ the attained EEDI, based on the potential vessel behaviour at *BN 3* for new builds certification purposes.

Therefore, in the numerator of the EEDI formula:

- to add the *BN 3* correction factor estimated using for example N.S.M.B Trial Allowances regression formulas, or, should sufficient data be provided, updated regression methods for individual ship types could be developed.

In the denominator of the EEDI formula:

- instead of maximum capacity, expressed as DWT for tankers, to use the DWT reduced by 10 percent.

In addition:

- to include on-board trim optimisation software as a mandatory requirement for a successful EEDI certification.

## **15 Suggestions for Further Research**

- To develop a model to full scale method of scaling the CLT propellers;
- to better understand the margins against cavitation erosion for propellers;
- to perform a research into alternative chemistries to create lighter in weight but higher power-dense battery cells suitable for bigger ship's main propulsion system;
- to expand the Ship Performance Simulation model to include the assessment and prediction of ship performance under changing fuel prices and freight rates;
- to expand the Ship Performance Simulation model for other ship types;
- to create an alternative regression method using latest ship performance data for estimation of the EEDI weather correction factors suitable for a range of ship types and sizes to reflect a realistic ship performance under representative weather conditions.

## References

- ABS, 2013. Ship energy efficiency measures.
- AEA Energy and Environment, 2008. Greenhouse gas emissions from shipping: trends, projections and abatement potential.
- Aertssen, G., 1963. Service performance and seakeeping trials on MV Lukuga. *The Royal Institution of Naval Architects*, 105, pp.293–335.
- Anderson, J., 2015. *Development of hybrid propulsion for small ro-pax ferries and the feasibility of a zero emissions hydrogen fuel cell powered ferry*. City University London.
- Anderson, M., Salo, K. & Fridell, E., 2015. Particle and gaseous emissions from an LNG powered ship. *Environmental Science & Technology*, 49(20), pp.12568–12575.
- Anink, D. & Krikke, M., 2011. Analysis of the effects of the new EEDI requirements on Dutch build and flagged ships. , pp.1–46.
- Bagniewski, M., 2013. LNG fuel for ships. A chance or a must? *DNV GL*.
- Banisoleiman, K. et al., Simulation of diesel engine performance. *Trans IMarE*, 105(3), pp.117–135.
- Bertram, V., 2012. *Practical Ship Hydrodynamics*, Elsevier.
- Boer, E. & Hoen, M., 2015. Scrubbers – an economic and ecological assessment.
- BP, 2015. BP statistical review of world energy.
- Bregliozzi, G. et al., 2005. Cavitation wear behaviour of austenitic stainless steels with different grain sizes. *Wear*, 258(1–4), pp.503–510.
- Breslin, J.P. & Andersen, P., 1994. *Hydrodynamics of ship propellers*, Cambridge Ocean Technology Series.
- Burrill, L.C., 1943. Developments in propeller design and manufacture for merchant ships. *Trans. of the Institute of Marine Engineers*.
- Carlton, J., 2012. *Marine Propellers and Propulsion* 3rd ed., Elsevier.
- Carlton, J.S., Smart, R. & Jenkins, V., 2011. The nuclear propulsion of merchant ships: aspects of engineering, science and technology. *Proceedings of the Institute of Marine Engineering, Science and Technology Part A: Journal of Marine Engineering and Technology*, 10(2), pp.47–59.
- Çelik, F., 2007. A numerical study for effectiveness of a wake equalizing duct. *Ocean Engineering*, 34(16), pp.2138–2145.
- Chryssakis, C. et al., 2014. Alternative fuels for shipping. , pp.1–28.
- Corbett, J. et al., 2009. *Second IMO GHG study*.
- Corbett, J.J. et al., 2007. Mortality from ship emissions: a global assessment. *Environmental science & technology*, 41(24), pp.8512–8.
- Corbett, J.J. & Winebrake, J., 2008. *The impacts of globalisation on international maritime transport activity*, Guadalajara, Mexico.

- Crist, P., 2009. Greenhouse gas emissions reduction potential from international shipping.
- Dedes, E. et al., 2011. Possible power train concepts for nuclear powered merchant ships.
- DNV GL, 2015. In focus - the future is hybrid: a guide to use batteries in shipping.
- Eastop, T.D. & McConkey, A., 1993. *Applied thermodynamics for engineering technologists*, Wiley.
- Egnell, R., 1998. Combustion diagnostics by means of multizone heat release analysis and NO calculation.. *Sae*.
- Faber, J. et al., 2015. Estimated index values of new ships - analysis of EIVs of ships that have entered the fleet since 2009. , (March).
- Faber, J., 2015. Historical trends in ship design efficiency. , (March).
- Flagan, R.C. & Seinfeld, J.H., 1988. *Fundamentals of air pollution engineering*, Prentice-Hall, Inc., Englewood Cliffs, New Jersey.
- Florentinus, A., 2012. Potential of biofuels for shipping.
- Flynn, D., 2003. *Thermal power plant simulation and control*, Institution of Engineering and Technology.
- Freund, R.J. & Wilson, W.J., 2003. *Statistical methods B*. Holland, ed., Academic Press.
- Gazley, I., 2007. UK environmental accounts: air emissions and energy use. *Economic #38; Labour Market Review*, 1(11), pp.18–27.
- Germanischer Lloyd, 2013. Guidelines for determination of the Energy Efficiency Design Index.
- Ghose, P.J.P. & Gokarn, R.P., 2009. *Basic ship propulsion*, Allied Publishers.
- Grim, O., 1980. Propeller and vanewheel. *Second George Weinblum Memorial Lecture, J. Ship. Res*, December(24(4)).
- Grothues-Spork, K., 1988. Bilge vortex control devices and their benefits for propulsion. *International Shipbuilding Progress*, 35(402).
- Hansen, H., GmbH, F. & Germany, P., 2012. Assistance tools for operational fuel efficiency. *9th Conference on Computer and IT Applications*, pp.356–366.
- Harrould-Kolieb, E., 2008. Shipping impacts on climate: a source with solution. *Oceana*, (July).
- Harvald, S.A., 1983. Resistance and propulsion of ships.
- Heywood, J.B., 1985. Internal combustion engine.
- Hirdaris, S.E. et al., 2014. Considerations on the potential use of Nuclear Small Modular Reactor (SMR) technology for merchant marine propulsion. *Ocean Engineering*, 79, pp.101–130.
- Hollenbach, K.U., 1998. Estimating resistance and propulsion for single-screw and twin-screw ships. *Ship Technology Research*, 45(2), pp.72–76.
- Holsonback, C. et al., 2006. System-level modelling and optimal design of an all- electric ship energy storage module.

- Holtrop, J., 1984. A statistical re-analysis of resistance and propulsion data. *International shipbuilding progress*, 31(363), pp.272–276.
- Holtrop, J. & Mennen, J.G.G., 1982. An approximate power prediction method.
- Hountalas, D., Sakellaris, N. & Zovanos, G., 2013. Optimization of 2- stroke marine diesel engine fuel consumption via VIT setting using a model based monitoring & diagnosis technique: on-board test case. In International Council on Combustion Engines.
- IMO, 2014a. Resolution MEPC.245(66): 2014 guidelines on the method of calculation of the attained Energy Efficiency Design Index (EEDI) for new ships., 245(April).
- IMO, 2013. Resolution MEPC. 231(65): 2013 Guidelines for calculation of reference lines for use with the Energy Efficiency Design Index (EEDI)., 231(May), pp.1–12.
- IMO, 2014b. Third IMO GHG study.
- IMO MEPC 63/INF.2, I.M.O., Bazari, Z. & Longva, T., 2011. Assessment of IMO mandated energy efficiency measures for international shipping: estimated CO2 emissions reduction from introduction of mandatory
- IPCC, 2014. Summary for policymakers in: climate change 2014, mitigation of climate change. Contribution of working group III to the fifth assessment report of the intergovernmental panel on climate change
- ITTC, 1999. Final report of the specialist committee on unconventional propulsors., (February).
- Jin, W. & Vassalos, D., 2013. Energy modeling of large 2-stroke marine diesel engine using CFD.
- de Jong, H.J. & Fransen, H.P., 1976. N.S.M.B. trial allowances 1976., pp.319–320.
- Kawabuchi, M. et al., 2011. CFD predictions of bubbly flow around an energy-saving ship with Mitsubishi air lubrication system. *Mitsubishi Heavy Industries Technical Review*, 48(1), pp.53–57.
- Kim, K.-H. & Fraas, J.F., 1992. Propeller parametric study for mid-term fast sealift ships. *Proceedings of the Twenty-Third American Towing Tank Conference*, pp.195–2001.
- Klimt-Møllenbach, C. et al., 2012. ECA retrofit technology.
- Koronowicz, T. et al., 2010. A complete design of contra-rotating propellers using the new computer system. *Polish Maritime Research*, 17(1), pp.14–24.
- Kristensen, H.O., 2012. Energy demand and exhaust gas emissions of marine engines.
- Lauer, A. et al., 2007. Global model simulations of the impact of ocean-going ships on aerosols, clouds, and the radiation budget. *Atmospheric Chemistry and Physics Discussions*, 7(4), pp.9419–9464.
- Leigh-Jones, C., 2008. *A practical guide to marine fuel oil handling*, IMarEST.
- Lun, Y.H. (Venus), Lai, K.H. & Cheng, T.C.E., 2010. *Shipping and logistics management*, Springer.
- MAN Diesel and Turbo, 2015. Diesel-electric propulsion plants. , pp.1–27.
- MAN Diesel and Turbo, Exhaust gas emission control today and tomorrow: application

- on MAN B&W two-stroke marine diesel engines.
- MAN Diesel and Turbo, 2011. G-type engine: revolutionary ultra-long-stroke.
- MAN Diesel and Turbo, 2014a. Low container ship speed facilitated by versatile ME/ME-C engines.
- MAN Diesel and Turbo, 2014b. Marine engine IMO Tier II programme 2014.
- MAN Diesel and Turbo, 2014c. Thermo efficiency system for reduction of fuel consumption and CO<sub>2</sub> emissions.
- MAN Diesel and Turbo, 2014d. Waste Heat Recovery System (WHRS) for reduction of fuel consumption, emissions and EEDI.
- Mcgill, R., Remley, W. & Winther, K., 2013. Alternative fuels for marine applications. , (May).
- MEPC.1/Circ.683, 2009. Guidance for the development of a ship energy efficiency management plan (SEEMP).
- MEPC.1/Circ.684, 2009. Guidelines for voluntary use of the ship Energy Efficiency Operational Indicator (EEOI).
- MEPC.1/Circ.796, 2012. Interim guidelines for the calculation of the coefficient *k<sub>w</sub>* for decrease in ship speed in a representative sea condition for trial use. , 44(0).
- MEPC.177(58) Annex 14, 2010. Amendments to the technical code on control of emissions of nitrogen oxides from marine diesel engines. In pp. 1–101.
- MEPC.184(59) Annex 9, 2010. 2009 guidelines for exhaust gas cleaning systems. , 184(July), pp.1–24.
- MEPC.207(62) Annex 26, 2011. 2011 guidelines for the control and management of ships “bio fouling” to minimize the transfer of invasive aquatic species. , 207(July), pp.1–25.
- MEPC.213(63), 2012. 2012 guidelines for the development of a Ship Energy Efficiency Management Plan (SEEMP).
- MEPC 12th Session & Agenda Item 6, 2007. Review of Marpol Annex VI and NO<sub>x</sub> technical code.
- MEPC 212(63) Annex 8, 2012. Guidelines on the method of calculation of the attained Energy Efficiency Design Index (EEDI) for new ships.
- MEPC 53th Session & Agenda Item 4, 2005. Prevention of air pollution from ships: MARPOL Annex 6.
- MEPC 57th Session & Agenda Item 4, 2008. Prevention of air pollution from ships: CO<sub>2</sub> emissions index per unit shipping capacity., (January), pp.1–2.
- MEPC 58th Session & Agenda Item 4, 2008a. Prevention of air pollution from ships: proposal for refining the draft formula for CO<sub>2</sub> design index for new ships., (August), pp.5–8.
- MEPC 58th Session & Agenda Item 4, 2008b. Prevention of air pollution from ships: report of the outcome of the first intersessional meeting of the working group on greenhouse gas emissions from ships., (July).

- MEPC 68/INF.30, 2015. 2015 industry guidelines on calculation and verification of the Energy Efficiency Design Index (EEDI), 30.
- MER, 2012. Driving fuel costs down. *Marine Engineers Review*, (April).
- Metz, B., 2007. Climate change 2007.
- Molland, A.F., Turnock, S.R. & Hudson, D.A., 2011. *Ship resistance and propulsion*, Cambridge University Press.
- Mortensen, N.B., 2009. Ship fuel efficiency in a historical perspective. *BIMCO Bulletin*, 104(1), pp.38–46.
- Moulijn, J.C. et al., 2006. A criterion for the erosiveness of face cavitation. In *6th International Symposium on Cavitation CAV2006*. Wageningen.
- Munro-Smith, R., *Ships and naval architecture*, Hobbs.
- Murphy, J. et al., 2013. Modelling ship emission factors and emission indices. *Low Carbon Shipping Conference 2013*, p.18.
- Ok, J.P., 2004. *Numerical investigation of scale effects of Schneekluth's duct*. Hamburg Technical University, Germany.
- Oosterveld, M.W.C. & Van Oossanen, P., 1975. Further computer-analyzed data of the Wageningen B-screw series. *International Shipbuilding Progress*, 22(251).
- Papanikolaou, A., 2014. *Ship design : methodologies of preliminary design*, Springer.
- Perez Gomez, G. & Gonzalez-Adalid, J., 1998. *Detailed design of ship propellers*, F.E.I.N.
- Pestana, H., 2014. Future trends of electrical propulsion and implications to ship design.
- RAE, 2013. Future ship powering options.
- Reichel, M., Minchev, A. & Larsen, N.L., 2014. Trim optimisation - theory and practice., 8(3), pp.387–392.
- RINA, 1973. RINA simposium on ducted propellers., London.
- Schneekluth, H. & Bertram, V., 1998. Ship design for efficiency and economy 2nd, ed. *ButterworthHeinemann*, p.226.
- Siemens, 2013. SINAVY PEM fuel cell.
- Smith, T., Argyros, D., et al., 2014. Global marine fuel trends 2030.
- Smith, T., Day, S., et al., 2014. Low carbon shipping – a systems approach.
- Suarez, S., Fuente, D. & Greig, A.R., 2013. Making shipping greener : ORC modelling in challenging environments. , pp.1–17.
- Torvanger, A. et al., 2007. Climate regulation of ships.
- Townsend, C., 2009. Marine fuels and engines. *Naval Architect, Guido Perla & Associates, Inc.*
- Townsin, R.L. et al., 1980. Speed, power and roughness: the economics of outer bottom maintenance. *Naval Architect*, (5), pp.459–483.
- Trodden, D. & Woodward, M., 2013. Reduction of greenhouse gas emissions by propeller design for ship-in-service conditions. Powering and performance methodology.

- Tsimplis, M. et al., 2012. Regulated slow steaming in maritime transport: an assessment of options, costs and benefits.
- UNCTAD, 2015. Review of maritime transport.
- UNFCCC, 1998. Kyoto protocol to the United Nations framework. *Review of European Community and International Environmental Law*, 7(2), pp.214–217.
- Veenman, H. & Zonen, N. V., 1970. *Wake adapted ducted propellers*.
- Wärtsilä, 2010. Boosting energy efficiency.
- Whitelegg, I. & Bucknall, R., 2013. Electrical propulsion in the low carbon economy., pp.1–13.
- Woodyard, D., 2009. *Pounder's marine diesel engines and gas turbines* 9th ed. D. Woodyard, ed., Elsevier.
- Woud, H.K. & Stapersma, D., 2012. *Design of propulsion and electric power generation systems*,
- Yamatogi, T. et al., 2009. Study on cavitation erosion of composite materials for marine propeller. *University of Tokyo*.

# Appendix I. The Energy Efficiency Design Index Methodology

## *Historical Background*

The Energy Efficiency Design Index (EEDI) has been developed by the IMO over the past several years through a series of submissions to MEPCs 57-68 under the supervision of the 1<sup>st</sup> and 2<sup>nd</sup> Working Groups on Greenhouse Gases. The most recent version of the EEDI Guidelines is presented in Annex 5, MEPC.245 (66) “2014 Guidelines on the Method of Calculation of the Attained Energy Efficiency Design Index (EEDI) for New Ships”. However, during its last 68<sup>th</sup> MEPC session, which took place on 6<sup>th</sup> of March 2015, the “Industry guidelines on calculation and verification of the EEDI” (MEPC 68/INF.30 2015) have been prepared in addition to mentioned above in order to clarify the estimation and verification processes by providing a number of examples of calculation for all ship types. The EEDI was initially introduced by Japan as an “CO<sub>2</sub> Emissions Index” during the 57<sup>th</sup> MEPC session. The “CO<sub>2</sub> Emissions Index” was developed for a preliminary assessment of a ship performance at the design stage measured in units of grams of CO<sub>2</sub> per transport work. The main idea was to make the calculation procedure simple and capable for many applications (MEPC 57th Session & Agenda Item 4 2008). Hereafter, during the first intersessional meeting of the Working Group on Greenhouse Gas Emissions from Ships, the final documents GHG-WG 1/2/1/ and 1/2/2 were developed by Japan and Denmark. The basic assumptions on environmental impacts divided by the benefit to society were retained in both documents and the equation was presented in the simplified form as follows (the components are defined later in this Appendix):

$$Design\ CO_2\ index = \frac{C_F * SFC * P}{Capacity * V_{ref}}$$

Thereafter, the Denmark group has proposed to separate the emissions into those produced by the propulsive engines and those produced by auxiliary power diesel generators and to include additional factors for ship’s specific design elements in front of each of the contributing engine CO<sub>2</sub> emission components, taking into account the unique design elements, such as ice strengthening, cargo gear, and so on. This equation was presented as:

*Design CO<sub>2</sub> index*

$$= \frac{\prod_{j=1}^m f_j * \sum_{i=1}^{n_{ME}} C_{F_{ME_i}} * SFC_{ME_i} * P_{ME_i} + \prod_{k=1}^l f_k * \sum_{i=1}^{n_{AE}} C_{F_{AE_i}} * SFC_{AE_i} * P_{AE_i}}{Capacity * V_{ref}}$$

Next, the conclusive summary of the first intersessional meeting of the Working Group on Greenhouse Gas Emissions from Ships was prepared for the 58<sup>th</sup> MEPC session as the “Draft Guidelines on the Method of Calculation of the New Ship Design Index”, which can be found in Annex 5 of the document (MEPC 58th Session & Agenda Item 4 2008b), where the attained “design CO<sub>2</sub> index” was represented by the previously suggested formula with an additional correction factor  $f_w$  for rough weather conditions proposed by Japan:

*Design CO<sub>2</sub> index*

$$= \frac{\prod_{j=1}^m f_j * \sum_{i=1}^{n_{ME}} C_{F_{ME_i}} * SFC_{ME_i} * P_{ME_i} + \prod_{k=1}^l f_k * \sum_{i=1}^{n_{AE}} C_{F_{AE_i}} * SFC_{AE_i} * P_{AE_i}}{Capacity * V_{ref} * f_w}$$

This new formula was now better defined making it applicable to various ship types. In addition, a new factor related to “innovative energy efficiency technologies” was introduced by the United States in the MEPC 58/4/35 (MEPC 58th Session & Agenda Item 4 2008a):

*Design CO<sub>2</sub> index*

$$= \frac{(\sum_{i=1}^{n_{ME}} C_{F_{ME_i}} * SFC_{ME_i} * P_{ME_i}) + (\sum_{i=1}^{n_{AE_i}} C_{F_{AE_i}} * SFC_{AE_i} * P_{AE_i}) - (\sum_{eff=1}^{n_{eff}} f_{eff} * C_{F_{eff}} * SFC_{eff} * P_{eff})}{Capacity * V_{ref} * f_w}$$

As an outcome of the 58<sup>th</sup> MEPC session, the “CO<sub>2</sub> Emission Index” became the “Energy Efficiency Design Index”. Moreover, a new component which represents the shaft input motors as well as the reductions in fuel oil consumption from the waste heat recovery technologies was added to the formula together with the correction factor  $f_i$ , which reflects technical or regulatory limits on capacity.

The revised equation became:

$$EEDI = \frac{(\prod_{j=1}^M f_j) (\sum_{i=1}^{n_{ME}} C_{F_{ME_i}} SFC_{ME_i} P_{ME_i}) + (P_{AE} C_{FAE} SFC_{AE}) + (\sum_{i=1}^{n_{PTI}} P_{PTI_i} - \sum_{i=1}^{n_{WHR}} P_{WHR_i}) C_{FAE} SFC_{AE} - (\sum_{eff=1}^{n_{eff}} f_{eff} C_{F_{eff}} SFC_{eff} P_{eff})}{Capacity * V_{ref} * f_w}$$

After the second intersessional meeting of the Working Group on Greenhouse Gas Emissions from Ships, the equation was refined to the following form, which remained the same until the 63<sup>rd</sup> MEPC session.

$$EEDI = \frac{(\prod_{j=1}^m f_j) (\sum_{i=1}^{n_{ME}} C_{F_{ME(i)}} SFC_{ME(i)} P_{ME(i)}) + (P_{AE} C_{FAE} SFC_{AE}) + f_i * Capacity * V_{ref} * f_w}{f_i * Capacity * V_{ref} * f_w}$$

$$\frac{+ \left( \left( \prod_{j=1}^m f_j * \sum_{i=1}^{n_{PTI}} P_{PTI(i)} - \sum_{i=1}^{n_{eff}} f_{eff(i)} P_{AE_{eff(i)}} \right) C_{FAE} SFC_{AE} \right) - \left( \sum_{eff=1}^{n_{eff}} f_{eff(i)} P_{eff(i)} C_{FME} SFC_{ME} \right)}{f_i * Capacity * V_{ref} * f_w}$$

Then, the updated formulation of the EEDI index, with added cubic capacity correction factor  $f_c$ , was adopted during 63<sup>rd</sup> MEPC session and then published as “2012 Guidelines on the Method of Calculation of the Attained Energy Efficiency Design Index (EEDI) for New Ships” (MEPC 212(63) Annex 8 2012):

$$EEDI = \frac{\left( \prod_{j=1}^n f_j \right) \left( \sum_{i=1}^{n_{ME}} P_{ME(i)} C_{FME(i)} SFC_{ME(i)} \right) + \left( P_{AE} C_{FAE} SFC_{AE} \right) + \left( \left( \prod_{j=1}^m f_j * \sum_{i=1}^{n_{PTI}} P_{PTI(i)} - \sum_{i=1}^{n_{eff}} f_{eff(i)} P_{AE_{eff(i)}} \right) C_{FAE} SFC_{AE} \right) - \left( \sum_{eff=1}^{n_{eff}} f_{eff(i)} P_{eff(i)} C_{FME} SFC_{ME} \right)}{f_i * f_c * Capacity * V_{ref} * f_w}$$

The most recent EEDI formula has been adopted during the 66<sup>th</sup> MEPC session and, as previously stated, is available in Annex 5, MEPC.245 (66) “2014 Guidelines on the Method of Calculation of the Attained Energy Efficiency Design Index (EEDI) for New Ships” supported by newly developed “Industry guidelines on calculation and verification of the EEDI”, which have been adopted during the recent 68<sup>th</sup> MEPC session (MEPC 68/INF.30 2015).

The final EEDI formula additionally includes the correction factor  $f_l$  designed for general cargo ships equipped with cranes and other cargo-related gear:

$$EEDI = \frac{\left( \prod_{j=1}^n f_j \right) \left( \sum_{i=1}^{n_{ME}} P_{ME(i)} C_{FME(i)} SFC_{ME(i)} \right) + \left( P_{AE} C_{FAE} SFC_{AE} \right) + \left( \left( \prod_{j=1}^m f_j * \sum_{i=1}^{n_{PTI}} P_{PTI(i)} - \sum_{i=1}^{n_{eff}} f_{eff(i)} P_{AE_{eff(i)}} \right) C_{FAE} SFC_{AE} \right) - \left( \sum_{eff=1}^{n_{eff}} f_{eff(i)} P_{eff(i)} C_{FME} SFC_{ME} \right)}{f_i * f_c * f_l * Capacity * V_{ref} * f_w}$$

However, the EEDI formula development has been continuously ongoing as it still has some deficiencies such as it is not applicable to a ship having diesel-electric propulsion, turbine propulsion or hybrid propulsion system, except for cruise passenger ships and LNG carriers.

### ***Explanation of Terms***

- Conversion factors ( $C_{FME}$  and  $C_{FAE}$ )

Non-dimensional conversion factors are given for the following categories of fuels used in the marine industry: diesel/gas oil, light fuel oil (LFO), heavy fuel oil (HFO), liquefied petroleum gas (LPG) in form of butane, LPG in form of propane, liquefied natural gas

(LNG), methanol and ethanol. These conversion factors, listed in the (IMO 2014a), define an equivalent mass of  $CO_2$  normally emitted during the complete combustion of a given mass of fuel. The type of fuel used in the calculation of EEDI should be the same as the fuel burned for the estimation of the specific fuel consumption (SFC) in the Engine International Air Pollution Prevention (EIAPP) certificate.

- Certified specific fuel consumption ( $SFC_{ME}$  and  $SFC_{AE}$ )

Certified specific fuel consumption (SFC) is divided into two categories: main engine and auxiliary engine fuel consumption. Main engine fuel consumption is the specific fuel consumption measured in g/kWh reported in the EIAPP certificate for the parent engine in accordance with the  $NO_x$  Technical Code at 75 percent of the Maximum Continuous Rating (MCR). Auxiliary engine fuel consumption is the fuel consumption reported on the parent engine's EIAPP certificate at 50 percent of the MCR. If different sized auxiliary engines are used, a single SFC is entered into the equation by taking the weighted average of the different engines.

- Power ( $P_{ME}, P_{AE}, P_{PTI}$ )

The main engine power  $P_{ME}$  used in the EEDI calculation is 75 percent of the MCR of the engine measured in kW minus the output of any shaft generators and should be calculated as follows:

$$\sum_{i=1}^{n_{ME}} P_{ME(i)} = 0.75 * \left( \sum MCR_{ME(i)} - \sum P_{PTO(i)} \right)$$

where  $P_{PTO(i)}$  is the 75 percent of the rated electrical output power of each shaft generator defined as  $0.75 * \sum P_{PTO(i)} \leq P_{AE}$

The power from auxiliary engines  $P_{AE}$  is determined by an empirical formula representing the hotel load and electrical needs for propulsion systems and machinery. Auxiliary power is taken as a function of the MCR of the main engine(s). The second formula is adjusted for vessels that have smaller propulsion engines with the installed MCR less than 10,000 kW. Additional shaft motor  $P_{PTI}$  inputs are given at 75 percent of the rated power consumption divided by the weighted average of the efficiency of the generators.

$$P_{AE(\sum MCR_{ME(i)} \geq 10000 \text{ kW})} = \left( 0.025 * \left( \sum_{i=1}^{n_{ME}} MCR_{ME(i)} + \frac{\sum_{i=1}^{n_{PTI}} P_{PTI(i)}}{0.75} \right) \right) + 250$$

$$P_{AE(\sum MCR_{ME(i)} \leq 10000 \text{ kW})} = \left( 0.05 * \left( \sum_{i=1}^{n_{ME}} MCR_{ME(i)} + \frac{\sum_{i=1}^{n_{PTI}} P_{PTI(i)}}{0.75} \right) \right)$$

- Innovative energy efficiency technologies ( $P_{eff}$ ,  $P_{AE_{eff}}$  and  $f_{eff}$ )

$P_{eff(i)}$  is the output of the innovative mechanical energy efficient technology for propulsion at 75 percent MCR of the main engine. Mechanical recovered waste energy directly coupled to shafts need not be measured, since the effect of the technology is directly reflected in the  $V_{ref}$ . In case of a ship equipped with a number of engines, the  $CF$  and  $SFC$  should be the power weighted average of all the main engines.

$P_{AE_{eff(i)}}$  is the auxiliary power reduction due to innovative electrical energy efficient technology measured at  $P_{ME(i)}$ .

$f_{eff(i)}$  is the availability factor of each innovative energy efficiency technology, which in the case of the waste energy recovery system should be equal to one.

- Ship's speed ( $V_{ref}$ )

The speed used in the EEDI calculation is the ship's speed measured in nautical miles when operating at draught corresponding to the *Capacity* as defined in paragraphs 2.3.1 and 2.3.3 of (IMO 2014a) and at trim as defined by the corresponding condition specified in the approved stability booklet. It is also assumed that ship's speed correlates to the shaft power  $P_{ME}$  of the engine operating in deep sea and assuming the weather is calm with no wind and no waves.

- Capacity (*Capacity*)

Capacity is defined as deadweight (DWT) for bulk carriers, tankers, gas carriers, LNG carriers, ro-ro cargo ships (vehicle carriers), ro-ro cargo ships, ro-ro passenger ships, general cargo ships, refrigerated cargo carrier and combination carriers. For passenger ships and cruise passenger ships, gross tonnage (GT) should be used as capacity. Capacity for containerships is adjusted to be 70 percent of the DWT.

Deadweight means the difference in tonnes between the displacement of a ship in water of relative density of 1,025 kg/m<sup>3</sup> at the summer load draught and the lightweight of the ship. The summer load draught should be taken as the maximum summer draught as certified in the stability booklet.

- Correction factors ( $f_j$ ,  $f_i$ ,  $f_c$ ,  $f_l$  and  $f_w$ )

The correction factor  $f_j$  accounts for ship specific design elements including ships designed with an ice class notation, shuttle tankers with propulsion redundancy, ro-ro cargo and ro-

ro passenger ships and general cargo ships, which calculation details can be found in section 2.8 of (IMO 2014a). For other ship types,  $f_j$  should be taken as one.

The correction factor  $f_i$  is related to any technical or regulatory limit on capacity in case of ice-classed ships, ships with specific voluntary enhancements or bulk carrier and oil tankers built in accordance with the Common Structural Rules (CSR) of the classification societies and assigned the class notation CSR. The calculation process of  $f_i$  is explained in section 2.11 of (IMO 2014a). For other ship types,  $f_i$  should be taken as one.

The factor  $f_c$  is the cubic capacity correction factor that should be added to EEDI calculations in case of chemical tankers, gas carriers with direct diesel driven propulsion system constructed or adapted to use for the carriage in bulk of liquefied natural gas and ro-ro passenger ships with a DWT/GT ratio of less than 0.25 in accordance to section 2.12 of (IMO 2014a). For other ship types,  $f_c$  should be taken as one.

$f_l$  is the factor for general cargo ships equipped with cranes and other cargo-related gear to compensate a loss of deadweight of the ship calculated in accordance to 2.13 of (IMO 2014a) or taken as one if not applicable.

$f_w$  is a factor representing the decrease in speed in certain sea conditions of wave height, wave frequency and wind speed (Beaufort Scale 6), and, if calculated according to the (MEPC.1/Circ.796 2012), the value for attained EEDI should be referred as  $EEDI_{Weather}$ . This weather correction factor can be determined by conducting the ship specific simulation on its performance at representative sea conditions. Otherwise, if the simulation is not available,  $f_w$  can be estimated using “standard  $f_w$ ” curve, which is only provided for bulk carrier, tanker and container ship as specified below:

$$f_w = a * \ln(Capacity) + b$$

where  $a$  and  $b$  are the parameters given in Table A 1.

Table A 1. Parameters for determination of standard  $f_w$  value.

Ship Type	A	b
Bulk carrier	0.0429	0.294
Tanker	0.0238	0.526
Container ship	0.0208	0.633

It is important to note, that inclusion of  $f_w$  is a voluntary option and should be taken as one in case of a conventional EEDI estimation process.

### ***EEDI Reference Line Methodology***

A methodology used for development of the reference line curves for the EEDI has been introduced by Denmark and, for the first time, suggested in the MEPC 58/4/8. Then, in GHG-WG 2/2/7, Denmark updated the methodology to reflect the latest update of the EEDI formula. The most recent version of the EEDI reference line calculation methodology has been adopted on 17<sup>th</sup> of May 2013. The document is titled “2013 guidelines for calculation of reference lines for use with the energy efficiency design index (EEDI)” (IMO 2013).

The reference lines are established for each of the following ship types: bulk carrier, gas carrier, tanker, container ship, general cargo ship, refrigerated cargo carrier, combination carrier, ro-ro cargo ship, ro-ro cargo ship (vehicle), ro-ro passenger ship and LNG carrier. It is noted that a method of calculating reference lines has not been established for passenger ships other than cruise passenger ship having non-conventional propulsion.

Generally, a reference lines defined as a curve representing an average index value fitted on a set of individual index values for a defined group of ships. The data used for the calculation of the reference line is derived from the IHS Fairplay vessel database of all ships of a particular type that were built in the period the years 1999-2009. In order to get baseline EEDI for each data point, simplifying assumptions were required to adjust for missing information in the IHSF database. Some of the simplifying assumptions are:

- Conversion factors ( $C_{F_{ME}}$  and  $C_{F_{AE}}$ )

A single fuel type, the heavy fuel oil (HFO), is assumed to be used in all engines, both propulsion and auxiliary. Therefore, the carbon emission factor is constant for all engines and equals to  $3.1144 \text{ g}_{CO_2}/\text{g}_{fuel}$ .

- Certified specific fuel consumption ( $SFC_{ME}$  and  $SFC_{AE}$ )

As the specific fuel consumption data was not always available in the IHSF database, a constant value of 190 g/ kW-hr has been applied to all propulsion engines. Auxiliary engine fuel consumption is also assumed to be constant and has been taken as 215 g/ kW-h.

- Power ( $P_{ME}$ ,  $P_{AE}$ )

Similarly to the EEDI formula,  $P_{ME}$ , is taken as 75 percent of listed MCR in the database.  $P_{AE}$  has been estimated using the same empirical formula as for the EEDI calculations.

- Speed ( $V_{ref}$ )

$V_{ref}$  used for the estimation of the reference line is the speed listed in the IHSF database.

- Capacity (*Capacity*)

*Capacity* remains as DWT at the deepest operational draught as available in the IHSF database.

- Innovative energy efficiency technologies ( $P_{eff}$ ,  $P_{AE_{eff}}$  and  $f_{eff}$ )

All innovative energy efficiency technology corrections are excluded from the reference line calculation even if data is available in the IHSF database.

- Correction factors ( $f_j$ ,  $f_i$ ,  $f_c$ ,  $f_l$  and  $f_w$ )

No correction factors are used.

The baseline index values have been calculated for all ships excluding containerships and re-re cargo (vehicle) ships as follows:

$$\text{Estimated Index Value} = 3.1144 * \frac{190 * \sum_{i=1}^{n_{ME}} P_{ME_i} + 215 * P_{AE}}{\text{Capacity} * V_{ref}}$$

For container ships, 70 percent of the DWT is used as capacity for calculating the estimated index value for each container ship as follows:

$$\text{Estimated Index Value} = 3.1144 * \frac{190 * \sum_{i=1}^{n_{ME}} P_{ME_i} + 215 * P_{AE}}{0.7 * \text{Capacity} * V_{ref}}$$

For ro-ro cargo ships the following equation is used:

$$\text{Estimated Index Value} = f_{RoRoV} * 3.1144 * \frac{190 * \sum_{i=1}^{n_{ME}} P_{ME_i} + 215 * P_{AE}}{\text{Capacity} * V_{ref}}$$

where  $f_{RoRoV}$

$$= \frac{-15571 * F_n^2 + 5538.4 * F_n - 132.67}{287} \text{ and } F_n \text{ is ship's Froude number.}$$

Data sets with missing values are omitted. A single regression line is then plotted through the values of the following form:

$$\text{Baseline} = a * \text{Capacity}^{-c}$$

Outliers from the regression lines of more than two standard deviations are removed and a new regression line is plotted.

The following Table A 2 lists the estimated values  $a$  and  $c$  for the required EEDI depending on the ship type as stated in (Germanischer Lloyd 2013).

Table A 2. Variables for calculating the required EEDI.

<b>Ship type</b>	<b>A</b>	<b>Capacity</b>	<b>c</b>
Bulk carriers	961.79	DWT	0.477
Gas carriers	1120.20	DWT	0.456
Tankers	1218.80	DWT	0.488
<b>Ship type</b>	<b>A</b>	<b>Capacity</b>	<b>c</b>
Container ships	174.22	DWT	0.201
General cargo ships	107.48	DWT	0.216
Refrigerated cargo ships	227.01	DWT	0.244
Combination carriers	1219.00	DWT	0.488
Vehicle/car carriers	$\left(\frac{DWT}{GT}\right) - 0.7 * 780.36$ where $\frac{DWT}{GT} < 0.3$ $\left(\frac{DWT}{GT}\right) - 0.7 * 1812.63$ where $\frac{DWT}{GT} \geq 0.3$	DWT	0.471
Ro-Ro cargo ships	1405.15	DWT	0.498
Ro-Ro passenger ships	752.16	DWT	0.381
LNG carriers	2253.7	DWT	0.474
Cruise passenger ships with non-conventional propulsion	170.84	GT	0.214

The required EEDI is planned to be reduced by 10 percent each five-year phase based on the initial value and depending on the vessel size.

## Appendix II. Propeller Design Procedure for Wageningen series

Based on tentative values of propeller diameter  $D'(m)$  and blade area ratio  $BAR'$  as well as a number of hull design parameters including moulded breadth  $B(m)$ , wetted surface area  $S(m^2)$ , length of the waterline  $L_{WL}(m)$ , ship's draught  $T(m)$  and draught aft  $T_A(m)$ , stern shape coefficient  $C_{stern}$ , ( $C_{stern} = 0$  in this case (Holtrop 1984)), viscous resistance coefficient  $C_V$ , longitudinal position of centre of buoyance  $lcb(\%)$ , prismatic  $C_P$  and block  $C_B$  coefficients calculate the mean design Taylor's wake fraction  $w$ , thrust deduction coefficient  $t$  and the relative-rotative efficiency  $\eta_R$  using the Holtrop and Mennen propulsion analysis regression based method as described in Chapter 5.1 ( equations 5.7–5.9). Alternatively, those provided in a model test report or other sources should be applied. Then calculate the hull efficiency  $\eta_H$ :

$$\eta_H = \frac{(1 - t)}{(1 - w)} \quad \text{A II. 1}$$

Based on the reference ship's speed  $V_S(knot)$  calculate the speed of advance  $V_A(knot)$ :

$$V_A = V_S * (1 - w_T) \quad \text{A II. 2}$$

Assume a range of delivered powers  $P'_D(BHP)$  suitable for this type of ship:

$$P'_D = (P'_{D_i}, P'_{D_{i+1}}, \dots, P'_{D_{n-1}}, P'_{D_n}) \quad \text{A II. 3}$$

Using the given rotational speed  $N(rpm)$  and a required number of the propeller blades  $Z$ , calculate the range of Admiral Taylor's coefficients  $Bp'$ , regression based van Gunsteren coefficients  $\delta'_{opt}$  for Wageningen B-Screw series, behind (actual) propeller diameters  $D'_b(ft)$ , behind hull  $\delta'_b$  coefficients, advanced coefficients  $J'$  and Reynolds numbers  $Rn'$  for each point of the delivered power  $P'_D$  range

$$Bp'_i = \frac{\sqrt{P'_{D_i} * N}}{V_A^{2.5}} \quad \text{A II. 4}$$

$$\delta'_{opt_i} = 100 * \left[ \frac{Bp_i'^3}{(155.3 + 75.11\sqrt{Bp_i'} + 36.76Bp_i')} \right]^{0.2} \quad \text{A II. 5}$$

$$* \left[ 0.9365 + \frac{1.49}{Z} - \left( \frac{2.101}{Z} - 0.1478 \right)^2 * BAR' \right]$$

$$D'_{b_i} = \frac{V_A * \delta'_{opt_i}}{N} * 0.96 \quad \text{A II. 6}$$

$$\delta'_{b_i} = \frac{D'_{b_i} * N}{V_A} \quad \text{A II. 7}$$

$$J'_i = \frac{101.33}{\delta'_{b_i}} \quad \text{A II. 8}$$

$$Rn'_i = \frac{\rho * n * D'_{b_i}{}^2}{\mu} \quad \text{A II. 9}$$

where  $\rho$  is water density ( $kg * m^{-3}$ ),  $n$  is the rotations per second ( $rps$ ),  $D'_b$  is behind the propeller diameters (A II. 6) converted to ( $m$ ) and  $\mu$  is the coefficient of dynamic viscosity in ( $Pa * s$ ).

Then, set up a range of pitch to diameter ratios  $(P/D)''$  applicable to the Wageningen B-screw series:

$$(P/D)'' = ((P/D)''_j, (P/D)''_{j+1}, \dots, (P/D)''_{m-1}, (P/D)''_m) \quad \text{A II. 10}$$

Using the Wageningen B-screw series regression based method with Reynolds number correction described in (Oosterveld & Van Oossanen 1975), obtain a range of torque  $K''_Q$  and thrust  $K''_T$  coefficients forming the matrix ( $n \times m$ ) such as  $n$  is the number of obtained diameters  $D'_b$  ( $m$ ) and  $m$  is the number of examinee  $(P/D)''$  values.

$$K''_{Q_{i,j}}, K''_{T_{i,j}} = f_{wageningen}(J'_i, (P/D)''_j, BAR', Z, Rn'_i) \quad \text{A II. 11}$$

where  $J'$  is the range of advanced coefficients and  $Rn'$  represents Reynolds numbers derived previously from A II. 8 and A II. 9 respectively.

Based on previously obtained  $K''_Q$  matrix (A II. 11), the matrix of Admiral Taylor's coefficients  $Bp''$  corresponding to the interlinked relationship between the delivered power  $P'_D$  (BHP) range and the pitch to diameter ratios  $(P/D)''$  could be calculated as follows:

$$Bp''_{i,j} = 23.77 * \frac{\rho * K''_{Q_{i,j}}}{J'^5_i} \quad \text{A II. 12}$$

where  $\rho$  is the mass density of water, in case of sea water  $\rho = 1.99$  ( $slug * ft^{-3}$ ), and  $J'$  is the range of advanced coefficients estimated using the equation A II. 8.

By means of cubic spline interpolation procedure, estimate the range of pitch to diameter ratios  $(P/D)'$  in relation to the delivered power  $P'_D$  values. More specifically, interpolate

individual  $Bp'$  values estimated by the equation (A II. 4) to each row of the  $Bp''$  matrix (A II. 12) and corresponded to it range of  $(P/D)''$  (A II. 10).

$$(P/D)'_i(Bp'_i) = (Bp''_{i,j}(P/D)''_j) \quad \text{A II. 13}$$

Obtain new torque  $K'_Q$  and thrust  $K'_T$  propeller coefficients in relation to the previously interpolated  $(P/D)'$  using the Wageningen B-screw series regression-based approach and, based on that, calculate the open water efficiency  $\eta'_O$  range:

$$K'_{Q_i}, K'_{T_i} = f_{wageningen}(J'_i, (P/D)'_i, BAR', Z, Rn'_i) \quad \text{A II. 14}$$

$$\eta'_{O_i} = \frac{J'_i}{2\pi} * \frac{K'_{Q_i}}{K'_{T_i}} \quad \text{A II. 15}$$

As such, a set of Quasi-Propulsive Coefficients  $QPC'$  and a range of effective powers  $P'_E(kW)$  can be calculated:

$$QPC'_i = \eta_R * \eta_H * \eta'_{O_i} \quad \text{A II. 16}$$

where  $\eta_R$  is the relative-rotative efficiency and  $\eta_H$  is the hull efficiency estimated by Holtrop and Mennen propulsion analysis procedure and equation (A II. 1) respectively.

$$P'_{E_i} = QPC'_i * P'_{D_i} \quad \text{A II. 17}$$

where  $P'_D$  is the initially drawn delivered power range in kW (A II. 3). Then interpolate the actual delivered power value  $P_D(kW)$  based on the previously obtained range of the effective powers  $P'_E(kW)$  and the initial effective power  $P_E(kW)$  derived from the Holtrop and Mennen power prediction procedure (Holtrop & Mennen 1982) or the model test report:

$$P_D(P_E) = (P'_{E_i} P'_{D_i}) \quad \text{A II. 18}$$

Based on the interpolated actual delivered power  $P_D(kW)$  repeat previously described procedure and calculate the correct values of Admiral Taylor coefficient  $Bp$ , regression based van Gunsteren coefficient  $\delta_{opt}$  for Wageningen B-screw series, the actual propeller diameter  $D_b(m)$ , behind the hull  $\delta_b$  coefficient, the advanced coefficient  $J$  and the Reynolds number  $Rn$ .

$$Bp = \frac{\sqrt{P_D} * N}{V_A^{2.5}} \quad \text{A II. 19}$$

where  $P_D$  is the actual delivered power converted from  $kW$  to  $ft$ ,  $V_A$  is the speed of advance in *knots* and  $N$  is the rotational speed in *rpm*.

$$\delta_{opt} = 100 * \left[ \frac{Bp^3}{(155.3 + 75.11\sqrt{Bp} + 36.76Bp)} \right]^{0.2} \quad \text{A II. 20}$$

$$* \left[ 0.9365 + \frac{1.49}{Z} - \left( \frac{2.101}{Z} - 0.1478 \right)^2 * BAR' \right]$$

$$D_b = \frac{V_A * \delta_{opt}}{N} * 0.96 \quad \text{A II. 21}$$

$$\delta_b = \frac{D_b * N}{V_A} \quad \text{A II. 22}$$

$$J = \frac{101.33}{\delta_b} \quad \text{A II. 23}$$

$$Rn = \frac{\rho * n * D_b}{\mu} \quad \text{A II. 24}$$

where  $\rho$  is water density ( $kg * m^{-3}$ ),  $n$  is the rotational speed (*rps*),  $D_b$  is behind the propeller diameter (A II. 21) converted to (*m*) and  $\mu$  is the coefficient of dynamic viscosity in ( $Pa * s$ ).

In order to estimate the actual pitch to diameter ratio  $P/D$  the procedures (A II. 11 – A II. 13) should be repeated, such as first calculate the range of  $K_Q'''$  and  $K_T'''$  propeller coefficients in correspondence to selection of  $(P/D)''$  (A II. 11) and newly received  $J$  (A II. 23) and  $Rn$  (A II. 24) and then, based on that, estimate a range of Admiral Taylor's coefficients  $Bp'''$ .

$$K_{Q_j}''', K_{T_j}''' = f_{wageningen}(J, (P/D)_j'', BAR', Z, Rn) \quad \text{A II. 25}$$

$$Bp_j''' = 23.77 * \frac{\rho * K_{Q_j}'''}{J^5} \quad \text{A II. 26}$$

where  $\rho$  is the mass density of water, in case of sea water  $\rho = 1.99$  ( $slug * ft^{-3}$ ).

The next step is to interpolate the actual  $P/D$  value from the  $(P/D)''$  set (A II. 10) based on the range of  $Bp'''$  coefficients (A II. 26) and the actual  $Bp$  value (A II. 19). Additionally,

the actual  $P/D$  value should be decreased by 1.5% in case of the Wageningen B4 series (4 blades).

$$P/D(Bp) = (Bp_j''', (P/D)_j'') \quad \text{A II. 27}$$

$$(P/D)_{mean} = \frac{P/D}{1.015} \quad \text{A II. 28}$$

At this point, calculate the final  $K_Q$  and  $K_T$  coefficients along with the expected open water efficiency  $\eta_0$ :

$$K_Q, K_T = f_{wageningen}(J, P/D, BAR', Z, Rn) \quad \text{A II. 29}$$

$$\eta_0 = \frac{J}{2\pi} * \frac{K_Q}{K_T} \quad \text{A II. 30}$$

The last step is to calculate an expanded blade area ratio  $BAR$ , which is in this case is estimated using the Burrill's method (Burrill 1943).

$$BAR = f_{Burrill}(T, CL, SW, V_A, N, K_T, P/D) \quad \text{A II. 31}$$

where  $T(m)$  is the ship's design draught,  $CL(m)$  is the height of shaft centre line from base line,  $SW(m)$  is the height of stern wave,  $V_A(knots)$  is the speed of advance (A II. 2),  $N(rpm)$  is the propeller rotational speed,  $K_T$  is the thrust coefficient calculated by (A II. 29) and  $P/D$  is the actual pitch to diameter ratio derived from (A II. 28).

This propeller design procedure should be repeated by implementing the received values of the actual delivered power  $P_D$  (calculated by the propeller analysis procedure), propeller diameter  $D_b$ , blade area ratio  $BAR$  and pitch to diameter ratio  $P/D$  until they stabilize.

### Appendix III. Blade Area Ratio Estimation Procedure

First, calculate the immersion to shaft centre line  $H(m)$  by deduction of the height of shaft centre line  $CL(m)$  from the ship's draught  $T(m)$ . However, for more accurate calculations add an approximate height of stern wave  $SW(m)$  to estimate the total immersion  $H_T(m)$ :

$$H = T - CL \quad \text{A III.1}$$

$$H_T = H + SW \quad \text{A III.2}$$

Calculate a static head  $P^{-e}(lbf * in^{-2})$  and a dynamic head  $q_T(lbf * in^{-2})$  based on Burrill's approach (Burrill 1943).

$$P^{-e} = 14.45 + 0.45 * H_T \quad \text{A III.3}$$

where  $\rho_0$  is static pressure of the shaft centre line,  $\rho_v$  is saturated vapour pressure and  $H_T$  is converted to  $ft$ .

$$q_T = \left(\frac{V_A}{7.12}\right)^2 + \left(\frac{N * D}{329}\right)^2 \quad \text{A III.4}$$

where the propeller diameter  $D$  is in  $ft$ . Further, based on previous calculations (A III.3) and (A III.4) estimate a local cavitation number  $\sigma$

$$\sigma = \frac{P^{-e}}{q_T} \quad \text{A III.5}$$

Using the Burrill's cavitation diagram for uniform flow taken from (Burrill 1943) interpolate a thrust loading coefficient  $\tau_c$  for 5 percent cavitation allowance (or 2.5 percent if desired) based on the previously obtained cavitation number  $\sigma$ .

$$\tau_c(\sigma) = (\sigma'_i, \tau_{c'_i}) \quad \text{A III.6}$$

where  $\sigma'$  and  $\tau_c'$  are the ensemble of points taken from Burrill's diagram 5 percent cavitation allowance curve (or 2.5 percent if desired). Then, calculate a total propeller thrust  $T(kN)$ :

$$T = K_T * \rho * n^2 * D^4 \quad \text{A III.7}$$

where  $K_T$  is the propeller thrust coefficient estimated by Wageningen B-screw series method using (A II. 29),  $\rho(kg * m^{-3})$  is water density,  $n$  is the rotational speed per second and  $D(m)$  is the propeller diameter. Based on the obtained thrust value  $T(kN)$  estimate a propeller projected area  $A_p(m^2)$ :

$$A_P = \frac{T}{\tau_C * \sigma} \quad \text{A III.8}$$

where  $\tau_C$  is converted from ( $lbf * in^{-2}$ ) to  $Pa$ .

To derive the expanded area  $A_E(m^2)$  from the projected area  $A_P(m^2)$ , Burrill provided the following empirical relationship which could be applied only for the conventional propeller forms:

$$A_E = \frac{A_P}{(1.067 - 0.229 * P/D)} \quad \text{A III.9}$$

where  $P/D$  is the pitch to diameter ratio. Finally, the blade area ratio  $A_E/A_O$  should be calculated as follows:

$$BAR = A_E/A_O = \frac{A_E}{\frac{\pi}{4} * D^2} \quad \text{A III.10}$$

where  $A_O(m^2)$  is a disk area.